

# Integrated Microcantilever Fluid Sensor as a Blood Coagulometer

Richard John Dunn

A dissertation submitted for the degree of Doctor of Engineering

Heriot-Watt University

School of Engineering and Physical Sciences

October 2010

The copyright in this thesis is owned by the author. Any quotation from the thesis or use of any of the information contained in it must acknowledge this thesis as the source of the quotation or information.

## **Abstract**

The work presented concerns the improvement in mechanical to thermal signal of a microcantilever fluid probe for monitoring patient prothrombin time (PT) and international normalized ratio (INR) based on the physical measurement of the clotting cascade. The current device overcomes hydrodynamic damping limitations by providing an internal thermal actuation force and is realised as a disposable sensor using an integrated piezoresistive deflection measurement. Unfortunately, the piezoresistor is sensitive to thermal changes and in the current design the signal is saturated by the thermal actuation. Overcoming this problem is critical for demonstrating a blood coagulometer and in the wider field as a microsensor capable of simultaneously monitoring rheological and thermal measurements of micro-litre samples. Thermal, electrical, and mechanical testing of a new design indicates a significant reduction in the thermal crosstalk and has led to a breakthrough in distinguishing the mechanical signal when operated in moderately viscous fluids (2-3 cP).

A clinical evaluation has been conducted at The Royal London Hospital to measure the accuracy and precision of the improved microcantilever fluid probe. The correlation against the standard laboratory analyser INR, from a wide range of patient clotting times (INR 0.9-6.08) is equal to 0.987 (n=87) and precision of the device measured as the percentage coefficient of variation, excluding patient samples tested < 3 times, is equal to 4.00% (n=64). The accuracy and precision is comparable to that of currently available point-of-care PT/INR devices. The response of the fluid probe in glycerol solutions indicates the potential for simultaneous measurement of rheological and thermal properties though further work is required to establish the accuracy and range of the device as a MEMS based viscometer.

*For Sarah and my family.*

### **Acknowledgements**

Thank you to Ejaz Huq, Ajoy Kar, John Curtis and Jeremy Peckham for the opportunity to work on a great project and the continued support from all. Special thanks to Slava Djakov for supervision during the project, productive discussions, and to the dedication of Slava and Ejaz to drive the technology forward.

Thank you to the Microvisk team who it has been a pleasure to work with and special thanks to Joe Booth for his many contributions and stimulating questions.

Many thanks' to John Pasi and his colleagues at The Royal London Hospital for the opportunity and support of clinical measurements, and to Bob Ibbotson for his early support of the first measurements in Chester and for performing mechanical sensitivity measurements.

The author acknowledges the contribution of Microvisk Ltd in the clinical evaluation presented in this thesis, which includes, performing the patient tests onsite at The Royal London Hospital, the choice of noise filter applied to the clinical data, and performing an excel routine to extract clotting time from the filtered data.



# ACADEMIC REGISTRY

## Research Thesis Submission



|   |  |   |  |
|---|--|---|--|
| Name:   |  |   |  |
| School/PGI:                                       |  |   |  |
| Version: <i>(i.e. First, Resubmission, Final)</i> |  | Degree Sought<br>(Award <b>and</b><br>Subject area) |  |

### **Declaration**

In accordance with the appropriate regulations I hereby submit my thesis and I declare that:

- 1) the thesis embodies the results of my own work and has been composed by myself
- 2) where appropriate, I have made acknowledgement of the work of others and have made reference to work carried out in collaboration with other persons
- 3) the thesis is the correct version of the thesis for submission and is the same version as any electronic versions submitted\*.
- 4) my thesis for the award referred to, deposited in the Heriot-Watt University Library, should be made available for loan or photocopying and be available via the Institutional Repository, subject to such conditions as the Librarian may require
- 5) I understand that as a student of the University I am required to abide by the Regulations of the University and to conform to its discipline.

\* *Please note that it is the responsibility of the candidate to ensure that the correct version of the thesis is submitted.*

|                         |  |       |  |
|-------------------------|--|-------|--|
| Signature of Candidate: |  | Date: |  |
|-------------------------|--|-------|--|

### **Submission**

|  |  |
|--|--|
| Submitted By <i>(name in capitals)</i> : |  |
| Signature of Individual Submitting:      |  |
| Date Submitted:                          |  |

### **For Completion in Academic Registry**

|  |  |       |  |
|--|--|-------|--|
| Received in the Academic Registry by <i>(name in capitals)</i> :   |  |       |  |
| <b>Method of Submission</b><br><i>(Handed in to Academic Registry; posted through internal/external mail):</i> |  |       |  |
| <b>E-thesis Submitted (mandatory for final theses from January 2009)</b>                                       |  |       |  |
| Signature:   |  | Date: |  |

Please note this form should bound into the submitted thesis.

Updated February 2008, November 2008, February 2009

## **List of Publications**

### **Patents**

- [1] V. Djakov, R. J. Dunn, and E. Huq, “Fluid Probe” International Publication Number WO 2007/104978, 16<sup>th</sup> March 2006.
- [2] V. Djakov and R. J. Dunn, “Fluid Probe” International Publication Number WO 2009/022121, 11<sup>th</sup> August 2007.

### **Journal Papers**

- [3] R. J. Dunn, E. Huq, and A. K. Kar, “Measurement of large microcantilever curvature using an autofocusing technique”, *J. Micro. Electro. Mech. Sys.* (Submitted to IEEE JMEMS, Presently under revision in the light of referee comments).
- [4] R. J. Dunn, V. Djakov, E. Huq, and J. Booth, “An integrated microsensor for fluid analysis”, *Applied Physics Letters*. (Submitted to APL but deemed unsuitable for that journal. To be revised and submitted to Sensors and Actuators A: Physical).
- [5] R. J. Dunn, V. Djakov, J. Booth, G. Jones, J. Pasi, and K. Langley, “An integrated nanomechanical fluid sensor as a blood coagulometer”, *Nature Biotechnology*. (To be submitted)

### **Conference Papers**

- [6] R. H. Ibbotson , R. J. Dunn , V. Djakov , P. Ko Ferrigno , and S. E. Huq, “Polyimide microcantilever surface stress sensor using low-cost, rapidly-interchangeable, spring-loaded microprobe connections”, *Microelectronic Engineering*, **85** (5-6), pp.1314-1317 (2008).
- [7] J. Pasi, K. Langley, J. Booth, V. Djakov, R. J. Dunn, and G. Jones, “Evaluation of novel micro-electro-mechanical sensors (MEMS) for measuring real-time blood coagulation”, *Haemophilia*, **14**, (Suppl. 2), 1-20 (2008).

## **Glossary of Terms**

### **Actuation Efficiency**

Describes the microcantilever tip deflection induced during thermal actuation, measured against the power dissipated in the device ( $\mu\text{m.mW}^{-1}$ ). In combination with the conversion efficiency ( $\mu\text{m.}^{\circ}\text{C}^{-1}$ ) the temperature increase measured against the power dissipated can also be quantified ( $^{\circ}\text{C.mW}^{-1}$ ).

### **Conversion Efficiency**

Describes the microcantilever tip deflection induced during thermal actuation, measured against the change in temperature in the device ( $\mu\text{m.}^{\circ}\text{C}^{-1}$ ). For multilayer microcantilevers with integrated heaters the temperature is measured from the change in resistance of the metal heater converted using the temperature coefficient of resistance of the metal film. For integrated heaters the temperature is measured as an average increase as a temperature gradient is expected on the beam.

### **Mechanical Sensitivity**

Describes the percentage change in resistance of the integrated piezoresistive sensor, presented as parts per million, for a mechanical deflection ( $\Delta R/R.\mu\text{m}^{-1}$ ) applied at the tip of the beam. The mechanical sensitivity is related to the piezoresistor Gauge factor, a material constant that describes the proportional change in material resistance for induced strain.

### **Thermal Crosstalk**

Describes the percentage change in resistance of the integrated piezoresistive sensor, presented as parts per million, for a change in temperature induced by powering the thermal actuation of the device ( $\Delta R/R.\text{mW}^{-1}$ ). The magnitude of the change in resistance is dependent on a material constant called the temperature coefficient of resistance (TCR).

### **Neutral Axis**

The neutral axis is defined as the plane in which the resultant axial force acting on the cantilever cross section is zero and is taken as the line at which the curvature of the beam is measured.

### Flexural Rigidity

The flexural rigidity of a cantilever beam describes the resistance to bending through the cross section by compression or tension. Mathematically this is defined as the force required to bend the structure by unit curvature. This is related to the moment of area of an element located a distance from the neutral axis and the elasticity of this element. The flexural rigidity of the fluid probe is an important parameter as this governs the power which is needed to actuate the device and the restoring force to pull the beam back through the fluid.

### Gauge Factor

The piezoresistor Gauge factor is a non-dimensional material constant that describes the proportional change in material resistance to induced strain in the material. For the fluid probe the integrated piezoresistor is realised through metal thin film deposition. For such films the Gauge factor is based on geometric changes in the film and has a value typically  $< 4$ .

### Temperature Coefficient of Resistance (TCR)

Describes the percentage change in resistance of metal films under a change in temperature. The change in resistance is given by  $\Delta R/R = \alpha \Delta T$  where  $\alpha$  is a material constant called the temperature coefficient of resistance (TCR). This factor is important in decreasing the thermal crosstalk signal of the piezoresistor, and also signal drift due to changes in temperature in the environment.

### Prothrombin Time (PT)

Patients with thrombotic disorders have an increased risk of forming life threatening clots and are medicated with anticoagulants to suppress the clotting cascade. To remain in a healthy therapeutic range patients receiving oral anticoagulant medication are closely monitored using a Prothrombin Time (PT) diagnostic test. This test measures the time for a clot to be detected based on the instrument used and reagent sensitivity. For clinical relevance the PT is converted to a recognised standard called the International Normalized Ratio (INR) through calibration of the International Sensitivity Index (ISI) and Mean Normal Prothrombin Time (MNPT) against the gold standard laboratory analyser.

### International Normalized Ratio (INR)

The International Normalized Ratio is a World Health Organization recommended basis for evaluating the results of Prothrombin time tests. The INR is a standardized result that eliminates the variability in PT measured for different combinations of thromboplastin reagent and detection platform and method. To convert PT to an INR result each platform is calibrated against the gold standard laboratory analyzer to evaluate the International Sensitivity Index (ISI) and Mean Normal Prothrombin Time (MNPT) of the reagent/platform combination. Essentially, patient INR measured on the gold standard should be consistent with any platform and reagent.

### International Sensitivity Index (ISI)

The International Sensitivity Index specifies the sensitivity of the thromboplastin reagent to an internationally standardised sample. The ISI is measured through calibration against the gold standard method, and used to convert PT measurements to clinically relevant INR values. An ISI of 1.0 would be a sensitivity equal to the international standard. An ISI lower than 1.0 would effectively prolong the clotting time and measured PT.

### Mean Normal Prothrombin Time (MNPT)

The Mean Normal Prothrombin Time is calculated from a range of normal PT times from non-medicated patients; essentially this is the PT time for a sample INR of unity. The MNPT is used in the conversion of PT measurements to clinically relevant INR values.

### Percentage Coefficient of Variation (%CV)

The percentage coefficient of variation is a measure of the interpatient result variability calculated as the standard deviation divided by the mean as a percentage value. This value is recommended by the Clinical and Laboratory Standards Institute to measure the overall imprecision of the instrument, and is a basis for FDA approval.

## Table of Contents

|   |           |
|---|-----------|
| <b>Chapter 1 – Introduction .....</b>   | <b>1</b>  |
| 1.1 Research Motivation .....   | 1         |
| 1.1.1 Current Microcantilever Technology at RAL .....   | 2         |
| 1.1.2 Oral Anticoagulation Drug Therapy .....   | 8         |
| 1.2 Brief Introduction to Microcantilevers .....  | 9         |
| 1.3 Previous Work and State of the Art .....  | 12        |
| 1.3.1 Thermal Bimorph Actuators (TBA) .....   | 13        |
| 1.3.2 Rheological Measurements Using Microcantilevers .....                                       | 17        |
| 1.4 Thesis Outline .....  | 21        |
| <b>Chapter 2 - Microcantilever Fluid Probe Design .....</b>                                       | <b>23</b> |
| 2.1 Introduction .....  | 23        |
| 2.2 Bending Solution of Multilayer Beams Based on Neutral Axis Analysis .....                     | 24        |
| 2.3 Optimised Piezoresistive Sensor and Microheater .....   | 30        |
| 2.4 Finite Element Simulations .....  | 35        |
| 2.4.1 TEM analysis of Benchmark Fluid Probe Device (MV1) .....                                    | 36        |
| 2.4.2 TEM analysis of Fluid Probe Design (MV2) .....  | 44        |
| 2.4.3 Realisation of MV2 Fluid Probe Design .....   | 51        |
| <b>Chapter 3 - ThermoElectroMechanical Characterisation of Microcantilever Fluid Probes .....</b> | <b>54</b> |
| 3.1 Introduction .....  | 54        |
| 3.2 Mechanical and Thermal Characterisation of Metal Thin Films .....                             | 55        |
| 3.2.1 Mechanical Sensitivity .....  | 55        |
| 3.2.2 Temperature Coefficient of Resistance .....   | 57        |
| 3.3 Characterisation of Microcantilever Deflection .....  | 61        |
| 3.3.1 Experimental Validation of the Autofocus Method .....                                       | 65        |
| 3.3.2 Comparison of Microcantilever Actuation Efficiency .....                                    | 71        |
| 3.3.3 Curvature Measurements of Static and Actuated Microcantilevers .....                        | 74        |
| 3.3.4 Short Pulse Characterisation .....  | 77        |
| 3.3.5 Response of Heaters during Pulsed Heating .....   | 79        |
| 3.4 Thermal Crosstalk .....   | 82        |
| 3.4.1 Measurement of Sensor Resistance during Actuation Pulse .....                               | 82        |
| 3.4.2 IR Thermal Imaging of Microcantilever Fluid Probe .....                                     | 88        |
| 3.5 Summary and Discussion of Design Simulation and Characterisation .....                        | 90        |
| <b>Chapter 4 – Microcantilever Fluid Probe Demonstration and Clinical Evaluation .....</b>        | <b>93</b> |
| 4.1 Introduction .....  | 93        |
| 4.2 Microcantilever Fluid Probe in Glycerol .....   | 93        |
| 4.3 Deconstruction of Signal from Microcantilever Fluid Probe .....                               | 99        |
| 4.4 Improvements to Drift in Signal Response .....  | 103       |
| 4.5 Microcantilever Fluid Probe Testing in Plasma and Whole Blood .....                           | 106       |
| 4.6 Clinical Evaluation at The Royal London Hospital .....  | 112       |
| 4.6.1 Preceding the Clinical Evaluation .....   | 112       |

|  |   |            |
|--|---|------------|
| 4.6.2  | During the Clinical Evaluationl.....                  | 117        |
| 4.6.3  | Data Reduction and Analysis .....                     | 120        |
| 4.6.4  | Prothrombin Time (PT) Results and Discussion.....     | 123        |
| 4.6.5  | ISI and MNPT Calibration Results and Discussion ..... | 125        |
| 4.6.6  | INR Results and Discussion.....                       | 126        |
| <b>Chapter 5 – Conclusions and Future Work.....</b>  |   | <b>129</b> |
| <b>Chapter 6 – Supporting EngD Material: PRONANO – Background and<br/>Demonstration of Surface Imaging .....</b> |   | <b>139</b> |
| 6.1  | Design and Characterisation.....                      | 143        |
| 6.2  | Demonstration of Surface Imaging.....                 | 148        |
| <b>References .....</b>  |   | <b>157</b> |
| <b>Appendix A – Neutral Axis.....</b>  |   | <b>170</b> |
| <b>Appendix B – Static Bimorph Equation.....</b>   |   | <b>172</b> |
| <b>Appendix C – Support Letter .....</b>   |   | <b>175</b> |

# **Chapter 1 - Introduction**

## **1.1 Research Motivation**

Microsystem technology has the potential for future commercialisation over a broad range of scientific fields and as an enabling platform for nanoscience. Exploitation of this technology has several inherent advantages, including the capacity to fabricate high density arrays for increased throughput of parallel information. Microcantilever sensors and actuators form essential components of microsystem technology, allowing controlled mechanical interaction and response within an environment. The application of microcantilevers cover a wide scope of activities with key areas in biological, chemical, and environmental sensors identified as high growth markets. A small number of examples include; label free detection of proteins for cancer screening [1-3]; detection of foreign aerosols and explosive compounds for homeland security [4-5]; gas sensors and detection of pollutants for environmental monitoring [6-7]; proximity and motion sensors for seismic detection, accelerometers, and biometrics [8]; and possible electromagnetic field and charged particle detectors [9].

The Bioscience MNT group at the Rutherford Appleton Laboratory (RAL) has a strong focus on polymer microcantilevers with integrated sensors and actuators. This technology is of central importance to several projects undertaken by the group and remains a major programme within the Micro and Nanotechnology Centre (MNTC). Microcantilevers continually prove to be an enabling technology in new scientific fields and have already shown the potential for complementing the Science and Technology Facilities Council (STFC) strategies in bioscience and detector technology. In the technical context of the wider scientific field, polymer microcantilevers have gained a growing interest. It has recently been shown that the sensitivity of polymer surface stress sensors can match and in some cases surpass the performance of conventional silicon microcantilevers due to the combined integration of high gauge piezoresistive sensor elements with a low stiffness structural material [10-11]. Polymers also have the advantage that they can be processed quickly using simple and low cost “spin-on” methods, there is a wide choice of materials with different mechanical, electrical and thermal characteristics to choose from, and polymers are not limited to processing on conventional silicon substrates.



Thermally actuated bimorph microcantilevers are desirable for a range of sensor and actuator applications that require large deflection in the micro domain compared to conventional techniques (e.g. electrostatic, piezoelectric). Thermal Bimorph Actuators (TBA) based on Gold and Polyimide (PI2562, Dupont) structural materials with integrated heaters and piezoresistive sensors have previously been designed and fabricated at the MNTC [12-14]. The motivation of the research presented here is to make improvements in current devices to demonstrate a biomedical fluid probe for measuring blood coagulation. This requires improvements in the actuation efficiency of TBA to reduce power dissipation into the device and to overcome issues with thermal saturation of the integrated piezoresistor signal due to internal heating. The principal scientific steps to achieve these improvements include mathematical and simulated performance of new microcantilever designs, and the development of testing and characterisation capabilities at MNTC for optimisation of fabricated devices. The improvements allow the demonstration of the technology as a platform for new scientific applications, specifically in the field of biological and chemical analysis.

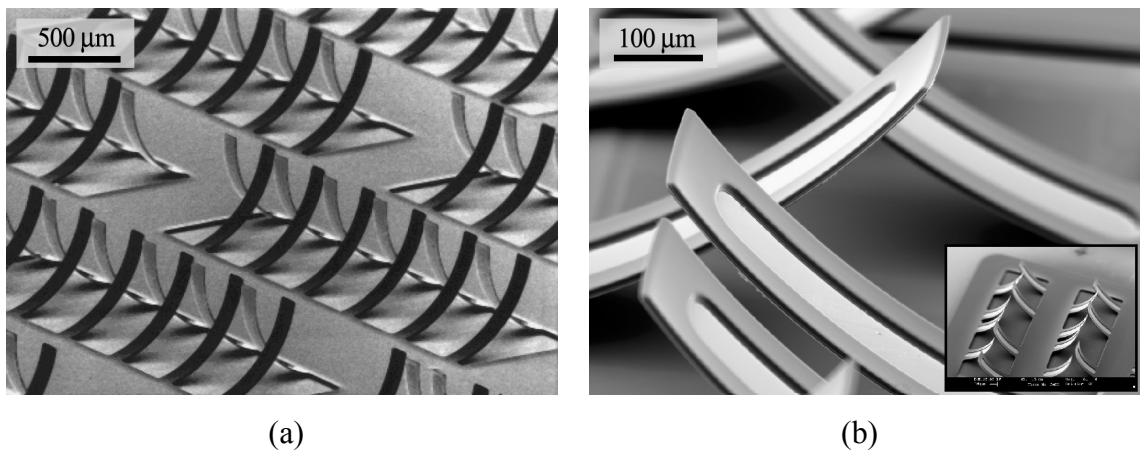


Figure 1-1 Microcantilevers previously fabricated by Djakov and Huq [12, 13] at the MNTC (1997-2002). (a) SEM image of a bimorph cantilever matrix for providing ciliary motion. (b) SEM image of a  $\Pi$ -shaped bimorph cantilever with optically reflective membrane.

### 1.1.1 Current Microcantilever Technology at RAL

TBA, shown in Figure 1-1, were originally developed at the RAL for a novel MEMS based walking “micropede” (1997-2001) [12], and later investigated to provide large deflection of optical membranes (2002) [13]. These initial studies were based on gold and polyimide (PI2566, Dupont) bimorph structures with large difference in coefficient

of thermal expansion (CTE), and aluminium microheaters. Bimorph microcantilevers were surface micromachined and released from the substrate using an etching process that exploits the weak adhesion of gold to the substrate. Upon release the residual stress in the structural layers from the fabrication process force the bimorph to curl-up and assume an initial out-of-plane position. Part of the initial studies at RAL involved fabrication of devices with varying thickness ratio to optimise the initial displacement of cantilever structures; this established an optimum range for the thickness of the material layers.

In 2003 the MNTC worked with the Central Laboratory Innovation and Knowledge Transfer (CLIK) group to exploit intellectual property and research for commercial opportunities. This collaboration resulted in a spinout company, Microvisk Ltd, whose core technology is to use TBA to provide rheological measurements of fluids. The first product being developed is a medical diagnostic device for measuring blood coagulation aimed at patients on anti-coagulant drug therapy. Proof of concept devices were based on original optical masks for TBA with gold-polyimide structural architecture that had previously been fabricated at the MNTC. Initial devices incorporated no sensor on the cantilever and thin film heaters were not encapsulated. The intention of these devices was to use the same thin film as a heater and strain gauge. Subsequent devices for initial proof of concept based on single cantilever beams had encapsulated gold heaters and sensors on the same deposition layer. These previous sets of probes were unsuitable for fluid applications as high actuation temperature within the structure created a significant thermal crosstalk on the mode of sensing resulting in an indistinguishable mechanical response [14]. The response also included high electrical, thermal, and vibrational noise in the sensor as no referencing or electronic balancing was used. This drives the motivation for a microcantilever fluid probe design which is both highly efficient and produces low thermal crosstalk.

The first original design for Microvisk, hereafter referred to as MV1 (Figure 1-2), was designed by Dr Vladislav Djakov and fabricated at the MNTC during 2005 by the author as part of this thesis. The microcantilever device was based on gold-polyimide (PI2562) structural layers with separate gold heater and sensor track sandwiched in the polyimide layer.

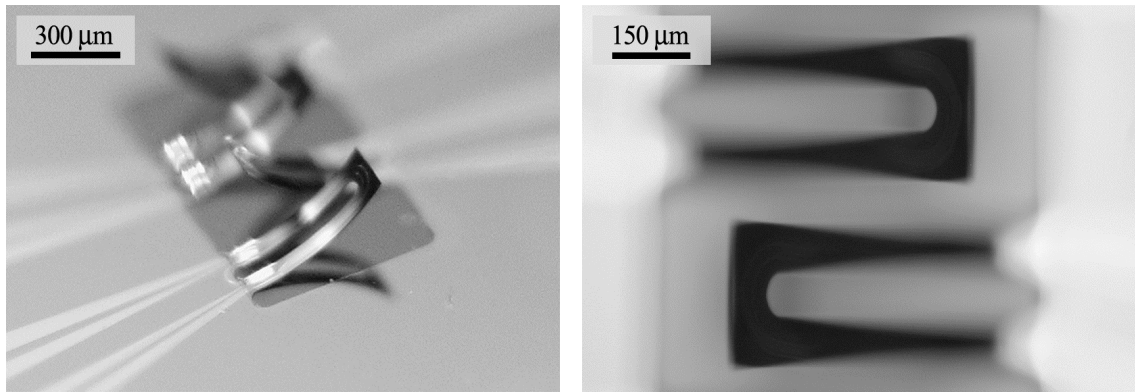


Figure 1-2 *Left*: Side image of the microfabricated MV1 Fluid Probe Design. *Right*: Top image focused on the microcantilever tip.

The MV1 microcantilever fluid probe has been operated in silicone standards and as a blood coagulometer by the author and Vladislav Djakov. Figure 1-3 shows the similar piezoresistor sensor response in 10 cP and 100 cP silicone viscosity standards during thermal actuation, using approximately 90 mW input power. The MV1 device has also been operated as a blood coagulometer with no successful confirmation of detecting the clot onset. The poor operation of the device can be explained by the mechanical and thermal sensitivity of the measured gold piezoresistor (presented in Chapter 3). The mechanical sensitivity of the microcantilever gold piezoresistor is  $20.8 \Delta R/R \times 10^{-6} \cdot \mu\text{m}^{-1}$  and the temperature coefficient of resistance of the gold film is  $1130 \Delta R/R \times 10^{-6} \cdot ^\circ\text{C}^{-1}$ .

If the sensor response shown in Figure 1-3 is dominated by the mechanical signal the deflection would be of the order of several hundred microns within a few ms. This is not observed, and is beyond the limit of the microcantilever. As will be presented in Chapter 3 it is estimated that the deflection in fluids (1-3 cP) is of the order 0.5 - 1  $\mu\text{m}$ . If the sensor response was dominated by the thermal crosstalk from the heater during actuation then the signal would account for an increase in the sensor temperature by a few degrees within a few ms. This is a reasonable assumption noting the proximity of the sensor to the heater, and the high power applied to the device. Figure 1-3 also supports that the thermal signal is dominating the sensor response of the MV1 device. The temperature in the beam is related to the loss of heat from the structure and therefore the thermal conductivity and heat capacity of the surrounding environment. Though the fluids have an order of magnitude difference in viscosity, the thermal conductivity and heat capacity are comparable. The dominance of the thermal crosstalk signal also explains the poor operation of the device as a blood coagulometer to

physically measure the clot onset. Though the MV1 device shows poor rheological discrimination of fluids and use as a blood coagulometer it serves well in this thesis as a benchmark to which new designs can be compared with and improvements shown.

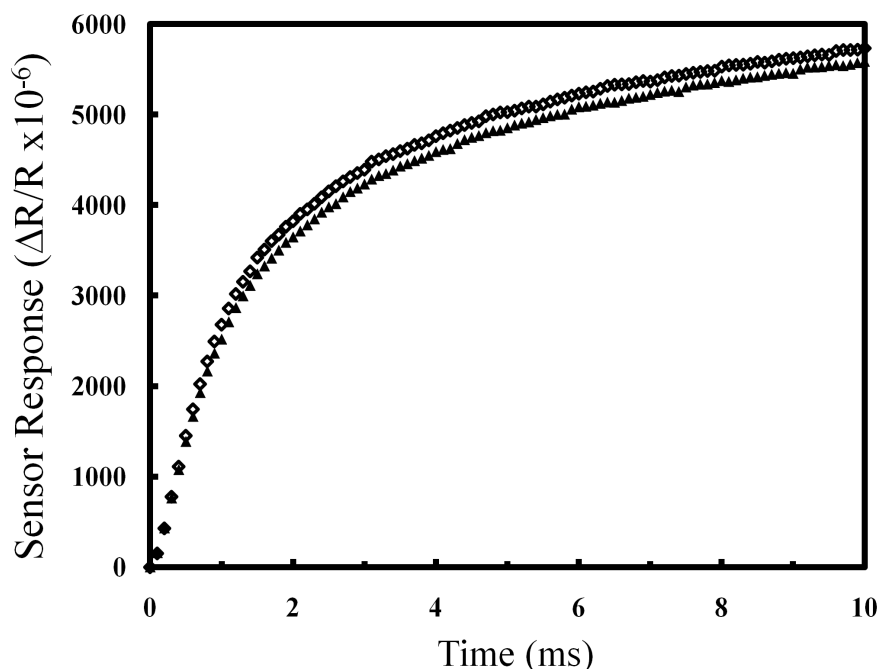


Figure 1-3 MV1 Piezoresistor sensor response in 10 cP (open diamond) and 100 cP (filled triangle) silicone viscosity standards. The actuation pulse to the heaters has a peak power of approximately 90 mW (3.5V).

The Bioscience MNT group has continued to focus activities on the development of polymer microcantilever devices and is currently operating a number of academic and European projects, with a combined budget of £1.5 million (2004-2008). Major activities based on microcantilevers include the fabrication of microcantilever surface stress sensors for the detection of specific protein binding for disease indicators, tunnelling spectroscopy using modified photoplastic microcantilevers, and polymer microcantilever arrays for life science and bio-sensing - Tools and Technologies for the Analysis and Synthesis of Nanostructures (TASNANO).

In April 2005 the group began work on a five year European Framework 6 project “Technology for the Production of Massively Parallel Intelligent Cantilever Probe Platforms for Nanoscale Analysis and Synthesis” (PRONANO). The role of the MNTC in the project is to develop scanning proximity probes (SPP) using alternative

architecture based on multilayer polymer microcantilevers as a platform for analysis and manipulation as illustrated in Figure 1-4. This technology offers an alternative to silicon based scanning probes using low power, large deflection capabilities to realise two-dimensional arrays, and a simple low cost route of manufacturing. The ultimate aim of the project is to realise a packaged massively parallel chip incorporating 4x16 proximal probes, each fully addressable with control and readout.

The project has synergies with the microcantilever fluid probe research as the critical task for the group is to produce very low power microcantilever devices and to resolve issues with thermal crosstalk from the actuation on the piezoresistive sensor. The design, realisation, and demonstration of polymer microcantilevers for surface metrology have also been undertaken within the EngD portfolio. The polymer scanning probes have been shown to be capable of resolving 30-40 nm step resolution using an integrated piezoresistor sensor and can be deflected over 100  $\mu\text{m}$ . The work is now focused towards achieving below 10 nm resolution and enhanced tip sharpness to meet the needs of critical dimension (CD) metrology in the semiconductor and nano-manufacturing industries. A background and summary of work by the author is presented as supporting material in Chapter 6.

The scanning probe work is interlinked with the fluid probe design and characterisation. The design of efficient multi-layer polymer actuators for the fluid probe presented in chapter 2 can be used towards efficient DC offset positioning for levelling cantilever arrays. The optical characterisation of beam curvature presented in chapter 3 has been used to show irregular shape and twisting deflection, and the mechanical characterisation has led to the choice of low thermal sensitivity nichrome piezoresistors. The scanning probe work also provides confirmation of the estimation in mechanical deflection of the fluid probe in chapter 4 by measuring the noise level of the scanning probe during mechanically driven deflection against a sample.

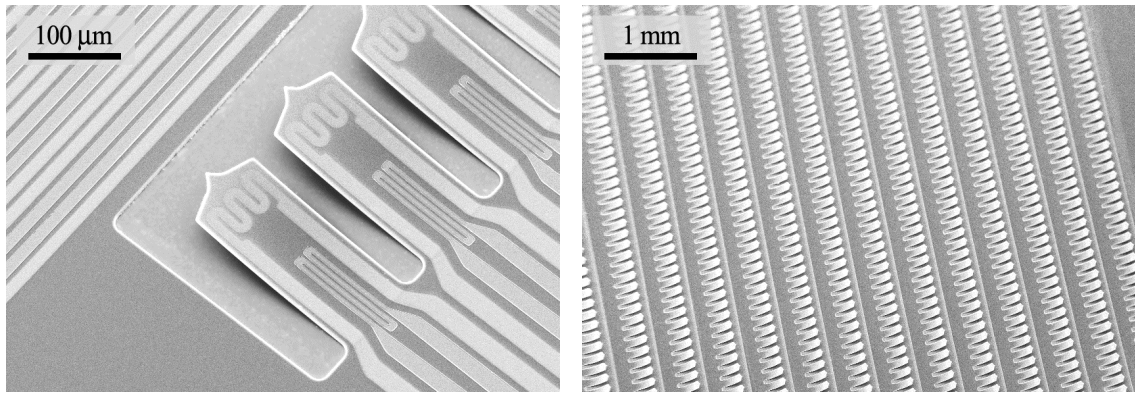


Figure 1-4 Microcantilever platforms for nanoscience designed by the author. Left: 1x32 microcantilever array with integrated heater and sensor. Right: 20x64 passive microcantilever array with 100% release yield.

A major part of the undertaking of these projects is to develop analytical tools and characterisation of microcantilevers for optimisation of devices. Previous to this project the group had limited electrical interrogation of devices and analysis was based on theoretical studies of two layer beams with uniform temperature distribution. Though current devices under development include an integrated piezoresistor for sensing cantilever deflection, the metal thin film tracks are susceptible to thermal crosstalk from the integrated actuation and therefore an external optical technique is desirable to confirm deflection amplitudes.

Standard optical techniques are difficult to implement on highly curved surfaces as a small angle approximation is no longer valid. Common techniques that have been reported include extracting dimensions from SEM images [15-16] and using optical microscopes to determine x and y coordinates [17-18]. Further to these techniques, Dr Mohamad Al Aioubi, a previous member of the Bioscience MNT group, mounted micromirrors on the cantilever and analytically retrieved tip deflection [18]. While these techniques extract the required information they can be slow and based on the individual's discretion. The techniques are also difficult to implement for dynamic measurements. Without the capabilities to make predictions and perform measurements it is difficult to approach new projects with an understanding of how the devices perform. This has driven the motivation to implement a better understanding of the analytical framework and design new characterisation tests to extend the current capabilities of the group.

### **1.1.2 Oral Anticoagulation Drug Therapy**

The coagulation cascade is a complex process which results in clot formation and is crucial for stopping blood loss from damaged vessels. Patients with thrombotic disorders, including atrial fibrillation, mechanical heart valves, deep vein thrombosis, and pulmonary embolism, have an increased risk of forming life threatening clots and are medicated with anti-coagulants to suppress the clotting cascade. To remain in a healthy therapeutic range patients receiving oral anticoagulant medication are closely monitored using a Prothrombin Time (PT) diagnostic test. This test gives an indication of how long the clotting process is taking and whether the course of anti-coagulants needs to be adjusted. As the therapeutic window is narrow and a number of external influences, such as diet, illness, alcohol, and drugs can adjust the patients PT, regular testing is essential.

Previous estimates of patients on anti-coagulation drug therapy are 7 million worldwide [19], with each patient requiring multiple tests per year. The largest market for diagnostics is in the United States, where Doctors can claim reimbursements for each test carried out. This financial incentive allows commercial viability presenting an attractive market where only few competitors are currently operating. The market for handheld PT devices has few competitors; The Coaguchek System (Roche), INRatio (Hemosense), and ProTime Microcoagulation System (Thoratec Corp), are currently the only companies operating with handheld PT Devices. A clear indication of the opportunity in this market is the recent acquisition of Hemosense by Inverness Medical Innovations for a reported \$243 million in November 2007.

Technologically, the latest Coaguchek XS device measures the PT as an electrochemical signal based on generation of phenylenediamine when thrombin cleaves a peptide electrocyme TH. This is an indicative measurement of the clot onset as thrombin generation is a level before the fibrin clot formation in the coagulation cascade [20]. The previous CoaguChek S device used a rheological method based on the damped motion of ferric oxide particles in an alternating magnetic field as the fibrinous clot is formed. The INRatio device uses an electrical measurement of blood coagulation by measuring the global impedance of the sample and identifying the changes in conductivity associated with clot formation. The ProTime device uses a rheological method based on detecting the motion of blood as it is pumped back and forth through a channel. The technique presented in this thesis uses a mechanical and physical measure

of the clot formation and therefore measures the true onset of the cross-linked fibrin clot.

## **1.2 Brief Introduction to Microcantilevers**

Microcantilevers form an essential component of many microsystem devices. They can be used to mechanically manipulate device elements, measure environment properties, or even provide robotic locomotion. For each application the mode of operation, method of actuation, and feedback mechanism for detecting microcantilever deflection must be considered. For the Microcantilever Blood Coagulometer presented in this thesis the choice of actuation and detection has been implemented previously, though alternative and state of the art techniques are considered in the following section. The section is not intended to provide a detailed discussion of each technology, as this is provided in text books [21-22], but to highlight any possible competing technologies and future consideration to alternative or enhanced operation.

Microcantilever sensors are highly sensitive to changes in mechanical properties induced by physical and environmental conditions, such as added mass, attractive and repulsive forces, energy imparted on the beam, or induced surface stress. The response to changes can be measured directly by passive deflection, or indirectly using techniques such as resonance. For example, Ilic et al have demonstrated femtogram single cell detection of E.Coli [23] and attogram sensitivity of added mass [24] to short silicon cantilever structures by measuring a shift in natural frequency (Figure 1-5a). If the E.Coli cell was measured as a passive mass deflection the deflection of the beam would be approximately 0.005 nanometres; beyond the resolving power of conventional techniques. An enhanced passive technique is based on the induced surface stress from an attached monolayer of a specific binding of chemical or biomolecular species. For example, Wu et al [1] have demonstrated label-free detection of two forms of prostate specific antigen using silicon microcantilevers functionalised with target antibodies, and Arntz et al [2] have demonstrated the detection of two cardiac biomarker proteins allowing the early and rapid diagnosis of acute myocardial infarction (Figure 1-5b).

The detection of a cross-linked fibrin clot by principle suggests a dynamic technique whereby the microcantilever motion is damped by the progressing clot formation. Though resonance is a potential choice for this application it has been shown that fluid damping in only moderately viscous fluids significantly reduces the Q-factor of the



measurement [14]. This suggests using a large forced deflection through the fluid with an appropriate actuation mechanism as discussed below. For future development, if the dynamics of the clot are such that the volume draws or pulls on the beam, a passive detection may be desirable as this would reduce the need for any actuation mechanism.

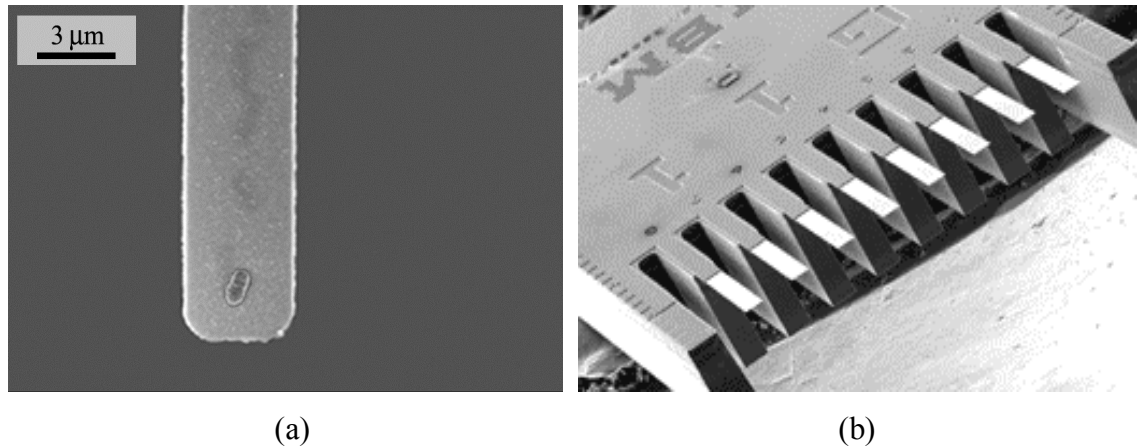


Figure 1-5 (a) Single E.Coli cell weighing approximately 665 femtograms on a silicon microcantilever giving a shift in natural frequency of 730 Hz [23]. (b) IBM “artificial nose” functionalised with antibodies for label-free detection of prostate specific antigens [24].

Common mechanisms of microcantilever actuation include electrostatic, piezoelectric, magnetic, shape memory alloys, and thermal. Hydraulic [25], light driven [26] and some exotic electrochemical [27] actuation methods also exist but are less common and have yet to mature and therefore these methods are not considered for the application. Shape memory alloys may also be rejected as the critical temperature at which the shape transition occurs is typically unsuitable for biological applications. Electrostatic and Piezoelectric actuation is appropriate for high-speed small precision deflection rather than large scanning applications, though this can be enhanced by overlapping several electrostatic actuators or stacking piezoelectric structural layers. Magnetic actuation may be realised in several forms though it is undesirable to integrate coils and moving magnets into a point-of-care instrument. Enhanced thermal actuation, either by using a two-arm flexural actuator [28] or multiple layers with different CTE [16], can provide large deflections though both techniques consume more power than other actuation techniques and have limited bandwidth dependent on thermal time constants. Therefore it is desirable to use a technique such as thermal actuation but produce a very efficient device that works at low power and temperature. Magnetic actuation may be of

consideration for future applications in high viscosity where large thermal powering would otherwise overheat or saturate an integrated sensor.

Optical detection techniques for microcantilever deflection include the optical lever method [29], interferrometry [30-34], and diffraction [35]. Electrical techniques include electron tunnelling [36-37], capacitive [38], piezoelectric [39], and piezoresistive [40]. Though optical methods can achieve angstrom sensitivity the alignment of an optical system in a handheld or desktop device for a microcantilever fluid probe presents a significant issue for packaging, high throughput, and ease of use. Optical techniques also limit fluid applications to suitably transparent fluids and require a reflective or diffraction layer to be incorporated into the microcantilever structure. For some applications, using an optical method is desirable as the detection will not be limited by thermal crosstalk during actuation; in this case the response is limited at low frequency by thermal mechanical vibrations and at high frequency by shot noise [41].

Electron tunnelling places high specification on the fabricated device and is therefore not considered as a detection mechanism for the fluid probe. Capacitive, piezoelectric and piezoresistive offer similar capabilities in sensitivity, though piezoresistance is described further below as the most suitable detection method due to the simplicity of integration. The piezoresistive effect is based on the induced change in resistance due to changes in geometry and material resistivity. Though metal films have a much lower gauge factor – product of strain and proportional change in material resistance – compared to semiconductor materials, the signal is enhanced using flexible substrates and larger deflection. Compensation for thermal mechanical vibrations, thermal and electrical drifts, and other environmental changes in the resistance can be made using a suitable Wheatstone bridge arrangement with reference arms [40]. In this arrangement an actuated microcantilever piezoresistor is used in a positive arm of the bridge and a second reference microcantilever piezoresistor is used in a negative arm of the bridge such that environmental thermal drift and mechanical vibration are compensated. A Wheatstone bridge arrangement also allows a balanced zero output voltage such that small changes can be amplified significantly. In a bridge arrangement the sensitivity is generally limited by Johnson noise given by fluctuations in electrical current due to thermal excitation. Metal films, such as gold and platinum, can also have a large thermal dependency, or temperature coefficient of resistance (TCR), measured as the percentage change in resistance due to changes in temperature. For example, a 100 nm

deflection of a microcantilever using gold sensors with  $0.3 \text{ ppm.nm}^{-1}$  mechanical sensitivity [10] is equivalent to a change in temperature of the sensor of  $0.008 \text{ }^{\circ}\text{C}$ . Certain alloys, such as constantan (CuNi) and manganin (CuMn) can have virtually zero TCR and are desirable for very low sensitivity to thermal crosstalk and environmental temperature drifts.

### 1.3 Previous Work and State of the Art

Thermally actuated microcantilevers are becoming increasingly important in a number of MEMS applications that require large out-of-plane deflections. This has been exploited in several areas, including, Microgrippers [42-44], Microrobotics [45] (Figure 1-6a), Optical Scanners [46-47], and Smart Surfaces [48, 15]. These applications are predominantly based on actuation, though a number of recent applications in the field use bimorphs as microsensors, including, Uncooled Infrared Detectors [49-51] and Calorimeter sensors [52-54] (Figure 1-6b). The improvement in efficiency and operation of bimorph actuators is predominantly driven by biological and chemical applications that require operation in liquids for manipulation, imaging, and sensing. Biological applications also place limitations on the maximum operating temperature of these devices. This section highlights previous work and state of the art in the field of thermal bimorph actuators and the use of microcantilevers as a rheological sensor.

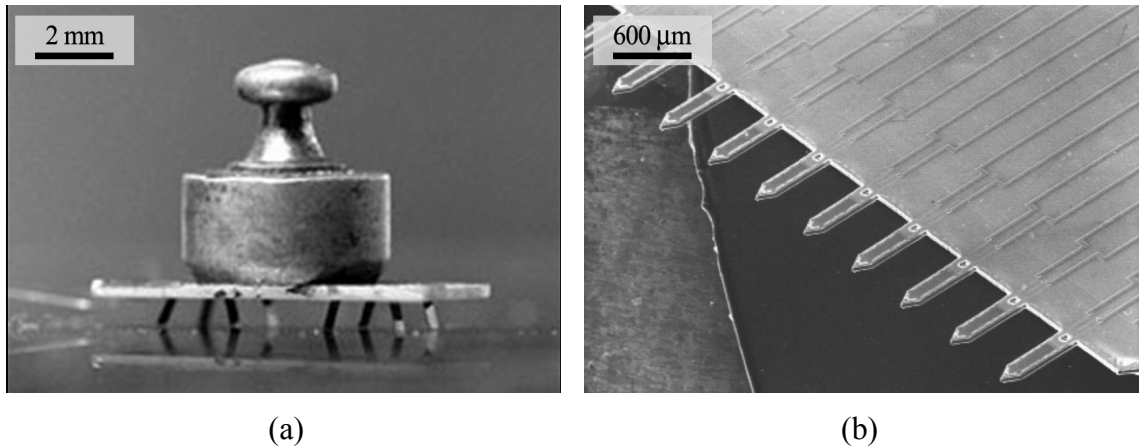


Figure 1-6 (a) Silicon chip with eight microcantilever legs to provide robotic locomotion [48]. (b) Piezoresistive microcantilever calorimeter array with a resistive thin film microheater [54].

### 1.3.1 Thermal Bimorph Actuators (TBA)

In 1988 Riethmüller and Benecke [16] proposed the first thermal microactuator devices based on the bimetal effect using boron doped silicon and gold structural layers with integrated poly-silicon heaters. The devices curled out of plane after sacrificial release and achieved a 100  $\mu\text{m}$  deflection for 200 mW of power dissipation; considerably more than conventional electrostatic or piezoelectric actuators. Benecke [55] suggested the use of such devices for electrically controlled switches, microvalves, microshutters, optical components for mirrors and displays, surface manipulation, and micromotors. Larger actuation efficiency ( $\mu\text{m.mW}^{-1}$ ) was noted by the group when changing the thickness ratio of the bimorph and further improved using a thin Silicon Oxynitride layer and meandering gold metal layer which functioned as a structural and heater layer [56].

The theory presented by Riethmüller and Benecke for estimating initial and thermal deflection is shown to be incomplete by Chu et al [57] and has been further derived based on small deflections and constant beam temperature. Read et al [17] have extended the theory for a generalised multilayer structure. From theory, Lammel et al [58] have noted the importance of the thickness ratio for bimorph structures in optimisation of initial deflection and actuation efficiency. This parameter is further discussed in the context of the thesis in Chapter 2. Peng et al [59] have performed a similar numerical analysis to show the dependence of deflection on material thickness in a two layer system.

Read et al [17] have developed TBA based on the Orbit 2  $\mu\text{m}$  double polysilicon CMOS process as a route for quick, low cost devices using commercially available foundry processes. The disadvantage of the process is that materials are limited and layer thickness is fixed. Microcantilevers were based on silicon dioxide and aluminium structural materials with an integrated polysilicon heater. For a 300  $\mu\text{m}$  long cantilever a tip displacement of approximately 38  $\mu\text{m}$  is reported for 27 mW input power indicating an improvement on previous work in the field. Later work [65] by the same group using the Multi-users MEMS Process (MUMPS) achieved 2.5  $\mu\text{m}$  with 40 mW input of a 100  $\mu\text{m}$  long gold – silicon dioxide microcantilever. Schweizer et al [46, 47 and 58] also fabricated TBA based on silicon dioxide and a thin film metal layer for application as optical microscanners in projection displays. Schweizer reported that a

mirror mounted to the tip of the cantilever had an initial angle of 135 degrees and when driven at resonance achieved 30 degrees deflection for 1 mW average power consumption.

Ataka et al [61] designed the first polymer based bimorph structures, noting that improved conversion of heat to displacement is achieved due to higher thermal expansion and lower Young's modulus in polymer films compared to metal. The group fabricated an array of polymer-polymer bimorph actuators with integrated metal heater for a ciliary motion system, achieving a reported tip deflection of 150  $\mu\text{m}$  with 33 mW dissipated power. Suh et al [15, 61, 62, 63] have fabricated a similar ciliary motion system for object manipulation based on dual polyimide structural layers with integrated TiW heaters and an aluminium layer for low power electrostatic pull-down (Figure 1-7a). Similar enhancements in thermal actuation efficiency are noted, with the addition of electrostatic pull down allowing low power holding once the beam has deflected a sufficient amount.

Low stiffness polymer based bimorphs have previously been suggested for use in biological fluid systems due to operation at lower power and temperature. Lin et al [42] fabricated a low stiffness gold-polyimide thermal actuator ( $0.06 \text{ N.m}^{-1}$ ) for handling living cells with the gold layer functioning as a heater and electrostatic layer. A full deflection in air from a fully curled position is reported for a power dissipation of 36 mW, though the cantilever became overheated when operated in water.

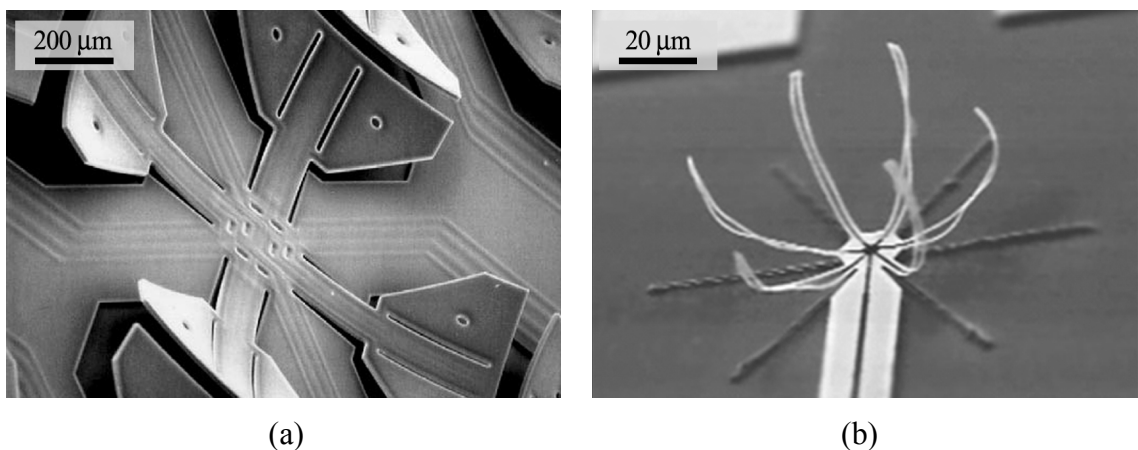


Figure 1-7 (a) Smart surface for micromanipulation [15]. (b) Normally closed microcage based on diamond-like carbon and nickel bimorph cantilevers [44].

Gold-polyimide thermal actuators have also been fabricated by Djakov and Huq at the MNTC for optical scanners [13] with heaters integrated as metalised tracks encapsulated in the polyimide layer. Al Aioubi [18] has characterised identical cantilevers with chrome heaters and reported an actuation efficiency of  $1.45 \mu\text{m.mW}^{-1}$ ; lower than that of Lin et al though devices had much higher stiffness ( $\sim 1.00 \text{ N.m}^{-1}$ ). Chan and Li [64] and Zhou et al [43] have developed an on-chip micro-robotic gripper that can manipulate and isolate cells to conduct localised cell probing and measurement. The gripper, based on thin polymer (Parylene C) layers with an encapsulated platinum heater, has been demonstrated in DI water with a reported tip deflection of 90 degrees with power dissipation of 100 mW. The cantilever beam was relatively long (2 mm), and only 600 nm thick, resulting in a very low stiffness at the tip of  $\sim 8 \mu\text{N.m}^{-1}$ . Luo et al [44] have also fabricated very thin (240 nm) thermal actuators based on a highly stressed diamond-like carbon and nickel bimorph to form microcages (Figure 1-7b). Using the nickel layer as a structural and heater layer a maximum tip deflection in air of 60-90 degrees is reported for power dissipation  $< 20 \text{ mW}$ .

Though these results indicate the high actuation efficiency of low stiffness TBA no mention is made of the low restoring force of the beam to pull back through the fluid. This restoring force is crucial for a microcantilever fluid probe operated at low frequency to pull the beam back through the fluid and therefore a very low stiffness beam is not suitable for the application. Table 1-1 gives a summary of above work where the thermal actuation capabilities have been reported. This includes the dimensions and materials of the microcantilever device and how actuation is integrated into the structure.

| Reference        | Year | Length<br>( $\mu\text{m}$ ) | Material<br>(Top / Bottom) | Thermal<br>Expansion<br>( $\times 10^{-7} \text{ K}^{-1}$ ) | Young's<br>Modulus<br>(GPa) | Width<br>( $\mu\text{m}$ ) | Thickness<br>( $\mu\text{m}$ ) | Release<br>Mechanism       | Heater                    | Stiffness<br>approx.<br>(N/m) | Actuation<br>Efficiency<br>( $\mu\text{m}/\text{mW}$ ) |
|------------------|------|-----------------------------|----------------------------|---|-----------------------------|----------------------------|--------------------------------|----------------------------|---------------------------|-------------------------------|--|
| Riethmüller [16] | 1988 | 500                         | Gold                       | 142   | 78                          | 80                         | 1.8                            | Silicon Etch               | Integrated<br>Polysilicon | 3.9                           | 0.37   |
|                  |      |                             | Silicon                    | 30  | 165                         | 100                        | 4                              |                            |                           |                               |  |
| Riethmüller [16] | 1988 | 500                         | Gold                       | 142   | 78                          | 80                         | 2.5                            | Silicon Etch               | Integrated<br>Polysilicon | 5.2                           | 0.57   |
|                  |      |                             | Silicon                    | 30  | 165                         | 100                        | 4                              |                            |                           |                               |  |
| Ataka [60]       | 1994 | 500                         | Polyimide                  | 500   | 3                           | 100                        | 3.6                            | Sacrificial<br>Aluminium   | Gold &<br>Nickel          | 0.2                           | 4.55   |
|                  |      |                             | Polyimide                  | 100   | 4.6                         | 100                        | 2.2                            |                            |                           |                               |  |
| Lin [42]         | 1995 | 200                         | Polyimide                  | 500   | 3                           | 45                         | 1                              | Sacrificial<br>Aluminium   | Structural<br>Gold        | 0.1                           | 3.53   |
|                  |      |                             | Gold                       | 142   | 78                          | 30                         | 0.1                            |                            |                           |                               |  |
| Read [17]        | 1995 | 300                         | Aluminium                  | 230   | 69                          | 100                        | 1.75                           | Silicon Etch               | Integrated<br>Polysilicon | 2.3                           | 1.41   |
|                  |      |                             | SiO <sub>2</sub>           | 4   | 74                          | 100                        | 1.5                            |                            |                           |                               |  |
| Suh [15]         | 1997 | 430                         | Polyimide                  | 500   | 2.7                         | Var                        | 4.5                            | Sacrificial<br>Aluminium   | Integrated<br>TiW         | 1.0                           | 1.80   |
|                  |      |                             | Polyimide                  | 20  | 8.6                         | Var                        | 4.5                            |                            |                           |                               |  |
| Tuantranont [65] | 2002 | 100                         | Gold                       | 142   | 78                          | Var 15                     | 4.5 -                          | Silicon Etch               | Integrated<br>Polysilicon | -                             | 0.06   |
|                  |      |                             | SiO <sub>2</sub>           | 4   | 74                          | Var 15                     | 4.5 -                          |                            |                           |                               |  |
| Djakov [18]      | 2002 | 600                         | Polyimide                  | 600   | 1.72                        | 80                         | 8.8                            | Gold Weak<br>Adhesion      | Integrated<br>Chrome      | 1.0                           | 1.45   |
|                  |      |                             | Gold                       | 142   | 78                          | 80                         | 1.2                            |                            |                           |                               |  |
| Chan [64]        | 2003 | 2000                        | Parylene C                 | 350   | 3.2                         | 100                        | 0.1                            | Sacrificial<br>Photoresist | Integrated<br>Platinum    | 0.000008                      | 7.80 in<br>water                                       |
|                  |      |                             | Parylene C                 | 350   | 3.2                         | 100                        | 0.3                            |                            |                           |                               |  |
| Luo [44]         | 2004 | 60                          | Nickel                     | 134   | 200                         | 12                         | 0.19                           | Silicon Etch               | Structural<br>Nickel      | 0.05                          | 1.20   |
|                  |      |                             | Carbon                     | Not given   | 600                         | 12                         | 0.04                           |                            |                           |                               |  |

Table 1-1 Summary of thermal bimorph actuator efficiency where given in literature. The bimorph is considered as the most significant top and bottom layers and neglects any thin insulator or heater layers. An approximate stiffness is given for each structure.

### 1.3.2 Rheological Measurements Using Microcantilevers

Rheology is fundamental to many industries such as food technology, automotive, printing, polymer processing, chemistry and biology. Traditional techniques for measuring rheological parameters often involve large mechanical apparatus and require relatively large sample volumes. The miniaturisation of such systems has many advantages including nano-litre sample volumes, portability, greater selectivity, and reduced setup and analysis time using disposable batch fabricated sensors.

It has been previously shown that when immersed in a fluid, the response of an AFM cantilever [6, 67, 70, 72, 81], rectangular beam [66, 78, 79, 82, 83], or composite cantilever beam [77], when excited to resonance by an internal or external force, is dependent on the properties of the medium, namely the viscosity and density of the fluid. The performance of a resonant sensor relies on many factors including materials, fabrication, type of resonator, mode of vibration, the quality of resonance, temperature sensitivity and method of excitation and detection [84].

Early work presented by Inaba et al [66] and Oden et al [67] using rectangular microcantilever beams indicated that fluid viscosity is manifested as a variation in the resonance frequency, quality factor and response amplitude. Inaba used a photothermally vibrated stainless steel cantilever immersed in ethanol, water, and a concentration of NaCl in water (viscosity range from 1 cP to 2.2 cP). The vibration amplitude of the cantilever was typically 200 nm in fluids indicating the small deflection amplitudes expected using a resonance method. Measurements of peak frequency response and the Q-factor were compared with a theoretical model by Ito and Nakazawa et al [68] considering reaction forces in fluids. It was shown that the sensing of both liquid density and viscosity was possible, though the accuracy is mainly determined by the Q-factor which is reduced as viscosity increases.

Oden et al [67] demonstrated viscosity measurements using a rectangular AFM silicon microcantilever monitored during ambient and driven excitation. The peak response frequency was measured in air, de-ionised water, and varying concentrations of water and glycerol ranging from pure water (0.89 cP) to 90% glycerol (1499 cP). Figure 1-8 shows the measured peak resonance and Q-factor versus viscosity for different concentrations of glycerol in water. Theoretical estimates were made using a 1-dimensional damped harmonic oscillator model from the drag force of an induced mass



on the cantilever [69]. The induced mass is due to a fixed determinable volume of fluid mass being carried along with the cantilever; this effectively lowers the resonance frequency and decreases the Q-factor.

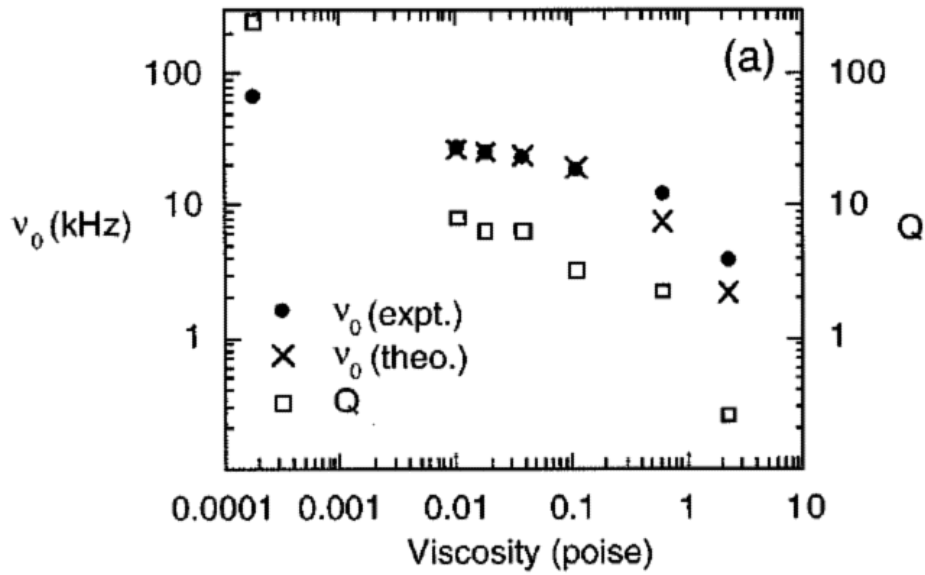


Figure 1-8 Experimentally measured peak resonance (filled circle) and Q-factor (open square) of a silicon microcantilever in a range of viscosity solutions adapted from Oden et al [67]. Theoretical estimates of the microcantilever peak resonance (cross) from a damped harmonic oscillator model are given for comparison.

Using the same theoretical model as Oden et al, Ahmed et al [70] have reported measurements of resonance frequency and Q-factor of a V-shaped AFM probe with low spring constant ( $60 \text{ mN.m}^{-1}$ ) when immersed in solutions of glycerol (0.89 cP – 8.82 cP), sucrose (1.00 cP – 5.98 cP), and a protein solution (1.00 cP – 1.75 cP). Ahmed et al also presented the use of the AFM probe to monitor a biochemical reaction attributed to DNase I hydrolysis of Herring Sperm DNA. During this reaction the resonance frequency of the probe increased from 2.9 to 3.5 kHz reflecting a change in viscosity of 1.5 cP, though no indication of thermal or mass loading contribution was reported.

In work by Sader et al [71, 72, 73, 6] excellent results have been demonstrated for measuring the rheological properties of a range of fluids with AFM cantilevers. The foundation of this work is an analytical model proposed by Sader [71] that can be used to simultaneously estimate the viscosity and density of a fluid based on the flexural resonance frequency and Q-factor of immersed cantilever beams. The basis of this model is a mathematically derived hydrodynamic function that describes the flow around rectangular cantilever beams. A model has also been proposed by Sader and

Green [73] for estimating torsional modes of vibration of rectangular cantilevers immersed in viscous fluids, and response of a cantilever beam in a fluid near solid surfaces [74-75]. A further paper on the dynamic response of a cantilever near a solid wall may also be found by Naik et al [76]. A validation of the flexural model is given in [72] using a series of single crystal silicon rectangular beams in known fluids. The experimentally measured resonance frequency for cantilever beams in acetone, water, 1-butanol and carbon tetrachloride ( $\text{CCl}_4$ ) show good agreement with the model.

A full demonstration of estimating the viscosity and density of several gases and liquids using Sader's model is given by Boskovic et al [6]. The paper sets out a rigorous step-by-step method for initially calibrating cantilevers in a known fluid, such as air, and then estimating the viscosity and density when immersed in another fluid. The calibration allows an explicit calculation of the cantilever linear mass density and natural vacuum frequency which is used in the estimation of rheological parameters. From the known viscosity and density of air, and measured resonance frequency and Q-factor, the calibrated vacuum frequency for a single crystal silicon microcantilever was 17.48 kHz and density  $2325 \text{ kg.m}^{-3}$ . This agrees with literature values of  $2328 \text{ kg.m}^{-3}$  for single crystal silicon. The expected resonance frequency and Q-factor extracted from the model of Sader [71] using the calibrated values of the silicon cantilever has been compared against the measured experimental values. For gases the theoretical estimate and measured resonance characteristics show excellent agreement showing the capabilities of the device as a sensitive gas sensor (Figure 1-9).

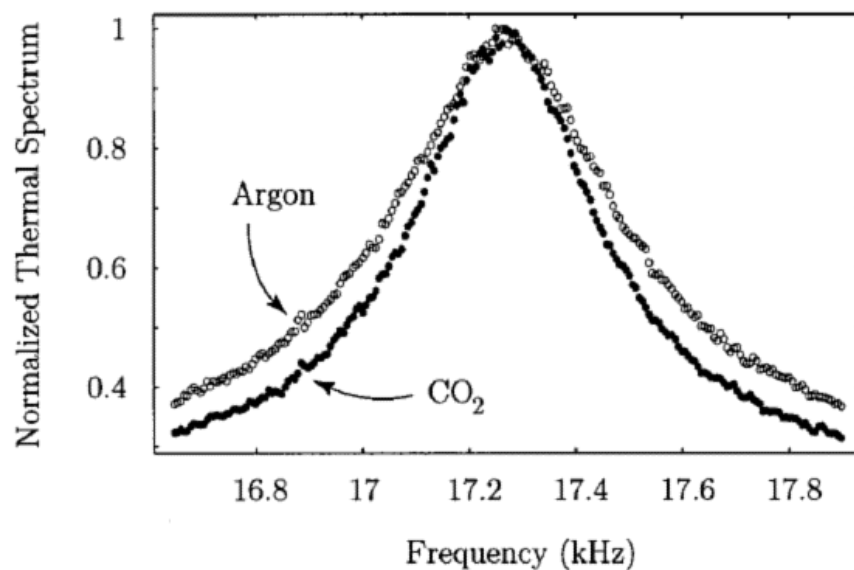


Figure 1-9 Frequency response of a microcantilever probe showing the ability to distinguish each gas using the Q-factor. From Boskovic et al [6].

A critical limitation of the resonating beam technique is that resonance peaks may not be distinguished accurately where the viscous damping on the beam by the fluid is large and the measured Q-factor drops below unity. In Boskovic's measurements the Q-factor approaches unity for only moderately viscous fluids (e.g. 1-butanol  $Q=1.2$   $\eta=2.8$  cP,  $\rho=810$  kg.m<sup>-3</sup>). It is noted that the Q-factor may be enhanced by changing the geometry and material of the cantilever; though a MathCAD algorithm derived from the mathematical model indicated that even with substantial changes in the cantilever geometry the Q-factor may still only increase by a small amount. This means the current resonant technique may be unsuitable for measuring the rheological parameters of moderately viscous liquids, for example, particular foods, motor oils, lubricants, inks and paints, and biological fluids.

Bergaud and Nicu [77] have extended the use of Sader's model to investigate resonances of SiO<sub>2</sub>-Au composite beams. Resonance frequency measurements were carried out in air, deionised water, ultra pure ethanol, and silicone oil. A peak frequency response for silicone oil (50 cP) was not found suggesting the possibility that the damping affect on the cantilever was too large and the Q-factor had fallen below unity. Bergaud and Nicu compared the experimental frequency measurements with theoretical values from Sader's model [71] showing good agreement for cantilevers immersed in air and water.

Shih et al [78] have presented an alternative theoretical method for simultaneous measurement of viscosity and density and validated this experimentally using a piezoelectric unimorph cantilever (PbO-ZrO<sub>2</sub>-TiO<sub>2</sub> on Stainless steel). Though this cantilever has some dimensions in the micro-domain (100  $\mu$ m thickness) it should be noted that this cantilever was approximately 4 cm long and 6 mm wide. Wilson et al [79] have re-evaluated the above work with cantilevers of similar dimensions and reported further results for glycerol. An alternative method for calculating the effect of fluids on resonating beams has been presented by Bhiladvala and Wang [80]. In this work, the resonance frequency and Q-factor are determined by considering fluid damping and flow properties of the medium. A detailed theoretical framework is given but no validation of the model has been provided.

Recent work by Papi [81] and McLoughlin [82] present simultaneous measurement of viscosity and density using uncalibrated AFM and rectangular microcantilevers though

it should be noted that the cantilever effective mass and natural frequency is found from operation in a known fluid, e.g. air or pure water, in a similar approach to Sader's method. Vančura [83] has also recently demonstrated viscosity measurements of electromagnetically driven rectangular cantilevers with integrated piezoresistive measurement in water and glycerol solutions. Technologically it should be noted that all previous work has used an optical measurement technique except for that of Vančura [83] and this adds a level of complexity to the instrument as discussed previously.

#### **1.4 Thesis Outline**

The work presented in this thesis aims to improve the actuation efficiency and mechanical signal of thermally actuated bimorph microcantilevers to demonstrate a whole blood coagulometer. A major part of the undertaking of this project was to develop new analytical tools and characterisation methods, specifically for measuring the deflection of large curvature cantilevers. These methods allow improvements to be quantified and compared with the benchmark first generation device. The outline of the thesis is as follows:

In chapter 2, analytical and simulation work is presented to support and aid the design of multilayer thermal microcantilever devices. This includes improvements in the current bimorph model to move away from the generally used thickness ratio and optimise structures based on constant stiffness. For complex structures a thermo-electro-mechanical simulation is used with extension to measuring thermal crosstalk in single probes. In this work a number of new designs in materials and footprint are presented for improvement of mechanical signal and reduction in thermal crosstalk.

In chapter 3, testing and characterisation of microcantilever devices is presented with comparison of performance in previous and new designs. A new optical technique for measuring tip deflection based on autofocus algorithms is presented with application to actuation efficiency and curvature. Piezoresistor mechanical and thermal sensitivity and the sensor and heater response during actuation are presented allowing an estimation of device mechanical signal and a lower limit on the improvement in the device. A summary of simulation and testing work is given at the end of the chapter to indicate the selection of devices for fluid tests.

Chapter 4 is dedicated to the application and considerations of the technology as a fluid probe and reports the results of a clinical evaluation at The Royal London Hospital to measure the performance of the microcantilever blood coagulometer against a laboratory standard Sysmex analyser. Work in known rheological fluids aims to extract the range and accuracy of the device and estimate the mechanical and thermal response using short pulse actuation. The final clinical evaluation results are compared with point-of-care instruments currently in the market.

Chapter 5 draws together the main results and conclusions of the microcantilever fluid probe work, and suggestions are made for possible future directions.

Chapter 6 presents the additional work on the Engineering Doctorate by the author on the European Pronano Project. The aim of the work is to develop polymer based scanning probe arrays with self-actuation and self-sensing. The chapter provides a background, thermal self-oscillation results for multilayer polymer based microcantilever, and the first demonstration of polymer scanning probes for surface imaging.

## Chapter 2 - Microcantilever Fluid Probe Design

### 2.1 Introduction

The use of numerical analysis and finite-element simulation of multilayered thermal actuators is important in establishing initial concepts and design rules for the microcantilever fluid probe. The aim of such analysis is to reduce the number of iterations needed in fabrication to achieve a working device, therefore reducing the overall time and cost in developing the fluid probe and future devices. The objective of the work presented is to aid improvements in the actuation efficiency, mechanical sensitivity, and thermal crosstalk compared to the benchmark device (MV1).

The current analytical framework of multilayered thermal actuators is based on Euler-Bernoulli small deflection beam theory using two principal structural layers presented here as the static bimorph equation [58].

$$\frac{1}{r_{initial}} = \frac{6(\varepsilon_1 - \varepsilon_2) \cdot (t_1 + t_2)}{\frac{E_2 t_2^3}{E_1 t_1} + \frac{E_1 t_1^3}{E_2 t_2} + 6t_1 t_2 + 4t_2^2 + 4t_1^2} \quad (2.1)$$

where,  $1/r_{initial}$  is the initial curvature of the microcantilever measured along the neutral axis,  $E_1$  and  $t_1$  are the Young's modulus and thickness of the top layer,  $E_2$  and  $t_2$  are the Young's modulus and thickness of the bottom layer, and  $\varepsilon_1$  and  $\varepsilon_2$  are the mean strain in the structural layers due to residual stress after processing. Read et al [17] and Han et al [85] have further derived a generalised formula for multimorph structures. The significance of equation 2.1 for optimising the deflection of bimorph microcantilevers has been recognised [13, 58, 59], noting the importance of the thickness-ratio term  $E_1 t_1^2 = E_2 t_2^2$  [58]<sup>1</sup>. The standard use of the thickness ratio term is limited to a two layer structure and uses beam thickness – varying stiffness - as a design parameter. The work presented in this chapter optimises deflection based on the position of the neutral axis of multilayered beams, with a fixed stiffness, as a means to maximise the ratio of bending moment to flexural rigidity.

---

<sup>1</sup> Note that in reference [58] the optimised thickness ratio has been incorrectly stated typographically as  $E_1 t_1 = E_2 t_2$

The dynamic bimorph equation is based on the induced linear strain difference due to a mismatch in thermal expansion of structural layers under heating noted previously in early work by Riethmüller and Benecke [16] and Chu [57], and derived in [58].

$$\frac{1}{r_{thermal}} = \frac{6(t_1 + t_2) \cdot (\alpha_2 - \alpha_1) \cdot \Delta T}{\frac{E_2 t_2^3}{E_1 t_1} + \frac{E_1 t_1^3}{E_2 t_2} + 6t_1 t_2 + 4t_2^2 + 4t_1^2} \quad (2.2)$$

where,  $1/r_{thermal}$  is the change in curvature due to thermal heating,  $\alpha_1$  and  $\alpha_2$  are the coefficients of thermal expansion of layer one and two, and  $\Delta T$  is the difference in temperature between the initial and final state assuming a uniform beam temperature.

To understand the transient behaviour during pulsed operation, theory and experimental results are presented based on joule heating and one dimensional heat conduction. This has implications for the optimisation of actuation and assists in describing unpredictable bending which has been seen in cantilever operation and is presented in chapter 3. For complex shaped structures with non-uniform cross section the use of steady state finite element simulation is presented with a technique to estimate the thermal crosstalk on the integrated sensor. Finally, the work is applied to the design and fabrication of a new microcantilever fluid probe (MV2).

## 2.2 Bending Solution of Multilayer Beams Based on Neutral Axis Analysis

To analyse the stationary position of the microcantilever beam the problem is assumed to be statically determinant with one end of the beam fixed and the other free. The materials are assumed to behave elastically and the dimensions of the cross section are small compared to the length of the beam. It can be shown that the shape of a released multilayer beam along the neutral axis is given by the Euler-Bernoulli equation

$$\frac{\frac{d^2 y}{dx^2}}{\left[1 + \left(\frac{dy}{dx}\right)^2\right]^{\frac{3}{2}}} = \frac{M(E_1, w_1, t_1 \dots E_i, w_i, t_i)}{EI(E_1, w_1, t_1 \dots E_i, w_i, t_i)} \quad (2.3)$$

where  $dy/dx$  is the slope and  $d^2 y/dx^2$  is the curvature at a point on the beam,  $M(E_1, t_1 \dots E_i, t_i)$  is the net bending moment acting on the beam due to residual

material stress, and  $EI(E_1, t_1 \dots E_i, t_i)$  is the composite flexural rigidity of the beam based on the Young's modulus and second moment of area of each layer. Equation 2.3 requires a complex solution [86-88] to preserve large deflections though this is not important in this work as the aim is to optimise the ratio of bending moment and flexural rigidity of the beam and therefore a small angle approximation can be used.

#### *Neutral axis*

The neutral axis is defined as the plane in which the resultant axial force acting on the cross section is zero and is taken as the line at which the curvature of the beam is measured. The second moment of area and bending moments for each material cross sectional area are calculated in relation to the distance from this axis, therefore it is important that the position of the neutral axis is first derived. For a beam with constant curvature it can be shown that the distance from the surface of the microcantilever to the neutral axis of a multilayer stack is equal to [Appendix A].

$$h = \frac{\sum_{i=1}^n E_i w_i \frac{t_i^2}{2} + \sum_{i=2}^n \left( E_i w_i t_i \sum_{m=1}^{i-1} t_m \right)}{\sum_{i=1}^n E_i w_i t_i} \quad (2.4)$$

where the layer width  $w_i$  has been introduced for completeness.

#### *Flexural Rigidity*

The flexural rigidity of a cantilever beam describes the resistance to bending through the cross section by compression or tension. Mathematically this is defined as the force required for bending the structure by unit curvature. This is related to the moment of area of an element located a distance from the neutral axis and the elasticity of this element. For a composite rectangular structure with  $n$  stacked layers the flexural rigidity can be written as

$$EI(E_1, w_1, t_1 \dots E_i, w_i, t_i) = \sum_{i=1}^n E_i I_i \quad \text{where} \quad I_i = \frac{1}{12} w_i t_i^3 + w_i t_i \hat{y}_i^2 \quad (2.5)$$

where the parallel axis theory is used to find the second moment of area  $I_i$  around an arbitrary axis, taken in this case as the neutral axis of the beam. For a multilayer stack it



is advisable to solve for the neutral axis position first and then solve numerically using the perpendicular distance  $\hat{y}_i$  between the neutral axis and area centroid.

### *Initial Bending Moment*

When the cantilever is released from the substrate a net bending moment due to residual stress in the structural layers causes the cantilever to bend out of plane and adopt an initial curved position. The residual stress in multilayer microcantilevers is predominantly due to the processing stress between thin films with different coefficient of thermal expansion (CTE). As the layers are stacked and become heated and cooled, the interface between the materials is fixed and becomes pulled. For example, if a high CTE polymer is used as the top layer of the bimorph and a low CTE polymer as the bottom layer, upon cooling from a curing temperature of approximately 300 °C the top layer will want to contract more than the bottom but this can not happen if the layers have already formed a good bond with each other. This induces stress between the films which when patterned as a cantilever and released will adopt an out-of-plane position such that all moments acting on the beam become zero. The total moment acting on a beam is given by summation of the stress acting over area elements a distance  $\hat{y}_i$  from the neutral axis of the beam [58].

$$M(E_1, w_1, t_1 \dots E_i, w_i, t_i) = \sum_{i=1}^n \sigma_i \hat{y}_i w_i t_i \quad \text{where} \quad \sigma_i = -E_i (\epsilon_i + \Delta\epsilon - \frac{\hat{y}_i}{r}) \quad (2.6)$$

where  $\epsilon_i$  is the mean strain due to process conditions,  $\Delta\epsilon$  is the strain variation when the beam is released, and  $-\hat{y}_i/r$  is the strain due to the curvature  $r$  of the cantilever [58]. The initial boundary condition is that the cantilever is flat and therefore the initial non-zero value of the moment is provided by the mean strain in the layers. As the cantilever bends, such that the total moment acting on the beam tends to zero and the cantilever comes to a statically determinant position, the curvature term balances the residual stress in the layers.

### *Optimisation of a bimorph structure*

Using the equation for bending moment (2.6) and flexural rigidity (2.5) the full form of the bimorph equation has been derived by the author [Appendix B]

$$\frac{1}{r_{initial}} = \frac{M}{EI} = \frac{\frac{1}{2} \left[ \frac{E_1 E_2 w_1 w_2 t_1 t_2}{E_1 w_1 t_1 + E_2 w_2 t_2} \right] (t_1 + t_2) (\epsilon_1 - \epsilon_2)}{\frac{1}{12} \left[ \frac{E_1 E_2 w_1 w_2 t_1 t_2}{E_1 w_1 t_1 + E_2 w_2 t_2} \right] \left( \frac{E_2 w_2 t_2^3}{E_1 w_1 t_1} + \frac{E_1 w_1 t_1^3}{E_2 w_2 t_2} + 6t_1 t_2 + 4t_2^2 + 4t_1^2 \right)} \quad (2.7)$$

where the above is reduced to equation 2.1 for a beam with constant width. It has been stated in previous literature that the bimorph equation is maximised when  $t_1 / t_2 = \sqrt{E_2 / E_1}$ , given constant width, and this has been termed the optimum thickness ratio. Though this optimisation is correct the ratio is limited to a two layer structure and indicates that the thickness of the device must be used as the main design characteristic.

For sensor applications it is desirable to control the stiffness of the microcantilever, such that the beam is either responsive to forced deflections, or in resonance mode the beam has a high natural frequency and Q-factor. For the fluid probe the stiffness of the microcantilever must be carefully considered. If the cantilever is very stiff it will be difficult to overcome the restoring force and move the cantilever through the fluid. If the cantilever is very flexible it might be possible to move through the fluid using lower actuation forces but the restoring force could be too weak to pull the cantilever back through the fluid. For the polymer scanning probe, presented in chapter 6, the stiffness must also be carefully considered. It is desirable to have relatively high stiffness to produce a high resonance frequency for high operational speed in tapping mode and to resist a static pull to the sample. If the scanning probe is too stiff the DC actuation becomes less efficient for levelling arrays which in turn produces more heat which can cause signal drift and a higher noise level.

If the full form of the bimorph equation (2.7) is considered the true optimisation being performed is to maximise the ratio of the initial bending moment to the flexural rigidity of the cantilever. For fixed overall thickness, a changing ratio of  $t_1$  and  $t_2$  leads to the initial moment and flexural rigidity having a maximum and inflection point

respectively. If  $t_2 = t - t_1$  the change in moment and flexural rigidity can be expressed as

$$\frac{dM}{dt_1} = \sigma_1 w_1 (h - t_1) - \sigma_2 w_2 (h - t_1) \quad (2.8)$$

$$\frac{dEI}{dt_1} = E_1 w_1 (h - t_1)^2 - E_2 w_2 (h - t_1)^2 \quad (2.9)$$

where the maximum initial moment and inflection of flexural rigidity is when the neutral axis is located at the interface of the bimorph layers ( $h = t_1$ ). This is equivalent to solving equation 2.4 using the optimum thickness ratio equation  $t_1 / t_2 = \sqrt{E_2 / E_1}$ . It should be noted that although the initial curvature of the beam is maximised the value must make sense, for example, for a cantilever of length  $L$ , if the curvature is greater than a quarter circle this would suggest the cantilever would start to curl back on itself or even form a complete circle. As a small angle approximation is also used the tip is mathematically located at a position  $x = L$  so it would not describe the shape of a highly curved surface.

#### *Constant Stiffness*

For small displacement of a microcantilever under an end load the restoring force of the beam is analogous to a spring restoring force and it has been shown that the stiffness  $k$  at the tip of the microcantilever is equivalent to  $3EI/L^3$  [37]. For optimised deflection ( $h = t_1$ ) the flexural rigidity of the bimorph reduces to

$$EI = \frac{1}{3} E_1 w_1 t_1^3 + \frac{1}{3} E_2 w_2 t_2^3 \quad (2.10)$$

Rearranging for the ideal thickness of layer one, where  $t_2 = t_1 \sqrt{E_1 w_1 / E_2 w_2}$  is a solution of equation 2.4 when the neutral axis is located at the bimorph interface gives

$$t_1 = \left( \frac{kL^3}{E_1 w_1 + (E_1 w_1)^{3/2} (E_2 w_2)^{-1/2}} \right)^{1/3} \quad (2.11)$$

This solution, derived by the author, allows the thickness of bimorph materials to be calculated based simply on the Young's modulus of materials, width, length, and required stiffness. Finding the ideal thickness of the layers and optimising the neutral axis is not the only way to achieve the largest out-of-plane deflection. The bending moment is proportional to the linear strain difference between the layers which can be changed during the processing conditions. For example, the polyimide retains stress due to the final curing process; to increase the stress in the layer the film can be cured at a higher temperature or a much steeper ramp and cooling rate can be induced.

### *Multilayer structures*

Microcantilever structures fabricated at the MNTC, including the microcantilever fluid probe, generally have several layers including integrated layers for heaters and sensors. By example a 3-layer microcantilever structure is presented where the neutral axis is initially kept in the reduced form of  $h$ . For a 3 layer structure the flexural rigidity and initial bending moment of the beam can be written as

$$EI = E_1 \frac{1}{12} w_1 t_1^3 + E_1 w_1 t_1 (h - t_1 / 2)^2 + E_2 \frac{1}{12} w_2 t_2^3 + E_2 w_2 t_2 (h - t_1 - t_2 / 2)^2 + E_3 \frac{1}{12} w_3 t_3^3 + E_3 w_3 t_3 (h - t_1 - t_2 - t_3 / 2)^2 \quad (2.12)$$

and

$$M = \sigma_1 (h - t_1 / 2) w_1 t_1 + \sigma_2 (h - t_1 - t_2 / 2) w_2 t_2 + \sigma_3 (h - t_1 - t_2 - t_3 / 2) w_3 t_3 \quad (2.13)$$

Where the neutral axis  $h$  is equal to

$$h = \frac{1}{2} \frac{E_1 w_1 t_1^2 + E_2 w_2 t_2^2 + E_3 w_3 t_3^2 + 2E_2 w_2 t_2 t_1 + 2E_3 w_3 t_3 (t_1 + t_2)}{E_1 w_1 t_1 + E_2 w_2 t_2 + E_3 w_3 t_3} \quad (2.14)$$

It has been found that the structure is optimised for bending when the neutral axis is located at the interface of structural layers. For example, for a 3 layer structure 2 zero crossing differential solutions exist at  $h = t_1$  and  $h = t_1 + t_2$  where one of these solutions will provide the optimum performance.

The solutions for multilayer cantilever beams show the suitability of using the neutral axis over the optimum bimorph thickness ratio. These solutions can also be applied to preserve constant beam stiffness in the generalised flexural rigidity equation though with several layers the ideal thickness of one layer is dependent on changing thickness of other layers. Therefore it is desirable to fix the thickness of subsequent layers or work through the solution numerically through trial and error.

### 2.3 Optimised Piezoresistive Sensor and Microheater

The sensitivity of an integrated metal piezoresistor track on a microcantilever for small deflections has been derived in previous work by Thayson [89]

$$\frac{\Delta R}{R} = \frac{3}{2} K \frac{(2L - \lambda) \hat{y}_s}{L^3} z \quad (2.15)$$

where  $\Delta R/R$  is the percentage change in resistance of the piezoresistor,  $K$  is the materials gauge factor,  $\lambda$  is the length of the piezoresistor along the beam,  $\hat{y}_s$  is the distance of the piezoresistor to the neutral axis, and  $z$  is the tip displacement of the microcantilever. Enhancement of sensitivity can also be made by choosing a material with high gauge factor and by placing the sensor far from the neutral axis, for example, on the microcantilever surface. The temperature coefficient of resistance (TCR) of the sensor material must also be considered as this will account for drifts due to thermal changes; materials such as nickel-chromium and constantan can have very low sensitivity to temperature. For applications in fluids the immersed sensor must be encapsulated and therefore it can not be placed on the surface. In such circumstances it is desirable to place the sensor close to the surface using a very thin encapsulation layer. Equation 2.15 is used in chapter 3 to measure the gauge factor of thin metal films on fabricated microcantilevers.

#### *Integrated Microheater*

Thermal actuation of a bimorph structure has previously been described by equation 2.2, indicating that the induced bending moment is provided by the difference in thermal expansion of structural layers assuming a uniform heating of the beam. In general, heating from an integrated metal heater or through one of the bimorph layers will generate a time dependent thermal gradient along the length and cross section of the beam. In this case it is desirable to consider the localised thermal bending moment of

each area element a distance from the neutral axis ( $M_i = \alpha_i \Delta T \hat{y}_i dA$ ) where the time dependent deflection is given by the difference of thermal expansion above and below the neutral axis. Understandably, describing the time dependent temperature at each position on the microcantilever is not a trivial matter and in such cases finite element simulation is a more suitable approach, though an analytical account of joule heating and thermal conduction will be presented here to show how performance of the fluid probe may be enhanced. Important considerations for integrated microheaters include:

- How quickly does the temperature increase?
- How quickly does heat transfer into the microcantilever structure?
- At what timescale does the heat influence the piezoresistor signal?
- How can thermal conversion to mechanical deflection be enhanced?

Aștefănoaei et al [90-91] have derived the time dependent temperature distribution in joule heated microwires analogous to embedded tracks in microcantilevers. The solution for the initial time dependent temperature of the microheater is given by [90]

$$T(r, t) = T_0 + [T_{ss}(r) - T_0] \left[ 1 - \exp\left(-\frac{\alpha \rho_0 I^2}{c \rho_m A^2} t\right) \right] \quad (2.16)$$

where  $T(r, t)$  is the radius and time dependent temperature of the heater,  $T_0$  is the initial temperature,  $T_{ss}(r)$  is the steady state temperature,  $\alpha$  is the temperature coefficient of resistance (TCR),  $\rho_0$  is the heater resistivity,  $I$  is the driving current,  $c$  is the specific heat capacity,  $\rho_m$  is the heater mass density, and  $A$  is the cross sectional area of the wire. Equation 2.16 is simplified by noting that the temperature at the outer radius ( $r$ ) of the metallic core is approximately equal to the central temperature and therefore  $T(r, t)$  can be treated simply as  $T(t)$ . The derivation by Aștefănoaei et al for heat transport in the cladding material to establish the steady state temperature of the heater ( $T_{ss}$ ) is unsuitable for application to the microcantilever as only radiation heat loss is assumed. This will overestimate the temperature of the heater as heat conduction through the microactuator base into the silicon die is significant.

For the microcantilever the average temperature of the heater can be estimated experimentally through measurement of the heater element resistance during actuation. The resistance can be converted to an average temperature using the measured TCR for

the material. Figure 2-1 shows experimental data of the measured gold MV1 microcantilever heater resistance during a 1V actuation pulse. The data has been fitted with an equation in the form of equation 2.16 where residuals to the curve have been minimised. The dashed line is the analytical solution to equation 2.16 for the microcantilever heater where the heater radius has been taken as the thickness 200 nm. Boundaries for a 20% uncertainty in the exponential value of equation 2.16 have been added to the analytical fit showing the sensitivity. The error will be dominated by the unknown values of heat capacity and density of the microwire. A small source of error is also in the driving current. In practice, the microcantilever fluid probe is driven with constant voltage and therefore as the resistance increases due to temperature the current must proportionally decrease and the dissipated power is reduced over time. For the increase of resistance in gold microheaters the reduction in dissipated power is  $< 1\%$ .

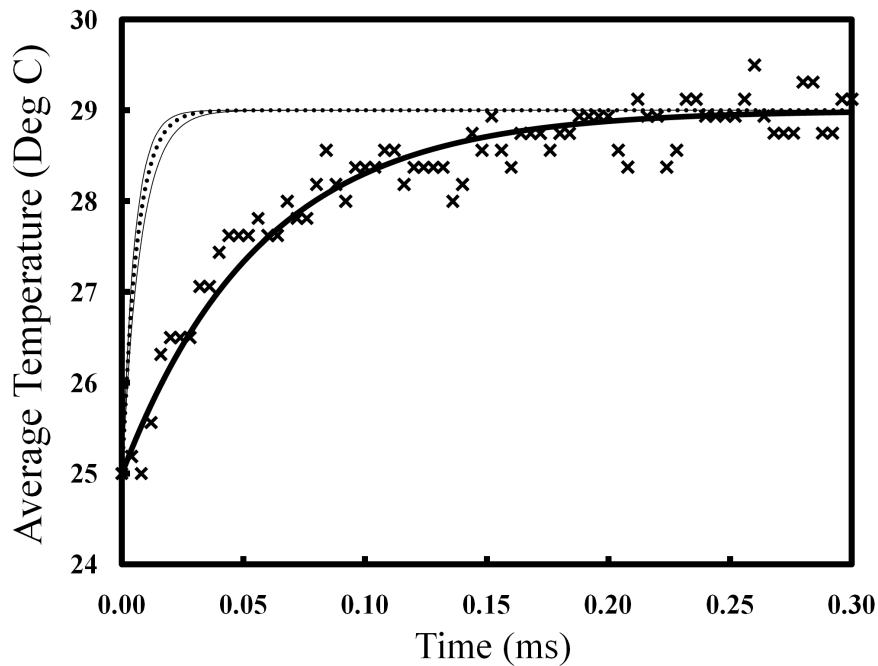


Figure 2-1 Response of the MV1 microheater during 1 V actuation (crosses) and the best fit (solid line) using an equation of the form 2.16. The dotted line represents equation 2.16 (no heat loss) where the heater radius is taken as 200 nm which is the approximate heater thickness. Error representing a 20% uncertainty in the exponential value in equation 2.16 is shown as solid lines against the analytical fit (dotted line).

The difference in experimental and analytical fits in figure 2.1 for the time dependent temperature of the microheater account for thermal conduction losses from the heater to the surrounding cladding. The thermal loss is dependent on the:

- Thermal diffusivity of the cladding materials and fluid.
- The conducting surface area of the heater.
- The conducting cross-section allowing heat to flow back through the heater to the base of the device.
- The volume that the heat is dissipated into.
- The heat convection coefficient from the surface of the microcantilever.
- The thermal gradient into the surrounding cladding and fluid.

This is an area of future interest to measure the efficiency of microheaters in microcantilevers. This has led to consideration of a multi-layer polyimide structure that allows high temperature activation for very short timescales due to lower heat loss to the surrounding material. From the analysis suitable microheater materials include gold, aluminum, and platinum being fully encased in an insulating cladding material. The concept of fast thermal actuation has also led to the modification of the heater shape by the author to be presented section 2.4.2.

Thermal conduction from the microheater into a high CTE encapsulating polyimide suggests enhanced deflection through increased local bending moments above the neutral axis. The heat transport between the microheater and sensor also creates crosstalk and therefore it is important to establish the transient heat profile in the polyimide over short time scales (< 50 ms). This is estimated using 1-dimensional heat conduction into a single thick material with constant temperature boundary condition [92].

$$T(x,t) = T_{heater} \cdot (1 - \operatorname{erf}\left(\frac{x}{2\sqrt{Dt}}\right)) \quad (2.17)$$

where  $x$  is the distance into the polyimide,  $t$  is the time,  $D$  is the thermal diffusivity constant of the polyimide equal to the thermal conduction divided by heat capacity and mass density, and  $\operatorname{erf}()$  is the Gaussian error function which returns a tabulated value for the argument. Figure 2.2 shows the temperature, as a percentage of the boundary temperature, across the polyimide at several instantaneous times. From characterisation of heater response, to be presented in section 3.3, the average temperature in the heater can increase by more than 10 °C at several microseconds with high peak power (250 mW). If the sensors are close to the heaters then a fraction of a degree change in



temperature can be equivalent to several microns of mechanical response of the piezoresistor. The MV1 probe heater and sensor are separated by 4 microns of polyimide, indicating a thermal crosstalk on short timescales (0.01 ms).

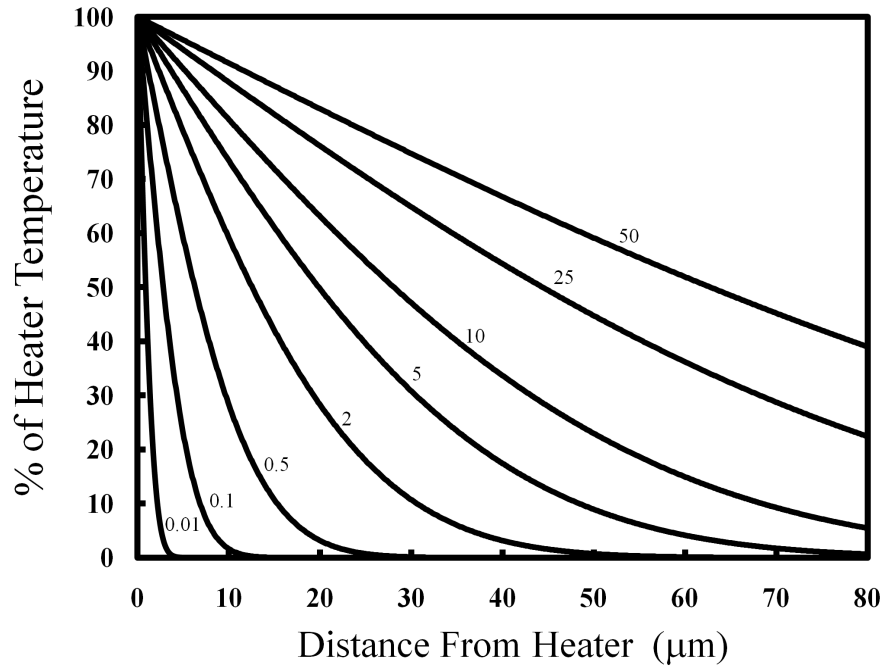


Figure 2-2 Thermal profile from the heater into the encapsulating Polyimide (PI2562) as a percentage of the boundary temperature. Each curve represents a snap shot in time (ms) as indicated.

The crucial design step for the improved probe is to separate the heaters and sensors geometrically and implement barriers (holes, conduction moats). Figure 2-2 indicates that for very short actuation pulses ( $< 2$  ms) a geometric separation of at least 50 microns is ideal. In chapter 3 the signal response from the microcantilever fluid probe indicates that for a separation of 80 microns the thermal crosstalk is still significant on timescales less than that indicated by figure 2-2. This suggests the possibility of a second conduction path possibly through the silicon, or underestimated heat conduction in this simplified analytical approach. It is also desirable to design a device with a high heat generation and a low loss parameter to create a large deflection quickly before heat transport can saturate the signal. This may be achieved through choice of materials in the bimorph and placement / shape of the heaters. A higher bending moment may also be achieved by placing the heaters further from the neutral axis, though this would have the effect of opposing initial deflection.

Figure 2-2 would also indicate that heat in the cross section reaches the surface of the cantilever (few microns) and the substrate very quickly - in less than 10 microseconds. This suggests that the rate of heating in the beam, and therefore also the rate of deflection and the thermal crosstalk on the sensor, is dependent on the medium thermal properties as well as rheological parameters.

## **2.4 Finite Element Simulations**

Finite element simulations allow an insight into the relative performance of complex multilayer thermal actuators with non-uniform cross section. The technique is presented with application to the benchmark fluid probe and a number of improvements by the author and Dr Vladislav Djakov including substitution of gold with a low CTE polyimide, an Epsilon shaped beam to geometrically separate heaters and sensors, and non-uniform gold heaters. Numerical output is given for microcantilever characterisation but should be viewed as a relative and not absolute measurement.

The finite element package used for microcantilever simulation is Intellisuite ThermoElectroMechanical (TEM) modelling for MEMS (Intellisense). This module is part of a wider package which includes design tools (3D Builder, Intellimask) for constructing the finite model. In practise, the simulation can give variable results relating to the definition of the finite model mesh though this is often a balance against the solver time. For example, a multilayered structure with approximately 20,000 nodes can take over an hour to analyse and each design requires several iterations at various actuation voltages.

Though the analysis module allows a dynamic solution of an actuated microcantilever, the full result is displayed as a final steady-state and the transient thermal distribution can only be viewed as a single node history plot against time. As the mechanical and thermal actuation may be on the order of micro- to milliseconds the time increment and iterations needed results in massive computation time. The software is further limited by a small angle approximation of deformed mechanical structures, for example, the x-coordinate of the microcantilever tip will remain constant and effectively stretch the beam. A consequence of the small angle approximation is that the initial deflection may be overestimated resulting in a lower stress being implied in material layers.

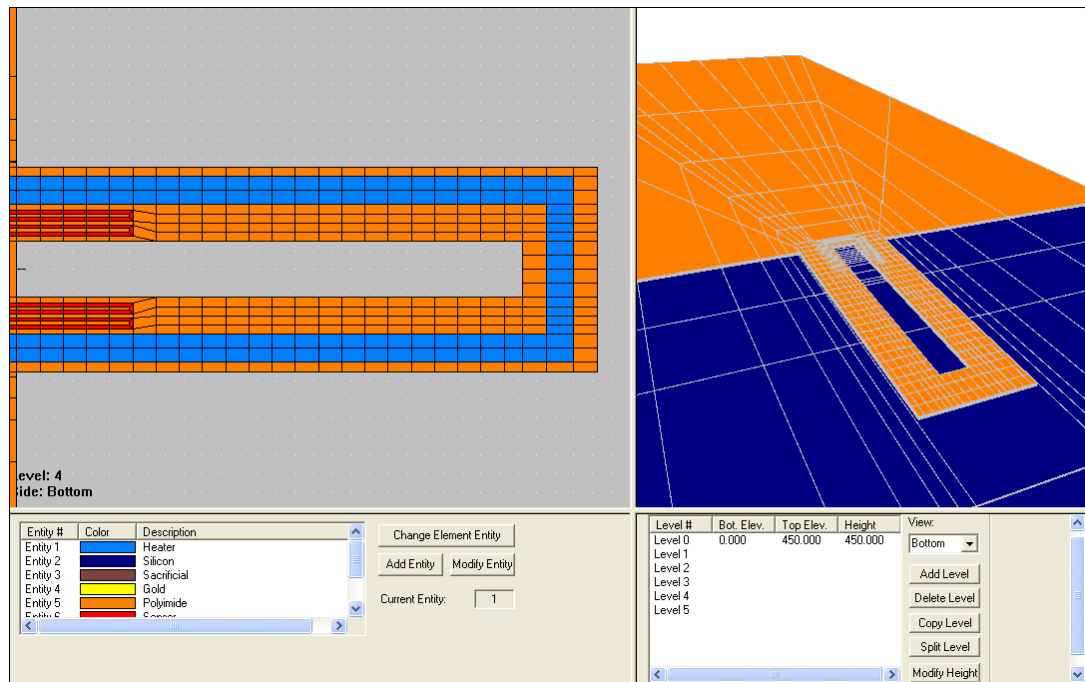


Figure 2-3 3D Build of the MV1 fluid probe device allowing control of thickness, entities, and mesh. This model is then exported to the TEM analysis.

The first step for TEM modelling is to build a solid 3D model of the device and mesh the structure to allow analysis of each finite element. The Intellisuite package includes 3D builder, a CAD program that allows a top down mask layout tool to define each layer of the model. Within the program the thickness of each layer can be controlled and elements are defined using the element entity colour (Figure 2-3). This allows alterations to the 3D model without the need to re-mesh. The final step is to apply a mesh to the 3D model. 3D Builder has an automated meshing tool which applies a mesh based on user input of mesh size. This tends to distort the model – smaller elements such as the sensor tracks can enlarge to the mesh size - and also provides no distinction between the areas of more importance. An alternative tool is a manual refinement of the mesh. This allows finer meshing in areas of interest such as on the microcantilever and a rougher meshing over areas of less importance such as the silicon substrate or on the die far from the device.

#### 2.4.1 TEM analysis of Benchmark Fluid Probe Device (MV1)

To present the process of TEM analysis and set the benchmark for making microcantilever improvements the first generation TBA design has been simulated. The design is based on gold-polyimide (PI2562) structural layers and interdigitated  $\Pi$ - shaped beams. These devices have been designed by Dr Vladislav Djakov and fabricated using

surface micro-machining techniques at the MNTC by the author. The fabrication of gold-polyimide bimorph actuators has been reported previously [13] and is outlined below. Some details have been omitted for commercial confidentiality.

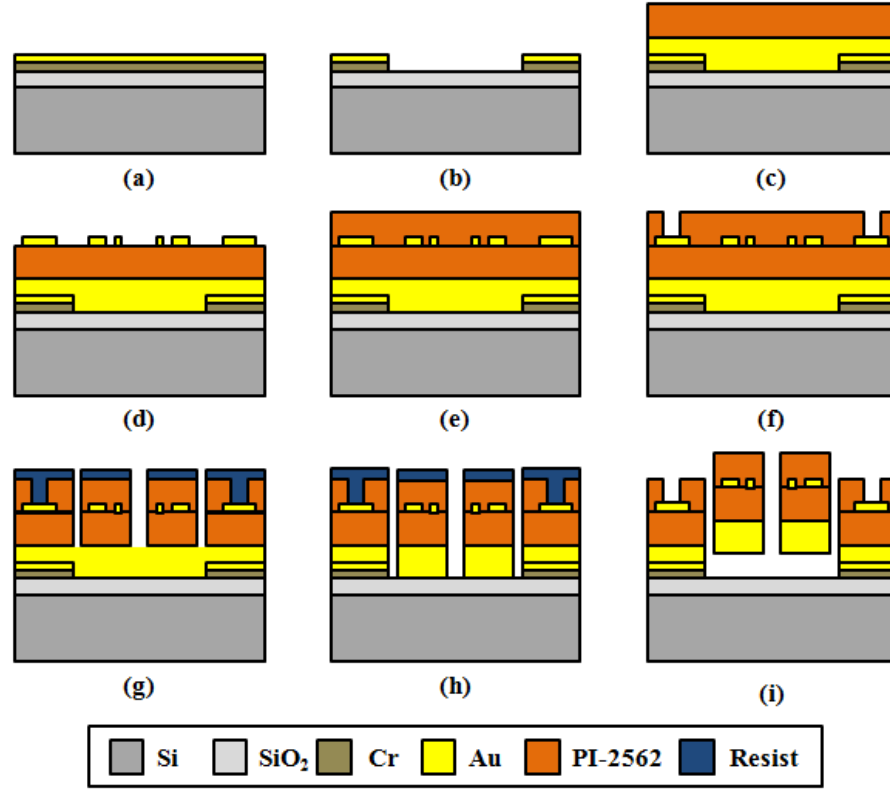


Figure 2-4 Microfabrication cross section of the MV1 microcantilever fluid probe. (a) Chrome / Gold evaporation. (b) Wet etching release areas. (c) Structural layer deposition. (d) Deposition and patterning of heaters, sensors, and contacts. (e) Encapsulation layer. (f) Dry Etching of polyimide to reveal contacts. (g) Dry Etching of polyimide to define microcantilever. (h) Wet etching of gold. (i) Release of structure.

In the first fabrication step a thin adhesion layer of chrome is plasma sputtered onto an oxidised silicon substrate. This is immediately followed by a layer of gold to prevent oxidation of the chrome upon exposure to air (Figure 2-4a). These layers are then patterned using standard optical lithography and chemical etching to define the bare SiO<sub>2</sub> areas where final bimorph structures will be released (Figure 2-4b). An important step in the fabrication process is the final release of cantilever structures for initial out-of-plane positioning. This process is accomplished using a sacrificial gold layer which exploits the weak adhesion of gold to the substrate. A final etch release step of the sacrificial layer forces each cantilever structure to delaminate from the substrate due to the residual stresses induced during the fabrication processes.

The next step is to deposit the structural layers of the bimorph (Figure 2-4c). The first layer is a thick plasma sputtered gold layer. The thickness has been established previously to offer good actuator results [13]. This is followed by a spin-coated polyimide (PI-2562) layer which is subsequently soft baked. By varying the spin speed the thickness of polyimide can be adjusted to achieve an optimum thickness ratio with the gold. After soft baking the wafer is hard baked to drive off solvent and stabilise the polyimide. In the next step a thin chrome adhesion layer and gold layer are plasma sputtered and patterned using standard lithography and wet etching techniques to define heater tracks, contact pads, and signal lines (Figure 2-4d). The signal lines are then encapsulated by a second spin-coated polyimide (PI2562) layer which is hard baked (Figure 2-4e).

To reveal contact pads for electrical connection standard lithography is carried out using a thick positive photoresist. This image is used as a hard mask for subsequent reactive ion etching (RIE) of the polyimide layer (Figure 2-4f). The resist is stripped and reapplied for subsequent RIE etching of polyimide to define cantilever structures and expose the gold structural layer (Figure 2-4g). The polyimide is etched in two stages otherwise pads would be exposed during the wet release of gold.

The final step is to release bimorph structures using a wet chemical gold etch using the previous photoresist as a masking layer (Figure 2-4h). Due to the residual stress in the structure the bimorphs naturally curl-up when the gold film contact with the beam is cleared, and therefore requires no special out-of-plane positioning (Figure 2-4i). Final  $\Pi$ -shaped bimorph structures are essentially two single bimorph beams measuring 600  $\mu\text{m}$  long, 80  $\mu\text{m}$  wide, separated by a 60  $\mu\text{m}$  gap and connected around the end. Gold heaters are 30  $\mu\text{m}$  wide passing down the centre of each beam and connected along the tip. Double meander gold piezoresistive sensors placed on each leg are 4  $\mu\text{m}$  wide and extend from the base of the cantilever 125  $\mu\text{m}$  into the beam. As sensors are implemented on the same layer as heaters and separated 4  $\mu\text{m}$  it is expected that the thermal actuation may have a significant impact on saturation of the microcantilever response. Using the analytical work presented in section 2.2, the previously established ideal thickness of bimorph layers positions the neutral axis very close to the bimorph interface. Each beam has a calculated stiffness at the tip of  $0.12 \text{ N.m}^{-1}$  and the metalised heater / sensor layer is located approximately 2  $\mu\text{m}$  above the neutral axis allowing good conversion to / from bending moments.

The 3D meshed model based on a single  $\Pi$ -shaped microcantilever is shown in Figure 2-3. The model includes the silicon die (Level 0) and signal lines to provide a realistic representation of the device as this is the main conduction path for heat transport. The sacrificial layer (Level 1) is represented as a single gold layer allowing the cantilever to bend free from the substrate layer. A mesh size of  $10 \times 25 \mu\text{m}$  is applied on the cantilever beam, this has been found to provide enough detail whilst limiting the computation time. The TEM analysis requires a number of mechanical, electrical and thermal boundary conditions to operate.

There is also a need to establish unknown values of material stress in the polyimide and electrical resistance of the heater and sensor tracks. The mechanical boundary condition is a fixed device except the free-end of the microcantilever to allow deflections. The electrical boundary conditions for the heater are a zero and non-zero voltage applied to each contact. The sensor has only one contact set to an applied voltage of zero and the other is set to an applied current, this allows a potential solution which when combined with the current gives a measure of the sensor resistance. The thermal boundary condition is a reference room temperature applied to the base of the silicon die and a convection coefficient applied to the top polyimide surface of  $5 \text{ W.m}^{-2}$  [43]. When electrically actuated the base temperature remains fixed at the ambient temperature. This should be a valid assumption as the silicon acts as a large heatsink and is unlikely to increase the temperature of the surrounding carrier at low energy. The simulation settings are based on a static TEM, with the result presented as the steady state. Displacements are set to large and “no piezo material” is selected.

Ideally it is desirable to find the sensor piezo signal when the cantilever is deflected, unfortunately the capabilities of the analysis is limited to materials with piezo tensor elements, such as silicon. Setting the material to non-piezo allows investigation of the thermal crosstalk in the device measured as a change in resistance only due to temperature. Material properties used in the simulation are given in Table 2-1.

|                      | Units                            | Gold                 | Silicon | PI2562             | PI2610             |
|----------------------|----------------------------------|----------------------|---------|--------------------|--------------------|
| Density              | $\text{g cm}^{-3}$               | 19.28                | 2.3     | 1.44               | 1.44               |
| CTE                  | $\times 10^{-7} \text{ K}^{-1}$  | 142                  | 30      | 600                | 30                 |
| Resistivity          | Ohm.cm                           | $2.2 \times 10^{-6}$ | 0.1     | $1 \times 10^{15}$ | $1 \times 10^{15}$ |
| Thermal Conductivity | $\text{W.cm}^{-1}.\text{K}^{-1}$ | 3.2                  | 1.48    | 0.00146            | 0.00105            |
| Specific Heat        | $\text{J.g}^{-1}.\text{K}^{-1}$  | 0.128                | 0.7     | 1.17               | 1.13               |
| Young's Modulus      | GPa                              | 78                   | 165     | 1.72               | 8.5                |
| Possion's Ratio      |                                  | 0.42                 | 0.27    | 0.36               | 0.36               |
| Dielectric Constant  |                                  | 6.3                  | 12      | 3.4                | 2.9                |
| TCR                  | $\times 10^{-3}.\text{K}^{-1}$   | 3.4                  | n/a     | n/a                | n/a                |

Table 2-1 Material constants used in the TEM simulation [93-96].

### *Establishing mechanical and electrical properties*

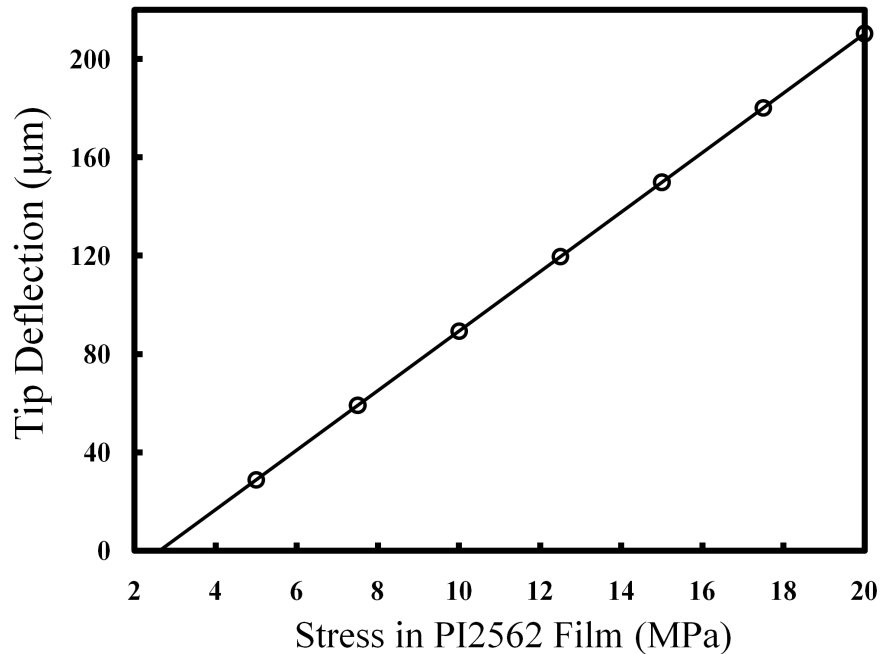


Figure 2-5 Result of the TEM simulation for the bimorph microcantilever tip deflection as the polyimide (PI2562) stress is varied.

The polyimide and gold film stress is not known but can be estimated using the TEM simulation with no applied heating to find the stress which gives an initial deflection estimate of 150  $\mu\text{m}$ . The intrinsic stress in the metalised gold layer is assumed to be near-zero after long curing of the polyimide at high temperature by annealing of the film. The intrinsic stress accounts for the initial deflection only and it is the linear strain difference due to a difference in thermal expansion when heating that characterises the

deflection capabilities. It is anticipated that the polyimide film stress will be underestimated as the small angle approximation will overestimate vertical deflection. Figure 2-5 shows the linear dependency of initial deflection on film stress in the polyimide from which a value of 15 MPa can be estimated<sup>2</sup>. Using the TEM simulation it is also possible to estimate the mechanical stiffness of the cantilever by applying a force perpendicular to the surface of the beam on a node at the very tip. Using several forces in the range 0 to 25  $\mu\text{N}$  the linear regression gives a stiffness of  $0.20 \text{ N.m}^{-1}$  at the tip which is close to the analytically calculated value of the individual arms as  $0.12 \text{ N.m}^{-1}$ .

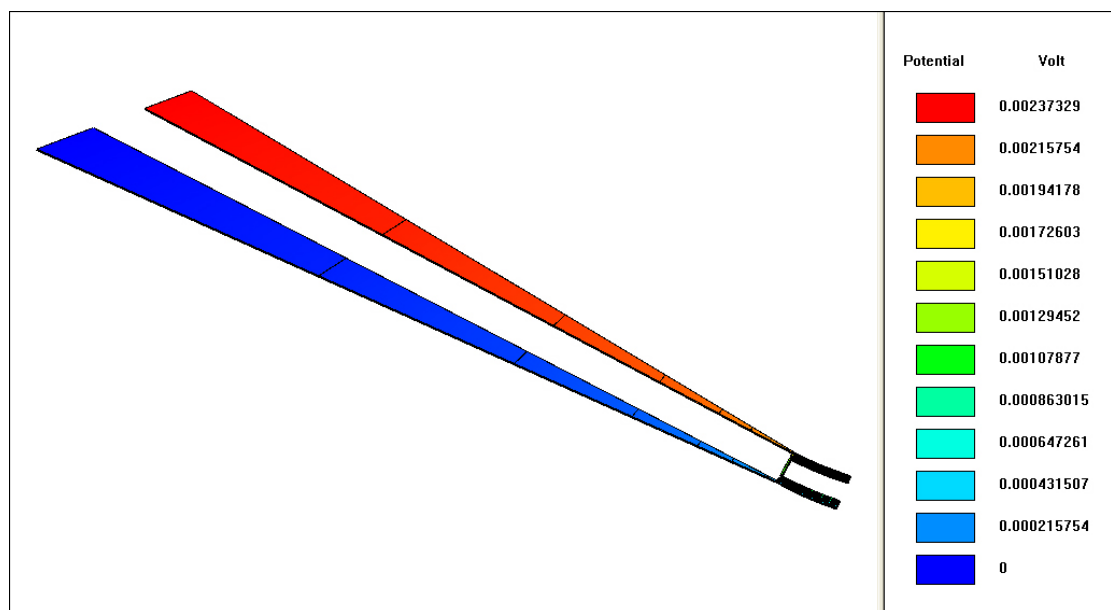


Figure 2-6 Electrical potential result of the sensor entity when a small sensing current is applied to the end contacts.

It is important to establish the initial resistance of the simulated heater and sensor tracks to establish the power input being applied to the microcantilever and the increase in resistance due to thermal crosstalk on the sensor. It is also important to establish the effect of self heating of the metal heater during actuation and the resulting change in power dissipation. To estimate the resistance of an entity, one side of the contact is set at zero volts and a current is applied through the entity by setting a non-zero current density to the contact area. After running the TEM analysis the resultant electrical result gives a potential of zero at the fixed electrode and a non-zero maximum value at the variable electrode, as shown in figure 2-6. As the applied current is known and the

<sup>2</sup> Film stress measurements during fabrication of MV3 indicates a stress in the range 22 – 59 MPa depending on processing conditions [97].



resultant voltage is measured the final resistance of the track can be calculated using Ohms law. As the sensing current approaches zero the calculated resistance tends to the nominal value as shown in figure 2-7. A final current density of  $1 \mu\text{A.m}^{-2}$  is selected resulting in power dissipation of  $0.1 \mu\text{W}$  in the sensor track, and a resistance of 45.640 Ohms. In practice a much higher sensing current is used as the output of the Wheatstone bridge is proportional to the input potential. The heater resistance is determined to be 11.759 Ohms using the same method. The actual measured value of resistance for fabricated microcantilevers is approximately 196 Ohms for sensors and 55 Ohms for heaters, though this includes a contact resistance from wire bonding and the chip carrier<sup>3</sup>. In the TEM simulation the heater resistor is fixed such that there is no self heating and power remains constant. In practise the heater resistance increases with fixed supply voltage and overall power dissipation decreases. Allowing the heater resistance to change in the TEM simulation the variation in power input in the range 0 to 10 mW is less than 2.5 %. From experimental measurements of the heater resistance, as in figure 2-1, the variation in power is approximately two orders of magnitude less, for example, at 5 mW input power the variation is 0.014 %.

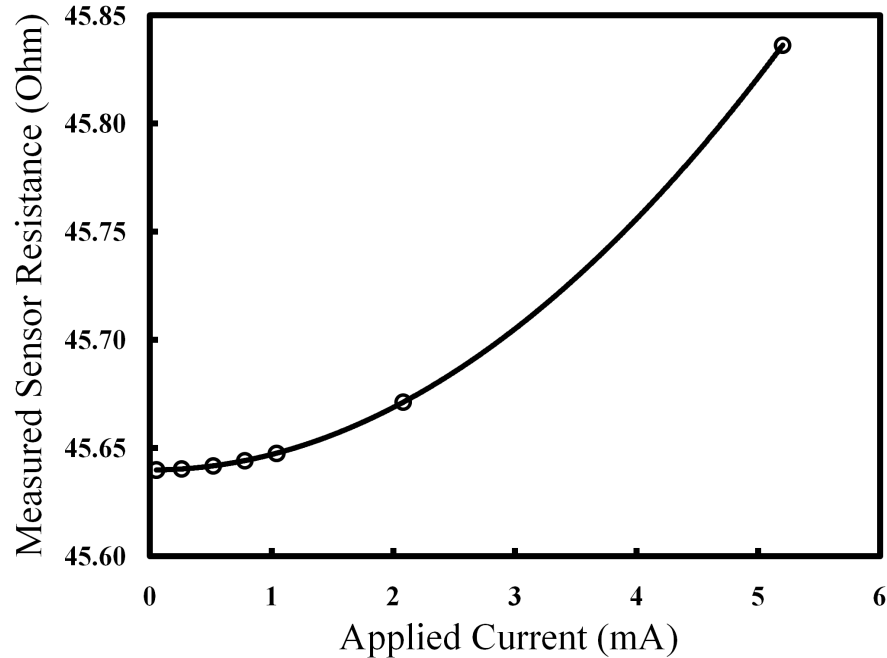


Figure 2-7 Measured sensor resistance from the TEM simulation potential result with variation in applied current. The variation in resistance is due to the self heating effect.

<sup>3</sup> Measured resistance probed directly on gold film and after bonding indicates an increase < 1% of the nominal resistance.

Using the mechanical and electrical results from the initial simulation it is possible to calculate a voltage to apply to the non-zero electrode of the heater for a given power dissipation. The objective of the full TEM analysis is to vary the power input of the heaters and to monitor the deflection of the device against power; the maximum temperature on the beam against power; and the change in sensor resistance due to heat dissipation. These measurements allow us to characterise the design and compare the result with changes to materials, dimensions, and layout. Figure 2-8 shows an example of an actuated device.

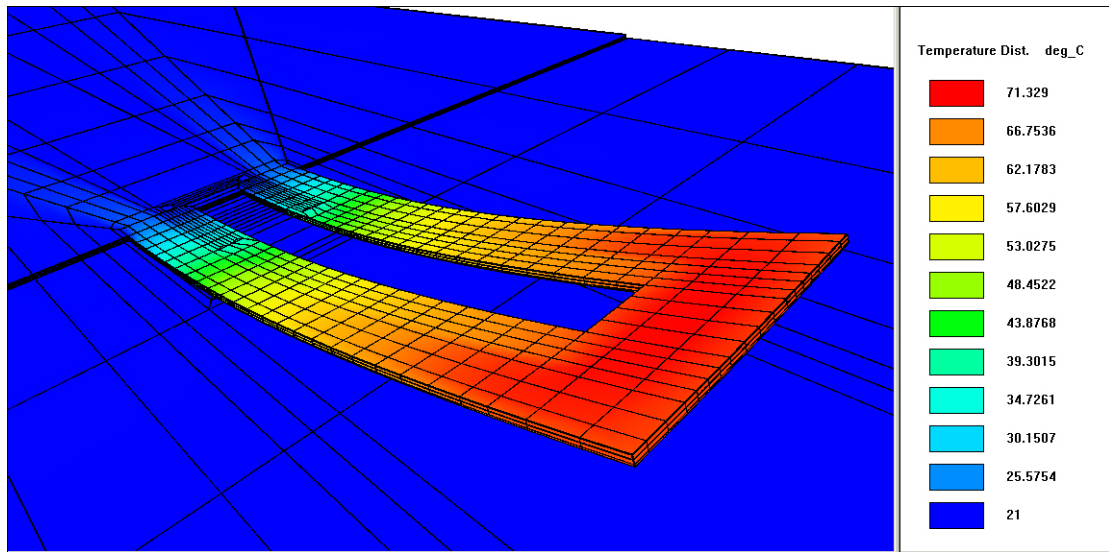


Figure 2-8 Example of steady state deflection and thermal distribution in the  $\Pi$ -shaped microcantilever with 20 mW actuation power.

The maximum temperature and deflection can be directly taken from the result, the sensor resistance is found by separating the entity and viewing the resultant potential as shown previously in figure 2-6. Figure 2-9 shows the deflection, temperature and sensor resistance results of the TEM simulation for the MV1 fluid probe with varying input power. From the simulation data the calculated actuation efficiency is  $1.92 \mu\text{m.mW}^{-1}$ , the increase in maximum temperature on the beam is  $2.50 ^\circ\text{C.mW}^{-1}$ , the conversion factor is approximately  $0.77 \mu\text{m.}^\circ\text{C}^{-1}$ , and the resistance change due to thermal crosstalk is  $8.11 \times 10^{-4} \Delta R_{\text{therm}}/R.\text{mW}^{-1}$ . The mechanical-to-thermal signal at steady state can be estimated by using the gauge factor for gold piezoresistor [10] and equation 2.13, and the thermal crosstalk directly extracted from the simulation result. Using a calculated deflection sensitivity of  $65 \Delta R/R.\text{ppm}.\mu\text{m}^{-1}$  and the equivalent thermal crosstalk  $423 \Delta R_{\text{therm}}/R.\text{ppm}.\mu\text{m}^{-1}$  at the required input power, the mechanical

signal as a proportion of the total signal is equal to 13.3%. This low value is not unexpected as at steady state it is expected that the sensor will be saturated by the heat dissipation. In practice the thermal crosstalk is variable; at very short times the thermal dissipation is limited to the heaters. As the heat transfers outwards the surrounding polymer increases in temperature but the heat has yet to reach the sensor. At these timescales the microcantilever will start to actuate and produce a mechanical signal on the sensor but the thermal crosstalk has yet to saturate the sensor. As the heat transfers to the sensor the signal becomes dominated by thermal crosstalk until at steady state the sensor is thermally saturated. Therefore, it is the very short timescales that are of interest in the operation of the fluid probe device.

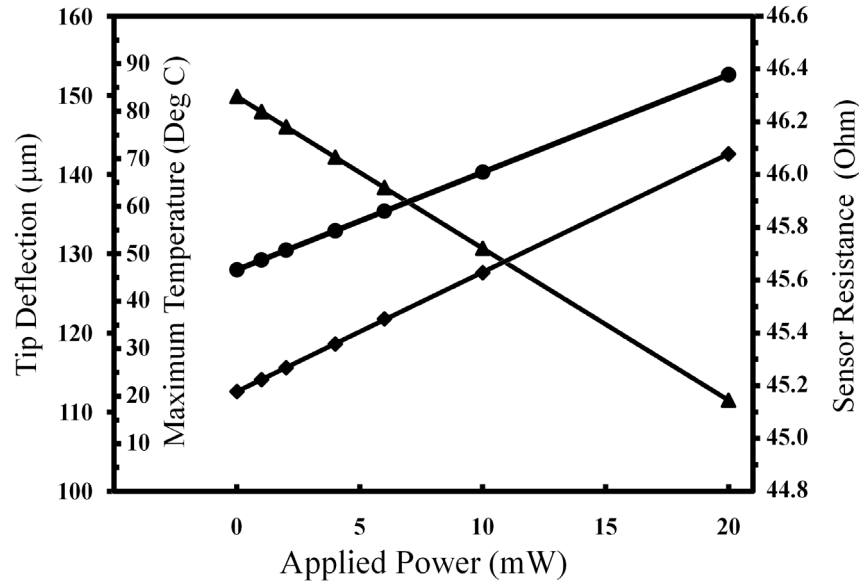


Figure 2-9 Deflection (triangle), maximum temperature (diamond) and sensor resistance (circle) results from the TEM simulation for the MV1 fluid probe.

#### 2.4.2 TEM analysis of Fluid Probe Design (MV2)

Characterisation of the benchmark fluid probe device (MV1), to be presented in chapter 3, shows a high thermal signal during actuation on the sensor. This is referred to as thermal crosstalk on the sensor and is separate from the thermal influence of the environment, and Johnson noise. The crucial aspect of this design is the proximity of the heaters to the sensors. By spatially separating the heater and sensor it is assumed that the heat transport to the sensor takes longer, giving a larger window for measurement before the sensor is saturated. It is assumed that if barriers are placed between the heater and sensor, such as a highly insulating material, this will also

increase our measurement window and lower the thermal crosstalk. This concept has led to a second generation design (MV2) by the Author and Dr. Vladislav Djakov based on a three-beam “Epsilon” shaped layout. In this design the outer heater arms provide the actuation and pull on the central sensor arm. As the heat is concentrated on the outer beams the thermal gradient towards the sensor is reduced. The thermal crosstalk should also be reduced by the air gaps in the structure which limit the conduction across the beam. Figure 2-10 shows the meshed 3D build of the Epsilon design; the solid design has air gaps filled.

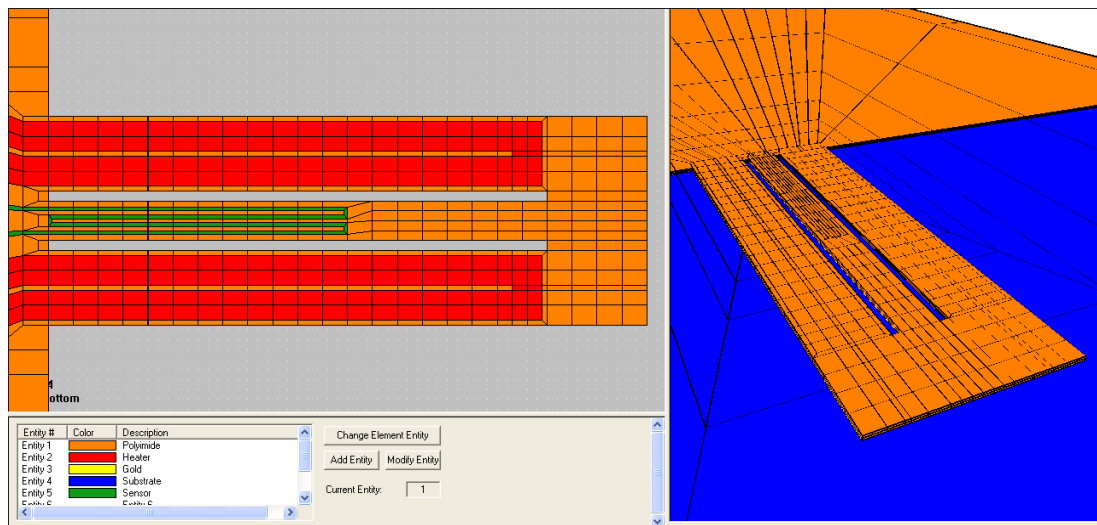


Figure 2-10 3D Build model of the Epsilon shaped fluid probe.

In the model there are a number of refinements that can be applied to size and shape – width of beam, width of air gaps, size of paddle – and heater and sensor placement, though this presents a large package of work. The aim here is to consider the relative impact on operation by the design rather than the refinements. For the current model the overall structure has a length of 600  $\mu\text{m}$ , and width of 210  $\mu\text{m}$ . Outer arms of the structure have a width of 75  $\mu\text{m}$  and the central beam has a width of 40  $\mu\text{m}$ . The air gaps have a width of 10  $\mu\text{m}$  and extend 500  $\mu\text{m}$  into the structure. The thickness and choice of materials have been set to the same configuration as the first set of simulations on the benchmark device to provide the most realistic comparison of performance. Each heater is confined to a single arm of the device, though it would also be possible to use a single path that connects across the end of the paddle. Heater width is 30  $\mu\text{m}$ , and passes 495  $\mu\text{m}$  microns into the beam. The sensor has a width of 4  $\mu\text{m}$ , has 2 meanders, and passes 300  $\mu\text{m}$  into the beam. The size of meshing along the structure is limited to 25  $\mu\text{m}$  segments. The heater resistance is found as before and each has a nominal value

of 9.015 Ohms and the sensor resistance is found to be 47.073 Ohms. In practice the two heaters are connected in series and therefore the total dissipated power in the simulation is the sum of both.

The TEM simulation result for a gold-polymer Epsilon and Solid configuration is presented in Table 2-2. The simulation results imply that both designs have a similar deflection efficiency and thermal conversion factor; this suggests that these factors are more dependent on the material configuration than the shape. As these simulations are in steady state and a thermally conductive material is used as one of the layers, the heat is likely to be distributed evenly so this suggests a similar deflection capability.

| Parameter                        | Units                                     | Π-Shape<br>Au-PI (MV1) | Epsilon<br>Au- PI (MV2) | Solid<br>Au-PI (MV2) |
|----------------------------------|---|------------------------|-------------------------|----------------------|
| Initial Deflection               | μm  | 149.9                  | 115.4                   | 130.5                |
| Actuation Efficiency             | μm.mW <sup>-1</sup>                       | 1.92                   | 1.07                    | 1.05                 |
| Maximum Temperature              | °C.mW <sup>-1</sup>                       | 2.50                   | 1.51                    | 1.35                 |
| Conversion Efficiency            | μm.°C <sup>-1</sup>                       | 0.77                   | 0.71                    | 0.78                 |
| Thermal Crosstalk                | $\times 10^{-4}$<br>ΔR/R.mW <sup>-1</sup> | 8.11                   | 9.59                    | 15.0                 |
| Mechanical Sensitivity           | ΔR/R.<br>ppm.μm <sup>-1</sup>             | 65                     | 55                      | 53                   |
| Equivalent Thermal Crosstalk     | ΔR/R.<br>ppm.μm <sup>-1</sup>             | 423                    | 896                     | 1427                 |
| Mechanical Signal / Total Signal |   | 13.3 %                 | 5.8 %                   | 3.6 %                |

Table 2-2 Comparison of simulated Epsilon and Solid MV2 Design.

The new design initially shows reduced mechanical to thermal signal compared to MV1. This is not unexpected as the MV1 sensor is placed near the base of the device where the steady state temperature is low due to conduction to the die. As the new sensors extend 300 μm into the beam they are placed in a higher temperature gradient of the beam and therefore thermal crosstalk is much higher. The Epsilon shape has a lower initial deflection than the Solid shape. This is also expected as the stress is being relieved in the layers that provide the initial bending moment by removing material. The important feature to note between the Epsilon and Solid design is the reduction in

thermal crosstalk by 37 % on the Epsilon design sensor due to a difference in thermal gradient as shown in Figure 2-11.

The author and Vladislav Djakov have suggested a further modification to change bimorph structural architecture from gold-polyimide to polyimide-polyimide layers. The modification is intended to improve actuation efficiency by selection of materials with a wider difference in the coefficient of thermal expansion and lower Young's modulus. The modification may also lower thermal crosstalk and increase localised heating due to lower thermal conductivity of the structural layers. The principal disadvantage of using two polymer layers is that the structure will have a slow relaxation after actuation due to slow thermal time constants. This places limitations on the maximum operating frequency of the microcantilever.

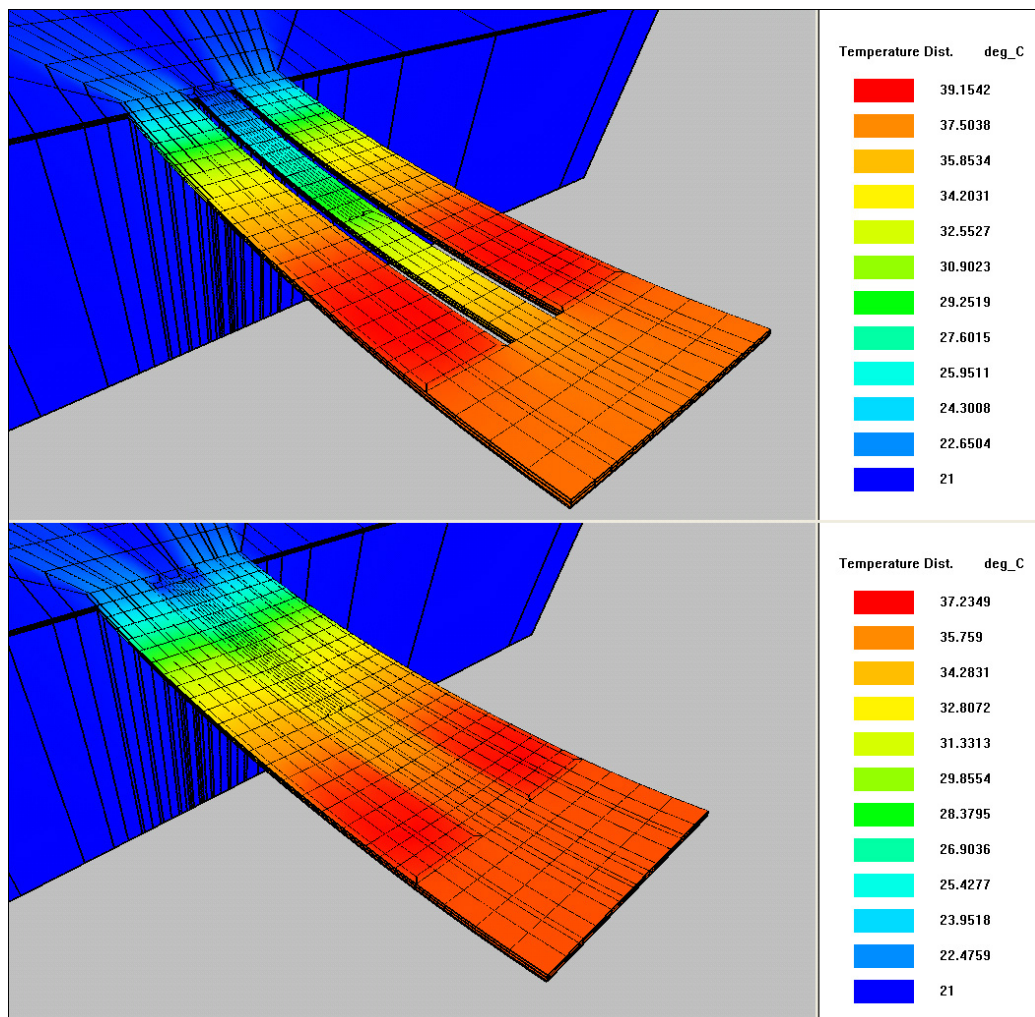


Figure 2-11 Comparison of steady state thermal distribution in gold-polymer MV2 Epsilon and Solid design under 12 mW total actuation power.

A second disadvantage of using a polymer layer is the consistency of thickness and stress in layers as the processing of the polymer is less controllable than the deposition of a metalised layer. The simulation material properties of the low thermal expansion polyimide (PI2610) have previously been given in Table 2-1. The TEM simulation is performed on the previous meshed structure though it should be noted that the distance of the heaters and sensor to the neutral axis of the beam is reduced and therefore thermal bending moments are not as large as before and the deflection sensitivity will fall. In the actual device the polyimide thickness can be chosen to optimise the neutral axis position to produce higher bending moments for a given flexural rigidity. For a Solid polymer-polymer structure with the same dimensions of the Epsilon structure the estimated stiffness at the tip is  $0.15 \text{ N.m}^{-1}$ .

Table 2-3 presents the deflection, temperature, and thermal cross talk results for the polymer-polymer Epsilon and Solid structure. The results immediately suggest polymer-polymer bimorph structures have significantly improved deflection efficiency over gold-polymer structures - approximately  $1 \text{ } \mu\text{m.mW}^{-1}$  to  $12 \text{ } \mu\text{m.mW}^{-1}$ . This improvement derives from the ability of the structure to retain the heat due to very low thermal conduction of the structural layers, and therefore increase in temperature substantially. At closer inspection the conversion factor has only improved slightly over gold-polymer structures. This suggests that improvements in actuation efficiency due to changes in materials will not lead to reduced thermal crosstalk as the mechanical signal is always driven by temperature in the beam. In practice the change in material should give improvements as the combination of fast heating and low conduction should produce more deflection and lower noise at very short timescales. As previous, the polyimide-polyimide Solid and Epsilon designs both have similar deflection capabilities, and the Epsilon design has a reduced initial deflection. The significant improvement of this configuration is the reduction in thermal crosstalk of >95% from Solid to Epsilon using the polymer-polymer architecture. This suggests the low thermal conductivity of the polymer layers is concentrating the power dissipation in the outer heater arms of the Epsilon structure and the air gaps are restricting the flow of heat around the structure.

| Parameter                        | Units                                    | Π-Shape<br>Au-PI<br>(MV1) | Epsilon<br>Au- PI<br>(MV2) | Solid<br>Au-PI<br>(MV2) | Epsilon<br>Design<br>PI- PI<br>(MV2) | Solid<br>Design<br>PI-PI<br>(MV2) |
|----------------------------------|--|---------------------------|----------------------------|-------------------------|--------------------------------------|-----------------------------------|
| Initial Deflection               | μm                                       | 149.9                     | 115.4                      | 130.5                   | 85.8                                 | 99.6                              |
| Actuation Efficiency             | μm.mW <sup>-1</sup>                      | 1.92                      | 1.07                       | 1.05                    | 12.14                                | 13.47                             |
| Temperature                      | °C.mW <sup>-1</sup>                      | 2.50                      | 1.51                       | 1.35                    | 13.33                                | 12.36                             |
| Conversion Factor                | μm.°C <sup>-1</sup>                      | 0.77                      | 0.71                       | 0.78                    | 0.91                                 | 1.09                              |
| Thermal Crosstalk                | $\times 10^{-4}$<br>$\Delta R/R.mW^{-1}$ | 8.11                      | 9.59                       | 15.0                    | 6.6                                  | 131.4                             |
| Deflection Sensitivity           | $\Delta R/R$<br>ppm.μm <sup>-1</sup>     | 65                        | 55                         | 53                      | 24                                   | 21                                |
| Equivalent Thermal Crosstalk     | $\Delta R/R$<br>ppm.μm <sup>-1</sup>     | 423                       | 896                        | 1427                    | 54                                   | 976                               |
| Mechanical Signal / Total Signal |  | 13.3 %                    | 5.8 %                      | 3.6 %                   | 30.1 %                               | 21.1 %                            |

Table 2-3. Comparison of simulated polymer-polymer Epsilon and Solid MV2 design. Previous simulation results for gold-polymer designs have also been included to allow direct comparison

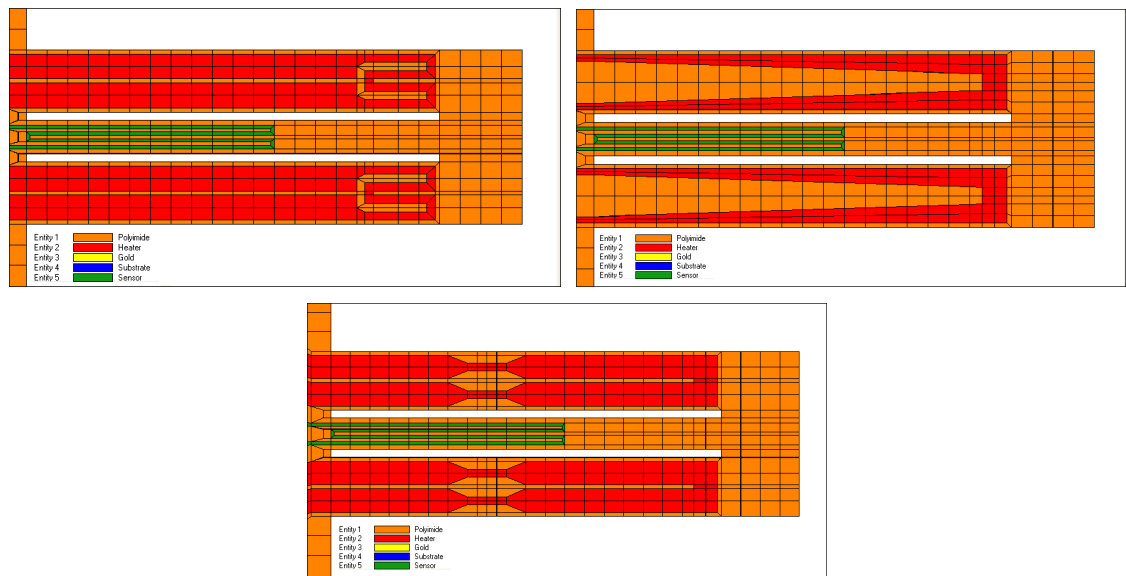


Figure 2-12 3D Models for heater comparison. *Top Left* – Concentrated Heater. *Top Right* – Tapered Heaters. *Bottom* – Pinched Heaters.



Further improvements to the device can be made from changes to heater configuration. This can involve changing the cross section of the heater to focus joule heating in specific areas, limit the heat conduction back through the metalised tracks, and allow easier bending due to the reduction of rigid material in the beam. For comparison to standard fixed width heaters, three configurations have been chosen. These include a concentrated heater and a varied width or tapered heater suggested by the author, and a pinched heater suggested by Vladislav Djakov. Each configuration can be seen in Figure 2-12. The concentrated heater is applied to focus the joule heating towards the end of the beam. This may result in higher actuation efficiency but the bending may not affect the sensor which is towards the base. The gradient heater may create a more uniform temperature gradient along the beam rather than a hot tip and cold base which is seen in Figure 2-8. The reduction in metalisation at the base of the structure may also improve initial and actuated bending. The pinched heater is effectively another form of concentrating heat to an area of the beam, it is anticipated that the pinch will generate more heat further down the beam, and the small cross section will also limit heat conduction passing from further along the beam back to the base. The reduction in metalisation in this area may also create an artificial bending axis. Table 2-4 presents the results for the different heater configurations as applied to the Epsilon design.

| Parameter                        | Units   | Standard | Concentrated | Tapered | Pinched |
|----------------------------------|---|----------|--------------|---------|---------|
| Initial Deflection               | $\mu\text{m}$                                   | 85.8     | 88.5         | 130.9   | 93.4    |
| Actuation Efficiency             | $\mu\text{m.mW}^{-1}$                           | 12.14    | 21.62        | 40.40   | 17.32   |
| Temperature                      | $^{\circ}\text{C.mW}^{-1}$                      | 13.33    | 30.24        | 33.13   | 18.92   |
| Conversion Factor                | $\mu\text{m.}^{\circ}\text{C}^{-1}$             | 0.91     | 0.71         | 1.22    | 0.92    |
| Thermal Crosstalk                | $\times 10^{-4}$<br>$\Delta R/R.\text{mW}^{-1}$ | 6.6      | 14.0         | 15.8    | 9.1     |
| Deflection Sensitivity           | $\Delta R/R$<br>$\text{ppm.}\mu\text{m}^{-1}$   | 24       | 24           | 24      | 24      |
| Equivalent Thermal Crosstalk     | $\Delta R/R$<br>$\text{ppm.}\mu\text{m}^{-1}$   | 54       | 65           | 39      | 53      |
| Mechanical Signal / Total Signal |   | 30.8 %   | 27.0 %       | 38.1 %  | 31.2 %  |

Table 2-4 Comparison of simulated heaters applied on the PI-PI Epsilon design.

The results suggest that making changes to the heater shape can have a significant impact on the deflection capabilities and thermal crosstalk. Concentrated heaters have the poorest conversion factor and high thermal crosstalk. From direct observations of the simulation the large thermal change for the concentrated heater are focused at the end of the structure. This has the effect of giving a high equivalent thermal crosstalk and poor deflection and therefore is not suitable to improve the device. The tapered configuration shows very good improvement in deflection capabilities and a significantly improved initial deflection. This may compensate for the reduction in initial deflection when the Epsilon design is used. Though the structure is heated substantially, the conversion to deflection is excellent and the overall improvement from standard heaters is an increase in the mechanical proportion of the total signal by approximately 24%. This implies similar deflection can be attained at lower power and lower temperature. The pinched heater configuration only provides a small improvement to deflection capabilities of the device, though is of interest as the pinch effectively creates an artificial bending point such that the structure deflects around the midpoint of the beam and the bend is also inline with the sensor placement.

#### **2.4.3 Realisation of MV2 Fluid Probe Design**

The mathematical and finite element simulations support a number of design changes on the original fluid probe device to improve the actuation efficiency and reduce thermal crosstalk of the integrated sensor. This includes:

- 1) Realisation of a new design based on an Epsilon shaped configuration
- 2) Replacing the gold structural layer with a low thermal expansion polyimide
- 3) Replacing the gold piezoresistor with a low TCR material such as NiCr or CuNi
- 4) Increasing the distance of heaters and sensors to the neutral axis possibly by using a thin final encapsulation layer
- 5) Realisation of tapered gold heaters

A final design consideration not mentioned in the analysis is the referencing of the device with a passive microcantilever in a half or full bridge configuration. This has been suggested previous to the development of the original probe and allows for compensation of drift and environmental temperature. Ideally the passive probe would also be actuated and the thermal crosstalk on the beam compensated but this is difficult without also compensating the mechanical signal.

The MV2 probe layout has been designed by Microvisk Ltd and the technology has been successfully transferred to a UK based microfabrication foundry. The realised probes are based on Solid and Epsilon polymer bimorphs with gold microheaters and NiCr sensors (Figure 2-13a). A number of probes have also been implemented with tapered heaters for comparison to standard heater layout. For characterisation of performance presented in Chapter 3, a small sample of probes from the 28 original designs has been chosen by the author; G is a Solid design with standard heaters; H is a Solid Design with tapered heaters; W is an Epsilon design with standard heaters; and X is an Epsilon design with tapered heaters. This sample allows a comparison to the previous MV1 design and a direct comparison between the Solid and Epsilon design, and the standard and tapered heater's.

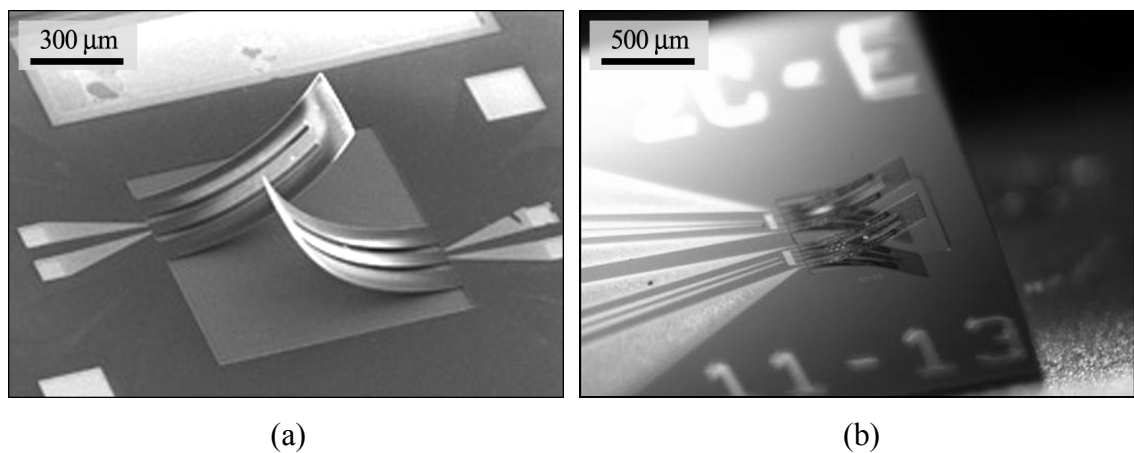


Figure 2-13 (a) Microfabricated Polymer-Polymer Epsilon design (MV2). The Solid design is without etched holes. (b) Pre-production design (MV3) device with active and reference microcantilever based on Polymer-Polymer Epsilon footprint.

The fabrication route of the fluid probe has been modified under the technology transfer with changes to the mechanism of release, patterning of integrated metal layers, and the substitution of gold with a low thermal expansion polyimide. Cantilever release by weak adhesion of gold has been replaced with a sacrificial aluminium layer which can be wet etched in a fast electrochemical reaction. The gold layer has been replaced with a low CTE polyimide (PI2610) that can be soft baked before application of the first high CTE polyimide layer and then hard baked for curing. The metalised heaters are then sandwiched in the structure with another polyimide layer and NiCr sensors are deposited and patterned using lift-off in a separate layer before a final encapsulation layer is added.

Final multilayer structures chosen for comparison are 800  $\mu\text{m}$  long and 300  $\mu\text{m}$  wide. Epsilon shapes have two 30  $\mu\text{m}$  wide air gaps extending 650  $\mu\text{m}$  into the structure with outer arms being 90  $\mu\text{m}$  wide and the central sensor arm 60  $\mu\text{m}$  wide. Standard heater width is 15  $\mu\text{m}$  and sensor track width is 4  $\mu\text{m}$  extending from 200 to 600  $\mu\text{m}$  into the structure. Tapered heaters are 15  $\mu\text{m}$  at the maximum point and 5  $\mu\text{m}$  at the minimum. Using section 2.2 the position of the neutral axis in the Solid structure is approximately 1  $\mu\text{m}$  from the heater layer and 3.2  $\mu\text{m}$  from the sensor layer. The estimated stiffness at the tip is approximately  $0.3 \text{ N.m}^{-1}$  which is slightly higher than the MV1 probe. For an Epsilon design there are effectively two beam structures, one with heaters and one with sensors. The neutral axis is located approximately 2.5  $\mu\text{m}$  below the sensor in the middle arm and 1.2  $\mu\text{m}$  below the heater in the outer arms. The calculated stiffness is approximately  $0.1 \text{ N.m}^{-1}$  in each arm.

Beyond this thesis a third pre-production device (MV3) has been designed by the author and Vladislav Djakov based on characterisation and fluid results from MV2. Device layout has been implemented in CAD by the author and has been fabricated at a MEMS foundry. The device incorporates referencing and realisation of two sensor configurations with platinum and constantan metalisation (Figure 2-13b). The MV3 design includes a pinched heater above the tapering and the overall thickness has been reduced with the final encapsulation layer reduced from 1.0 to 0.3  $\mu\text{m}$ . Though this reduces the distance of the sensor to the neutral axis to 2  $\mu\text{m}$ , the overall beam stiffness is reduced by around 50% and therefore the restoring force that opposes the actuation force is also reduced by the same amount. For the pre-production probe design Dr. Vladislav Djakov has designed a serpentine sensor that has equal resistance and location to the active probe whilst having a reduced mechanical response such that the reference device compensates more of the thermal crosstalk component of the response. This implementation has shown a further improvement in observation of the mechanical signal in fluids over the thermal crosstalk. The platinum and constantan piezoresistor testing is included in chapter 3 and an indication of the device response is given in the closing chapter to demonstrate the possible future operation.

## Chapter 3 - ThermoElectroMechanical Characterisation of Microcantilever Fluid Probes

### 3.1 Introduction

In the previous chapter analytical and finite element simulations provided a foundation for design improvements to microcantilever fluid probe devices. These improvements aim to improve the mechanical signal and lower thermal crosstalk of the integrated piezoresistor for operation in fluids. This can be achieved by improving deflection efficiency ( $\mu\text{m.mW}^{-1}$ ) and piezoresistor mechanical sensitivity ( $\Delta R_{\text{mech}}/R.\mu\text{m}^{-1}$ ), and reducing the thermal cross talk ( $\Delta R_{\text{thermal}}/R.\text{mW}^{-1}$ ) and piezoresistor thermal sensitivity ( $\Delta R_{\text{thermal}}/R.\text{K}^{-1}$ ). These improvements also provide a foundation for the design of polymer scanning probes presented in Chapter 6. The author's contribution to design changes from the benchmark fluid probe (MV1) include implementing an Epsilon shaped microcantilever, tapering of metal heaters towards the cantilever base, suggested material changes from a gold base layer to a polyimide, and high TCR sensor to a low TCR material. In the new design metalisation for heaters and sensors has also been separated by an additional layer of polyimide.

The work presented in this chapter uses developed mechanical, thermal, and electrical tests to characterise the performance of the above changes against the benchmark fluid probe. This information provides a validation of the new probe design and acceptable limits of quality control.

Section 3.2 presents experimental results for the mechanical and thermal sensitivity of metal thin films as a basis for quantifying absolute resistance of the heater and sensor during actuation. Section 3.3 presents electro-mechanical testing based on a newly developed optical autofocusing technique for measurement of large curvature microcantilever tip deflection. The technique is used to measure deflection efficiency, initial deflection, and fully reconstruct the curvature of the beam. Electrical measurements of the heater during actuation also allow an estimation of the beam temperature and rate of temperature increase. Section 3.4 presents the thermal crosstalk and self heating of the microcantilever device with electrical measurements and thermal imaging.

### 3.2 Mechanical and Thermal Characterisation of Metal Thin Films

The microcantilever fluid probe has integrated metal films for sensing mechanical deflection by the piezoresistive effect – this has been discussed previously in chapters 1 and 2. The MV2 (2006) and pre-production MV3 design (2008) have separate metalisation for heaters and sensors. This is an advantage as although gold is suitable for heaters – high thermal conduction, low thermal heat capacity, and relatively high thermal expansion – it has a high temperature coefficient of resistance (TCR) and is therefore susceptible to large changes in resistance due to temperature. For example, a 100 nm deflection of a microcantilever using gold sensors with  $0.3 \text{ ppm.nm}^{-1}$  sensitivity [10] is equivalent to a change in temperature of the sensor of  $0.008 \text{ }^{\circ}\text{C}$ . Therefore it is desirable to find a sensor material with high gauge factor and low TCR. A second advantage is that the sensor can be placed close to the microcantilever surface, further from the neutral axis using a very low thickness encapsulation layer. A third generation pre-production device (MV3) has been fabricated by an external foundry using platinum (high Gauge factor and high TCR) and constantan (low Gauge factor and low TCR) sensors. These devices are also included in mechanical and thermal testing for comparison of a larger range of materials.

#### 3.2.1 Mechanical Sensitivity

The mechanical sensitivity ( $\Delta R_{\text{signal}}/R.\mu\text{m}^{-1}$ ) of the microcantilever fluid probes has been established using a computer controlled contact probe to deflect the microcantilever tip<sup>4</sup>. The setup consists of a linear XY stage for control of the probe-cantilever position, a high magnification telescope with CCD camera (Infinity 2-1, Lumenera) for viewing the measurement via PC, a computer controlled translation stage (VT-60, Micos) with fixed vertical probe, and Wheatstone Bridge electronics close to the device in half bridge arrangement using a second on-chip microcantilever. The electronics is connected via a BNC router (NI BNC-2110, National Instruments) to a PC data acquisition card (NI PCI-6221, National Instruments) running LabView (LabView 7.0, National Instruments). The change in resistance of the microcantilever can also be directly measured using a high precision DMM (2100 6 ½ Digit USB Digital Multimeter, Keithley).

---

<sup>4</sup> The probe station and measurement, including electronics and software, has been performed by Robert Ibbotson

The change in resistance for a known tip deflection allows a direct measure of the mechanical sensitivity. To compare piezoresistive films equation 2.15 is used, where the length of the microcantilever and the controlled tip deflection is known and the neutral axis of the microcantilever cross section can be estimated, to find the gauge factor.

There are a number of errors in the final measurement to minimise. Firstly the contact probe should always be at the tip of the cantilever; this is not always the case as the probe slips along the beam due to a large difference between the initial and final horizontal position. As the probe slips along the beam the tip is effectively moving further than the controlled deflection and therefore the change in resistance appears to increase. This error can be minimised by only taking the first increments after the probe has been aligned. The second error exists in the conversion of voltage output to resistance which derives from inaccurate measurement or drift in nominal bridge resistors, supply voltage (1V), and amplifier gain. The variation in voltage to the bridge and amplifier is significantly smaller than the drift in bridge resistors. As the signal drift – due to resistor drift - can be monitored through LabView this can also be controlled and through accurate measurement of the bridge resistors with a 6 ½ digit DMM (2100 6 ½ Digit USB Digital Multimeter, Keithley) the conversion error is not significant. The largest error in the measurement is based on the estimation of the neutral axis in the multilayer structure using data sheet material properties for Young's modulus and the target thickness. For example, the actual film thickness measured during fabrication of polymer-polymer devices for the scanning probe project at the same facility deviated in some cases by up to 10% from the target value and had an average difference of 6% from the target thickness.

As the measurement is partly destructive due to damage by the tip slipping along the beam, and chip supply is limited for characterisation tests, only single tests on each device have been performed. The method used is consistent for each measurement and is indicative of the relative deflection efficiency between each design. Table 3-1 gives the mechanical sensitivity and calculated gauge factor of the metal films. The error in Gauge factor, from equation 2.13, is dominated by the error in the distance of the sensor from the neutral axis. Using the variation in film thickness measured above the Gauge factor error for MV1, MV2 and MV3 is 8.5%, 7.4%, and 8.6% respectively. The results of mechanical testing indicate that platinum has the highest gauge factor and constantan

the lowest. The unexpected result is a low gauge factor in gold, equal to 1.3, which is below that of published values [10] and other internal testing<sup>5</sup>. This could be due to the chrome adhesion layer such that the heater is explicitly a composite structure; issues have also been seen previously with chromium migrating into the gold at high curing temperatures.

| Measurement        | Sensor Material | Mechanical Sensitivity ( $\Delta R_{\text{mech}}/R \cdot \mu\text{m}^{-1}$ ) | Calculated Gauge Factor |
|--------------------|-----------------|--|-------------------------|
| MV1 – $\Pi$ -Shape | Gold            | 20.8 ppm   | 1.3 +/- 0.1             |
| MV2 – Solid        | NiCr            | 16.0 ppm   | 1.3 +/- 0.1             |
| MV2 – Solid        | NiCr            | 16.1 ppm   | 1.4 +/- 0.1             |
| MV2 - Solid        | NiCr            | 16.6 ppm   | 1.5 +/- 0.1             |
| MV3 - Epsilon      | CuNi            | 9.0 ppm  | 1.1 +/- 0.1             |
| MV3 - Epsilon      | Platinum        | 29.0 ppm   | 3.4 +/- 0.3             |

Table 3-1 Experimental results for mechanical sensitivity and calculated gauge factor of microcantilever piezoresistive sensors.

### 3.2.2 Temperature Coefficient of Resistance

The resistance of the sensor piezoresistor is susceptible to large changes and drift due to changes in temperature from thermal crosstalk and the environment. The change in resistance is given by  $\Delta R/R = \alpha \Delta T$  where  $\alpha$  is a material constant called the temperature coefficient of resistance (TCR). The measurement is conducted in a temperature controlled incubator environment with 0.1 °C stability (Digital Block Heater QBT2, Grant). Each device has been mounted and bonded to a ceramic DIL carrier; this adds a small error in the resistance measurement as the gold bonding wires and gold carrier has been found to account for <1% of the thin film value – this error is systematic through measurement of each metal film.

To established best practice for the measurement a MV1 microcantilever is placed in a ZIF socket inside a machined aluminium block heater. To encapsulate the microcantilever to reduce any potential air flow over the device an aluminium lid with

<sup>5</sup> Robert Ibbotson has fabricated polyimide surface stress sensor with gold piezoresistor with  $K = 4$



two small access holes is placed on top of the block heaters. The resistance is monitored in real-time using a 6 ½ digit DMM (2100 6 ½ Digit USB Digital Multimeter, Keithley) connected through the block heater. The block heater is set to a temperature of 60°C and the resistance of the microcantilever is monitored until it reaches a thermal equilibrium. After 30 minutes the resistance settles and the measurement of resistance can be confidently taken. To measure the impact of the block heater lid, and whether measurements should be taken directly with a DMM, a gold sensor resistance is continuously measured while probed. Figure 3-1 indicates the effect of removing the measurement chamber lid to take a reading; the effect of removing the chamber lid and using standard DMM probes in contact with the device carrier to take a reading; and the effect of interrogating a low TCR Constantan wire that is directly connected through the lid into the ZIF socket.

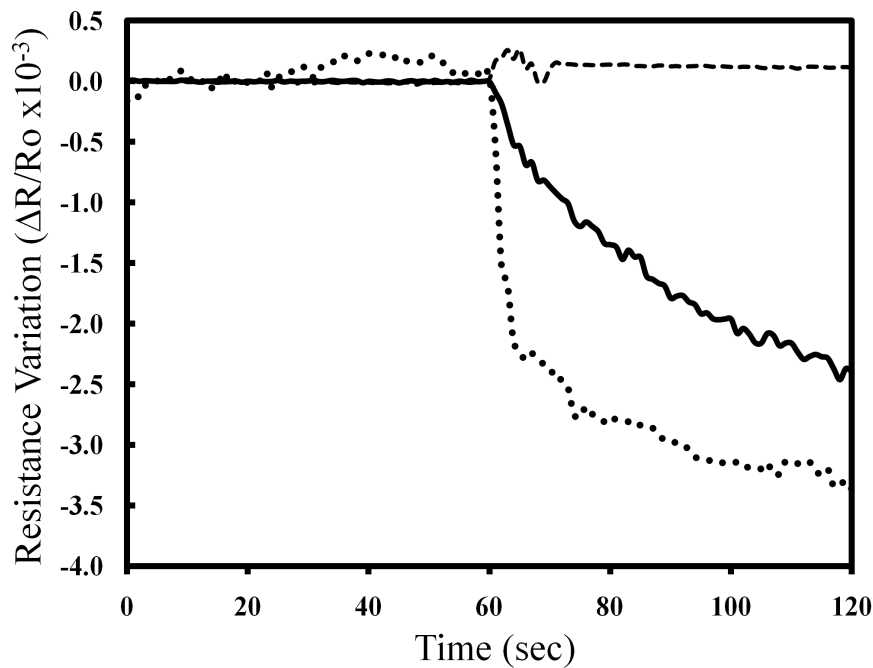


Figure 3-1 Real time monitoring of the proportional change in gold sensor resistance when the block heater lid is removed (solid line), metal DMM probes are placed on chip in the heater (dotted line) and DMM probes are connected to external constantan wires (dashed line). In each case the measurement is taken after 60 seconds.

The TCR measurement is repeated 10 times on gold, nickel-chromium, platinum, and constantan films across a low range of temperatures (30 – 90 °C) that are expected during thermal actuation of the probe. From the previous measurement the resistance is probed using a 6 ½ digit DMM connected to Constantan wires connected through the block heater lid. Figure 3-2a shows the time dependent resistance of a gold thin film

when the incubator is increased from 30 °C to 50 °C. The steady state, where the average is taken, requires approximately 30 minutes, making the measurements time consuming for each set. Figure 3-2 shows an example of the gold sensor resistance versus temperature, giving a linear relationship that allows determination of the material TCR. The material resistance at steady state typically varies by less than 0.1%. Using a large sample at the steady state temperature further minimises the error in the measurement.

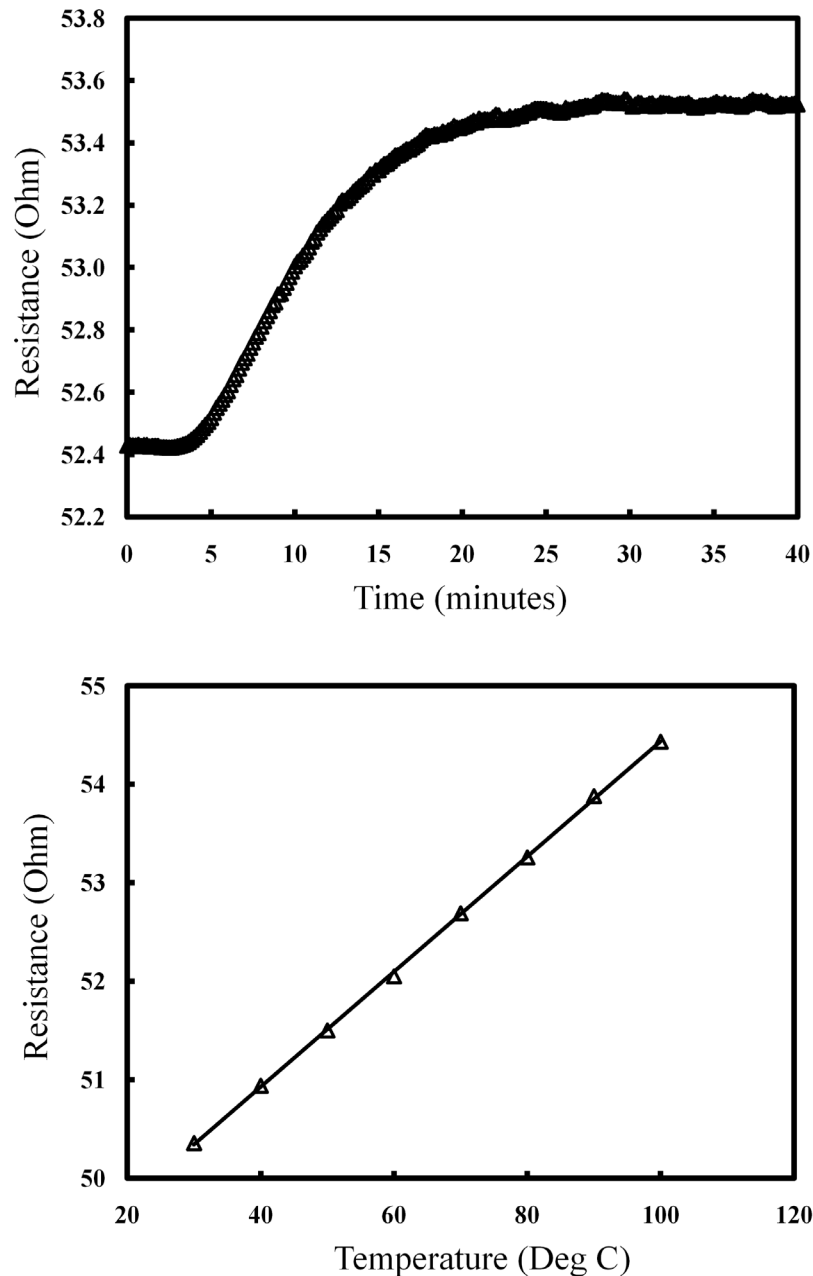


Figure 3-2 Top: Example of gold sensor resistance measured continuously from 30 °C to 50 °C. Bottom: Resistance versus temperature for a gold thin film. The resistance measurement varies < 0.1% at steady state.

For gold and platinum films the resistance change is large and therefore easily determined, whereas for nickel-chromium and constantan the resistance change is small and it is good practice to choose tracks with larger nominal resistance e.g. choosing a multiple turn piezoresistor rather than a single turn. Table 3-2 shows the results of the repeated thermal tests where a linear relationship is applied to the resistance versus temperature measurements to derive a TCR for each metal film.

|          | Bulk TCR Value<br>( $\Delta R/R \cdot ^\circ\text{C}^{-1} \times 10^{-3}$ ) | Measured TCR<br>( $\Delta R/R \cdot ^\circ\text{C}^{-1} \times 10^{-3}$ ) | Standard Deviation<br>( $\Delta R/R \cdot ^\circ\text{C}^{-1} \times 10^{-3}$ ) |
|----------|---|---|---|
| Platinum | 3.92  | 1.79  | 0.04  |
| Gold     | 3.4   | 1.13  | 0.06  |
| NiCr     | 0.4   | 0.10  | 0.02  |
| CuNi     | +/- 0.02  | 0.04  | 0.01  |

Table 3-2 Measured TCR value of the sensor thin film compared to the bulk value [98-99].

The thermal change in sensor resistance, presented in Table 3-2, represents three separate elements and a size effect. The three elements are; a change in resistivity due to temperature (TCR), a thermal strain due to thermal expansion [100], and a difference in thermal expansion between the film and substrate [101]. Warkusz [102] also notes a size effect as film resistivity is not equal to a bulk resistivity. The film resistivity relation to bulk resistivity is based on the Fuchs-Sondheimer function [103-104] which is dependent on the ratio of film thickness to electron mean free path, and the fraction of electrons specularly scattered at the external surface. Warkusz also noted that the size effect due to material grain size becomes important when considering thin films [105]. As each of these elements represents noise in the sensor the comparison of material TCR remains valid without further separation of the different parts. The size effect noted by Warkusz due to film thickness and grain size should be considered as further work to improve the piezoresistive sensor. The measurement may be improved by considering a 3-wire bridge arrangement. In this arrangement one lead – including the carrier and wire bond - is placed in the positive arm of the bridge and the second is placed in the negative arm to compensate. The third lead is effectively part of both arms and therefore does not contribute to the measurement. A 3-wire measurement has not been made in this work as the third wire must be wire bonded prior to testing.

### **3.3 Characterisation of Microcantilever Deflection**

Measurement of microcantilever tip deflection is a crucial parameter for optimising initial and actuated deflection for exploitation of sensors and actuators. For the fluid probe application it is desirable to achieve a large initial deflection of the multilayer structures otherwise adhesion to the substrate can be an issue in release and performance. The maximum initial deflection is limited by the proposed height of the microfluidic channel that will feed to the device and therefore the initial tip deflection should be less than 300  $\mu\text{m}$ . For the scanning probe application it is desirable to achieve a deflection with the in-plane tip that provides a good contact angle with the sample to be imaged. Deflection efficiency is important in the fluid probe device as both the thermal crosstalk and fluid environment are influenced by the dissipated power, therefore it is desirable to have a high deflection at very small input power and temperature.

Standard measurement techniques of microcantilever deflection include optical lever method [29], interferometry [30-34], diffraction [35], electron tunnelling [36-37], capacitive [38], piezoelectric [39], and piezoresistive [40]. Though current devices under development include integrated piezoresistors for sensing microcantilever deflection, the metal thin film tracks are susceptible to thermal crosstalk from the integrated actuation and therefore an external optical technique is desirable to confirm electrical measurements. Standard optical techniques are difficult to implement on highly curved surfaces as a small angle approximation is not valid and therefore a parallel reflecting surface is not present. Common techniques that have been reported include extracting dimensions from SEM images [15-16] and using optical microscopes to determine x and y coordinates [17-18]. Further to these techniques, Dr Mohamad Al Aioubi, a previous member of the Bioscience MNT group, mounted micro-mirrors on the microcantilever and analytically retrieved tip deflection [18]. While these techniques extract the required information they can be slow and based on the individual's discretion. Evaporating a conducting layer for SEM and mounted mirrors also directly change the mechanical properties of the cantilever under investigation.

A new technique for measuring deflection of highly curved microcantilevers is proposed by the author based on standard optical microscopy with contrast and resolution based autofocus algorithms. Retrospectively, it has been found that Miao et al [106] have proposed the same method for measurement of tri-layer polymer

microcantilevers reported by Chan et al [64]. In this work Miao uses the same three focus measures for static and actuated microcantilevers. The work presented here goes beyond Miao's work to extract the full curvature of the microcantilever in static and actuated states. Using an automated computer based autofocus technique offers a consistent method between testing and characterisation, and comparison of microcantilever structures. The work presented here uses contrast and resolution based autofocus algorithms [107-110] to establish the most repeatable and accurate method for determining the tip deflection. The technique can also be used to extract the full curvature information of the beam, rather than deriving the deflected shape analytically, from applying several image sections along the microcantilever length. The microcantilever curvature has important implications on bending, heater performance, and in appreciating the fluid shear rate on the moving parts of the beam. It is considered that the technique may also be extended to low frequency ( $< 10$  Hz) dynamic measurements with an increased frame rate of the image capture device. This would allow critical analysis of the time dependent deflection and curvature of the beam to extract real shear rate information.

An optimal focus position can be achieved by analysing image content at several vertical positions and maximising, or minimising, the value of a chosen focus function. Image content focus functions are based on the assumption that as the focus improves, the contrast and resolution of the image increases, and that these characteristics can be quantified. Mathematically, from Fourier optics, the resolution can be measured by analysing the frequency content of an image. When the image is focused the detail improves (edge sharpness) giving high frequency content. The analysis can be further improved by isolating these high frequencies using a high pass or gradient filter. Image contrast can be described mathematically by the change in intensity standard deviation or variance across the image. The analysis can be further improved by normalising the output to compensate for lighting conditions. Conventionally, a sample is automatically scanned through focus at discrete steps and returned to the level where the focus function is optimised. For measuring the tip deflection or curvature of a microcantilever a discrete operating level is not required, only the extrapolated position of the maximum from the focus function curve. As the focus curve is parabolic around the focal plane a higher precision than the discrete stepping can be achieved by quadratic interpolation around the detected optimum. Referencing of the technique is

provided by imaging two separate sections of the image in the field of view to extrapolate the position of the tip and the position of the surface.

Several autofocus functions have previously been presented and compared in literature for bright field microscopy [107-109]. The criteria for comparison suggested by Groen et al [107] includes (1) Unimodal focus function, i.e. only a single maximum or minimum; (2) Accuracy, the optimum is detected when the image is in focus; (3) Reproducibility, a sharp extremum is measured consistently; (4) Range, the vertical scan distance over which the function will return the correct focus; (5) General applicability, or the ability to be used on different types of image; (6) Insensitivity to other parameters; (7) Video signal compatibility; and (8) Implementation, or a function which is quick and easy to implement. For measurement of tip deflection the critical criteria are unimodal, accuracy, and reproducibility. On the basis of these criteria three focus functions have been chosen based on both resolution (Squared Gradient, One Dimensional Laplacian) and contrast (Normalised variance) algorithms. These functions have been shown to perform best in comparison tests and are each applied to the work here to experimentally find the most suitable function.

The Squared Gradient function [111-114] is mathematically the summation of the square of the first derivative of the image intensity. This is effectively a band pass filter that enhances higher spatial frequencies (edge sharpness) close to the highest value. The square of the derivative further increases the difference between low and high spatial frequencies. From Groen et al [107] the equation of the function is given by

$$F = \iint_{image} E \left( \frac{\partial g(x,y)}{\partial x} - \theta \right)^2 dx dy \quad (3.1)$$

where  $g(x,y)$  is the pixel grey value at position  $(x,y)$ ,  $\theta$  is an arbitrary threshold value which in this work is set as zero, and the first-order derivative can be approximated as

$$\frac{\partial g(x,y)}{\partial x} \cong \frac{\Delta g}{\Delta x} = g(i,j) - g(i,j-1) \quad (3.2)$$

where  $(i,j)$  is the pixel coordinates at row  $i$  and column  $j$ .

The One Dimensional Laplacian function [112-114] is mathematically the summation of the square of the second derivative of the image intensity. Spectrally, the higher spatial frequencies are enhanced more by this second order difference filter than the first order gradient filter. It has been previously noted that higher order functions do not perform as well as the first and second order due to an increase in noise effects. From Groen et al [107] the equation of the function is given by

$$F = \iint_{\text{image}} E \left( \frac{\partial^2 g(x, y)}{\partial x^2} - \theta \right)^2 dx dy \quad (3.3)$$

where the second-order derivative can be approximated as

$$\frac{\partial^2 g(x, y)}{\partial x^2} \cong \frac{\Delta^2 g}{\Delta x^2} = g(i, j+1) - 2g(i, j) + g(i, j-1) \quad (3.4)$$

The Normalised Variance contrast function gives a measure of the space varying intensity of an image. As power can be divided into a DC and AC components, where DC power is the mean squared value and AC power is the time varying component, an image can be defined in a similar manner.

$$P = \frac{1}{N} \sum_i \sum_j (G_{ij})^2 = E\{G^2\} \quad (3.5)$$

where P is the power,  $G_{ij}$  is the pixel grey value at row i and column j, N is the total number of pixels in the image, and E is the expected value operator. The DC component is equivalent to  $(E\{G\})^2$  and the space varying AC component is given by  $E\{G^2\} - (E\{G\})^2$ . As the image is focused the DC component does not significantly change, but the AC component increases with image sharpness. The AC component of an image can be directly measured as the variance of the image pixels. A normalisation of the variance to compensate for image brightness can be implemented by dividing by the squared mean of the image. From Groen et al [107] the equation of the function is given by

$$F = \frac{1}{g^2} \iint_{image} |g(x, y) - \bar{g}|^2 dx dy \quad (3.6)$$

where  $\bar{g}$  is the mean grey value over the image and  $\overline{g^2}$  is the squared mean of the image.

### 3.3.1 Experimental Validation of the Autofocus Method

Figure 3-3a shows an optical image of the test structures used for initial and actuated tip deflection measurements. The structure is a  $\Pi$ -shaped Gold-Polyimide (PI2562) thermal bimorph actuator (MV1), 600  $\mu\text{m}$  long, with 80  $\mu\text{m}$  wide arms separated by a 60  $\mu\text{m}$  gap, and an overall thickness of 5  $\mu\text{m}$ . Metalised gold tracks for heaters and piezoresistive sensors are positioned at the centre of the polyimide layer to provide electrical insulation.

The deflection and load characteristics of previously fabricated  $\Pi$ -shaped gold-polyimide (PI2566) microcantilevers with larger overall thickness has been previously measured [18] using reflecting mirrors and initial out-of-plane displacements up to 250  $\mu\text{m}$  are reported. The microcantilever device to be tested has been fixed and bonded into a ceramic DIL package. The chip is mounted on a custom electronics board and fixed to a 3-axis piezo-controlled stage (Thorlabs NanoMax) with a manual differential adjuster to provide a minimum stage adjustment of 500 nm fine resolution, and a travel range of 400  $\mu\text{m}$ . The stage can accommodate modular drives with up to 5 nm resolution with closed loop feedback piezoactuators, though this is significantly higher than the resolution required (approximately 1 micron).



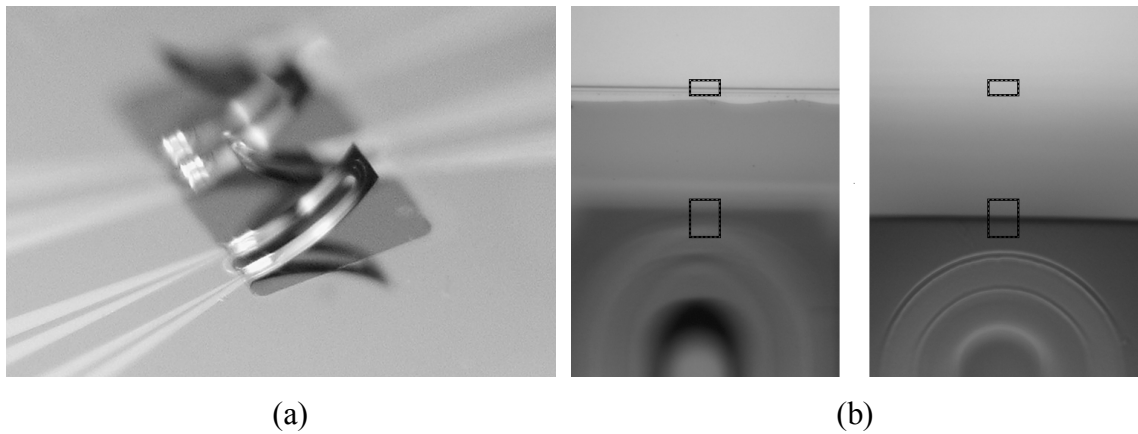


Figure 3-3 (a) Optical image of interdigitated  $\Pi$ -shaped Gold-Polyimide (PI2562) thermal bimorph actuators with integrated heaters and piezoresistive sensors. (b) Optical image of focused wafer detail and focused cantilever tip showing an example of the analysis window.

For tip measurement the stage is mounted under a Nikon Metaphot bright field microscope with 40x magnification lens and 0.65 numerical aperture. This lens provides a large enough field of view to provide focus information on the cantilever tip and wafer surface providing a differential method to measure tip deflection. For curvature measurements of microcantilevers a 20x magnification and 0.4 numerical aperture lens is used to provide a larger field of view. The ceramic package limits higher magnification and numerical aperture to reduce the depth of field as the silicon die is recessed from the carrier edge. Images are remotely captured at each stage height using a Digital Camera (Canon Powershot S5 IS) mounted to the phototube of the microscope using a suitable conversion lens (LA-DC58E) and microscope adaptor (Martin Microscopes, MM99-58). The measurement setup and image processing is computer controlled using a custom LabView (LabView 8.20, National Instruments) program. LabView controls the electronics and sensor feedback using a data acquisition card (M-Series, NI PCI-6221) routed through a shielded BNC connector block (NI BNC-2110). Actuation voltage is provided by an arbitrary waveform generator (Agilent, 33220A) controlled over USB from within the LabView program.

Images are captured and stored in the remote capture software and automatically analysed by LabView to provide the focus score of each autofocus function on a selected analysis window. The analysis window is applied to each image to extract the focused position of the chosen area. It has been found that using two analysis windows separated for the tip position and wafer position provides increased resolution than a

single window covering both details. This is because a unimodal focus function would not exist, but rather two peaks which must be resolved. A single analysis window would also contain extra pixels between the two areas with no important information. Figure 3-3b shows an example of the two analysis windows applied to a real image to capture the focus of the substrate detail (a) and the deflected tip (b). The stage is initially positioned below the focus of the substrate detail to allow the image to be taken *through focus* of the substrate and past the focus of the microcantilever tip. This provides enough lead-in and lead-out to apply a quadratic curve fit to the focus score and extrapolate the position of best focus.

For the current validation the focus score is a single discrete output value from the function applied to the image window. If an image was taken several times at a specific stage height the variation of pixel intensity in the analysis window would allow an averaged focus score and measure of standard deviation. The source of this variation is due to movement in the image due to camera shake and mechanical stability of the stage, and the imaging source and lighting which will change each pixel intensity. For the work presented here, the focusing routine is repeated 4 times on the same microcantilever device (MV1) to consider the reproducibility and accuracy of each function. Within each set of images the analysis window is reapplied to look at the variability with placement of the window. The best method is then applied to compare old and new microcantilever designs.

Preliminary testing indicates the application of a narrow and concentrated analysis window is preferential to a large window as this produces a sharper focus function. Figure 3-4 shows the focus score of the normalised variance function for a large, small, and single line analysis window as the microcantilever is taken through focus. As the focus function outputs a single discrete value for each image capture height no error bars are shown. For a single focus scan of initial and actuated deflection and for curvature measurements a small narrow window is chosen to analyse the data.

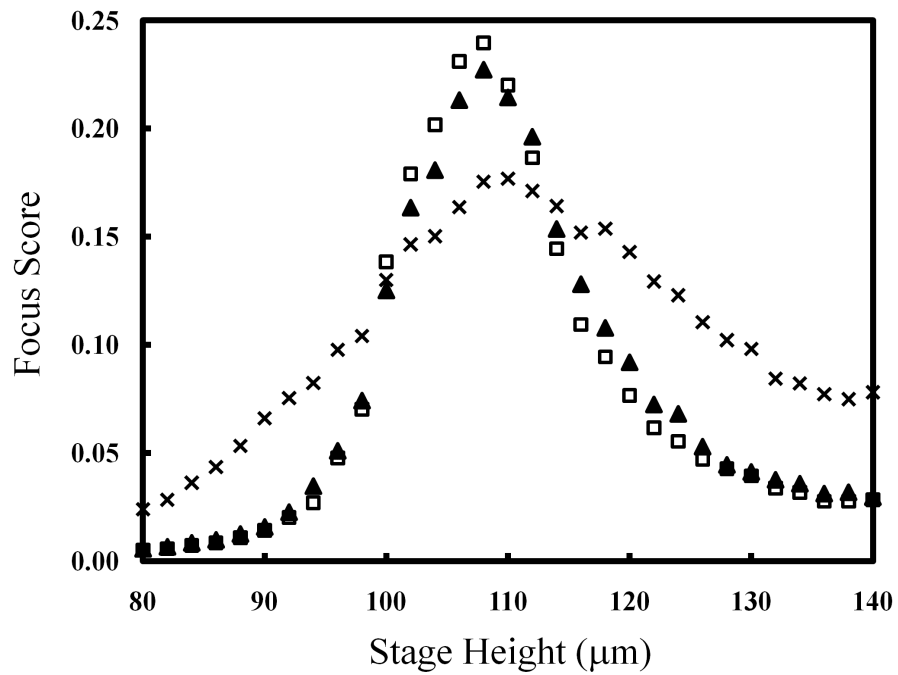


Figure 3-4 Normalised Variance focus score for analysis of the microcantilever tip when a single line (filled triangle), small window (square), and large window (cross) is applied.

Figures 3-5, 3-6, 3-7 show the focus score from the Normalised Variance, Squared Gradient, and One-Dimensional Laplacian functions on a single set of image data from the MV1 device. The stage has been taken through a distance of 200 microns at 2 micron steps and images have been analysed for substrate detail (window 1 – circle) and microcantilever tip detail (window 2 – triangle).

For each function the maximum focus score is identified by LabView and a quadratic function is fitted to the data within 8  $\mu\text{m}$ . The maximum position is then determined by finding the position for which the differentiation of the quadratic equation is equal to zero. For comparison, the position of maximum score over several iterations is also considered as a simple alternative to extrapolating the position - though in practice a single scan would only give an accuracy of twice the stage increments. The results of the focus function comparison based on the initial deflection of the benchmark microcantilever device are given in Table 3-3.

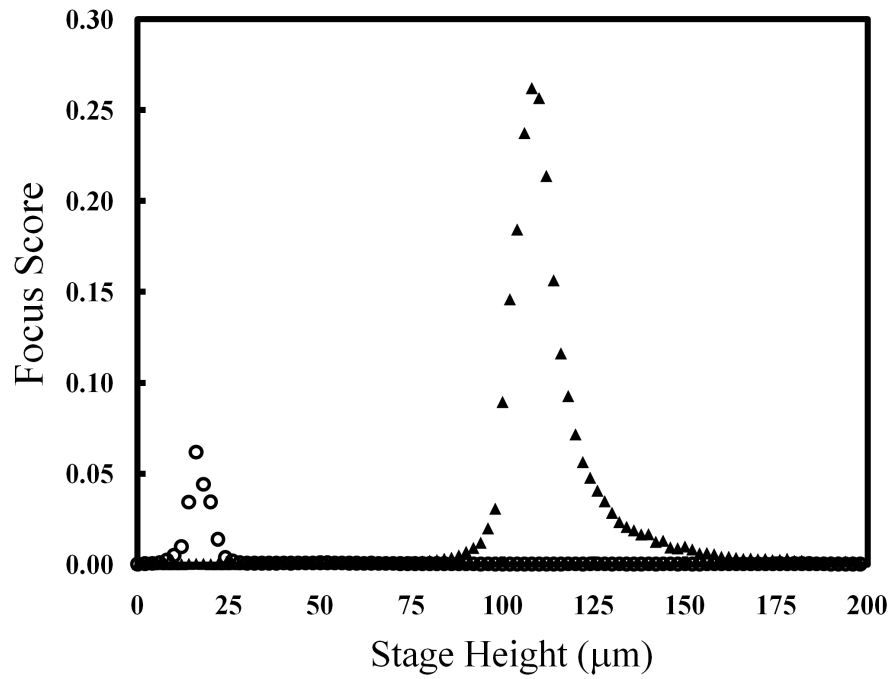


Figure 3-5 Normalised Variance focus function score of substrate (circle) and MV1 microcantilever (triangle) analysis window.

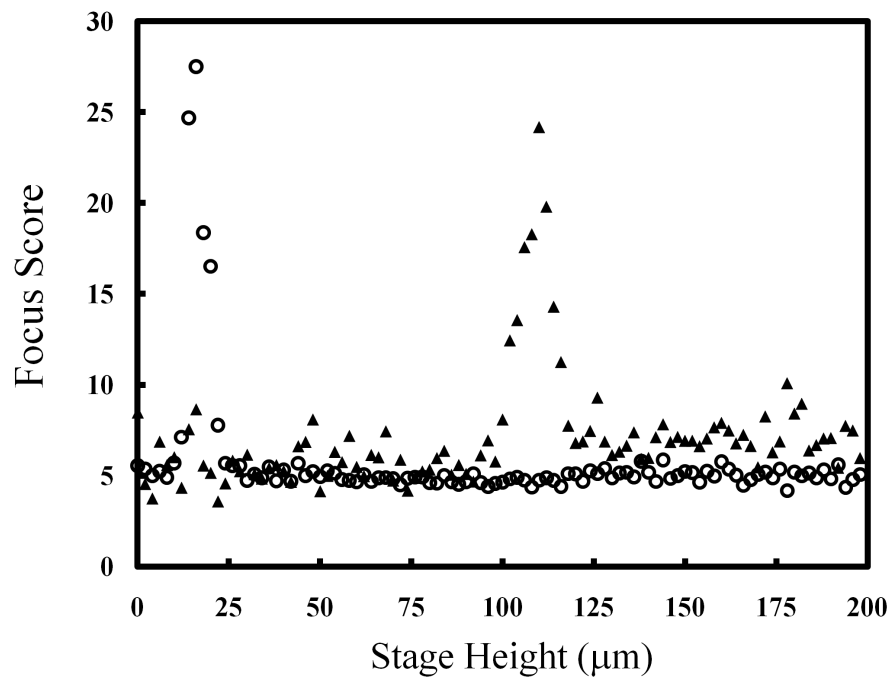


Figure 3-6 Squared Gradient focus score of substrate (circle) and MV1 microcantilever (triangle) analysis window

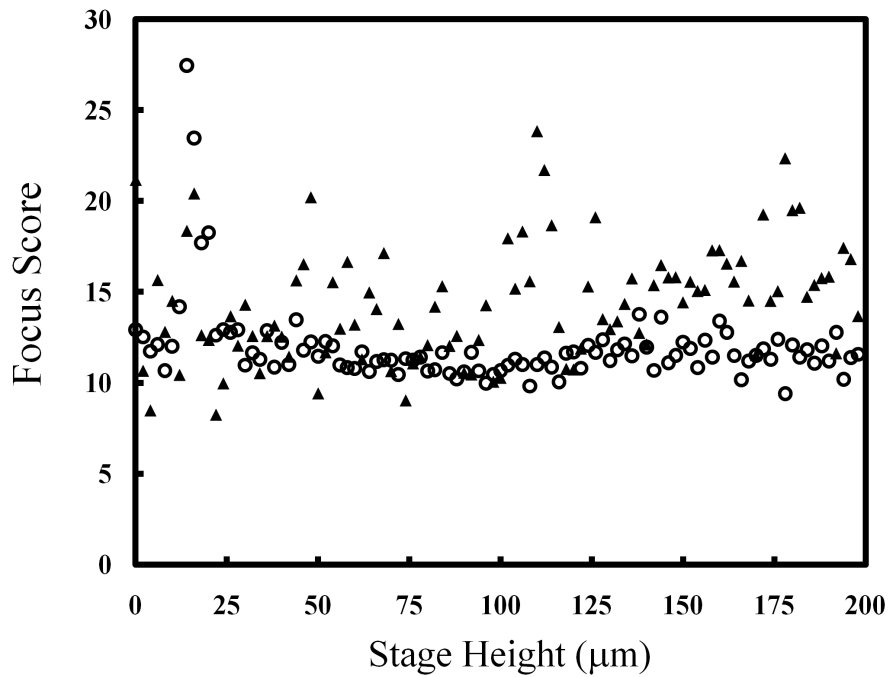


Figure 3-7 One Dimensional Laplacian focus score of substrate (circle) and MV1 microcantilever (triangle) analysis window

| Autofocus Function        | Quadratic Method |                         | Max Value Method |                         |
|---------------------------|------------------|-------------------------|------------------|-------------------------|
|                           | Mean (μm)        | Standard Deviation (μm) | Mean (μm)        | Standard Deviation (μm) |
| Normalised Variance       | 92.4             | 1.2                     | 92.2             | 1.4                     |
| Squared Gradient          | 92.7             | 1.3                     | 92.7             | 1.7                     |
| One Dimensional Laplacian | 92.1             | 2.4                     | 92.8             | 3.4                     |

Table 3-3 Comparison of the Normalised Variance, Squared Gradient, and One Dimensional Laplacian autofocus functions for measurement of microcantilever (MV1) tip deflection.

The preliminary results show the validity of the autofocus method for tip deflection measurements of large curvature microcantilevers. The resolution of the technique is approximately 1-2 microns over several measurements, and though this is much lower than optical lever or interferometric measurements, for large deflections in the range 100 to 200 microns this is sufficient. The Normalised Variance contrast function performed best in tests and is ideal for microcantilever measurements as the basis of the focus score is not based on the orientation of the analysis window. The Squared Gradient and One Dimensional Laplacian resolution functions give a sharper focus

score response but increased noise levels introduce more uncertainty. The method of simply finding the maximum focus score stage height produces a result consistent with the fitted quadratic method, though for single scans the result will be limited by the stage height increment. For comparison of actuation efficiency only the Normalised Variance function is used.

### 3.3.2 Comparison of Microcantilever Actuation Efficiency

To measure actuation efficiency the tip deflection is measured at zero input power and at several increased increments of power. Currently the technique can only measure the steady state deflection of the cantilever as the frame rate of the image capture device is too low to capture motion; the steady state deflection still provides useful information on the microcantilever efficiency. Actuation is connected directly from the function generator (Agilent, 33220A) output, having a 50 Ohm series resistance. As previously noted the error in applied power to the microcantilever due to self heating and accounting for the unknown resistance due to bonding and carrier is approximately 1 %. Figure 3-8 shows the Normalised Variance focus score for the microcantilever tip (MV1) in the range 0 to 15 mW where values are normalised (maximum = 1) and shifted on the x-axis according to the maximum score in the substrate analysis ( $x = 0$ ).

The established substrate and tip position at each power gives an approximately linear relationship of  $8.2 \mu\text{m.mW}^{-1}$  away from the substrate; the direction has been confirmed visually under the microscope. At large deflections the efficiency tends to become non-linear as the tip deflects upwards beyond a quarter circle. Comparing with published results for thermal bimorph actuation efficiency (Table 1-1) shows that the benchmark microcantilever fluid probe (MV1) has improved over the previous device fabricated at MNTC [18]. It should be noted that the device has a lower restoring force, and that the deflection is away from the substrate. Assuming thermal actuation is analogous to a uniform force and extrapolating the length of all devices for comparison the microcantilever fluid probe (MV1) is comparable to previously published work on polymer-polymer devices [15, 60] but lower than devices where the actuation is integrated as one of the structural layers [42, 44].

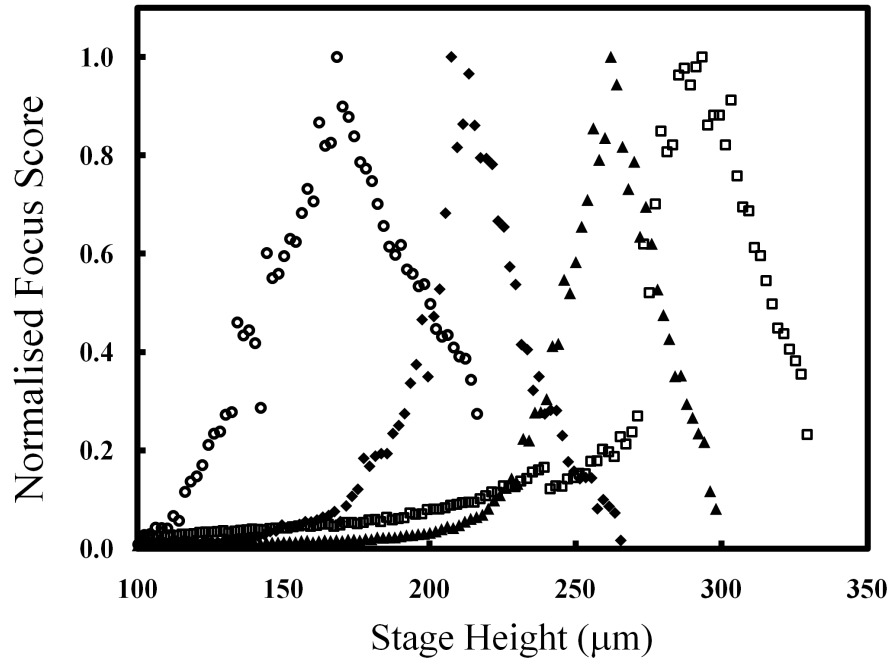


Figure 3-8 Normalised focus score for analysis of the MV1 microcantilever tip using the Normalised Variance function at a power input of 0 mW (circle), 5 mW (diamond), 10 mW (triangle), and 15 mW (square). The data has been shifted to the maximum of the substrate position to allow comparison.

The tip actuation has also been measured for MV2 Epsilon (W) and Solid (G) design with standard heaters, and the Epsilon (X) and Solid (H) design with tapered heaters in the range 0 to 20 mW. Both G and H microcantilever designs have a steady state deflection in the power range that remains within the error of the measurement technique (1.8  $\mu\text{m}$ ). As these results cannot confidently give useful actuation efficiency the results are omitted from below. In W and X microcantilever designs a linear relationship cannot be established as in each case the deflection is initially away from the substrate (0 to 10 mW) before deflecting towards the substrate (10 to 20 mW). The direction has again been confirmed with visual inspection. Figure 3-9 shows the tip measurements of the MV2 W and X device for the range of power tested.

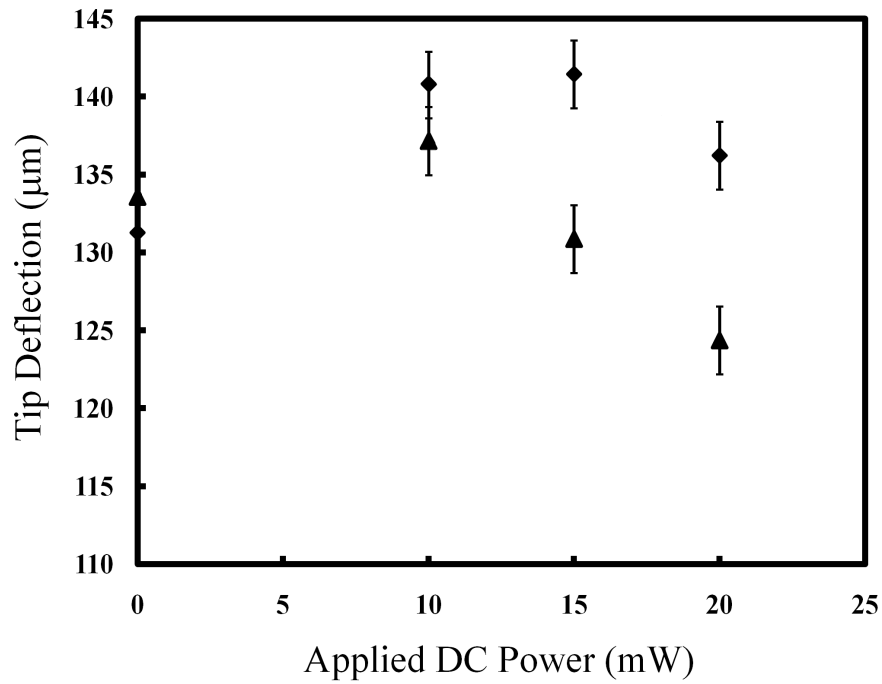


Figure 3-9 Measured tip deflection under DC actuation for MV2 Epsilon design with standard heaters (W) (filled triangle) and tapered heaters (X) (filled diamond).

The negative deflection results for both generations of design indicate that multilayer thermal actuators with integrated metal heaters are not simply described as a classical bimaterial strip. In conventional analysis the heating of a bimaterial strip will cause a linear deflection governed by the higher thermal expansion layer pushing towards the lower thermal expansion layer. Considering the multilayer cross-section and neutral axis position, the volume expansion below the axis must dominate for a negative deflection.

An explanation is that the expansion in the upper section is restricted by the metalised heater and sensor tracks. For the MV1 device the fill factor of gold heaters and sensors is high and chrome has been used to improve adhesion. Chrome and gold have low thermal expansion ( $4.9 \text{ ppm.K}^{-1}$  and  $14.2 \text{ ppm.K}^{-1}$  respectively) compared to the surrounding polyimide ( $60 \text{ ppm.K}^{-1}$ ) and therefore may limit expansion. The MV2 devices only show negative deflection at low temperature. In MV2 the fill factor of metalisation in the device is lower than MV1 and the lower structural polyimide has a very low thermal expansion ( $3 \text{ ppm.K}^{-1}$ ). A section of the high CTE polyimide is also estimated as being below the neutral axis. Considering the differential heating, it is possible that at higher temperatures the very low thermal expansion of the bottom layer is simply overcome and that the higher heat gradient moves to less metalised areas of



the beam which are not restricted to expand. Certainly this is an area of interest to develop further understanding if, for example, the microcantilever was to be used as an optical reflector, gripper, or valve. For future deflection measurements using the autofocus method it is of interest to reduce the resolution of the camera as it is likely the image is being over sampled which may increase noise and increases the processing time.

### 3.3.3 Curvature Measurements of Static and Actuated Microcantilevers

During measurement of initial and actuated deflection the curvature along the cantilever can also be extracted. The first step is to convert pixel number in to a lateral x-position ( $\mu\text{m}$ ) using a known distance in the image window. A second method for converting pixels to position is to first reconstruct the curvature of the microcantilever and use the known beam length to match the summation of all segments along the beam.

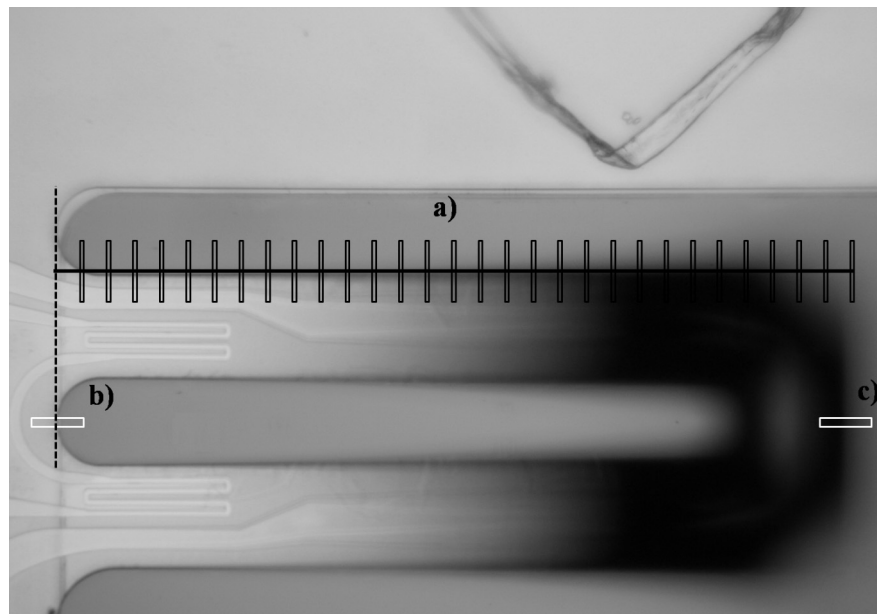


Figure 3-10 (a) Analysis windows placed along the length of the microcantilever to reconstruct the curvature of the MV1 device. (b) A window is placed to give the zero position at the base. (c) A window is placed to give the tip position

A single analysis window is applied perpendicular to the microcantilever length at 20 micron increments along the beam, as shown in Figure 3-10. The vertical height of the stage is then taken through a focused position below the microcantilever base past the tip of the device with images captured at every 2 micron step. In this series of captured images the Normalised Variance focus function is applied to each analysis window. The extrapolated maximum of the focus function in each analysis window provides a

height that intersects the focused edge of the microcantilever. To complete the analysis a horizontal analysis window across the polyimide edge on the wafer (Figure 3-10b), and the tip of the microcantilever (Figure 3-10c) is applied to give the zero position of the y-axis and the tip deflection.

Figure 3-11 shows the reconstruction along the MV1 microcantilever device at 0 and 15 mW input power. The dashed and solid lines represent constant microcantilever curvature given the tip deflection, taken from the analytical model of a circle as used in [13]. Error bars are based on the standard deviation of the Normalised Variance focus function method taken from Table 3-3.

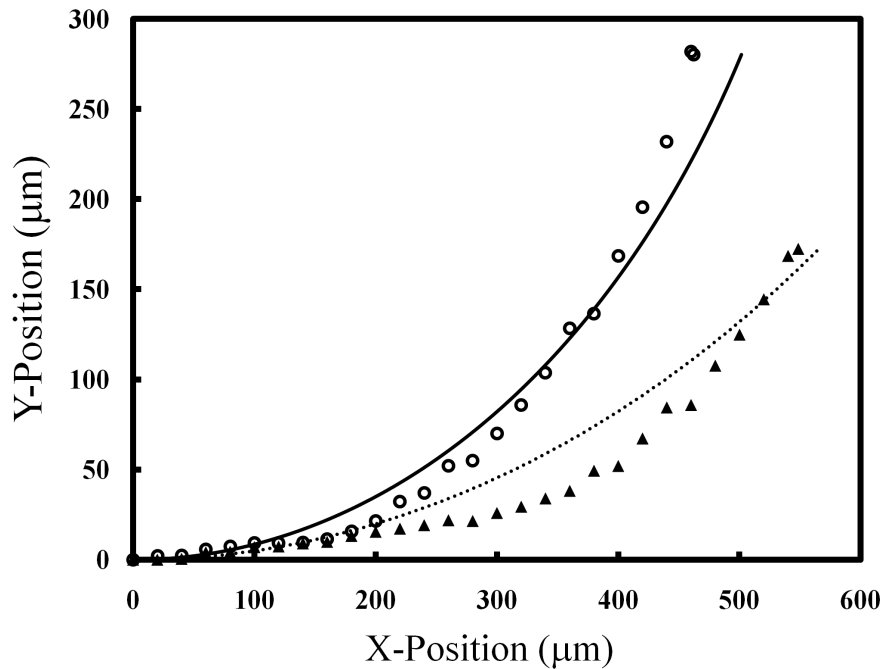


Figure 3-11 Reconstruction of the MV1 microcantilever devices along the length of the beam at 0 mW (triangle) and 15 mW (circle) input power. The dotted and solid line is an approximation of the beam shape using a constant radius of curvature [13] based on the tip deflection for 0 mW and 15 mW respectively. Standard deviation in the measured Y-position using the Normalized Variance technique is approximately 1.2 microns.

The result indicates that it is not appropriate to estimate the microcantilever shape as having a constant radius of curvature. It is also not appropriate to use a small angle approximation given the tip x-position is significantly less than the length of the beam ( $L = 600 \mu\text{m}$ ).

The curvature reconstruction has been applied to second generation devices (Figure 3-12) though as in the case of measuring the tip deflection the steady state deflection is comparable to the error in the measurement. As a single result the curvature appears inconclusive, but several devices have shown similar deflection including those fabricated for the scanning probe project. The results imply a twisting in the microcantilever during actuation. This is to say that towards the base of the device the microcantilever deflects away from the substrate and at the tip the beam moves towards the substrate. This leads to a non-linear deflection where at low temperature the upwards deflection can dominate but at higher temperature the deflection at the tip gives a downwards deflection. The negative deflection appears to only occur in areas of sensor metalisation extending into the beam.

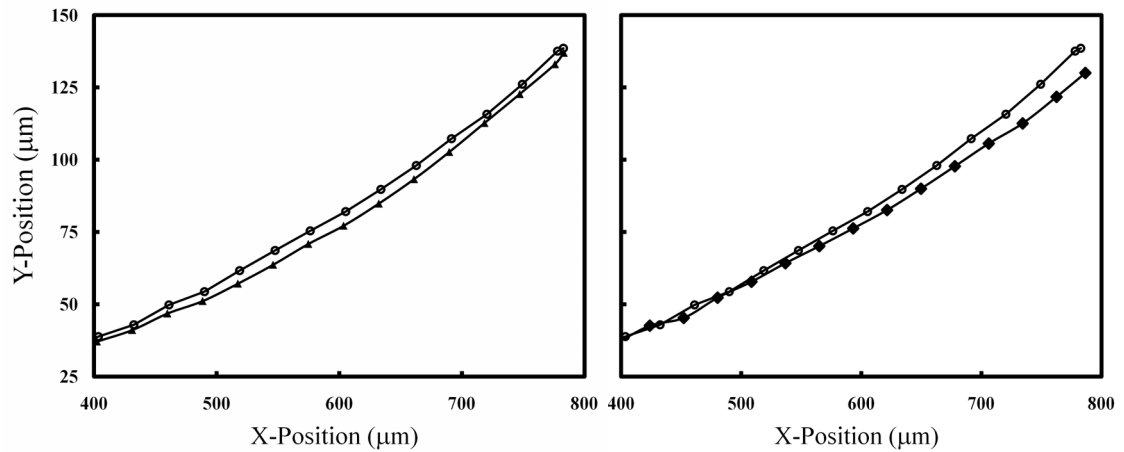


Figure 3-12 Left: Reconstruction of the MV2 G device at 0 mW (triangle) and 10 mW (circle) input power. Right: Reconstruction of the MV2 G device at 10 mW (circle) and 20 mW (diamond) input power. Standard deviation in the measured Y-position using the Normalized Variance technique is approximately 1.2 microns.

Certainly the reconstruction of the microcantilever curvature produces a more rigorous treatment of the deflection and creates a number of questions that are interesting for future measurements. With controllable x- and y- axis on the nanomax stage a higher magnification and smaller depth of field can be achieved by imaging a centered window and then moving the stage to a new position along the beam.

### 3.3.4 Short Pulse Characterisation

Under visual observation the MV1 microcantilever device initially deflects towards the substrate and then move back to a steady state position behind the static equilibrium, giving the negative deflection as seen in the previous section. Similarly, the MV2 microcantilever devices initially deflect towards the substrate and then pull back close to a position around the static equilibrium.

This can be explained by a time dependent differential heating whereby the heaters above the neutral axis initially force the microcantilever downwards but as heat expansion occurs below the neutral axis and the upper expansion is restricted the microcantilever is pushed back. It is the forced downward motion which can be exploited for the fluid probe device and therefore it is appropriate to also try and characterise the microcantilever using short pulses.

The previously presented autofocus method is unable to measure short pulse deflection due to the low frame rate of the imaging camera. The same measurement is possible to achieve manually using low frequency pulses (5 Hz and 100 ms pulse width) by focusing on the extreme deflections of the cantilever which appear as dark in-focus lines. The device does not operate in high frequency, whereby the imaging device would see a blurred motion between two extremes, as the devices demonstrate a very low cut off frequency i.e. the heat does not have enough time between pulses to dissipate and therefore creates an artificial start and end point. It is desirable to also compare the microcantilever deflection for very short pulses ( $< 1$  ms) with very high peak power ( $> 200$  mW). This cannot be resolved by eye and therefore an interferometric setup is desirable. This has not been achieved in this work and is discussed as a future investigation in the closing chapter.

The microcantilever device is connected directly to a function generator (Agilent, 33220A) and tip deflection is measured over several input powers to derive a linear relationship. At each power input the measurement of each microcantilever actuation is repeated at least 3 times to resolve difficult measurements more accurately. Figure 3-13 shows the measurement for MV1 where error bars represent the limitation of the measurement. For the measurement a comparison of 8 for each MV2 design and 7 of the MV1 design is made. Table 3-5 shows the deflection results for 100-ms pulse activation.

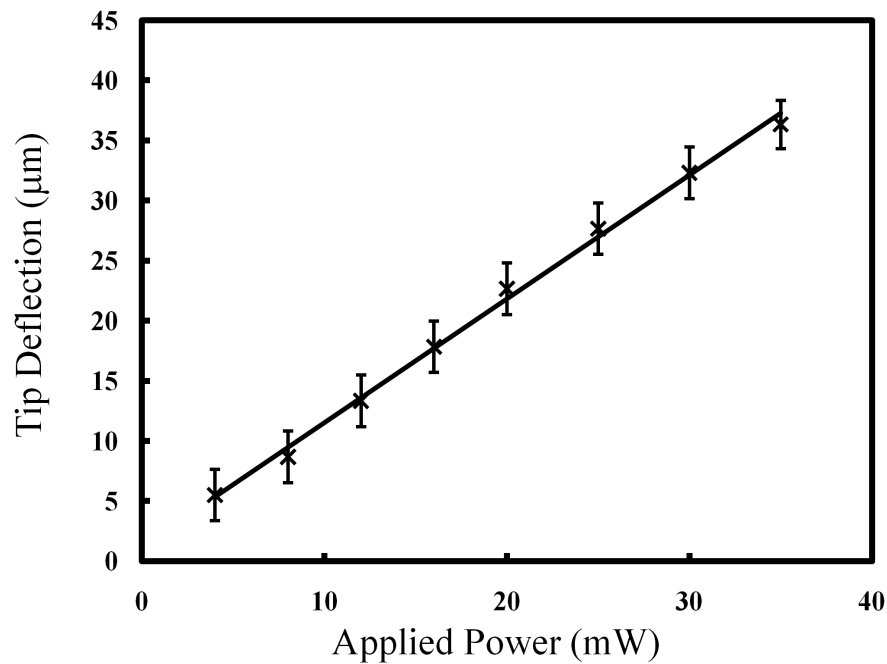


Figure 3-13 Estimated tip deflection versus actuation input power for the MV1 microcantilever using a manual focusing method.

| Microcantilever Device              | Mean Deflection ( $\mu\text{m.mW}^{-1}$ ) | Standard Deviation ( $\mu\text{m.mW}^{-1}$ ) |
|-------------------------------------|---|--|
| MV1 – Benchmark                     | 1.2                                       | 0.2  |
| MV2 – Solid Design (G)              | 5.7                                       | 1.2  |
| MV2 – Epsilon Design (W)            | 5.2                                       | 0.3  |
| MV2 – Solid & Tapered Heaters (H)   | 4.2                                       | 0.5  |
| MV2 – Epsilon & Tapered Heaters (X) | 4.3                                       | 0.2  |

Table 3-5 Deflection Efficiency of the benchmark and second generation microcantilever fluid probe device based on a 100 ms pulse.

Short pulse and DC actuation characterisation give two different perspectives of the microcantilever devices. DC actuation indicates that the thermal expansion is limited by the metalised tracks through the device. For short pulse operation the thermal expansion is significant above the microcantilever neutral axis giving an enhanced deflection greater than that seen in DC powering. It is also possible to significantly increase the input power due to the short duty cycle of the pulse.

Polymer-polymer devices that have a low thermal conduction show an improvement in deflection over the benchmark device though it should be noted that the beam length is different. Taking this into consideration the improvement in actuation efficiency is approximately 50%. Devices with tapered heaters (X and H) show a lower deflection than standard heaters; this is most likely due to the increased proportion of power dissipated at the base being conducted into the substrate and also the heat being in an area with restrictive motion from the metalised tracks. Devices with standard heaters (W and G) are expected to have a more uniform dissipation along the microcantilever and importantly give heat to the free end of the beam.

### **3.3.5 Response of Heaters during Pulsed Heating**

During actuation the gold heater resistance increases due to temperature and therefore provides a measure of the rate of heating and the average increase in temperature. It is desirable for the rate of heating to be as fast as possible and the conversion factor to be high. This allows the actuation pulse to be shorter and lower, reducing the thermal crosstalk on the sensor.

Using a fixed voltage supply from a function generator (Agilent, 33220A) a potential divider arrangement is used to measure the potential drop across the microcantilever heater. The heater resistance of each test device is measured during long pulses (100 ms) and short pulses (1 ms) to allow investigation of approximate steady state and high peak power respectively. The heater resistance change over the nominal resistance is converted to average temperature using the previously measured temperature coefficient of resistance. Figure 3-14 shows a comparison of microcantilever heaters for 100 ms pulses at 10 mW input power. Measurements have been averaged over 10 identical actuation cycles. The pulse response is very repeatable and errors < 1% can be attained after only a few averaged pulses.

The thermal steady state of the heater in polymer-polymer devices follows the deflection measurements in Table 3-5. This reinforces the statement that it is the increase in temperature that is driving the deflection. The steady state temperature indicates the power loss in each device, for example, in the MV1 device the gold structural layer provides a conduction path for heat transport whereas the highly insulating polymer devices retain heat and gives higher deflection. The tapered design is expected to generate more heat dissipation in the thinner section due to higher current

density. This design shows higher heat loss possibly as this area is close to the main conduction path into the silicon substrate.

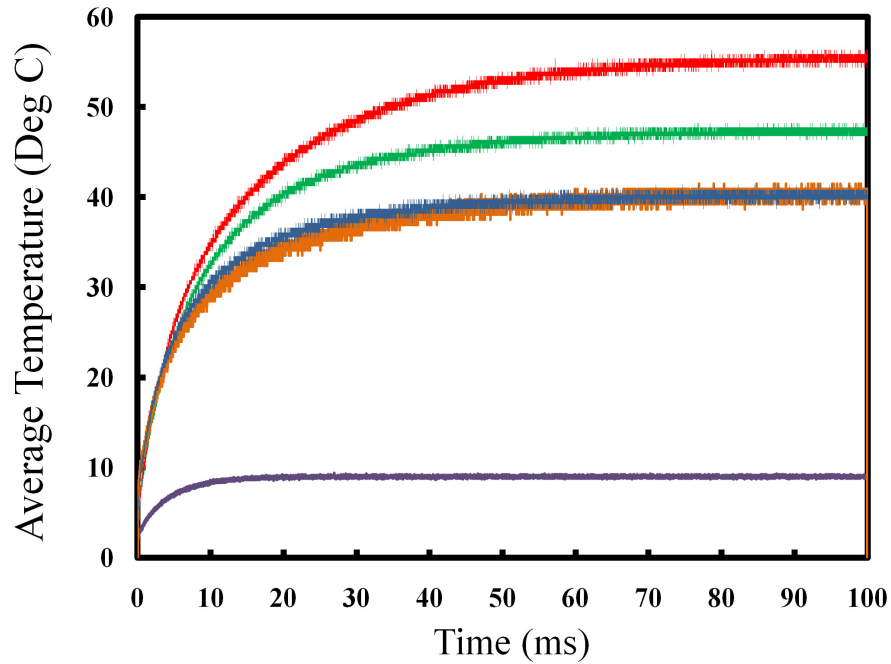


Figure 3-14 Response of the microcantilever heater during long pulse (100 ms) actuation at 10 mW power dissipation. The plot shows the MV2 G (red), MV2 W (green), MV2 X (blue), MV2 H (orange), and MV1 (purple) measurements.

The results in Figure 3-14 indicate more heat loss in the Epsilon device (W) compared to Solid (G) but this is difficult to understand as both the volume and surface area have been reduced. One possible explanation is the thermal diffusivity – the thermal conductivity divided by the heat capacity and mass density – of polyimide compared to air. For the same volume the low density and mass of air gives a higher thermal diffusion. A second possibility is that the air flow through the structure in the Epsilon device increases heat loss from the microcantilever during deflection.

Short actuation pulses (1 ms) allows the peak power to be increased beyond 30 mW, such power would otherwise cause the device to melt using long or DC actuation. It has been found that the increase in average temperature of the heater during a 1 ms actuation pulse is proportional to the power input of the device. Figure 3-15 shows the estimated increase in average temperature, in air, during a 1 ms actuation pulse with 250 mW peak power. Measurements have been averaged over 10 identical actuation cycles.

The rate of temperature increase, previously noted as an important characteristic in section 2.2, is higher in the polymer-polymer devices, specifically the tapered heater design. This can be explained by the variable current density in the track. In comparison to standard heaters the tapered device gives a higher current density in the thin section of the track and a lower current density in the standard part of the track. The area of higher current density increases the rate of joule heating above that of the standard heater. Using constant thin heaters with high nominal resistance has found to give a very high change in temperature but the conversion factor is poor at steady state [115]. It is possible that the lower surface area of the heater lowers the conduction into the surrounding polyimide, limiting the actuation with thin heaters. In practice, the voltage supply is also limited and therefore higher nominal resistance from thin tracks limits the current, and therefore power, that can be applied in a short pulse.

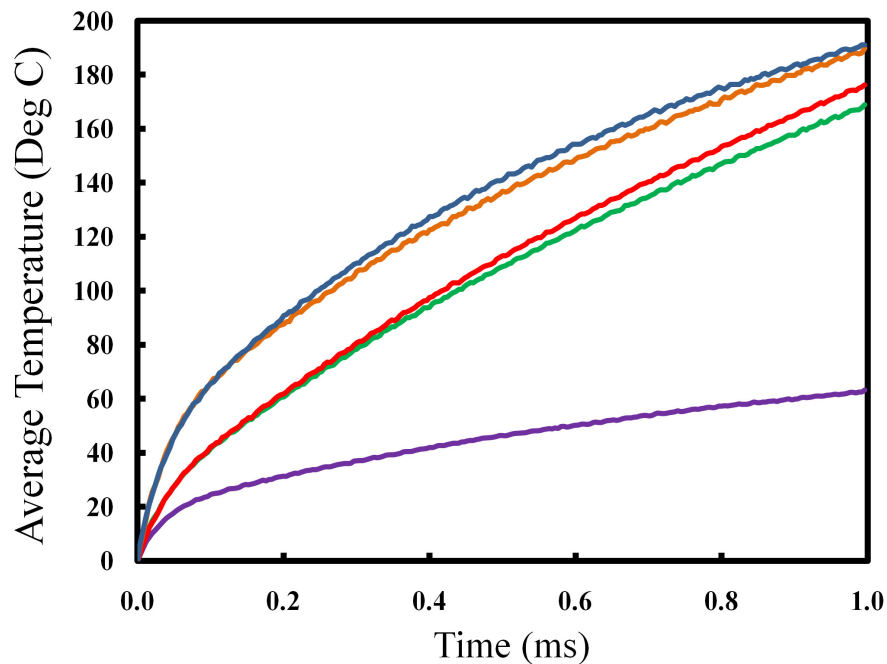


Figure 3-15 Response of the microcantilever heater during short pulse (1 ms) actuation using 250 mW peak power. The plot shows the MV2 G (red), MV2 W (green), MV2 X (blue), MV2 H (orange), and MV1 (purple) measurements.

From this characterisation it is shown that the tapered heaters give a higher rate of change in temperature over small time scales and the second generation devices benefit from the dual polyimide structure by lower heat loss. This is very important for the microcantilever fluid probe as if the thermal dissipation and conversion to mechanical deflection is slow in fluids, the device will not generate a high force to push through the



fluid and give an observable mechanical deflection. For future work it is recommended that the characterisation of heat generation is performed on devices to show the performance of the heaters.

### **3.4 Thermal Crosstalk**

The principal aim of the work is to improve the observation of mechanical signal from the microcantilever sensor by improvements in mechanical actuation and reduction in thermal crosstalk. The mechanical signal is difficult to measure directly as the piezoresistor output of the sensor contains unknown mechanical and thermal signals. The mechanical signal can be estimated using the known actuation efficiency (Table 3-5) at 100 ms pulse width and the mechanical sensitivity (Table 3-1). The presentation of sensor electrical measurements in this section is supported by a comparative investigation of the Solid and Epsilon design using IR Thermography.

#### **3.4.1 Measurement of Sensor Resistance during Actuation Pulse**

The aim of the experiment is to measure the increase in resistance on the integrated piezoresistor sensor during 100 ms actuation pulses. This allows an estimation of the thermal signal using the known deflection and mechanical sensitivity. To make this estimation an assumption is made that the beam deflection is analogous to the probe deflection experiments (section 3.2.1) to measure mechanical sensitivity.

All experiments are conducted on calibrated electronics interfaces developed by Microsystem Ltd, Bulgaria. The electronics is based on  $\frac{1}{4}$  bridge completion circuit with digitally controlled gain (x39, x390, x3900, x39000) and null-balancing of two digital potentiometers using an SPI interface. The bridge balancing, to give an initial zero output uses two daisy-chained 256-step 20 KOhm digital potentiometers with inverse logic for a ‘rough’ and ‘fine’ balance. The adapted Wheatstone bridge circuit is shown in Figure 3-16. The circuit has been calibrated using a known shunt-resistor to simulate resistance measurements. This allows direct conversion at the chosen gain of bridge output voltage to absolute changes in sensor resistance. To minimise error in the conversion factor a shunt resistor has been chosen that produces a change in output voltage over the full measurement range (0 – 10V).

The unknown fixed reference resistor ( $R_{\text{ref}}$ ) has been calibrated using several known high precision nominal resistors in the position of  $R_s$ . The calibration gives a fixed

reference resistance arm equal to 4423 Ohms. This is suitable for the full range of MV2 microcantilever devices (3000 – 9000 Ohm). An identical circuit using a fixed reference resistor equal to 1000 Ohms was also calibrated for application to MV1 devices which have a much lower sensor resistance (250 Ohm)

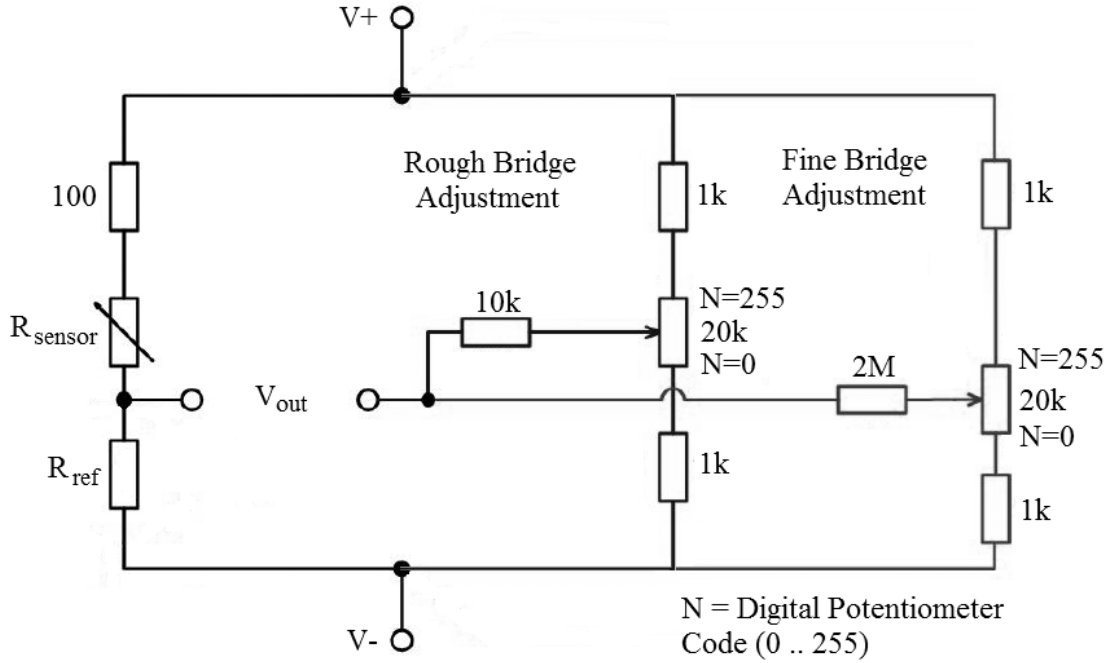


Figure 3-16 Wheatstone quarter-bridge circuit for sensor measurement.

All control and readout of the electronics has been implemented in LabView by the author. LabView controls the electronics and sensor feedback using a PC data acquisition card (M-Series, NI PCI-6221) routed through a shielded BNC connector block (NI BNC-2110). The electronics gain ( $\times 390$ ) and the bridge supply voltage (1 Volt) used in calibration is implemented for the microcantilever measurement.

For long pulse measurements (100 ms) and short pulse measurements (1 ms) the full change in bridge output voltage is measured in the range 2-10 mW peak power for MV2 devices, and 5-25 mW peak power for MV1 devices. Measurements have been repeated several times and a final conversion averaged  $\Delta R/R_0$  has been made. The variation between the piezoresistor sensor output in each pulse is  $< 0.2\%$ . Several microcantilever devices have been measured over the power range for each design. It has been found that the  $\Delta R/R_0$  output has a linear response to power (mW) for short pulses. For 100 ms pulse width, the total sensor signal ( $\Delta R_{total}/R_0 \cdot \text{mW}^{-1}$ ) is measured

from the linear response and the mechanical signal ( $\Delta R_{mech}/R_0 .mW^{-1}$ ) is estimated. The thermal signal ( $\Delta R_{therm}/R_0 .mW^{-1}$ ) is assumed to be the remaining component of the total sensor signal. For 1 ms pulse width only the total sensor signal ( $\Delta R_{total}/R_0 .mW^{-1}$ ) is measured as the mechanical deflection is unknown.

Figure 3-17 shows a comparison of each microcantilever device actuated with a single 1 ms pulse width, 6 mW input power. The response shows the signal overshoot and a capacitive charging/discharging effect. The capacitive effect is isolated and discussed further in Chapter 4 when deconstructing the signal in a liquid.

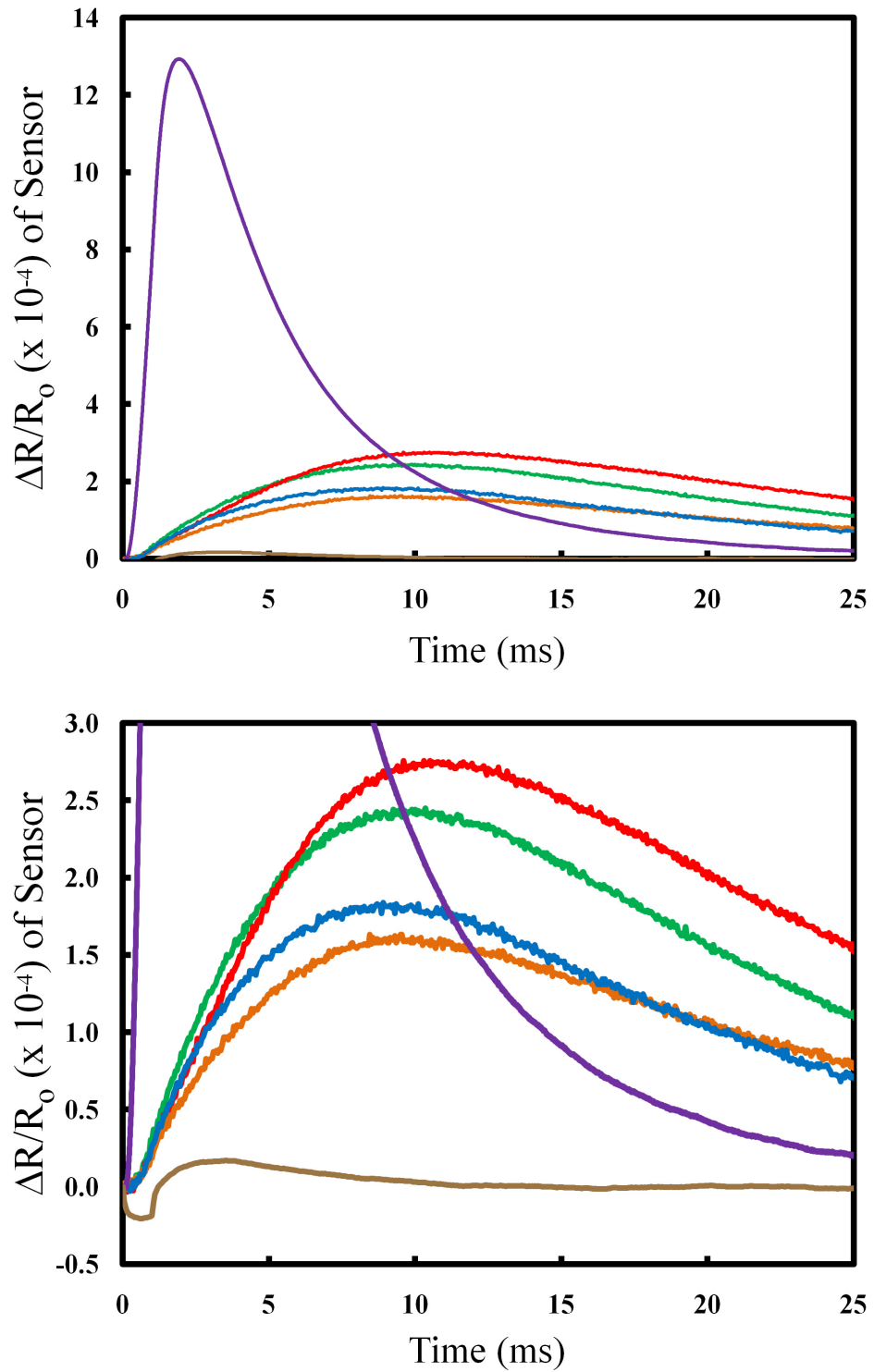


Figure 3-18 Relative change in the sensor resistance during and after actuation for a pulse width of 1 ms and power dissipation of 6 mW. The bottom plot shows a closer view of the initial overshoot. The plot shows the MV2 G (red), MV2 W (green), MV2 X (blue), MV2 H (orange), MV1 (purple) measurements, and MV3 Epsilon design (brown) having a constantan sensor.

Table 3-6 gives the measured total percentage change in resistance per mW for 100 and 1 ms pulse width, and the estimated mechanical and thermal components for 100 ms pulse width.

| Chip Designation   | MV1      | MV2-G    | MV2-H   | MV2-W    | MV2-X   |
|--|----------|----------|---------|----------|---------|
| Layout   | II       | Solid    | Solid   | Epsilon  | Epsilon |
| Sensor Material  | Gold     | NiCr     | NiCr    | NiCr     | NiCr    |
| Heater Configuration   | Standard | Standard | Tapered | Standard | Tapered |
| <b><i>100 ms Pulse Width</i></b>                                 |          |          |         |          |         |
| Total Signal<br>$\Delta R_{total} / R_0 .mW^{-1} (x10^{-4})$     | 27.6     | 10.5     | 6.2     | 8.6      | 5.5     |
| Mechanical Signal<br>$\Delta R_{mech} / R_0 .mW^{-1} (x10^{-4})$ | 0.25     | 0.92     | 0.68    | 0.84     | 0.70    |
| Thermal Signal<br>$\Delta R_{therm} / R_0 .mW^{-1} (x10^{-4})$   | 27.3     | 9.55     | 5.52    | 7.75     | 4.79    |
| Mechanical Signal / Total Signal                                 | 0.9 %    | 8.8 %    | 11.0 %  | 9.8 %    | 12.7 %  |
| <b><i>1 ms Pulse Width</i></b>                                   |          |          |         |          |         |
| Total Signal<br>$\Delta R_{total} / R_0 .mW^{-1} (x10^{-4})$     | 2.15     | 0.46     | 0.27    | 0.41     | 0.28    |

Table 3-6 Relative change in resistance of the integrated sensor for the benchmark and second generation devices per mW using a 100 ms pulse.

Characterisation and experimental results presented in Table 3-6 allow a comparison and discussion of design modifications. This includes changes in material of the structure and sensor, implementation of an Epsilon footprint and tapered heaters, and enhancements in short pulse operation.

#### *Comparison of Gold- and NiCr-Sensor Design (100 ms Pulse Width)*

Results from 100 ms pulse width actuation indicate an improvement between the benchmark design (MV1) and the new standard design (G) through a significant reduction in thermal signal on the microcantilever sensor. To understand this, if the benchmark device is actuated (4.75 mW) to give the same mechanical deflection as design G (1 mW), the thermal signal is 13.6 times higher. This improvement is

dominated by the 11.3 times reduction in sensor thermal sensitivity (TCR) by replacing Gold with NiCr metalisation.

*Comparison of Gold-Polymer and Polymer-Polymer Design (100 ms Pulse Width)*

Using the previous logic, the changes in structural design and geometric separation of heater and sensor between the benchmark design and the new standard design (G) also provide a further improvement in the observed mechanical signal. Again, if it is assumed the MV1 device is powered to the same deflection as G, and that gold sensors have been replaced by NiCr, the further reduction in thermal signal is approximately 18%. This reduction could be a mechanical enhancement from higher conversion efficiency, or a reduction in thermal crosstalk.

*Comparison of Solid and Epsilon Design (100 ms Pulse Width)*

The Solid design with standard heaters (G) can be directly compared against the Epsilon design with standard heaters (W), and the Solid design with tapered heaters (H) against the Epsilon design with tapered heaters (X). In both cases the Epsilon design improves the mechanical signal as a proportion of the total signal, approximately 11% between G and W, and 15% between H and X. Given that the expected conversion efficiency is similar between second generation designs, and this is supported by the measurement of the heater resistance during actuation, the improvement derives from the reduction in thermal crosstalk.

*Comparison of Standard and Tapered Heater Designs (100 ms Pulse Width)*

The Solid design with standard heaters (G) can be directly compared against the Solid design with tapered heaters (H), and the Epsilon design with standard heaters (W) against the Epsilon design with tapered heaters (X). In both cases the tapered heater design improves the mechanical signal as a proportion of the total signal, approximately 25% between G and H, and 30% between W and X.

*Enhancements in short pulse (1 ms) operation.*

It is expected that short pulse operation will enhance the mechanical signal as a proportion of the total signal in new designs through reduced heat transfer. As the mechanical deflection for 1 ms pulse width is unknown it is only possible to use the total signal response to extract limits for improvement. For example, the reduction in total sensor response for the two experimental pulse widths is approximately 80 %

higher in design G compared to the benchmark design. Working through the limits of mechanical and thermal signal this indicates a lower limit improvement of approximately 30% in reduced thermal signal either through improved conversion efficiency or reduced thermal crosstalk.

The Solid design with standard heaters (G) can be directly compared against the Epsilon design with standard heaters (W), and the Solid design with tapered heaters (H) against the Epsilon design with tapered heaters (X). In this case the total signal is comparative between designs. This is perhaps an indication that at short time scales the Epsilon design is not advantageous as thermal conduction is already limited. Comparison of tapered heaters to standard heaters shows lower overall signal. If an assumption is made that the mechanical signal is reduced linearly with pulse width for all designs, this is again indicative that the tapered heater is an improvement over standard heaters.

### **3.4.2 IR Thermal Imaging of Microcantilever Fluid Probe**

An investigation of microcantilever temperature distribution during actuation has been conducted with Dr. Martin Kuball at the University of Bristol, recently founded as the Center for Device Thermography and Reliability (CDTR). The principal objective was to qualitatively note any differences between the Solid design with standard heaters (G) and the Epsilon design with tapered heaters (X). The experiments were set out by the author and Dr Vladislav Djakov (STFC), and experiments were conducted by Dr. Andrei Sarua (Bristol University) with documenting support from Microvisk.

The temperature mapping has been conducted using a QFI Infrared thermal imaging system (Quantum Focus Instruments Infrascopes). The Infrascopes detect thermal radiation using an InSb 256 x 256 pixel array detector, cooled with liquid nitrogen. The detector is mounted onto a Leica microscope with adapted optics for focusing IR wavelengths, including a custom x15 Si/Ge objective lens with high numerical aperture of 0.5. The detector provides approximately 1.6  $\mu\text{m}$  per pixel resolution with a field of view of roughly 400 x 400  $\mu\text{m}$  and working distance of 15 mm. The depth of field is approximately 40  $\mu\text{m}$  and therefore only the thermal mapping from the central focused section of the beam should be taken with confidence.

Firstly the measurement is compensated for the emissivity of each material - a measure of how efficiently the material emits photons. This is made by a pixel by pixel

calibration of the material emission over a range of temperatures using a Peltier stage underneath the sample. The measurement requires approximately 2 minutes for the stage to come to temperature and several minutes for the sample to reach equilibrium. The sample, in this case the microcantilever, is then imaged with no power to confirm the emissivity correction and then with the sensor connected and actuation of the heaters using a function generator (Agilent, 33220A). The microcantilever is imaged in the steady state as the camera does not have the time resolution to view  $\mu$ s to ms heat transport. With no power the image shows an emissivity contrast and therefore the calibration was not ideal, this is probably because from later TCR measurements it takes 20-30 minutes for the chip to reach a steady state temperature in a heated environment. Figure 3-19 shows the temperature mapping images of Design G at 3.3 mW input power and Design X at 9 mW, the rectangle represents focused areas of interest on the beam.

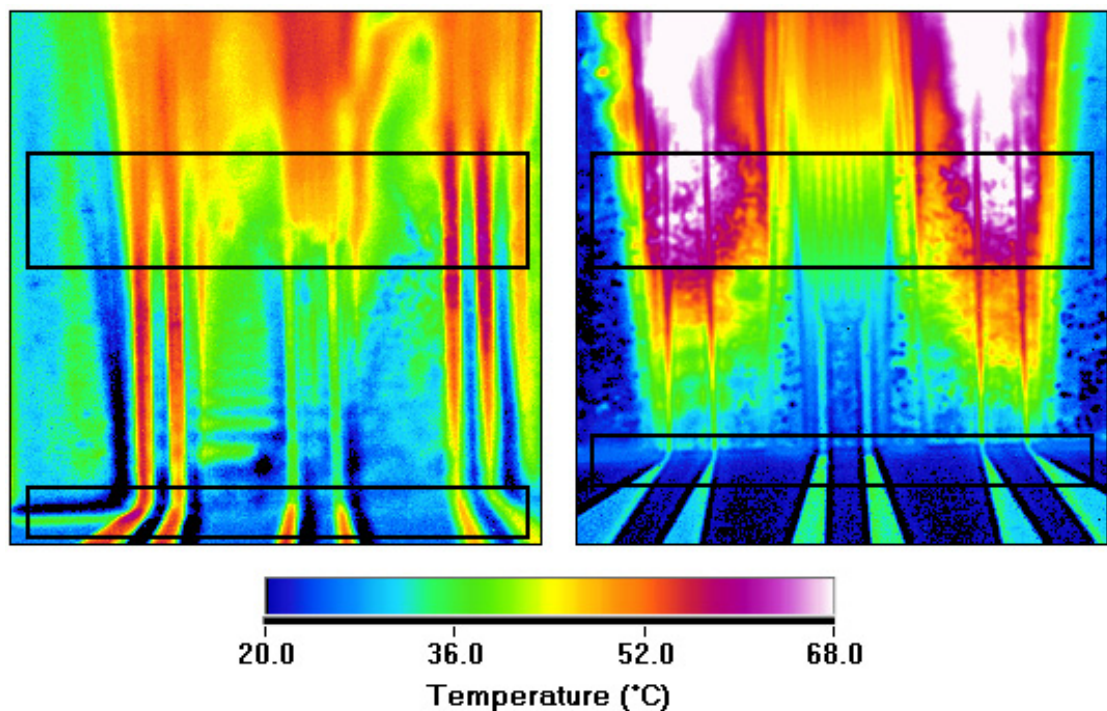


Figure 3-19. Thermal images of Design G (3.3 mW) and Design X (9.0 mW) using the QFI Intrascopes IR imaging system. The two rectangular boxes represent focused areas of interest; the lower box indicates the connecting tracks out from the device and the upper box represents a cross section through the heaters and sensor.

Thermal imaging supports the experimental measurements presented in Table 3-6 for reduction in thermal crosstalk from Solid design G to Epsilon design X for steady state pulses as 49.8%. In figure 3-19, the thermal image of the Solid design (G) indicates a sensor temperature during actuation that is approximately equal to the heater



temperature. For the case of the Epsilon design (X) the sensor temperature ( $\sim 36^{\circ}\text{C}$ ) is approximately half of the heater temperature ( $\sim 68^{\circ}\text{C}$ ).

A second observation is that in the standard heater configuration (Figure 3-19 - left image) the metal tracks out of the microcantilever are equal in temperature to the heater on the device; this is not seen in the tapered configuration (right image). This is possibly due to the variation in current density in the tapered heater which has approximately twice the resistance of the standard heater. This would half the current needed to achieve the same power and therefore in the tapered design the power dissipated in the standard part of the track is reduced by a factor of 4.

### **3.5 Summary and Discussion of Design Simulation and Characterisation**

The aim of characterisation is to validate the design modifications made through analytical and simulation work, and to select devices for the clinical evaluation. The main results of characterisation are:

- NiCr piezoresistive sensors have a comparable mechanical sensitivity to Gold piezoresistive sensors and significantly lower thermal sensitivity (TCR) leading to a reduction in the thermal crosstalk signal by 11.3 times.
- Reduction in thermal signal at 100 ms pulse width by 18% between the benchmark gold-polymer design (MV1) and the standard polymer-polymer design (G) through higher conversion efficiency and a reduction in thermal crosstalk.
- Improvement in mechanical signal as a proportion of the total signal for 100 ms pulse width by 11-15% between Epsilon and Solid design through reduction in thermal crosstalk.
- Improvement in mechanical signal as a proportion of the total signal for 100 ms pulse width by 25-30% between tapered and standard heater design through reduction in thermal crosstalk.
- Enhancement in operation at very short pulse width (1 ms) with a lower limit improvement of approximately 30% in reduced thermal signal either through improved conversion efficiency and/or reduced thermal crosstalk.
- Non-linear negative and twisting deflections in multi-layered microcantilevers with integrated heaters and sensor.

Simulation and characterisation indicates that all design modifications have improved the microcantilever fluid probe device, and in combination will produce a total response with a minimum mechanical component of 12-17%; a significant improvement on the benchmark MV1 device of 1%. From this work the Epsilon design X and W have been selected as a priority for post-processing for the clinical evaluation.

Simulation of design modifications in chapter 2 supported improvements in the microsensor operation, including an Epsilon shaped beam, tapered heater, and changing the gold structural layer for a second polyimide. These improvements are validated by experimental work, though comparison with simulations shows a number of inconsistencies.

Comparison of simulated Epsilon and Solid designs (Table 2-3) indicates the Polymer-Polymer Epsilon design has 95% less thermal crosstalk than the Polymer-Polymer Solid Design. The experimental results (Table 3-6) support only an 11-15% difference. Also, the simulated MV1 design has a lower thermal crosstalk than the standard polymer-polymer solid design. This indicates an issue with the simulated thermal profile along the beam. Visually the temperature at the base of the microcantilever in simulations is very low due to thermal conduction into the silicon (Figure 2-8 and Figure 2-11), this is not seen in the IR thermography (Figure 3-19). In this situation the MV1 sensor, concentrated at the base, has a low thermal response, and the MV2 sensor that extends along the beam has a high thermal response.

The second inconsistency between simulation and experiments is the mechanical deflection of polymer-polymer microcantilevers and tapered heaters in the simulation. In simulations all devices are predicted to have a linear deflection towards the substrate and for polymer-polymer devices the deflection is greatly overstated. Presented in characterisation of microcantilever deflection (section 3.3), the steady-state deflection of MV1 is away from the substrate and the deflection of MV2 devices is a twisting that gives non-linear deflection. In simulations the tapered heaters give a significant increase in deflection of the device related to power and temperature conversion. From experiments, the deflection of devices with tapered heaters (Table 3-5) and temperature of the heater response (Figure 3-14) is lower than that of standard heaters. In the characterisation it is the decrease in thermal crosstalk of the tapered design that improves the overall operation over the standard heaters.

Joule heating in tapered heaters dissipates three times more heat at the base of the microcantilever than the tip, compared to constant dissipation in the standard width heater. For equal power applied to both types of heater, the tapered design dissipates effectively half the energy in the top half of the heater compared to the standard width heater. This leads to the fabricated sensor, concentrated between 200 and 600 microns along the beam, being in a lower thermal gradient for tapered heaters.

An issue in the simulation could be that a chrome adhesion layer has not been included for the metal heater in the simulation which the author believes will restrict the expansion of the volume above the neutral axis. Chrome has a low thermal expansion ( $4.9 \text{ ppm.K}^{-1}$ ) compared to the surrounding polyimide ( $60 \text{ ppm.K}^{-1}$ ). In analysing the cross-section both gold heaters and NiCr sensors are above the neutral axis. Upon heating the volume below the neutral axis is free to expand, and above the axis is potentially limited. It is also possible that although our mesh in-plane to the microcantilever is sufficient, the detail needed to calculate the localised thermal bending moments in the z-plane is limited. If the simulation is to become a fair indication of the design for new devices these two aspects must be taken into account in future simulation.

One consistent remark is that although the actuation efficiency of devices changes with the modifications the conversion factor, which is the driving force, remains similar across all devices. This is reflected in the characterisation where the estimated heater response during actuation (Figure 3-14) closely follows the deflection capabilities of the devices, again reinforcing that it is the temperature in the beam that drives the device.

Further simulation and characterisation by the author has not been attempted beyond the clinical evaluation, as the devices work successfully and fabrication has moved to a pre-production design incorporating the polymer-polymer Epsilon design with tapered heaters.

## **Chapter 4 – Microcantilever Fluid Probe Demonstration and Clinical Evaluation**

### **4.1 Introduction**

In the previous chapter the original microcantilever fluid probe (MV1) has been tested against second generation designs (MV2), and a number of improvements have been made in actuation and thermal crosstalk. The aim of improving the device sensor response is to confirm a distinguishable mechanical signal in standard known fluids and then study the formation of a clot in plasma and whole blood. Chapter 4 presents the piezoresistor response from actuation in known glycerol solutions, and attempts to deconstruct the response into mechanical, thermal, and electrical components using polymerisation. The work leads to the operation, data capture, and analysis of clotting response in plasma and whole blood and the evaluation of the technology in a clinical trial at The Royal London Hospital. Results are presented with comparison to the laboratory standard analyser, and the final accuracy and precision of the measurement is compared with other commercial point of care devices.

### **4.2 Microcantilever Fluid Probe in Glycerol**

Previous characterisation tests indicated that in air the thermal component of the microcantilever response exceeds the mechanical component even with improvements made in the second generation design. The aim is to deconstruct the microcantilever response into thermal, mechanical, and electrical components and therefore allow the signal-to-noise to be estimated. From the analysis of thermal transport in chapter 2 it is anticipated that the response is dependent on rheological and thermal properties of the medium, namely the thermal conduction and heat capacity. For example, the heat convection coefficient from the surface of the microcantilever to air is approximately 40 times less than water [43] and therefore heat is sustained in the microcantilever giving higher temperatures and a greater overall response in terms of thermal crosstalk and mechanical deflection. Testing in glycerol solutions with known rheological and thermal properties allows the microcantilever mechanical and thermal response to be studied against best operation. The operation and response analysis is then suitable for application to clotting events in plasma and whole blood. Table 4-1 gives the rheological properties and thermal conductivity of air and standard glycerol solutions at 20 °C [72, 116-117]. The specific heat capacity of air is  $1.01 \text{ J.g}^{-1}.\text{K}^{-1}$  [118] and the

range of heat capacity of water-glycerol solutions is 4.18-12.14 J.g<sup>-1</sup>.K<sup>-1</sup> [118, 119] at 20 °C with pure water having the lower value.

| Fluid        | Viscosity<br>(cP) | Density<br>(g.cm <sup>-3</sup> ) | Thermal<br>Conductivity<br>(W.m <sup>-1</sup> .K <sup>-1</sup> ) |
|--------------|-------------------|----------------------------------|--|
| Air          | 0.019             | 0.00008                          | 0.025  |
| 0% Glycerol  | 1.005             | 0.99823                          | 0.591  |
| 30% Glycerol | 2.50              | 1.07270                          | 0.482  |
| 70% Glycerol | 22.5              | 1.18125                          | 0.352  |
| 80% Glycerol | 60.1              | 1.20850                          | 0.327  |
| 99% Glycerol | 1150              | 1.25850                          | 0.284  |

Table 4-1 Rheological and Thermal Properties of Air and Glycerol Solutions at 20 °C [72, 116-119]. Glycerol solutions are measured as percentage weight with respect to pure water.

The actuation and sensor measurement is performed using the previously calibrated electronics interface (Section 3.4.1) developed by Microsystems Ltd, Bulgaria. The actuation heat pulse is controlled from the function generator and connected through the electronics. In the initial fluid measurements the electronics (SPI interface and digital gain / channel selector) is controlled through software provided by Microsystems Ltd, and the sensor response is recorded through a LabView program that provides triggered data acquisition of a single analog channel. The bridge output is routed through a shielded BNC connector block (NI BNC-2110) connected to a PC data acquisition card (M-Series, NI PCI-6221). The M-Series card has a resolution of 16-bit and an adjustable range ( $\pm 0.1, 1, 5, 10$  Volts). This range is set during each measurement to maximise the accuracy. The data acquisition card has a maximum sampling rate of 250 KS/s, though this creates a high load on the PC when recording continuous data. For the current measurements the sampling rate is set at 100 KS/s giving 10  $\mu$ s resolution. Preliminary testing has found that operating frequencies up to 10 Hz and a pulse width of 0.5 ms provides good operation across all devices; this provides 99.5 ms for cooling of the device between pulses. The voltage of each actuation pulse is set to achieve a dissipated energy of 150  $\mu$ J and peak power of 300 mW<sup>6</sup>. For Glycerol testing the frequency has been set to 1 Hz, measurement limits are  $\pm 1$ V, gain is equal to x390,

<sup>6</sup> This has been established by Microvisk as the optimum pulse [120].

and the total number of samples is 5000. Each sample is saved as a 6 decimal place double precision integer in a LabView measurement file (.lvm) with time information, where each actuation event is saved to a new file for easier access. In practice the balanced Wheatstone bridge output is not zero but slightly offset. When this is amplified the baseline voltage can be a few mV above zero, also the baseline can drift over time when using a quarter bridge circuit. This baseline does not affect the absolute change in voltage signal due to a change in resistance and therefore each actuation event can be shifted to zero to allow a comparison between microcantilever devices. Before each measurement the chip type, reference number, and resistance of the microcantilever heater and sensor is recorded and a measurement across the Wheatstone bridge supply is made. Each device has been potted with a silicone sealant around the microcantilevers by Dr Vladislav Djakov to stop the fluid moving onto electrical contact pads. Figure 4-1 shows averaged microcantilever response (n=10) in pure water for W, G, X, and H devices conducted in the period 5<sup>th</sup>-24<sup>th</sup> May 2007<sup>7</sup>. All devices show a mechanical oscillation and therefore could all potentially be used to monitor mechanical damping due to rheological properties. Error bars of the microcantilever response in pure water are < 1% and have not been shown.

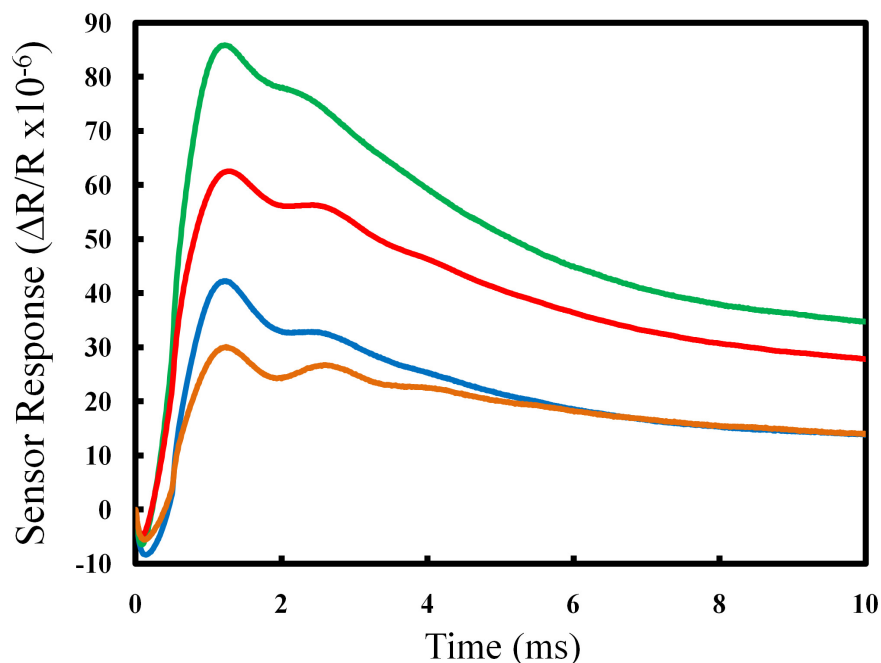


Figure 4-1 Single microcantilever response of MV2 W (green), MV2 G (red), MV2 X (blue), and MV2 H (orange) in pure water using a short (0.5 ms) actuation pulse. The power and energy of the actuation pulse is 300 mW (150μJ) for MV2 W, 270 mW (135μJ) for G, 181 mW (90μJ) for X, and 179 mW (90μJ) for H.

<sup>7</sup> X and H performed by V. Djakov, J. Booth, and the Author. W and G performed by V. Djakov.

Unfortunately the results in Figure 4-1 do not provide a reliable comparison between all devices as the pulse optimisation has been measured incorrectly [120]. Returning to the pulse optimisation in August 2008 the Microsystems Ltd. electronics actuation driver was characterised using a known input voltage (Agilent, 33220A). The actual voltage across the device was then measured directly using a 6.5 digit voltmeter (Keighley 2100). Whilst the input voltage has a maximum limit of 10 Volts the Microsystems Ltd electronics output saturates at approximately 6 Volts (Figure 4-2). For the earlier characterisation on standard heaters this corresponded with the resistance as giving an energy pulse of 150  $\mu\text{J}$  for a 0.5 ms pulse width. As the X and H device both have higher heater resistance, due to tapering, the same energy can not be generated as the input voltage is clipped to 6 V. The corrected power and energy of pulses used for the glycerol testing is 300 mW (150  $\mu\text{J}$ ) for the W device, 270 mW (135  $\mu\text{J}$ ) for the G device, 181 mW (90  $\mu\text{J}$ ) for the X device, and 179 mW (90  $\mu\text{J}$ ) for the H device. The corrected power is noted in further experiments and the clinical evaluation.

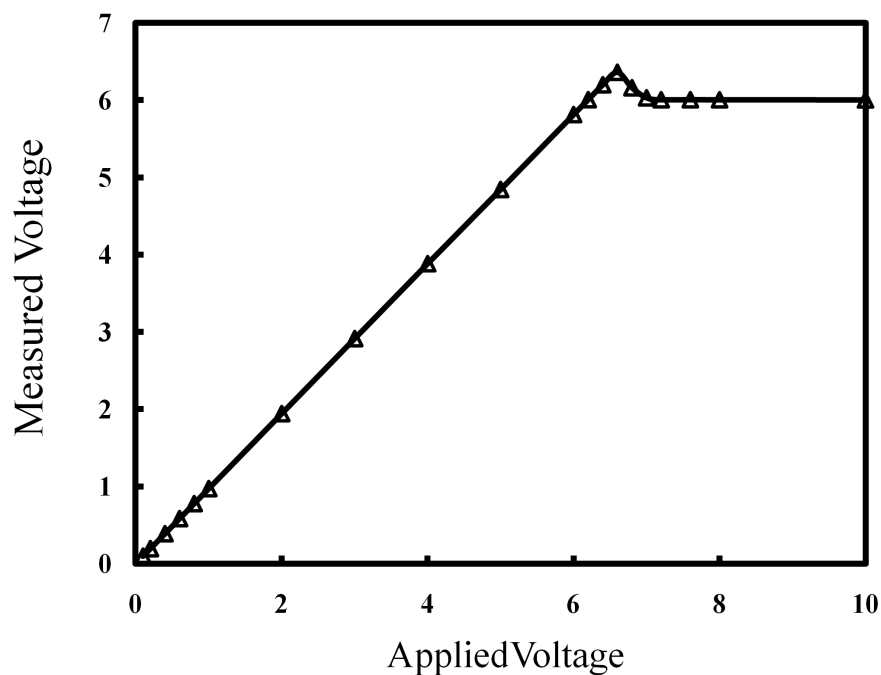


Figure 4-2 Applied and measured voltage across the microcantilever device when the actuation pulse is routed through the Microsystems Ltd electronics.

The X and H devices from the glycerol testing can be compared directly due to almost identical actuation power. The Epsilon device X has the most prominent first peak, and the Solid device H clearer oscillations. The W and G device follow this trend with the first peak pushed higher relative to the second peak in the Epsilon device and the

oscillations clearer in the solid design. Mechanically, the Epsilon design should decrease the opposing fluid drag force, allowing the device to reach a higher velocity and therefore deflection with a fixed pulse of energy. Under this further displacement the restoring force pulling the microcantilever back through the fluid could be distorting the ringing of the beam. If the difference was a thermal effect it is expected that the whole signal response would increase. As seen in figure 4-1, the signal after 6 ms is identical in both X and H devices. In this preliminary evaluation in fluids towards the clinical work, time and resources were not available to conduct simulation work of devices operating in fluids.

These results lead to an indication of the applicability of designs to different sensing applications. For looking at relative changes in the viscosity and density during a reaction the enhanced first peak of the Epsilon design provides a more distinct parameter to monitor. Also for moving to fluids with very high damping the reduction in area decreases the effective forces acting on the motion of the beam. On the other hand the Solid design provides distinctive secondary mechanical oscillations in the fluid. To measure both viscosity and density simultaneously several parameters will be needed. The Solid design could provide this through the position and amplitude of several peaks. Normalising the response of each device the tapered designs X and H improve the resolution of the mechanical oscillations though it is difficult to establish whether this is due to overpowering the W and G design or if this is due to the heater design.

Figure 4-3 shows the response of a single X microcantilever device in 0 to 99 percentage weight glycerol with respect to water solutions. The actuation pulse has a 1 Hz frequency and a corrected energy of 90  $\mu$ J (0.5 ms pulse width and peak power of 180 mW). The device is chemically treated and dried between tests though it is unclear how such treatment may affect the following tests. The response of the microcantilever in the lowest viscosity solution (0 wt%) shows an overshoot and second oscillation which is believed to be a mechanical artifact. In the next solution (30 wt%) the oscillation is damped and the peaks move to the right. This is expected if the response is a mechanical artifact as the microcantilever will move less through the fluid and at a slower rate. The peak height is also expected to be reduced though this is not initially measured. As the response also has a thermal artifact the lower thermal conductivity of the 30 wt% glycerol means more heat is retained in the microcantilever inducing a



higher thermal crosstalk on the sensor. Measurements in higher wt% glycerol solutions have no distinguishable oscillation and the peak height falls although thermal conduction continues to decrease. This trend is likely due to the rheological properties increasing substantially (viscosity increases from 2.5 cP to 1150 cP) from 30 wt% to 99 wt% glycerol while thermal conduction – that would otherwise make the peak height increase - falls by approximately half. As the measurements are not purely mechanical it is difficult to place an accuracy and range on the device as a viscometer or density meter. Certainly there is potential for the device as a simultaneous rheological and thermal fluid sensor; this is discussed further in the conclusion.

The response during the actuation pulse has been analysed and shows no significant differences between viscosity standards. This is due to the time resolution and limited mechanical sensitivity of the integrated piezoresistor that make the response indistinguishable at very short times.

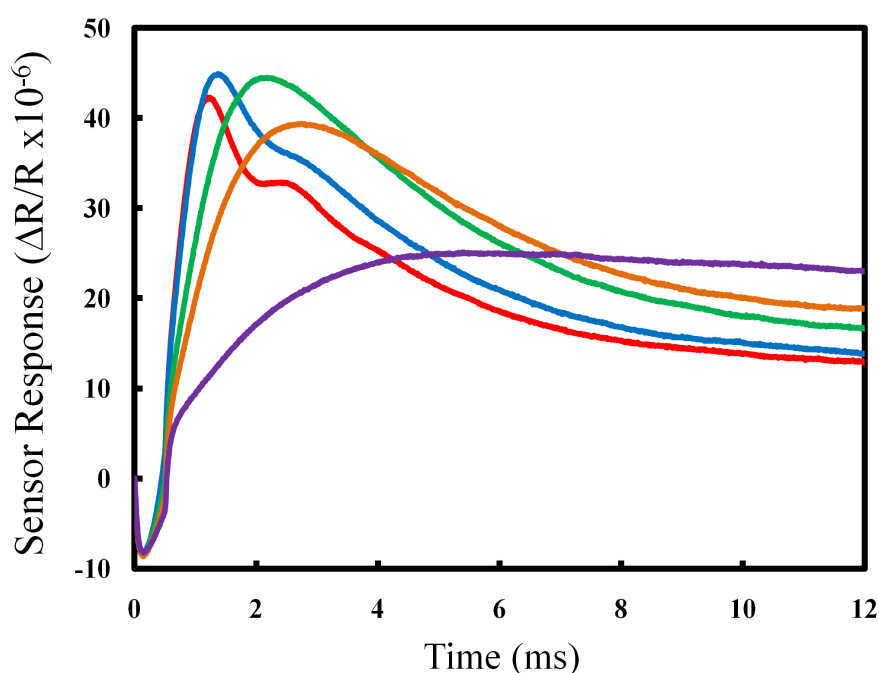


Figure 4-3 Microcantilever response of the second generation MV2 X device in several glycerol by percentage weight solutions using a short (0.5 ms) 90  $\mu$ J actuation pulse. The plot shows measurements at 0% (red), 30% (blue), 70% (green), 80% (orange), and 99% (purple), concentrations. Error bars of the microcantilever response in pure water are < 1% and have not been shown.

### **4.3 Deconstruction of Signal from Microcantilever Fluid Probe**

The glycerol results presented in the previous section indicate a capacitive effect during the pulse and an overshoot in the microcantilever response after the actuation pulse. The significant result is the damped signal oscillation after the overshoot which is further damped towards higher viscosity/density. Though the total signal contains a thermal component it is expected that this artifact is mechanical. The aim of deconstructing the signal is to estimate the absolute level of mechanical signal against the thermal and capacitive signal.

To extract the mechanical signal it is desirable to measure the deflection of the microcantilever in liquids using an optical technique and compare with the electrical response. As the microcantilever actuation is low frequency, and deflection is expected to be in the order of a few microns, an interferometer or optical image capture is possible if a stroboscopic technique is used. This allows synchronisation between the actuation pulse and the optical image capture. On each actuation pulse the image capture has a fixed delay, effectively capturing the position of the microcantilever at each time. A high-speed line scan camera has also been considered, where the camera is aligned along the microcantilever. Optical measurements before the clinical evaluation have not been conducted but present an area for future work to derive a more robust rheological fluid probe.

A second possibility is to make the assumption that the microcantilever will have zero or near zero deflection in very high viscosity solutions and therefore the signal is all thermal; this is possible but it is a difficult assumption to make without an optical measurement to confirm there is no deflection. A third possibility is to measure the response in a fluid which initially allows a mechanical deflection but then becomes solid such that the microcantilever becomes fixed and only a thermal component is measured. In previous experimentation by the author, superglue was dispensed on microcantilevers, and monitored as the glue hardened [14]. Unfortunately as the glue hardened the device became twisted and electrical connections broke. In the same work, testing fixed unreleased microcantilevers does not provide a realistic thermal component as the heat is lost instantly into the substrate giving a “top-hat” response.

Mr. Joe Booth (Microvisk) has suggested the use of an acrylamide/bis-acrylamide solution (Sigma Aldrich A9926) where polymerisation is initiated on the device to

create a solid casing around the microcantilever. A tris(hydroxyamino)methane (TRIZA base, Sigma Aldrich T6066) base solution is mixed with acrylamide and water and is activated with a second solution of Tetramethylthylenediamine (TEMED, Sigma Aldrich T9281) and Ammonium Persulphate. The test has been conducted with a MV2 Device (H) and a corrected actuation pulse of 96  $\mu\text{J}$  (0.5 ms pulse width and 192 mW peak power) through Microsystems Ltd calibrated electronics. The response has been measured continuously at 1 Hz in air and from application of the solution (24 seconds) to solidification, the sampling rate is 100 KS/s and measurement limits are set at  $\pm 1$  volt and gain is equal to x390. During polymerisation the solution temperature increases by a maximum of 9 °C after the first minute and then cools as the material reaches the final gelling stage. The fluid temperature will affect the base line resistance of the microcantilever probe though it is expected that the thermal conductivity and rheological properties are dominated by the cross linking and increase in molecular weight rather than the temperature dependency.

Hansen and Ho [121] have shown that the thermal conductivity is proportional to the square-root of molecular weight and therefore it is expected that the thermal conductivity during polymerisation will increase. This is supported in Figure 4-4 which shows the general curve falling. If the thermal conductivity of the solution was decreasing the microcantilever would heat up further and produce a larger thermal crosstalk. Venkateshan and Johari [122] have measured the thermal conductivity during polymerisation of cross-linked network structures and note that the thermal conductivity initially increases with the molecular weight and density, and at longer time decreases to a value close to the initial value upon structural relaxation. The increase in thermal conductivity gives an upper limit to the estimated mechanical response of the microcantilever. Figure 4-4 shows the microcantilever sensor response at 28, 35, 40 and 180 seconds. The final time is averaged from 175 to 185 seconds as the variation in signal response increases as it becomes lower. The first result given is 4 seconds after application of the acrylamide solution as the measurement requires a settling time.

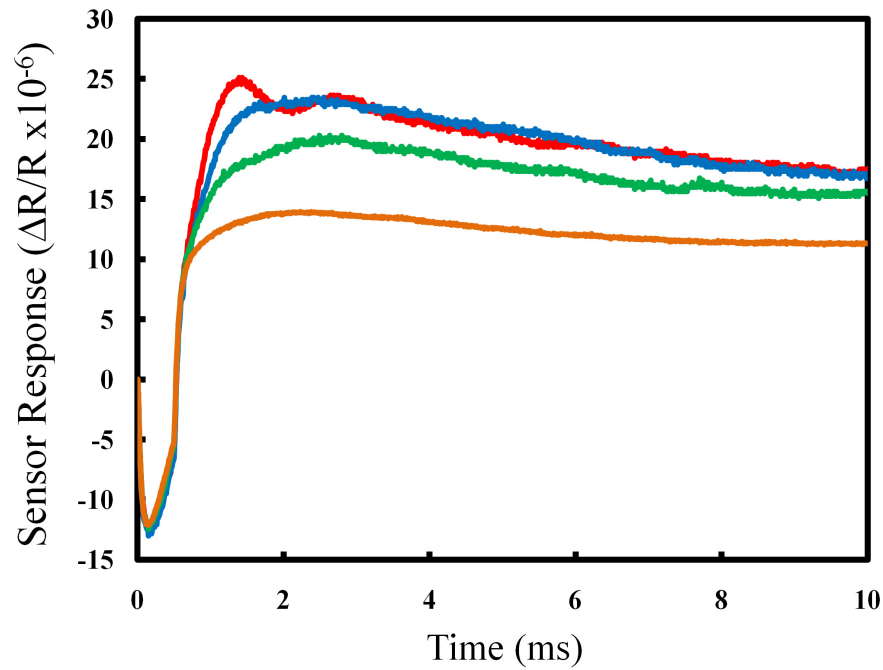


Figure 4-4 Piezoresistor response of a single MV2 H device in a 5% Polyacrylamide gel (PAG) at 28 seconds (red), 35 seconds (blue), 40 seconds (green), and 180 seconds (orange).

To extract the electrical component of the 28 second response, the data up to 0.25 ms after the rising and falling pulse edge is rejected. The remaining data during the pulse is shifted upwards and fitted with data between 0.75 and 1.4 ms using a third order polynomial with minimised residuals. The 180 second response does not reduce in the same manner; in this case a trend is fitted during the pulse for data between 0.3 and 0.5 ms, is extrapolated back to the axis and shifted up by the intercept value. This data and the data between 0.75 and 1.25 ms are fitted with a third order polynomial to complete the missing section just after the pulse. Figure 4-5 shows the estimated electrical component at 28 and 180 seconds, believed to be a capacitive charging effect between the heater, substrate and sensor.

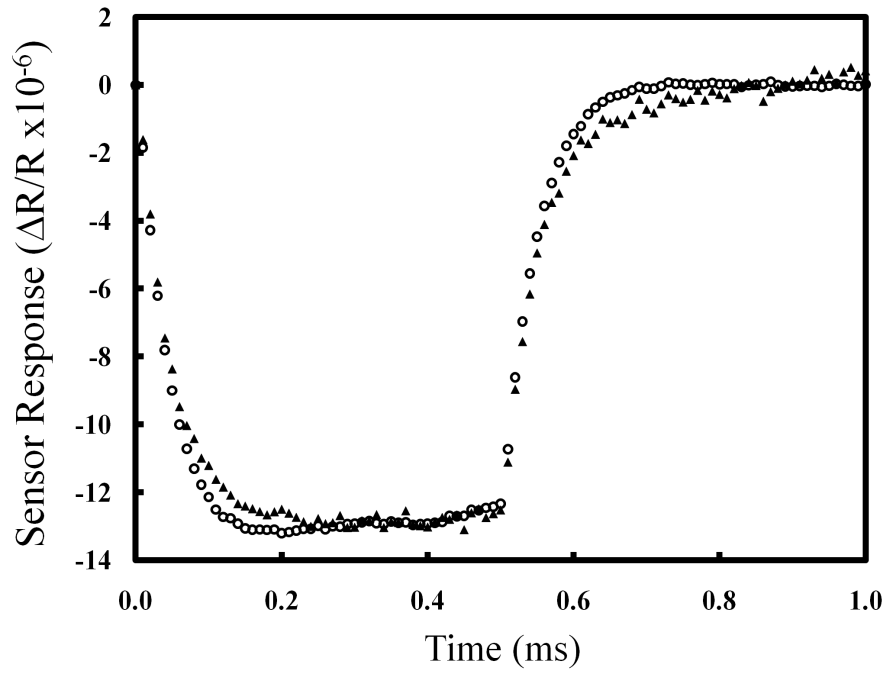


Figure 4-5 Extracted electrical artifact in the microcantilever response at 28 seconds (triangle) and 180 seconds (circle).

After deducting the capacitive component from the original signal the 28 second and 180 second response is shown in Figure 4-6. If an assumption is made that the initial response has mechanical and thermal signals, and the final response is only the thermal signal after the device has become fixed it is possible to estimate the upper limit of the mechanical signal in the response, change in temperature on the sensor, and mechanical deflection. As the fluid is evolving it is difficult to establish statistical variation at a given pulse time. By analogy with previous measurements of several microcantilever devices in glycerol solutions the error in the response is consistently below 1%, with a standard deviation of approximately 2 – 3 %.

At the mechanical overshoot of the beam the maximum mechanical signal is 48% with an enhanced signal-to-noise over the general trend. The maximum thermal response in the polymerised state is  $14.0 \times 10^{-6} \Delta R/R$  giving an internal increase in average sensor temperature of  $0.14^\circ\text{C}$  using the measured TCR value in chapter 3. The maximum value of the mechanical response is  $12.1 \times 10^{-6} \Delta R/R$  giving a maximum deflection of 0.75 microns using the mechanical sensitivity value. The amplitude of the oscillation is approximately 240 nm and the width of the line representing the noise corresponds to a measurement limit of 40 nm. It has been found in later studies that the noise limit when

probing NiCr sensors is approximately 30-40 nm, therefore validating the approximate microcantilever deflection.

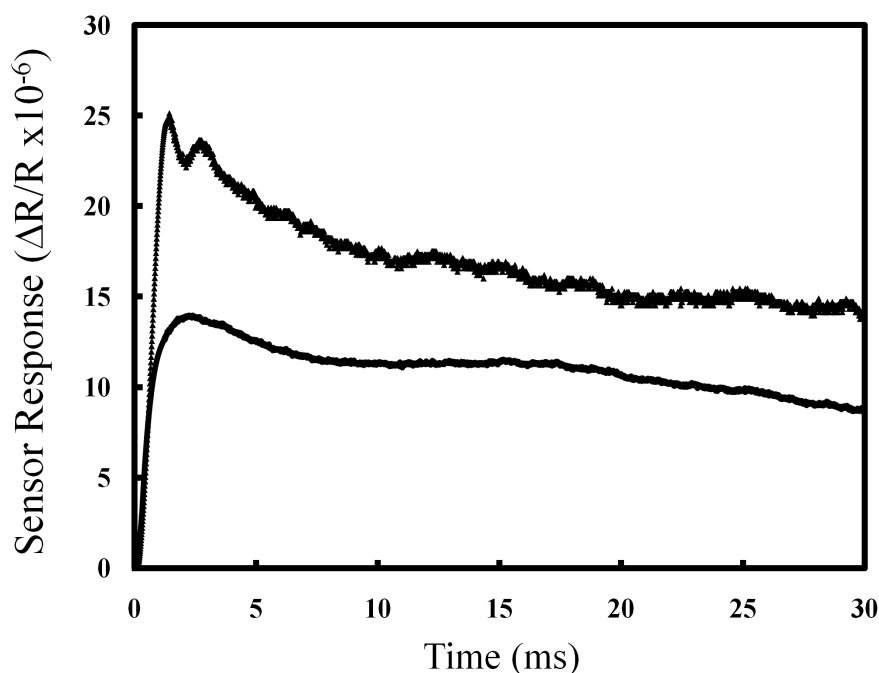


Figure 4-6 Thermo-Mechanical response (top) of the microcantilever fluid probe (H) when first immersed in the polyacrylamide gel and thermal response (bottom) when the gel has set and the microcantilever is unable to move.

The rheological properties of the initial polyacrylamide solution are unknown, though glycerol testing on a calibrated H device shows a similar mechanical oscillation period comparable to 30% glycerol. Unfortunately there is not enough information to deconstruct the glycerol measurements due to the changing thermal and rheological properties and therefore it is difficult to establish a range and accuracy for the microcantilever fluid probe. The result from the PAG work is the enhancement in mechanical signal when the probe is operated in fluid with short pulses due to a mechanical overshoot of the beam. The work also indicates the ability to measure the evolving rheological and thermal properties of a solution over time analogous to the intended use as a coagulometer.

#### 4.4 Improvements to Drift in Signal Response

In many strain gauge applications it is more suitable to use a half-bridge with a reference resistor. This reference should be subjected to the same environment as the active resistor and therefore compensate for thermal, and environmental fluctuations.

This arrangement has not been used in the previous measurements as the focus was on the thermal crosstalk within the cantilever and if two devices were connected as a half bridge and both actuated the mechanical signal would also be compensated. It has been shown by the author that it is still desirable to use a half bridge arrangement for environmental referencing as presented below.

In previous measurements the baseline voltage of the response can significantly go out of balance and drift over time. This is due to the dissimilar temperature of the fluid that is dispensed onto the microcantilever and a re-establishment of a thermal equilibrium over time. If the signal goes out of range of the selected data acquisition limits the signal is lost and the experiment has to be stopped. The drift in signal also means that larger limits have to be used ( $\pm 1$  Volt) and therefore the resolution is reduced. With a more stable signal the limits can be set lower ( $\pm 0.1$  Volt) and resolution increased. The drift can also influence the shape of the response, for example, if the response was on the sharp rise of the baseline signal then the response will be stretched and an artificially high Zero-to-Peak value is measured. Figure 4-7 shows the unreferenced signal baseline and the effect of using the second microcantilever as a passive reference during application of a 10 cP silicone oil. The measurement is conducted at room temperature, the microcantilever device is actuated at 1 Hz with a 5 Volt peak and 0.5 ms width pulse. The signal baseline is effectively the first value measured in every actuation pulse. The result shows the long settling time when the device is unreferenced. This is undesirable as the clotting mechanism could be masked by this artifact.

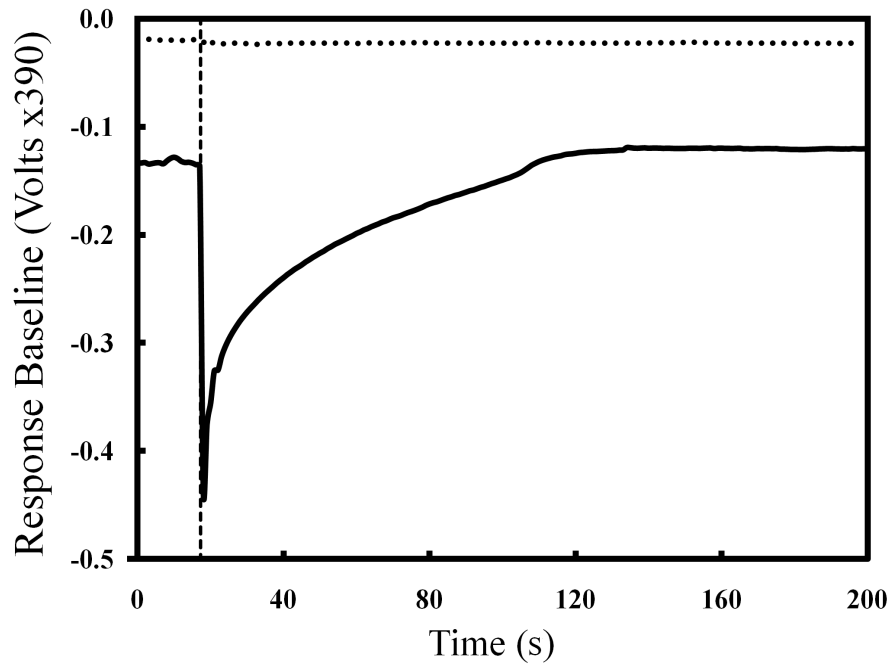


Figure 4-7 First value of the microcantilever response, indicative of the baseline temperature, measured at 1 Hz before and after 10 cP Silicone Oil is dispensed (dashed line) in a quarter bridge (solid line) and half bridge (dotted line) configuration.

A second improvement in signal drift is to apply a multilevel actuation for clotting measurements. In practice the actuation and data acquisition is started when the plasma or whole blood is mixed with the reagent. This occurs externally 4-6 seconds before being dispensed on the microcantilevers. During this initial period the microcantilevers are actuated at 10 Hz in air with a very high level. As it has already been noted, in air the heat is retained in the device and the active device warms up very quickly. The drift in signal base line is nearly 2 Volts before the level settles, with approximately 1 Volt drift within the first 5 seconds. One solution is to rebalance the device at this new level though in the standard electronics the actuation is disabled before balancing and this can take 10-20 seconds to complete.

A Wheatstone bridge balancing LabView program has been written by the author which allows balancing while pulsing by using the first value of each measurement rather than the DC level output. Unfortunately this retains the artificial temperature of the active cantilever and when the sample is dispensed onto the device a large drift is noted as the active device cools. The solution is a two stage actuation; on sample mixing the data acquisition and actuation is started at a low voltage level and on dispensing the fluid the actuation level is increased. It is important to have some level of actuation in air as this



might be used for calibration in future analysis. The low level of actuation in air limits the drift to below 0.1 Volt and therefore in future measurements the lower limits and higher accuracy can be used.

#### **4.5 Microcantilever Fluid Probe Testing in Plasma and Whole Blood**

The previous measurements in known glycerol solutions indicate that a mechanical signal can be extracted from the response, and in higher viscosity/density solutions the mechanical response is damped. For standardisation the measurement of plasma and whole blood prothrombin time are performed in an incubator at 37 °C (Grant, QBT1). This is important as rheological parameters can change with the temperature of the fluid. The measurement is first performed on blood plasma which is largely composed of water (~90%) and a variety of proteins, minerals, and trace elements. Working with whole blood is more complex as the fluid has several non-Newtonian characteristics. The percentage red cells, or haematocrit, in the fluid create more damping on the microcantilever and also have an elastic component that changes with shear flow rates, for example, at low shear flow the cells tend to clump and at high shear flow the cells elongate and can form stratified layers in the plasma [123].

In previous studies [124] the viscosity of plasma and whole blood at 37 °C for normal patients is 1.22 cP and 3.63 cP respectively which is comparable to the work with low concentration glycerol solutions. There are several further points that would make an absolute measurement of the plasma and whole blood viscosity difficult. Squeeze film damping or elastic effects may arise due to the proximity of the microcantilever to the substrate as the beam is displaced. There is also the possibility that particles could become trapped at the anchorage under the device or in the Epsilon holes thereby limiting movement. Finally, the microcantilever's curved shape and velocity profile would make shear rate calculations difficult, and as previously mentioned the mechanical and thermal properties of the microcantilever and environment can both be variable over time and temperature. These are not critical for the clotting measurements as the change is simply a relative increase in the damping and therefore no calibration or absolute measurement is required.

Plasma and whole blood clotting (PT) measurements have been conducted with citrated samples. These are samples mixed with sodium citrate or citric acid that prevent the blood from coagulating during storage. To re-activate coagulation the citrated sample is

recalcified with a reagent containing  $\text{Ca}^{2+}$  and thromboplastin (Factor III). Thromboplastin is used as the prothrombin time measurement represents the extrinsic pathway of the clotting cascade, where the tissue clotting factors in the circulatory system contact thromboplastin when damage occurs. Samples have been stored at 4 °C and are heated to 37 °C before testing. To confirm a clot during the microcantilever measurement the tilt tube method is conducted in parallel. Handling of the biological samples and manual detection of the clot has been performed by Mr Joe Booth (Microvisk), the setup and measurement is performed by Dr Vladislav Djakov and the author, and data analysis is performed by the author. The measurements are conducted using the previous actuation and sensor settings used in glycerol testing. Data is recorded using the continuously triggered data acquisition program previously used for glycerol testing. The data acquisition and a stop watch are started upon mixing of the citrated sample and reagent in a pipette to provide a zero time. The mixed sample is pipetted onto the microcantilever device and data is recorded for a further 90-120 seconds. During this testing period the microcantilever devices are re-used due to the high individual cost associated with packaging and wire bonding. A cleaning protocol is performed on each device to remove the clot and in further tests the relative measurement does not degrade.

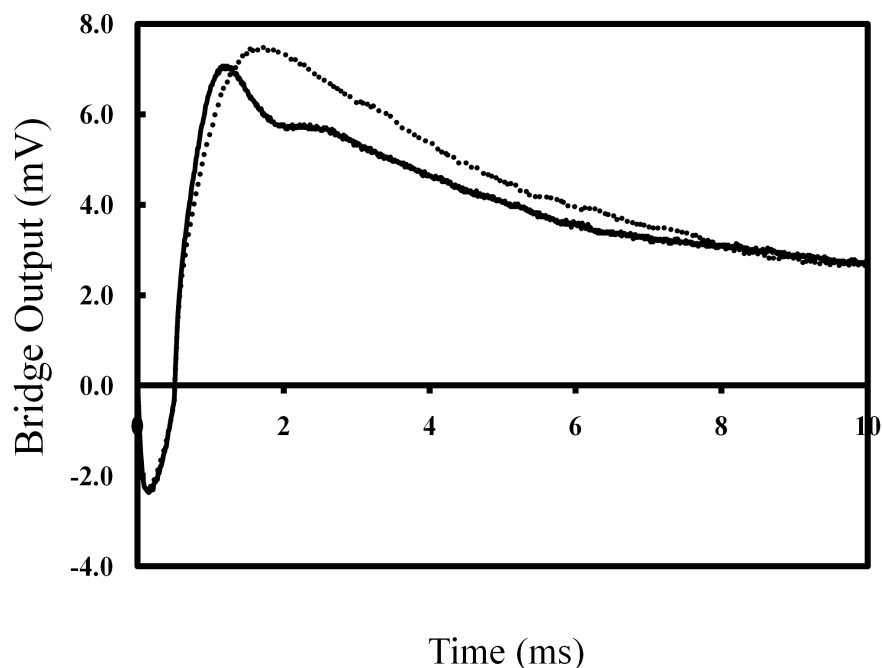


Figure 4-8 First confirmation of mechanical damping in whole blood before (solid line) and after (dotted line) clotting, measured with MV2 X device on 11/05/2007. The heater resistance is 180.7 Ohms giving a modified actuation pulse of 100  $\mu\text{J}$ .

Recording continuous data at 100 KS/s for approximately 2 minutes creates a large amount of information to analyse, where each actuation event must be selected in excel. In initial measurements, data is selected from several files representing a response before and after clotting, as shown in Figure 4-8. This processing is slow and does not indicate a true real time measurement of the clot formation. To process all information faster a LabView analysis program has been written by the author. In the first version the program allows the user to select a portion of the sensor response curve to analyse as an averaged value and gradient, and then reads in every data event and plots the factor over time.

In this preliminary analysis Dr Vladislav Djakov and the author looked at the response both during and after the actuation pulse. No discernable difference was noted during the actuation pulse time (0.5 ms) for unclotted and clotted samples but a measurable difference was found in the peak value, peak position, and the rate of the rising edge on the overshoot of the signal. The expected damped oscillator peak response as rheological properties increase is a decrease in amplitude, increase in broadness, and a shift in position to longer times. For whole blood presented in Figure 4-8 the damping of the mechanical oscillations, shift to longer times, and broadness of the peak is seen, but the overall peak height increases. This is similar to the effect seen in glycerol solution tests where the increase was attributed to a decrease in the thermal diffusion to the solution that creates more heating in the microcantilever.

To characterise these factors for analysis of the clot formation a second version of the software has been made that detects (1) the zero-to-peak value, or peak height of the measurement, (2) the peak position, and (3) the half-width at percentage maximum of the response hereafter referred to as the width measurement. The third parameter is taken as a percentage drop from the peak and towards the rising edge of the response. This is because the response tails off slowly due to the thermal cooling and therefore a full width would not be indicative of the mechanical response. The percentage drop is limited to a maximum of 40% for current devices otherwise the width measurement passes into the actuation region of the response which contains the electrical capacitive effect and therefore a high level of uncertainty.

The analysis program routine has been built into the data acquisition program for clinical measurements and is presented in the next section and can be found in [125].

The analysis works using the following steps. To find a rough first peak position the curve is smoothed using a binned average of samples, this reduces the identification of artifact peaks due to random noise and reduces the identification of the second peak as the first. A LabView peak finder routine is used and the first peak is selected. For the current data 50 points are taken around the rough peak location and a third order polynomial is fitted. This value produces optimum results otherwise the first valley and second peak create a poor curve fit. A third order polynomial is used to take account of the skew of the peak response. The polynomial is then differentiated and the zero crossing values of the equation are found. The zero crossing closest to the peak estimate is found to give our second measure, the peak position. The peak position is then placed back into the fitted polynomial equation to give the peak value. As the peak value is relative to the baseline of the measurement the peak-to-zero value, or peak height, is found using the first value. To find the width a third order polynomial is fitted between the data after the actuation turns off and the capacitive discharge occurs to just after the peak position. A peak position is found again to check the curve fit and is generally only found to differ by 0.01%. A percentage reduction in the peak-to-zero value is made and a limiting pass filter is used to find the “x” position where “y” is greater than the reduced value “ $y_0$ ”. The width is solved in this manner as finding solutions in  $y = Ax^3 + Bx^2 + Cx + D$  is difficult and time consuming to achieve. In the pass filter solution the third order polynomial is replotted with interpolated data at 0.5  $\mu$ s deviations to find a more accurate pass. The data which passes the equality  $y > y_0$  is given a zero value and data  $y < y_0$  is given a unity value. By knowing the total data points and the proportion of passed data points, the peak position minus the position on the rising edge can be deduced to give the width measurement.

A discussion of combining the factors or multiplication by a function has been made but it should be noted that each factor contains an error and combining factors or multiplying combines or increases the error, and therefore in the first case the measurement should be based on using the factors which have the highest change in mechanical signal. It should also be considered that the routine must be implemented in a final handheld device and therefore a simple measured factor is desirable.

Figure 4-9 and 4-10 shows the peak height, peak position, and width analysis of the microcantilever (W) response from each actuation pulse (10 Hz) in citrated plasma and whole blood. The width of the actuation pulse has been increased to 0.6 ms and the

energy when the microcantilever is immersed in the fluid has been maintained at 150  $\mu\text{J}$ . This reduces the peak power dissipation in the measurement from 300 mW to 250 mW. To limit the signal drift in the measurement the initial actuation in air is limited (1.0 V) and the second microcantilever is used in half-bridge configuration as an environmental temperature reference. The electronics DC response of the microcantilever is synchronised with the rising edge of the function generator trigger and writes 500 samples at a sampling rate of 100 KS/s. The electronics is set to x3900 gain and measurement limits of the DAQ card are  $\pm 5$  V.

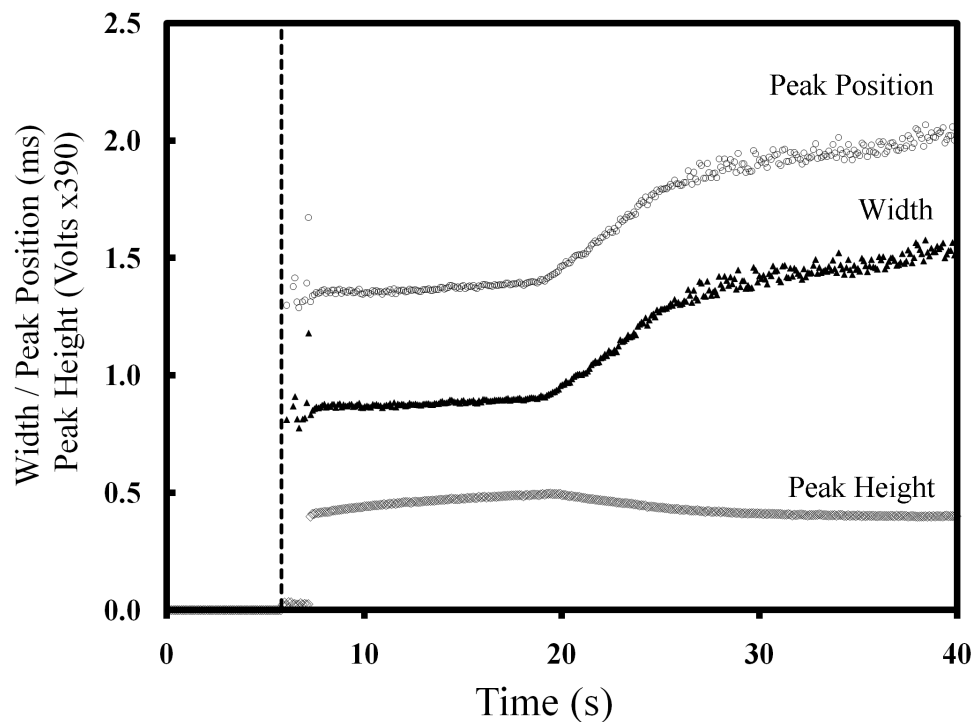


Figure 4-9 Analysis of microcantilever MV2 W response in citrated plasma sample actuated at 10 Hz with a peak pulse power of 250 mW and pulse width of 0.6 ms. The dashed line represents application of the mixed sample.

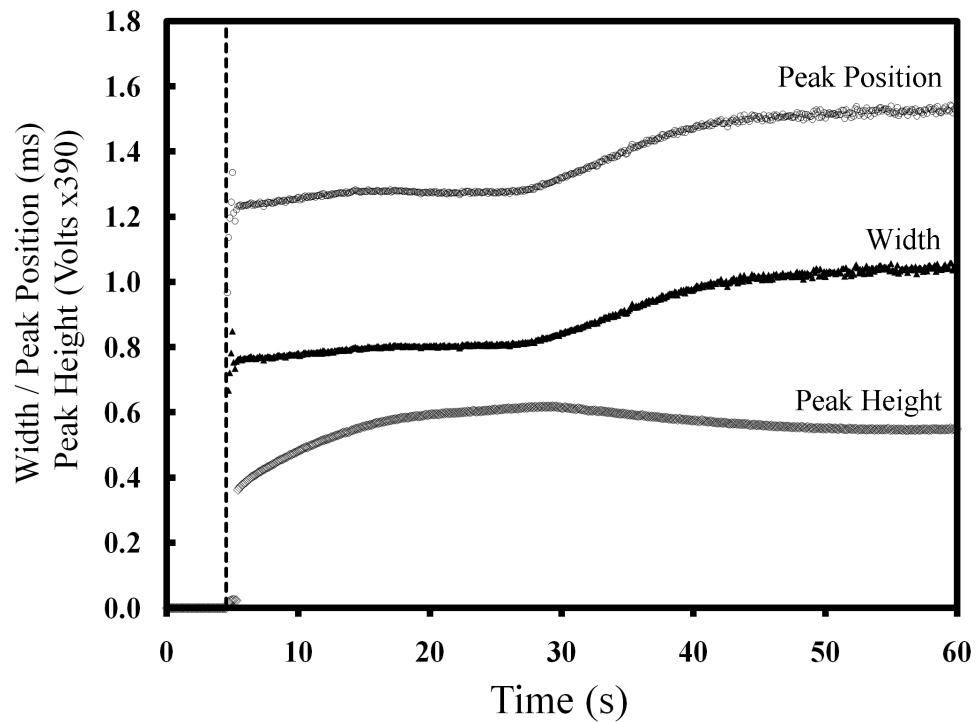


Figure 4.10 Analysis of microcantilever MV2 W response in citrated whole blood sample actuated at 10 Hz with a peak pulse power of 250 mW and pulse width of 0.6 ms. The dashed line represents application of the mixed sample

The plasma result (Figure 4-9) shows how the peak position, width, and peak height change at the clot onset (approximately 19 seconds). When normalised, the peak position and width change by an almost identical amount and increase at the same rate where as the peak height change is more subtle. Beyond the crest of the response the data becomes noisy indicated by the scatter of data points; it is believed that at this point the deflection of the microcantilever is minimal and the dominant thermal response gives more fluctuation. The peak height is not a good measure of the mechanical response in current devices, as shown in the glycerol testing, due to the association of thermal properties of the fluid and retained temperature on the sensor. For whole blood (Figure 4-10) measurements the initial mechanical deflection is further damped due to the haematocrit, or percentage of red blood cells, of the sample. From the initial baseline measurement the peak position and width change is again almost identical though the absolute change is almost half of that compared to plasma measurements. The peak height measurement shows a large drift over the first part of the experiment and a minimal change at the clot onset. The drift in both fluids could signify either the beam moving more freely in the mixture, for example, the polymer becomes more

pliant, or the fluid has less thermal diffusivity which could be a consequence of the fluid kinetics.

#### **4.6 Clinical Evaluation at The Royal London Hospital**

A clinical evaluation was conducted at The Royal London Hospital Haemostasis Laboratory during the period 2<sup>nd</sup> – 5<sup>th</sup> of July 2007 to evaluate and calibrate the performance of the microcantilever coagulometer and biochemistry against a standard laboratory analyser (Sysmex CA7000). For evaluation of the microcantilever sensors an estimate of the prothrombin time (PT) and the World Health Organization recommended International Normalized Ratio (INR) is made from patient whole blood and plasma with a wide range of clotting times. This required collection of raw data and development of an automated reduction and analysis method to provide a single PT and INR value from each sample. The calibration of PT for the microcantilever sensor and thromboplastin combination is made against the laboratory analyser to give the International Sensitivity Index (ISI) and Mean Normal Prothrombin Time (MNPT). This calibration is required due to the variability of clot formation and detection technique for different combinations of analyser and reagents. The ISI value specifies the sensitivity of the reagent to an internationally standardised sample and the MNPT is calculated from a range of normal PT times from non medicated patients; essentially this is the PT time for a sample INR of unity. The ISI and MNPT normalise the combination of reagent and detection method and return the measured PT as INR values which are then clinically relevant for monitoring oral anticoagulant therapy.

##### **4.6.1 Preceding the Clinical Evaluation**

The work preceding the trial, including the microcantilever testing presented in Chapter 3, has identified the Epsilon design and tapered heaters as the preferential microcantilever choice for the clinical trial. To increase the number of devices available for the trial the X and W design is complemented by the S design which is identical to W (Epsilon and standard heaters) but the sensor only has 1 meander rather than 3. This should not influence the sensitivity  $\Delta R/R$ , but the absolute change in resistance  $\Delta R$  will be lower. In preparation Dr Vladislav Djakov has applied a non-corrosive silicone rubber (RS, part #RS494-118) surrounding the active microcantilevers to prevent contact of fluid samples with the electrical contacts. Prior to the clinical evaluation the author has significantly improved the data acquisition and analysis software to make efficient use of the limited time available on the trial. The aim of the software was to

provide a complete and easy to use interface for senior clinical scientist Mr Joe Booth (Microvisk) as the author and Dr Vladislav Djakov were not present during the evaluation. Figure 4-11 shows the front panel interface of the LabView software and data flow diagram. The full programming can be found in [125] and a brief description is given below. The data collection and analysis processing system has been solely developed by the author.

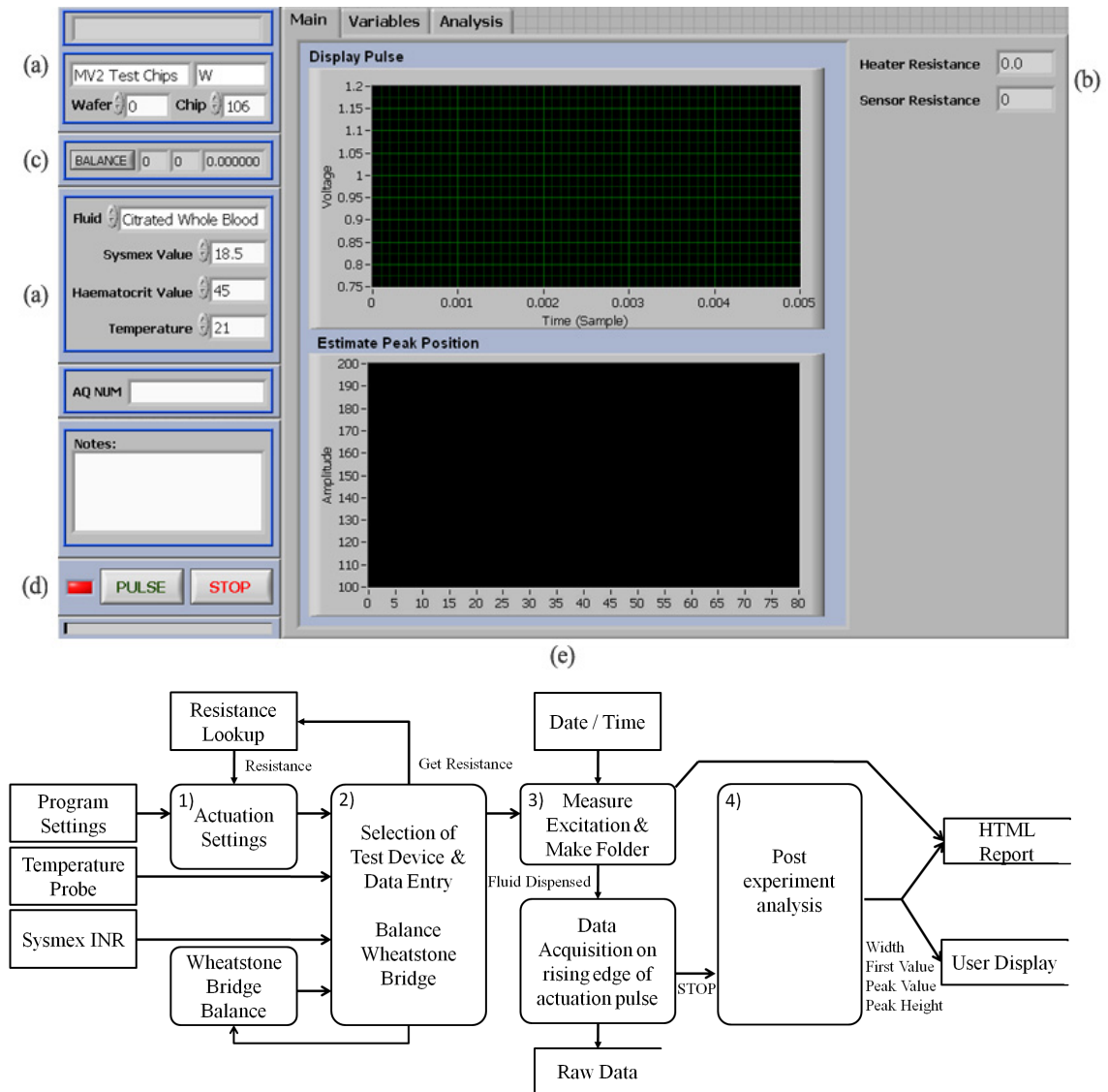


Figure 4-11 LabView program front panel used during the clinical evaluation and data flow diagram. (a) Data entry sections. (b) Device lookup resistance. (c) Null offset compensation of Wheatstone bridge. (d) Start and stop program – LED indicates whether the measurement can be started. (e) Plot of raw microcantilever response and the peak position as the measurement is taken.



The programming has been divided into four sections; a program initialisation; data entry and device setup; data acquisition; and data analysis and report generation. The first section reads in the default program settings from a text file allowing updates on best operation to be exchanged between Microvisk locations. The default program settings include the data acquisition settings (analog input channel, input voltage limits, data sampling rate, samples to read, and data trigger), function generator settings (pulse type, nominal voltage and load, pulse width or duty cycle) and now includes control of the third party electronics (input channel select, gain setting, and null offset circuitry). The channel and gain select are controlled using two sets of direct digital lines that allow an address of 00, 01, 10, and 11 to be used for selectable channel (Ch1 – Half Bridge, Ch2 – Half Bridge, Ch3 - Unused, Ch4 - Unused) and gain (x39, x390, x3900, x39000).

The null offsetting is controlled using an SPI interface (Clock, Sync, and Data digital lines) that is daisy chained to a rough and fine balance digital potentiometer for each channel. When Synced the negative edge of the Clock signal shifts each Data bit into the data-in pin. The first bit is the address, either '0' for the rough potentiometer or '1' for the fine potentiometer, followed by an 8-bit word (0-255) to set the resistance. As the potentiometers are daisy chained the code is loaded in sequence from channel 4 to 1 such that in total a 36 digit code is sent. The SPI interface uses inverse logic so every data bit is also inversed e.g. the address of the rough potentiometer becomes '0'. The second part of the initialisation loads in text data for device designation, fluid list, and the measurement I/O channels. All information is loaded from a text document which allows simple changes to be made outside the program and future proofs against introduction of further microcantilever devices. The measurement channels can be set using a separate VI which allows a new setup on a different computer to be reconfigured. The VI is used to set the USB channel for VISA communication; digital lines for selection of gain, channel, and SPI interface to the digital potentiometers; and analog input channels from the electronics including a Wheatstone bridge excitation measurement channel and trigger input.

The second part of the program is for data entry and measurement setup. This is to document every test and allow further analysis between devices beyond the clinical trial. The device and fluid data entry (Figure 4-11a) works on a number of populated drop-down menus that allow quick selection. The incubator temperature, patient sample

number, calibrated Sysmex INR value for the sample, and where available the haematocrit are also recorded. Any further details can be recorded in the notes section. A further module has been built into the software called “get resistance”; this is linked to a spreadsheet document which contains the heater and sensor resistance values of every prepared device. When a device is chosen the module gets the resistance from the spreadsheet and also calculates the actuation based on this figure (Figure 4-11b). The device setup includes balancing the Wheatstone bridge for null offset compensation using the SPI interface. On the front panel the balance button initiates a number of SubVI's to firstly balance the rough potentiometer and then the fine potentiometer (Figure 4-11c). This is done by starting at the central resistance of the digital potentiometer and taking a DC reading, the digital code then moves to minimise the DC output as close to zero as possible. If the balanced bridge output voltage is greater than  $\pm 0.2$  Volts an error message is displayed to the user acting as a first level of quality control. The experiment can only be started when all the data has been entered and the chip has been satisfactorily balanced, otherwise a message is sent back to the user directing them to complete a number of tasks first.

The third part of the program is the data acquisition. When the Pulse button (figure 4-11d) is first pressed a Wheatstone bridge excitation measurement is made, the saved data location is set, and the lower actuation voltage (1V) is sent to the function generator. The file destination is constructed from the design prefix, cantilever subset, and chip reference (e.g. MV2-W-103). This allows a user to search specifically in one design or subset, and on one specific chip or fluid. If a folder already exists for a device in the same fluid the folder is given an integer value, this way the old data is not rewritten or deleted. An information file is also created to accompany the data files and create the final reports. The time/date and experiment details are recorded along with the data acquisition parameters, electronics, and function generator settings. This allows specific information to be extracted when the data files are analysed. The microcantilever response is recorded on the rising edge of a trigger signal synced with the function generator actuation pulse and records for a limited number of samples. This reduces the volume of data that is written to each file limiting issues with hard drive writing speed and minimising extra data analysis steps. Each sample is written as a 6 decimal place double precision integer and recorded with sample time to a LabView Measurement file. Each file contains 10 pulses of data to limit the computer creating new measurement files on each pulse. The time recorded in the file is based on the

operating system internal clock which can give inaccurate readings for the start of the pulse, though this is much smaller than the time between pulses (100 ms). An assumption of 10 Hz operation can be a problem if the PC hangs and the trigger is missed due to interrupt requests from programs which have not been closed down (e.g. virus checkers, disk clean tools, wireless network tools). When the user dispenses the fluid onto the device a second Pulse button press initiates the higher actuation voltage to achieve 150  $\mu$ J pulse energy. During the data acquisition the raw sensor response is displayed in the top window and the estimated peak position, using position of maximum value, is shown in the bottom window (Figure 4-11e). This allows the user to monitor whether the cantilever is working and estimate whether the curve is changing. When the user is satisfied that the experiment is finished the stop button initiates the final part of the program.

The fourth part of the program initiates the analysis of the response automatically. This analysis has been described in chapter 4.5. The analysis extracts the first value of each pulse (to monitor the thermal drift), the peak position, peak value, and width measurement. These measurements are shown to the user allowing an immediate feedback on the progress of the clinical evaluation. The final part of the program creates an automatic report with the experiment information and plotted variables. Unfortunately during the trial, though the trend of the curves could be seen the time axis was skewed due to the program mishandling of the time array. This required the data to be replotted from the recorded raw data after the clinical evaluation.

Prior to the clinical tests at The Royal London Hospital, ethical approval has been sought by Professor John Pasi and Microvisk for testing of patient samples on the microcantilever blood coagulometer. The initial stage is an agreement between Microvisk and the clinical partner to perform the tests and a trial protocol document. The protocol documents the testing, including; the purpose of the project; how the results might be applied; the method/design of the study; inclusion and exclusion of subjects to the study; what data is to be collected and what is to be measured; how the data is processed and analysed. The protocol also contains patient information sheets and consent forms though in the Microvisk evaluation the blood samples were destined for destruction (samples had already been tested elsewhere) and were consented by the patients. Once the protocol is accepted by the Trust R&D committee an IRAS (Integrated Research Application System) application must be submitted. This is a

document where everything about the clinical testing is described. Once complete it is submitted to an ethics committee. The ethics committee questions the study and passes a decision to reject or approve the tests. Once ethics approval is granted the IRAS application passes back to the Trust R&D committee for final approval and the study can start.

#### **4.6.2 During the Clinical Evaluation**

The clinical evaluation has been conducted onsite by Mr Joe Booth (Microvisk Senior Clinical Scientist) and Prof. Gareth Jones (Microvisk Consultant) with support from Prof. John Pasi (Professor of Haemostasis and Thrombosis), Ms. Kathryn Langley (Chief Biomedical Scientist), Mr. Chris Dale (Senior Specialist Biomedical Scientist), and Mr. Shaun Bevan (Trainee Clinical Scientist) at The Royal London Hospital. The original PC, monitor and internal PCI data acquisition card has been replaced with a laptop and PCMCIA data acquisition card (E-Series, NI-6036E). The National Instruments E-Series card has 16-bit resolution and a maximum sampling rate of 200 KS/s. The absolute accuracy in the recorded data is 152  $\mu$ V which corresponds to an unamplified signal of 40 nV. Figure 4-12 illustrates the experimental setup used in the clinical evaluation and a close-up of the machined block heater and test device.

Mr Joe Booth has prepared the incubator and liquid handling for the evaluation including the treatment of the device to minimise bubbles and sample preparation. A Grant QBT2 Block Heater has been machined to hold the microsystems microcantilever electronics, four Gilson D200 pipette tips and four Eppendorf tubes. Compressed aluminium foil is used to fill the void space in the heater block around the electronics ZIF socket and a removable lid has been implemented to retain heat. A temperature probe (-50 to 200 °C) is inserted into the ZIF and monitored and recorded using a digital thermometer (Tenma 72-2060). The heater is switched on at the beginning of each day of the trial to reach a stable temperature of 37 °C.

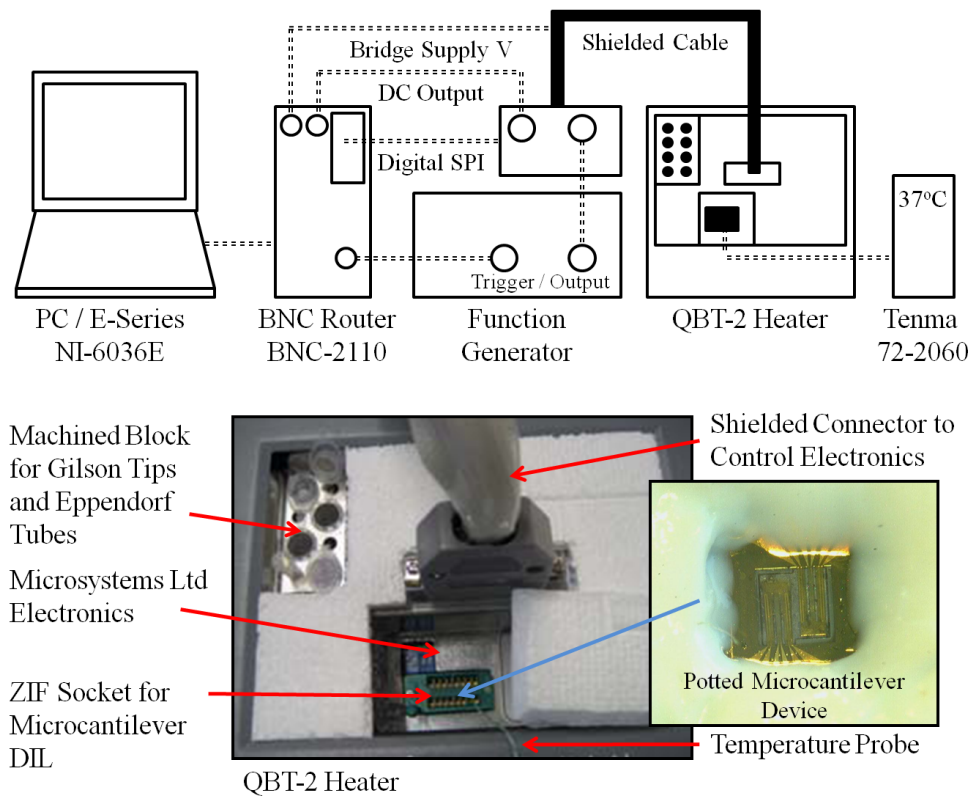


Figure 4-12 Experimental setup used in the clinical evaluation.

Each patient citrated blood sample has been previously tested on one of three calibrated laboratory Sysmex CA-7000 coagulometers. The Sysmex CA-7000 is an automated coagulation analyser that uses an optical detection of fibrin formation in a cuvette. The same thromboplastin reagent used in the analyser has been used with the microcantilever measurement device. The reagent was prepared on the first day of the trial and stored at 2-8 °C over night. Patient blood samples for the trial ranged from 0.9 to 6.08 INR on the Sysmex analyser and recorded haematocrit levels between 27% and 52.5%. For each test the Sysmex INR and haematocrit is recorded with the patient number and sex of the patient. To prepare for each test the chosen patient sample tube is inverted a number of times to ensure resuspension of the red cells and 100  $\mu$ l is pipetted into an Eppendorf tube in the block heater. The reagent is also pipetted into an Eppendorf tube and placed in the block heater to warm up.

For the clinical evaluation the energy of the actuation pulse when the microcantilever is immersed in the fluid has been set at 150  $\mu$ J, the width of the pulse is set to 0.6 ms, and the actuation frequency is 10 Hz, as in pre-trial whole blood and plasma testing. The chosen pulse corresponds to a peak power dissipation of 250 mW though this can not be achieved in higher resistance tapered heaters due to the limited electronics driver as

shown in section 4.2. For X devices used in the trial this clipping reduces the pulse energy to 100 - 140  $\mu\text{J}$  (170 - 230 mW) for the range of resistance measured. The initial actuation in air is 1.0 V and the second microcantilever is used as an environmental temperature reference to limit signal drift. The DC response of the microcantilever is synchronised with the rising edge of the function generator trigger and writes 500 samples at a sampling rate of 100 KS/s. The electronics is set to x3900 gain and measurement limits of the DAQ card are  $\pm 5$  V.

For each test a microcantilever device and patient sample was selected and recorded in the LabView software. When ready the Wheatstone bridge is balanced through the software and the reagent, air gap, and blood sample is drawn into a pipette (Gilson Concept C100 programmable pipette). The sample mix in the pipette is initiated and the operator signals the activation of the LabView program to start recording data in air. After a 4-6 second delay the reagent / sample mix is pipetted on the active area of the microcantilever and the operator signals the activation of the higher actuation pulses. Microcantilever response and position of maximum is monitored throughout the test to confirm expected operation and judge the end of the measurement. After each test, the microcantilever device is removed and a cleaning protocol is used to remove the clot, wash, and dry the device. After the cleaning protocol the device is inspected under a microscope and the surface is treated again to minimise bubbles.

In total, 154 tests were attempted over a four day period yielding 96 whole blood clotting results and 3 plasma results. The testing strategy was to allow a measurement of the accuracy and regression of the device against the calibrated Sysmex analyser, and therefore to conduct tests across the range of INR samples available, and to measure the reproducibility on a single device using the same sample. 31 tests were rejected before dispensing the sample when the Wheatstone bridge rough balance code was less than 125 or greater than 131 as the sensor output would fall out of range ( $\pm 5\text{V}$ ) during the test. The digital potentiometer has an 8-bit code between 0 and 255, if the cantilever active and reference resistance is perfectly equal the balance will be in the centre. 7 tests were rejected due to operator error either in liquid handling, software operation, or in one case testing of a sample without a Sysmex INR value. 17 tests were rejected due to being insensitive to the post analysis method predominantly due to very high noise in the measurement. This included 5 tests identified as very noisy response during the test, 5 tests where a second higher peak is observed and the width measurement fails, and 7

tests where no appreciable change occurs or the analysis identifies a residual artefact as the clotting point – this occurred once and the test was performed again.

#### 4.6.3 Data Reduction and Analysis

The aim of the microcantilever response analysis is to provide a consistent and automated method for converting each test into a single clotting time result. Data reduction and analysis has been performed by the author (data reduction), Prof. Gareth Jones (data filtering), and Mr Joseph Booth (regression solver). The blood response has been shown in section 4.4 and has been quantified by the author using the half width at 40% maximum, here in referred to as “width” measurement. The width measurement yields a curve response against time and though visually a clot onset “elbow” can be seen in the data this must be identified using a more consistent scientific approach. Figure 4-13 shows the width against time for two tests, indicating typical good data and bad data. All sets of good and bad data are included in the post-analysis; measurements are only rejected if they fail the analysis as described in the previous section. Ideally it is desirable that the response is completely flat and produces a sharp angle at the clot onset point, but there are thermal artifacts in the data that cause the data to drift and also to initially find a baseline steady state.

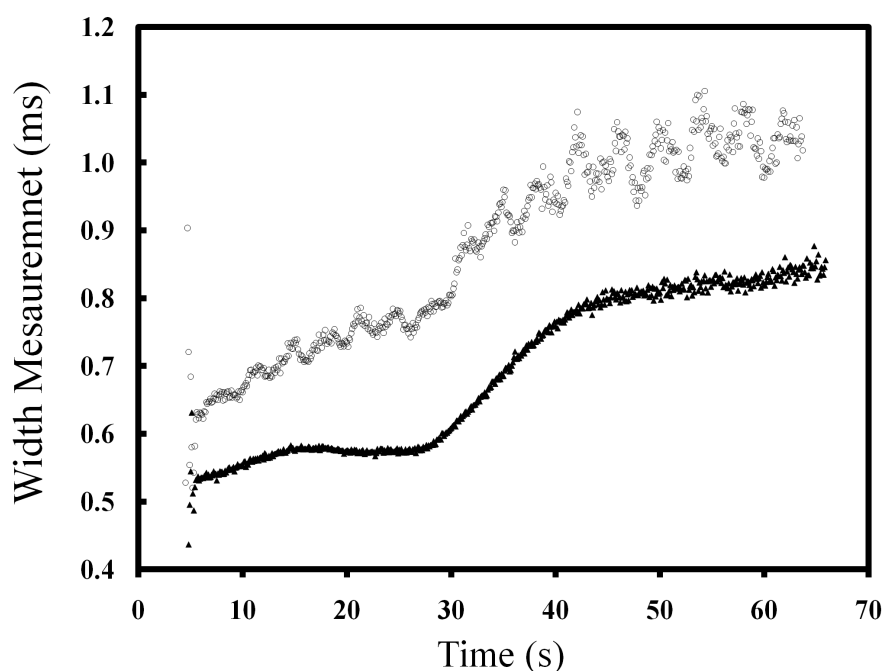


Figure 4-13 Typical good output (bottom) of analysed response for a whole blood clot (Chip W106 CWB5) and bad output (top) of analysed response (W103 CWB5).

The bad data shows oscillations in the data at various frequencies though this is not unexpected as the device is at a breadboard stage and not fully shielded. It is anticipated the electrical, electromagnetic, and mechanical vibrations may all affect the response at this stage. Prof Gareth Jones has implemented a Fourier filtering routine using a cosine function rather than a sharp cut-off or pass filter to smooth the transition data of the clot onset. The central data is filtered in frequency space using an extended time centered Hann window of the form

$$W(n) = \cos^{2s}\left(\frac{\pi n}{N}\right) = \left[0.5 + 0.5 \cos\left(\frac{2\pi n}{N}\right)\right]^s \quad (4.1)$$

where  $s$  is a single adjustable parameter giving the narrowness of the function ( $S = 1$  is the original von Hann filter),  $n$  equal to frequency in the frequency domain, and  $N$  is the total number of data points used in a centered data set (typically an integer power of 2). For the central filtering  $s = 200$  and  $N = 2048$ . A Hann window was also used to add wings to the data 6.4 seconds at the beginning ( $s = 0.5$ ) and for the last 12.8 seconds ( $s = 1$ ) to ensure the data started and ended with a zero value and had a smooth transition into the data. Figure 4-14 shows the data before and after the filtering

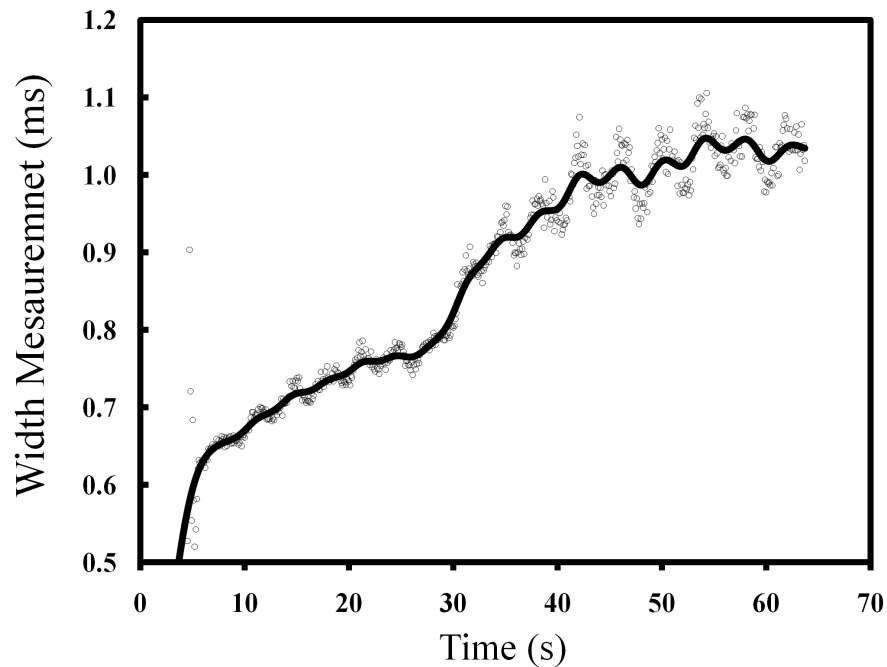


Figure 4-14 Bad data indicated in Figure 4-12 (W103 CWB5) before (circle) filtering and the response after Fourier filtering with a cosine function (solid line).



The filtered data is passed on to a slope fitting routine to identify the “elbow” of the clot onset. The simplest description of the elbow is to find the intersection of two best fit straight lines fitted before and after the clot onset. Data before blood is dispensed and the top 20% of the remaining normalised data is rejected. Data long after the clot should be treated as very low signal to noise as it is expected that upon clotting the mechanical motion of the microcantilever is damped to near zero and the residual signal is fluctuating thermal measurements. The analysis routine firstly establishes a rough find on the Fourier filtered width data with an initial estimate of the intersection at the centre of the data window. Excel solver moves the intersection point to minimise the sum of the square of the residuals for slope, intercept, and the intersection. The rough intersection estimate is used to extract a narrower data window 15 seconds either side from the raw width data. The top 20% of the normalised data is again removed. Excel solver again returns an intersection value from minimisation of the sum of the squares of the residuals for slope, intercept, and intersection. The measured intersection point is recorded as the sample clot time. Figure 4-15 shows the regression fit to the raw width data of a single whole blood test where the intersection is taken as the clotting time.

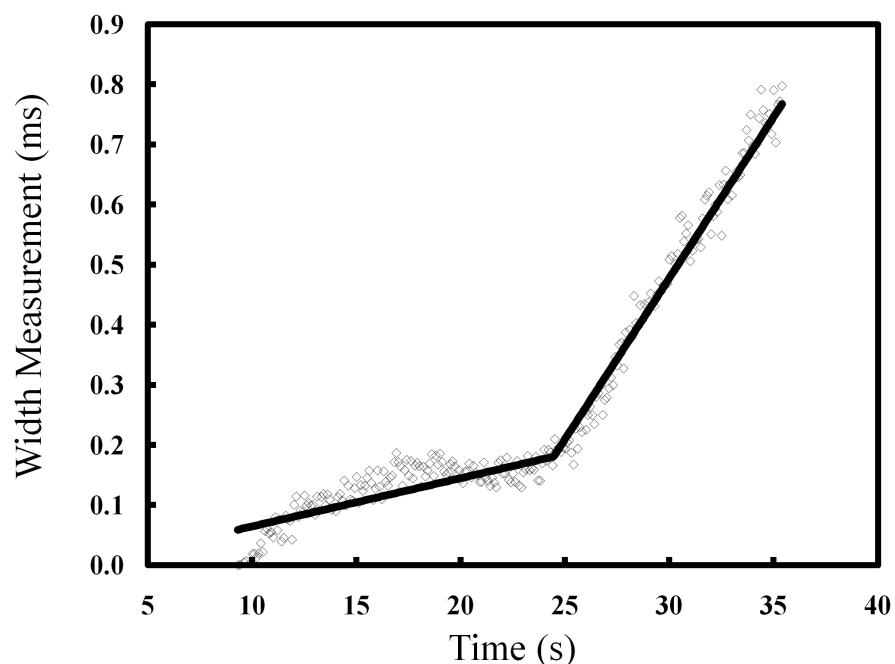


Figure 4-15 Plot of the intersection position of two straight lines fitted to the raw width data where residuals of the slope and intercept are minimised. The intersection position found in the raw data is deemed to be the prothrombin time.

#### 4.6.4 Prothrombin Time (PT) Results and Discussion

Figure 4-16 shows the combined microcantilever PT clotting results for W and X devices against the Sysmex PT analyser results for 87 tests. Nine tests from the S design are not included as the data analysis was not consistent and subsequently the device was dropped from the trial. The combined and individual PT results show excellent correlation ( $r > 0.98$ ), to the standard Sysmex analysers. To quantify clinical variation in the measurement the mean percentage coefficient of variation (%CV) has been calculated as 5.91%. The %CV is equal to the average of standard deviation divided by the mean where replicates of a known sample were tested at least 3 times ( $n=64$ ). The Microvisk team regards these figures as excellent for a device at this stage of development. The gradient of the individual device and combined linear regression is 1.87, indicating a possible under activity of thromboplastin in the microcantilever trial chemistry. This is most likely due to testing with whole blood samples whereas the Sysmex analyser tests plasma samples [126].

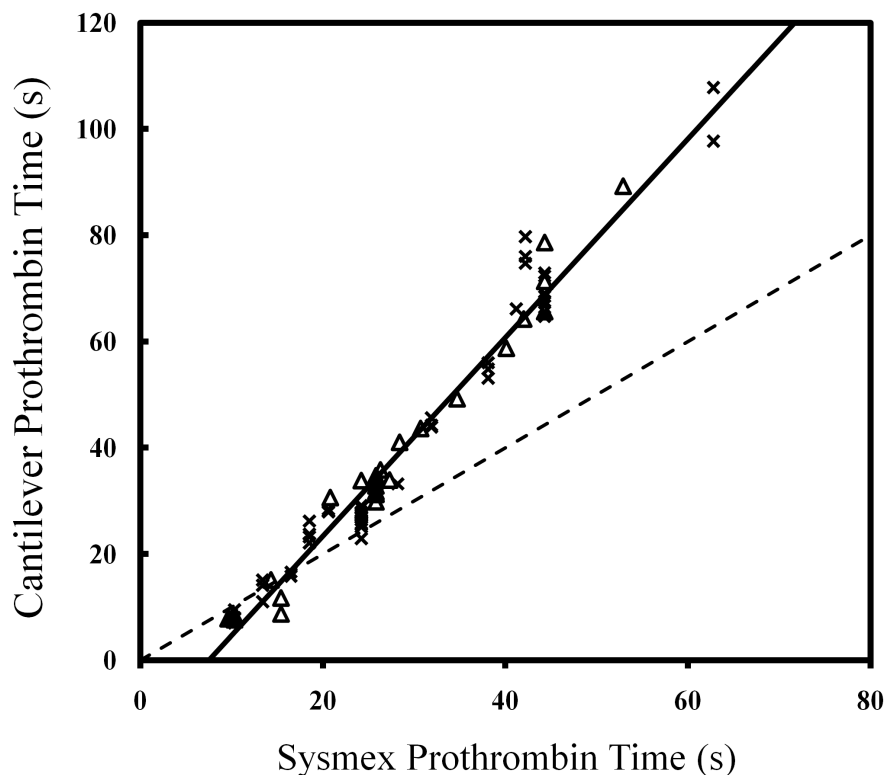


Figure 4-16 Combined PT clotting results for W (cross) and X (triangle) microcantilever devices against the Sysmex analyser sample results. The dashed line represents the position where the Sysmex and Microcantilever PT would be equal.

The Sysmex analyser always tests with plasma to thromboplastin ratio of 1:2 but for the same whole blood volume the plasma is reduced by the fraction of red cells, for example, a haematocrit of 40% would give a ratio of 0.6:2. This is confirmed in the whole blood and plasma results of a single patient sample from the trial. The average PT measured on a W device in four whole blood replicates is 23.8 seconds and in two plasma replicates is 17.9, compared to the Sysmex analyser result of 18.5 seconds. It is important to note that the PT correlation remains excellent in the microcantilever whole blood testing, indicating valuable use in the haematocrit range tested (27%-52.5%). The device and combined regression has a negative intercept indicating a technique bias and possible systematic error in the measurement. This would suggest that the microcantilever device is unable to measure a clot below the 'x' axis intercept – a Sysmex PT of 7.5 seconds. Using equation 4.2 and the International Sensitivity Index (ISI) and Mean Normal Prothrombin Time (MNPT) supplied by the laboratory for the Sysmex analyser this accounts for an INR < 0.7. This result is unlikely to occur and in such cases where INR < 0.75 the result is deemed to be 'activated' by the laboratory and the sample is retested using the tilt tube method.

A technique bias exists between different analysers and the determination of the PT result from the clotting curve. The microcantilever device measures the physical onset of the clot whereas the Sysmex might identify a point later in the clotting curve, for example, as a percentage increase above the baseline or the end point of the clot. As the regression has high correlation a possible fixed systematic error may also be present in the measuring system that is giving artificially low results. One error identified was a short fixed delay (<1s) in the pulse activation due to LabView preparing the file structures and directories, this would give a missing time at the beginning of the test. It is also possible that in the chemical handling the thromboplastin taken into the pipette before the air gap lines the pipette tube and the blood sample starts to react with the thromboplastin left at the tip. More variation in the results might be expected if this was the case as the time from taking up the blood sample to the mix stage is not fixed. It is unclear how the surface activation and cleaning of devices may affect the coagulation reagents, particularly the plasma membranes in which the thromboplastin is embedded [127]. The final aspect is the unknown temperature on the microcantilever surface and local environment; this may give a higher steady state temperature in the sample and increase the activity, therefore shortening the clotting time.

#### 4.6.5 ISI and MNPT Calibration Results and Discussion

Technique and chemistry variation discussed in the previous section confirm the need for calibration and standardisation as set out by the World Health Organisation (WHO) specification [128]. The basis of the calibration is to provide a common scale, known as the International Normalized Ratio (INR), for combinations of thromboplastin and coagulometer. This provides consistency in adjusting oral anti-coagulant medication for patients. To adjust Microcantilever PT measurements into clinically relevant INR measurements the International Sensitivity Index (ISI) and Mean Normal Prothrombin Time (MNPT) for the microcantilever coagulometer is calibrated against the known Sysmex Analyser results using the equation

$$INR_{sysmex} = \left( \frac{PT_{mcr}}{MNPT_{mcr}} \right)^{ISI_{mcr}} \quad (4.2)$$

The microcantilever technique ISI and MNPT were calibrated by orthogonal regression against the Sysmex analyser INR values using the natural logarithm of PT versus the natural logarithm of INR (equation 4.3)

$$\ln(PT_{mcr}) = \frac{1}{ISI_{mcr}} \ln(INR_{sysmex}) + \ln(MNPT_{mcr}) \quad (4.3)$$

The microcantilever technique ISI is equal to the inverse of the gradient and the MNPT is equal to the inverse natural logarithm of the intercept. For statistical evaluation of the microcantilever technique ISI and MNPT the WHO specification states “*INRs outside the 1.5 – 4.5 range shall be excluded*” and “*Any samples with a perpendicular distance greater than 3 residual standard deviations from the regression line should be excluded*”. From the 87 experimental results, 21 samples are excluded outside the INR range, and 8 samples are excluded outside 3 residual standard deviations from the regression line. The samples are only excluded for the calibration and not from the final INR measurements. The exclusion of these samples does not affect the clinical use outside of the 1.5 – 4.5 INR range.

The combined microcantilever PT results calibrated against the known Sysmex INR give an ISI equal to 0.673 and a MNPT of 8.08. The ISI of the combined and individual device result is lower than the target thromboplastin ISI of 1.00 though this is expected

due to the high gradient of the PT results and the reasons described above. The ISI and MNPT constants are applied to the microcantilever PT times to give an INR result for each patient sample tested using equation 4.2.

#### 4.6.6 INR Results and Discussion

Figure 4-17 shows the combined INR results for the microcantilever coagulation test against the Sysmex Analyser INR results. The Sysmex INR values have been calculated using the ISI and MNPT specific to each analyser therefore reducing the inter-analyser variability in PT values and increasing the correlation to the microcantilever test. As the microcantilever coagulometer INR is calibrated against the Sysmex INR the correlation is expected to have a low offset and a gradient close to unity.

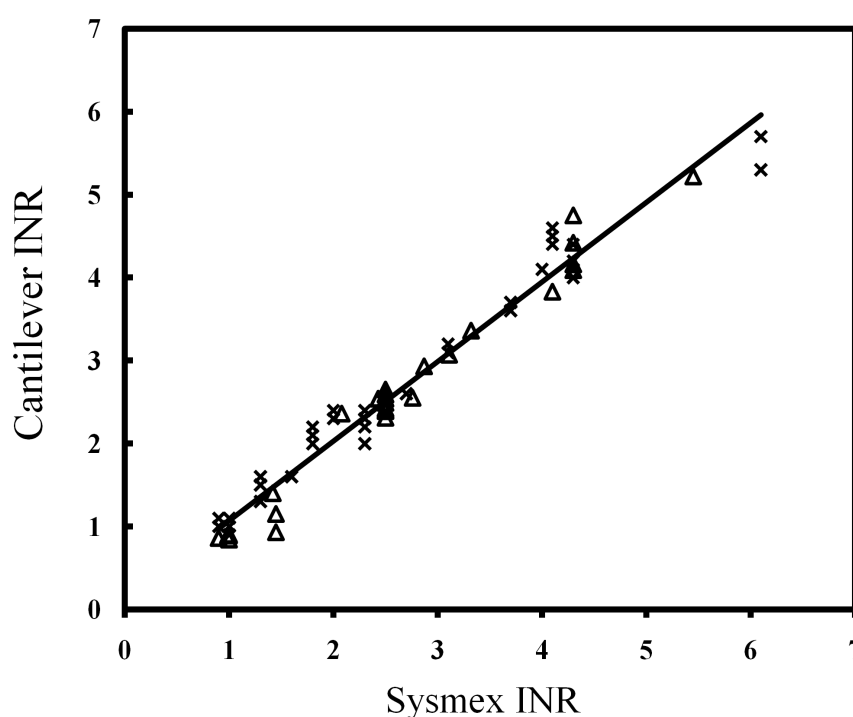


Figure 4-17 Combined INR results for W (cross) and X (triangle) microcantilever devices against the Sysmex analyser results.

The accuracy of the Microcantilever fluid probe device measured as the correlation of the linear regression against the reference INR is equal to 0.987 (n=87 sample tests). The precision of the device measured as the percentage coefficient of variation (%CV), excluding patient samples tested < 3 times, is equal to 4.00% (n=64). The fall in %CV for INR from the PT results is expected with the calibrated ISI. The %CV of the INR results should approximate to the %CV of the PT results multiplied by the ISI [129], for

example, PT %CV (5.91%) x ISI (0.673) = 3.98%. The final result is excellent compared to currently available point-of-care PT/INR testing.

The Roche Coaguchek XS has a published accuracy of 0.974 against a reference of Innovin thromboplastin on a Sysmex analyser, and a %CV of 5.19 [130]. The Hemosense INRatio has a published accuracy of 0.93 against a reference of Innovin on a MLA Electra 900c analyser, and a %CV of 10 [131]. The ITC Protime 3 has a published accuracy of 0.93 against a reference of Innovin on a MLA Electra 900 analyser, and a %CV of 10 [132].

In independent testing by the NHS Department of Health Evaluation Centre against a Sysmex CA-7000 analyser with Innovin thromboplastin the measured accuracy of the instruments is 0.97 for the Coaguchek XS [133], 0.94 for the INratio [134] and 0.69 for the Protime 3 [135]. INR Measurements > 0.5 and > 1.0 against the reference result respectively were 10% and 0% for the Coaguchek XS [133], 16.1% and 1.6% for the INratio [134], and 33% and 6% for the ProTime 3 [135]. By comparison the Microvisk INR results > 0.5 INR from the Sysmex CA-7000 result in this study is only 2.3%, and those > 1.0 INR is 0%. It was also noted in the reports that the failure rate of the INratio device was quite high (20%) as was the ProTime 3 (10%), The Coaguchek was very low (1%). The Microcantilever device failure rate during the trial was quite high (18%) though this is at a pre-development stage and predominantly was the failure of the analysis to cope with noise in the measurement setup.

| Coagulometer                 | Accuracy | Measured INR<br>> 0.5 from<br>correct value | Measured INR<br>> 1.0 from<br>correct value | Failure Rate |
|------------------------------|----------|---|---|--------------|
| Roche<br>Coaguchek XS        | 0.97     | 10%   | 0%  | 1%           |
| Hemosense<br>INRatio         | 0.94     | 16.1%                                       | 1.6%  | 20%          |
| ITC<br>Protime 3             | 0.69     | 33%   | 6%  | 10%          |
| Microvisk<br>Microcantilever | 0.99     | 2.3%  | 0%  | 18%          |

Table 4-3 Summary of PT/INR coagulometer evaluation by the NHS Department of Health Evaluation Centre and the Microvisk MEMS based coagulometer in this study.

Repetition of 8 tests on a single device (W103) using the same patient sample (Sysmex INR = 2.3) gave good reproducibility with a measured INR in the range 2.2 to 2.4, a mean of 2.29 and standard deviation of 0.06 (%CV of 2.8). For 17 tests on the same patient sample (Sysmex INR = 2.3) across different devices the measured INR was in the range 2.0 to 2.4, with a mean of 2.26 and standard deviation of 0.09 (%CV of 4.1). These individual results are very promising at the current development stage. Tighter quality control in the final device is likely to further reduce the chip variation. It is also important to note that the target INR will be in a therapeutic range and dosing will be discrete. For example, for warfarin therapy the target INR range might be 2.0 – 3.0 and to achieve this, the dose will be given as multiples of 1 mg tablets. Certainly the results from the clinical evaluation show that the microcantilever fluid probe device is more than capable to be used in this therapy.

## Chapter 5 – Conclusions and Future Work

The clinical evaluation conducted at The Royal London Hospital to measure the accuracy and precision of prothrombin time (PT) and international normalized ratio (INR) measurements using the microcantilever fluid probe has shown excellent results. The correlation against the standard laboratory analyser INR, from a wide range of patient clotting times (INR 0.9-6.08) is equal to 0.987 (n=87) and precision of the device measured as the percentage coefficient of variation, excluding patient samples tested < 3 times, is equal to 4.00% (n=64). These results are excellent when compared to currently available point-of-care PT/INR devices from Roche (Coaguchek XS accuracy 0.974 and %CV 5.19 [130]), Hemosense (INRatio accuracy 0.93 and %CV of 10 [131]), and ITC (ProTime 3 accuracy of 0.93 and %CV of 10 [132]).

The repeatability for a single patient sample (INR = 2.3) tested 17 times over 4 devices under identical conditions and procedure was also excellent with a mean INR of 2.26 and standard deviation of 0.09. The reproducibility on a single device using the same sample 8 times also gave excellent INR results in the range 2.2 to 2.4 with a mean of 2.29 and standard deviation of 0.06. These results are very promising considering the device was largely unoptimised, for example, the Wheatstone bridge supply voltage had not been investigated, an incorrect optimisation of the actuation pulse has been used, no electrical or vibrational shielding was applied to the interface, and the electronics had been designed to operate over a broad number of devices. Certainly an area to improve is the current device failure rate, though the devices have always been intended to be disposable after one test and not repeatedly handled and cleaned as in the evaluation. The key significance of the result is that a physical mechanical measure of the clot, rather than an indicative chemical measurement, looks to be very reproducible and accurate.

Professor John Pasi at The Royal London Hospital regards the results as “*very promising, robust and equally provides us with the opportunity to look forward for other significant applications within coagulation, to produce novel systems and more rapid ways of assessing coagulation based on this unique technology*”. The support letter from Professor John Pasi is included in Appendix C.



The excellent clinical evaluation outcome has resulted from the significant improvement in operation of the microcantilever fluid probe through a reduction in thermal crosstalk. This has been accomplished by using a low temperature coefficient of resistance sensor material, geometric separation of heaters and sensors, structural change from gold-polymer to polymer-polymer to limit heat conduction, tapering of metal heaters, and shortening of the actuation pulse width. The individual improvements are:

- NiCr piezoresistive sensors have a comparable mechanical sensitivity to Gold piezoresistive sensors and significantly lower thermal sensitivity (TCR) leading to a reduction in the thermal crosstalk signal by 11.3 times.
- Improvement in mechanical signal as a proportion of the total signal for 100 ms pulse width by 11-15% between Epsilon and Solid design through reduction in thermal crosstalk.
- Improvement in mechanical signal as a proportion of the total signal for 100 ms pulse width by 25-30% between tapered and standard heater design through reduction in thermal crosstalk.
- Enhancement in operation at very short pulse width (1 ms) with a lower limit improvement of approximately 30% in reduced thermal signal either through improved conversion efficiency and/or reduced thermal crosstalk.

The results indicate that all design and operation modifications have improved the microcantilever fluid probe, and will produce a response with an estimated 12-17% mechanical signal as a proportion of total signal for operation in air with 100 ms pulse width. A further enhancement has been measured when operated in moderately viscous fluids, comparable to plasma and whole blood samples, with very short actuation pulses and high peak power. The measured upper limit of mechanical signal is approximately 48%, achieved due to mechanical overshoot of the microcantilever; this makes the measurements of the first peak ideal to track the clotting cascade.

An important result from the characterisation experiments is that non-uniform multilayer microcantilevers cannot simply be described as a classical bimetallic strip and treated as such, in for example, the finite element simulations in chapter 2. The localised thermal bending moment and neutral axis along the beam must be considered as both variable and complex. The actuation results and curvature measurements in section 3.3.3 both show the non-linear bending along the beam where movement is

restricted, or negative, in areas with metalisation, and free in areas without. The curvature measurements also show that the bending along the beam does not have a constant radius. The author believes that the expansion in the upper sections of the beam is being restricted by the metalised heater and sensor tracks, especially when a stiff and low thermal expansion metal, such as chrome, is used as an adhesion layer. If the actuation is also predominantly from the expansion of the gold heater in very short pulses and not the polyimide as first thought, the adhesion layer is considerably limiting expansion. The suggestion for future devices would be to try different adhesion layers, for example titanium ( $8.6 \text{ ppm.K}^{-1}$ ) or an electrically conductive polymer, and to limit the cross section of the heater to reduce stiffness through the beam. Unfortunately the trade off is that thermal conduction into the polyimide, which may assist bending, is limited and therefore an optimised solution will exist.

The realisation of a fluid microsensor based on a thermally driven microcantilever with integrated piezoresistive sensor is a challenging task. To the author's knowledge, the architecture and operation of the microsensor presented in this thesis and developed by the team at STFC and Microvisk is unique and shows the potential for simultaneous environmental measurement of mechanical, thermal, and electrical properties. Several groups have published work on simultaneous viscosity and density measurements using the natural frequency and Q-factor of microcantilever's. The resonance technique requires the measurement of vibrational amplitude over a frequency range, and is generally performed with an optical technique requiring alignment, calibration, and suitably transparent fluids. Though the goal of the work was to achieve a relative measurement of rheological changes in whole blood and plasma the technique shows future potential for absolute measurement of viscosity and density (section 4-2 and 4-3).

The results on viscosity standard glycerol solutions (Figure 4-1 and Figure 4-3) and the analysis of the microcantilever response in a Polyacrylamide Gel (Figure 4-4) allow a discussion of the sensor ability to measure viscosity and density, and impact on the Reynolds number. The Reynolds number is a dimensionless constant equal to the ratio of inertial forces to viscous forces that describes the flow conditions in the system. As the sensor device is scaled to the micro domain the viscous forces per unit volume increase more than the inertial forces per unit volume. This is due to a squared dependency on the length scale for inertial forces and only a linear dependency for viscous forces. Therefore, at the microscale the viscous forces dominate and the

Reynolds number is characteristically low ( $Re < 1$ ). This suggests that the flow will be laminar and as a result no mixing will tend to occur. Given the viscosity dominates it is expected that the mechanical damping measured in Glycerol and PAG is almost solely dependent on the viscosity. Certainly, use of the damped mechanical oscillations can be used analogous to a vibrational viscometer. This leads to the question of whether density can be measured by the use of microcantilevers at low Reynolds numbers. Previous literature suggests that simultaneous measurement of viscosity and density is possible [6, 78, 79, and 82] and that the acceleration of material swept up by the microcantilever leads to a shift in the resonance frequency of microcantilever probes. The ability of the microcantilever to feel the inertial forces of the fluid are dependent on the width of the device and the velocity. As the velocity of the probe increases the inertial forces increase by the square of the velocity while viscous forces increase by a linear dependency. For the polymer microcantilever fluid probe the velocity can be estimated from Figure 4-4. From the analysis a deflection of 0.75 microns and peak position at 1.25 ms, gives a velocity of  $0.6 \text{ mm} \cdot \text{sec}^{-1}$  in low viscosity (1 - 2.5 cP). This would suggest that by increasing the size of the microcantilever or the speed of actuation – for example by optimising heaters (Figure 3-15) – inertial effects can be increased and measured. An interesting visual result of the coagulometer work in clear plasma samples (Chapter 4-5) was that a recorded video at 15 Hz showed turbulent flows around the sides of the microcantilever. If the Reynolds number was low, and viscous forces dominate this is not expected. An explanation could be natural convection, or the squeezed fluid between the cantilever and substrate which has to push outwards.

Absolute measurement of viscosity and density needs to be approached carefully in future work. Firstly, the device is not a simple drag flow viscometer. Such devices have a parallel surface operated at a constant rotational velocity, therefore removing inertial acceleration that describes the density. The viscosity is measured by varying the velocity (shear strain) and measuring the shear stress – usually as torque – on the rotator. The viscosity is equal to the slope of the shear stress versus shear strain plot. Unlike previously published work that use a flat microcantilever the work presented in this thesis uses a curled beam with non-linear curvature; the thermal gradient created in the beam is also non-linear resulting in variations of velocity along the surface and it is difficult to relate the actuation to a range of shear rates. The pulsed nature of the operation gives a fluid acceleration and deceleration which introduces the density as an

effective volume and mass swept up by the microcantilever. Firstly the movement of the microcantilever needs to be studied to see if the actuated part of the beam can be estimated as a flat moving surface, and how the velocity (shear strain) of the probe changes with input power. To extract the viscosity and density from the response it is likely that two parameters will have to be measured, as for example the natural frequency and Q-factor is measured in resonating beams. It is therefore important to achieve the mechanical oscillations as first seen in Figure 4-1 to describe the decay or damping coefficient of the oscillations and period. This may limit the current probes use in thicker fluids.

A second issue is that the thermal properties of the medium are coupled to the measurement, even if the piezoresistive sensor had zero thermal noise. This is because the thermal actuation pulse, and therefore mechanical deflection, is dependent on the thermal conduction of the fluid. For example, in a lower thermal conduction fluid the heat is retained on the actuation arms allowing a higher temperature to create a larger, more forced, deflection. This is not a negative point; in fact, it allows the simultaneous measurement of rheological and thermal properties of the fluid, namely the thermal conductivity and heat capacity. Though the response is complex with several variable dependencies, a rigorous experimental evaluation in several fluid standards with known parameters will allow the response to be further understood. For example, in short actuation pulses the peak response width and position, and damping of mechanical oscillations provides rheological data, whereas longer actuation analogous to standard thermal conductivity measurements can provide thermal data from the rise-to and level of the steady state equilibrium.

A further effect given the thermal actuation is coupled to the medium could be the influence of the thermal actuation on the rheological parameters in the localised measured fluid. Certainly the measurements indicate conduction to the fluid and this cannot be ignored. In relative measurements of whole blood and plasma clotting (such as Figure 4-9 and Figure 4-10) the lowest pulse energy that has been used is 90  $\mu\text{J}$ . Using an energy balance equation for heat generation and transfer, as by Zhou et al [43], including the conduction path back through the metalised tracks the prediction is that approximately 10% of dissipated heat goes into the fluid at steady state. For the typical fluid volume placed on the device (20  $\mu\text{L}$ ) the energy dissipated into water from this pulse gives a rise in temperature of 0.0001  $^{\circ}\text{C}$ . The heat balance equation is only a

simple analytical tool and the energy dissipated into the fluid could be more or less; it is also the author's belief that the current devices are being overpowered and therefore the energy input can be further reduced. For example, Figure 4-1 show no loss in definition of mechanical oscillation when accidentally using a lower energy pulse, in fact the oscillation become more smoothed out in the W (150  $\mu$ J) and G device (135  $\mu$ J).

Temperature also has several other effects in the device; the heater resistance changes which varies the current and therefore power over the actuation pulse; the strain sensitivity is known to be dependent on temperature as is the structures material properties; and the rheological properties of the fluid are sensitive to thermal changes. The internal material properties and dimensions of the device can also vary across a wafer, for example it was noted in chapter 3 that the thickness of layers can vary up to 10%. The thermal coefficient of expansion, Young's modulus, heat capacity, thermal conductivity, residual stress, is all unknown and variable. These variations are expected and a calibration could be performed in a known fluid, such as air, before the actual measurement to provide a reference response.

The final point is non-linear fluid effects that might be exaggerated by the device. The Epsilon shape is complex and contains two gaps that fluid could pass through. It is unknown if particles could block these gaps and the likely effect on the response. The microcantilever is also surface mounted, that is to say that the microcantilever does not extend from the body of the device as in bulk silicon microcantilevers. These present two possible issues, the first is at the base of the device and accounts for particles that may get trapped and cause a grinding, the second is the opposing wall or gap between the beam and substrate and how this affects the flow. The second point may again be beneficial as it may introduce a compression, and therefore measurement of elasticity of the fluid. Certainly this is not a simple task, but with consistent experimental work using fluids with known rheology and thermal properties it is the author's belief that a sensitive platform can be realised.

The main result of the analytical work in chapter 2 is the understanding of the full bimorph equation (equation 2.7) and optimisation of deflection beyond the use of the standard thickness ratio. Based on an optimisation of the initial bending moment and flexural rigidity through the position of the beam neutral axis, it has been found that the maximum is achieved when the axis is located at the structural interface. This

relationship has allowed the optimisation for a two layer structure with constant stiffness to be achieved (equation 2.10). Beyond a two layer structure it has been found that the solution for the maximum deflection exists where the neutral axis is at a layer interface though numerically this becomes more complex to solve where each layer thickness can be changed.

Analytical work on the performance of the microheater indicated that for short pulse operation a fast heat generation and low heat loss due to conduction into the surrounding medium is desirable (equation 2.16). Characterisation in chapter 3 on the response of heaters during pulsed heating (section 3.3.5) supports the use of lower cross section tapered heaters for higher temperature increase (Figure 3-15) and the reduction in heat loss from a change in structural material from gold to polyimide (Figure 3-14). Though tapered heaters produce the fastest temperature increase in the metal heater the steady state level is less than that of standard heaters (Figure 3-14) indicating there is significant heat loss from the tapering at the base of the device. Equation 2.16 further suggests a metal heater with low heat capacity and mass density, and it is also indicative that the fast actuation is from the thermal expansion of the heater material. Therefore it is suggested that the gold metal heater is replaced with aluminium in future work. Heat conduction across the device has been greatly underestimated in analytical work compared to characterisation (Figure 3-18) of the sensor during actuation. The work in chapter 4 has shown that the conduction and convection into the fluid has an effect on the transient thermal profile, as does the conduction into the substrate shown in the heat loss from tapered heaters. In addition the testing of MV2 devices in a polyacrylamide gel shows the sensor thermal response is instantaneous to the heater actuation even though the two are geometrically separated. This indicates the possibility of a separate conduction path off the beam. For future work it would be of interest to try a non-silicon substrate to see if the substrate conduction path is a major influence.

The microcantilever fluid probe has now been realised in a third design that is based on the Epsilon polymer-polymer microcantilever with gold microheater and using a constantan piezoresistor. The aim of the design is not to improve the clinical results but to move towards a pre-production prototype with an external MEMS facility. The tapering of the heater has been kept but a new “pinch” has been placed further along the beam; this has yet to be tested and therefore is unclear whether this is an improvement. The device also uses larger electrical contact pads implemented by the author located

away from the active area which allows the use of spring loaded probes which are a quicker and cheaper alternative to wire bonded packages [136]. Dr Vladislav Djakov has also utilised a serpentine reference sensor on a second microcantilever with nominal resistance close to the active microcantilever. A similar sensor design has previously been utilised on silicon [137] but only to compensate environmental noise and not, as in this design, to compensate a thermal actuation crosstalk. In this configuration both microcantilevers are actuated, theoretically compensating the thermal crosstalk and environmental changes. In practice it is difficult to attain a full compensation due to differences in resistance and the second device will also cancel some of the mechanical sensitivity. The mechanical sensitivity of the active beam has been measured as  $9 \text{ ppm} \cdot \mu\text{m}^{-1}$  and the reference beam is  $0.5 \text{ ppm} \cdot \mu\text{m}^{-1}$  [138] therefore the mechanical response is reduced approximately 6% in a half bridge configuration. It is envisaged that the reduction in thermal crosstalk will be greater than this decrease and therefore overall will increase the mechanical proportion of the total signal of the device. The thermal sensitivity has also been measured and shows a reduction from  $100 \text{ ppm} \cdot \text{K}^{-1}$  in NiCr to  $40 \text{ ppm} \cdot \text{K}^{-1}$  in constantan. Certainly as a rheological sensor constantan is an excellent choice and in future work could be optimised further. For example a better matching thermal expansion in the substrate or adhesion material [101], and optimised deposition conditions for thickness and grain size [102, 105].

Taking into account the reduction in thermal and mechanical sensitivity for constantan and assuming that the actuation efficiency is comparable to MV2 devices in air, the mechanical component of the response is increased to approximately 30%. The enhancement in fluids by mechanical overshoot of the response gives an estimated upper limit of the mechanical signal to total signal as 69% using constantan sensors. An exciting result from the latest device is a visible oscillation in air when the active and reference microcantilever is actuated with  $70 \mu\text{J}$  energy –  $0.5 \text{ ms}$  pulse width – and the measurement is based on the AC coupled signal (Figure 5-1). This would allow such a device to potentially be used as a gas sensor.

Further changes have been made in the fabrication of the device including, changing the electrochemical sacrificial release with a dry release implemented by Dr Vladislav Djakov, and thinner polyimide encapsulation layers as suggested by the author. The electronics has also been modified to increase the range of gain and digital control of pass filters. The author has modified LabView software by using temporary paths for

data acquisition, thereby eliminating the short delay in measurements, and has implemented new controls for the modified electronics.

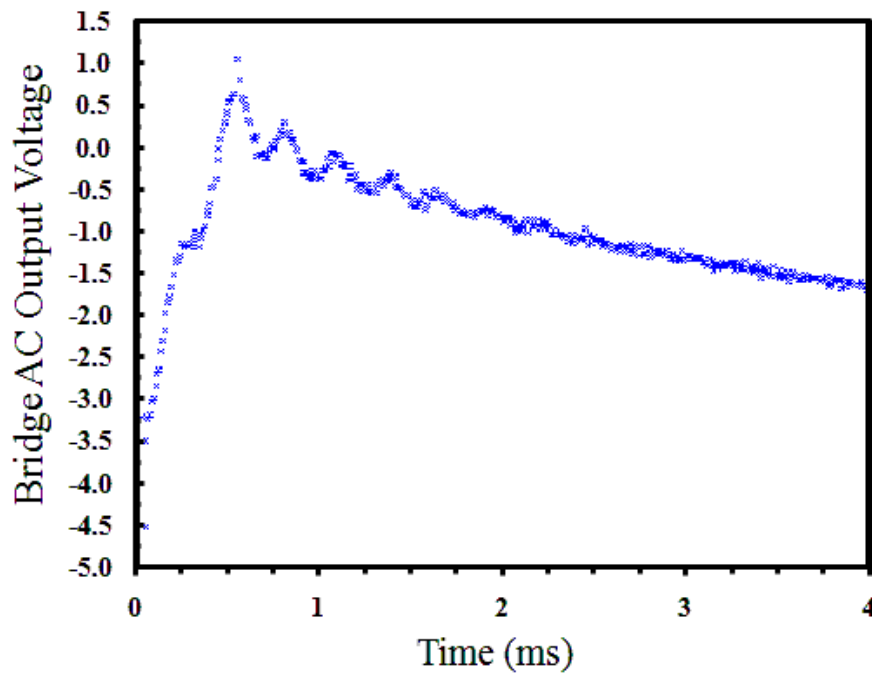


Figure 5-1 LabView Screenshot of the AC coupled response of third generation microcantilever fluid probe in air using a constantan sensor and active reference microcantilever.

A number of the characterisation experiments have developed over the course of the project each time making the measurement more accurate. There are still a number of improvements that can be made for future experiments including larger sample sizes. For the mechanical sensitivity testing a finer precision stage and controllable probe orientation would allow more steps to be taken and therefore a better statistical average of the change in response. The current thermal sensitivity measurements include a contribution in lead wires resistance, and this has been taken into account by using constantan wires. It would be ideal to compare this with a 3-wire bridge that compensates for any resistance changes in lead wires by having opposing leads in opposite arms of the bridge. The measurement is also very slow and therefore it would be easier to make several measurements on a number of devices at the same time. This is currently being incorporated into a new microscope stage that will be heated from below and allow not only TCR measurements but a deflection measurement to be taken while uniformly heated. A thermocouple close to the device would allow a more definitive measurement of the chip temperature to confirm the displayed incubator



temperature. This is a difficult task as the size of a standard thermocouple is much larger than the small area of the sensor, and it cannot be placed directly on the microcantilever. For future deflection measurements an optical lever technique or interferometer is critical as it is simply unfeasible to make reasonable measurements at time scales less than 50 ms. Based on the interpretation of results from the work presented, the deflection of the microcantilever is not as large as has been previously thought and therefore the small deflections should allow these types of measurement. The setup would be especially useful for confirming deflections in fluids with no associated thermal noise. For example, a laser vibrometer would be useful for measuring the mechanical oscillations after the actuation pulse.

The potential of this technology to be applied across many research and commercial applications is very exciting and the future is not necessarily to be focused on incremental improvements to the device. The current generation allows a platform for rheological and thermal measurement of nano-litre samples and therefore new uses can already be considered not only in medical and health care, but industrial automation, food production, automotive, inks and paints, chemical processing, and environmental monitoring, amongst others. Hopefully this will become a disruptive MEMS technology that contributes to the economic competitiveness of the United Kingdom in nanoscience and can improve the quality of life for its people and others worldwide.

## **Chapter 6 - Supporting EngD Material: PRONANO - Background and Demonstration of Surface Imaging**

The previous thesis chapters have provided a foundation for design and characterisation of multi-layer polymer microcantilevers with integrated actuator and sensor. The concepts and results are exploitable for other application including the demonstration of polymer based scanning probes. The design of bi-layer probes with constant stiffness governed by equation 2.11 in chapter 2 has been used in the Pronano project to show that the merger of silicon and polymer to improve actuation efficiency is not desirable. This is because the optimised structure would require several microns of polymer, thereby reducing the resonance performance. The results from characterisation of metal thin film heaters and sensors in chapter 3 has led to the decision to choose gold heaters and low thermal sensitivity nichrome piezoresistors. The optical characterisation technique also presented in chapter 3 has been applied to polymer scanning probes to show a non-linear bending profile and twisting in deflection when a DC actuation is applied.

The development of polymer scanning probes in parallel operation also provides a foundation for exploiting multiple biological measurements using the previously presented microcantilever fluid probe. It is highly desirable to perform multiple tests in a single device from analysis of complex diseases to time critical intervention in emergency situations. Multiple testing also provides business viability through a premium placed on the device. The knowledge that can be exploited includes the hardware and software setup for controlling and readout of multiple channels, how to fan out electrical connections and contact pads, and thermal crosstalk between adjacent probes.

The following chapter provides supporting material undertaken on the Engineering Doctorate towards the European FP6 project PRONANO. I have designed the fabrication route and lithographic masks for technology transfer and post-processed devices in the STFC cleanroom; characterised the performance of microcantilevers including electrical sensing during thermal self-oscillation; and developed a platform for scanning measurements of single and parallel microcantilevers.

Current surface metrology tools and advanced detection systems using microcantilevers are in general based on single probes, resulting in limited processing capability. According to the International Technology Roadmap for Semiconductors (ITRS) a major problem for the electronic industry is the real-time line width measurement below 10 nm. Of the techniques currently available scanning proximity probes are the most appropriate in terms of accuracy and application for these dimensions. However, real-time in-line measurements require a solution capable of high speed and high throughput beyond the capacity of single probes. The development of massively parallel arrays yields superior speed and information, having the potential to overcome future limitations in industrial metrology for nanoelectronics manufacturing.

Microcantilever arrays are also a promising platform technology for nanoscience. For example, IBM has developed a passive array of 8 microcantilevers that can be differentially coated with specific receptors for biological and chemical identification [2, 139]. The ability to measure several biological disease markers in a single sample at point of care will have significant impact in medical diagnostics, from time-critical intervention to resource poor environments. UK economic impact throughout the NHS would result from reduced infrastructure (equipment and training) needs, reduced patient pathways and morbidity by early intervention, and improved life-long care through point of care monitoring.

The development of polymer based microcantilever arrays with self actuation and piezoresistive sensing is under investigation by STFC-MNTC within the framework of the European FP6 project PRONANO: Technology for the Production of Massively Parallel Intelligent Cantilever - Probe Platforms for Nanoscale Analysis and Synthesis Project (IP 515739-2 PRONANO). PRONANO is a 5-year project with 16 partners from academia and industry and a combined budget of €14.2 million. The aim of the project is to manufacture and demonstrate a massively parallel microcantilever chip with 128 x 128 proximal probes, each with fully addressable control and read-out based on through wafer electrical interconnects.

Current state of the art scanning-probe arrays have been developed by the Quate Group at Stanford University [140], IBM Research Laboratory [141], and LG Electronics Institute of Technology [142]. The Quate Group has demonstrated a linear 1 x 50 silicon array with integrated ZnO piezoelectric actuation and piezoresistive silicon

sensor for parallel AFM. The group have also demonstrated a 2-D array (2x7) utilising through wafer electrical connections [143]. IBM Research Laboratory has demonstrated a 64 x 64 silicon array with integrated thermal actuation and thermal feedback for parallel data storage with terabyte per square inch density. LG Electronics Institute has also fabricated a mechanical data storage device based on a 128 x 128 silicon array with integrated thermal actuation and piezoelectric position feedback. Though large arrays have been realised for data storage applications the devices are specific to thermo-mechanical data storage and LG have yet to demonstrate multiple-probe operation.

The core technology proposed in PRONANO is based on silicon micromachined cantilever sensors using standard CMOS processing [144]. Each silicon cantilever has integrated sensing based on implanted piezoresistors in a full Wheatstone bridge arrangement [137] and thermally driven actuation. The integration of electrical sensing on individual cantilevers overcomes the read-out limitation of laser-based optical detection which requires precise alignment between a laser and position sensitive detector for each cantilever in the array. Integrated actuation offers advantages over piezotube z-actuators for scaling to massive arrays. Firstly, the feedback speed of the microcantilever is improved through higher flexural resonance frequency as the vibrating mass is reduced to a single addressable probe compared to the non-discreet actuator stage in commercial AFM systems. Also, for thermal actuation the excitation can be realised as an alternating current that drives resonance with a direct current component that controls the deflection offset of the microcantilever. This has advantages in alignment/orientation of the 2D array and for maintaining tip-sample distance. To enhance the actuation efficiency of silicon microcantilevers an aluminium nitride layer is deposited prior to release to create a bimorph.

The major challenges faced by the consortium in realisation of large parallel scanning probe arrays include; Very large scale integration (VSLI) in micro- nano-manufacturing of vertical interconnections for electrical connection; Multichannel ASIC design for control and read-out of sensor and actuation; High speed data acquisition; Packaging; and thermal, electrical, and mechanical crosstalk between cantilevers.

Polymer microcantilevers with integrated thermal actuation and metal piezoresistors are under investigation by STFC-MNTC within the PRONANO project as an alternative

architecture to silicon cantilevers. Polymers can be processed using simple spin-on methods and are available with a wide range of thermal, electrical, and mechanical properties. For wider exploitation, polymer microcantilevers are not limited to fabrication on silicon substrates allowing larger area volume production on polymer or glass substrates and lower device cost. For exploitation of microcantilever arrays in chemical and biological sensing, high volume and low cost will be critical, for example, commercially available single AFM silicon probes have a retail cost c.a. £10 and therefore could be prohibitively expensive when scaled to larger arrays.

Though polymers are unlikely to match the imaging resolution of silicon based scanning probes with ultra-sharp tips, such platforms offer alternative application. For example, polymers are inherently soft and flexible, permitting imaging of soft matter, for example biological cells, and large surface features beyond several tens of microns. MNTC propose the fabrication of stressed polymer bimorph cantilevers with large difference in coefficient of thermal expansion (CTE) to realise truly out-of-plane structures over two-dimensional surfaces. Bimorph cantilevers also provide enhanced deflection when thermally actuated allowing low power consumption for very large arrays.

The disadvantages of integrated polymer microcantilevers for scanning probe arrays include reduced tip sharpness and low sensitivity in metal piezoresistors. Poor tip sharpness compared to silicon probes is due to polymer devices being realised by surface micromachining as apposed to bulk micromachining. Whereas silicon tips can be formed by etching along selective crystal planes, polymer tips are formed by moulding in pre-etched pits. Metal piezoresistors have a significantly lower Gauge factor than silicon based piezoresistors ( $\sim$  factor of 20) and therefore can be limited in resolution against electrical noise and drift.

Previous work on polymer scanning probes in the field is limited to single probes and optical readout. Pechmann et al [145] have fabricated photoresist scanning probes with electron beam deposited tips and demonstrated contact mode imaging. IBM Research Group and collaborators have fabricated photo-plastic (SU-8) scanning probes [146, 147] with integrated tips for demonstration in tapping mode on DNA samples. Gaitas et al have fabricated polyimide bimorph scanning probes with integrated gold heaters and demonstrated in contact mode [148] and tapping mode [149] though excitation frequency was less than 100 Hz. Gaitas et al note oscillation amplitudes  $< 10$  nm for

polyimide bimorphs which is below the resolution of metal piezoresistors. All authors note the use of polymer scanning probes for low spring constants and imaging of soft matter including biological material.

## **6.1 Design and Characterisation**

Polyimide based scanning probes have been designed by the author and fabricated through technology transfer to facilities at INEX UK, and internally at STFC-MNTC. The concept is based on using stressed bimorph cantilevers with in-plane tips to provide a “stylus” probe. This concept has been realised to aid alignment of 2-dimensional arrays and bring probes away from the substrate given they are not truly suspended from a holder as in practical AFM probes. Using a bimorph to stress the beam out of plane also allows enhanced thermal actuation by choosing materials with a suitably large difference in coefficient of thermal expansion. The in-plane tip is effectively formed by pattern transfer and dry etching during the lithographic process to define cantilever shapes. Stressed probes based on NiZr metal layers have been realised for high topography AFM imaging by researchers at PARC [150-151]. These probes also use an in-plane tip but have no integrated sensor and heater and are based on single probes.

The design and fabrication of polyimide based probes has been realised with two combinations of materials; low CTE Polyimide (PI-2610) and high CTE Polyimide (PI-2562); and Gold and high CTE Polyimide (PI-2562). The decision by the author for using gold as one route is to improve thermal response by introducing higher thermal conductivity elements. For Gold-Polyimide bimorphs the integrated gold heater (150 nm thickness) is sandwiched in the polyimide layer as it must be electrically isolated from the metal structural layer. In the Polyimide-Polyimide bimorph the heater is sandwiched at the interface of the structural layers. In both designs a NiCr piezoresistor element is located on the surface of the cantilever to yield the largest distance to the beam neutral axis and therefore maximum stress. NiCr has been chosen for the similar gauge factor to other metallic films but lower temperature coefficient of resistance. As the thermal actuation of polymer structures is expected to be slow a number of arrays have been designed that only have a piezoresistive sensor. This allows contact probing and potential use as a platform for passive chemical and biological measurements. Figure 6-1 shows final polyimide bimorph scanning probes.

Previous devices fabricated at the MNTC [13] used the poor adhesion of gold to silicon to release cantilever devices. This produced very good yields but the release uses a wet etch process which is not controllable on the undercut of the gold structural layer. For the current fabrication the release layer is E-beam deposited aluminium, 0.5  $\mu\text{m}$  thick. The step is kept to a minimum to keep subsequent films continuous. The aluminium layer is subsequently patterned using photolithography and wet chemical etching to outline areas where microcantilevers will be released. For Gold-Polymer devices a 75 nm NiCr layer is sputter deposited, followed by 0.4  $\mu\text{m}$  of gold. The barrier layer is required to stop gold reacting with aluminium and producing intermetallic compound  $\text{AuAl}_2$  which is difficult to remove during the sacrificial release. To remove the sacrificial layer the microcantilever device is submersed in aluminium etchant to provide lateral undercutting. At room temperature and with no agitation this process can take approximately 21 hours. To improve the speed of the release the aluminium etchant can be heated to 50-60  $^{\circ}\text{C}$ , reducing the release time to approximately 6-7 hours. In both cases this is a long process and in future devices a copper or chrome sacrificial layer will be utilised to allow faster lateral etching.

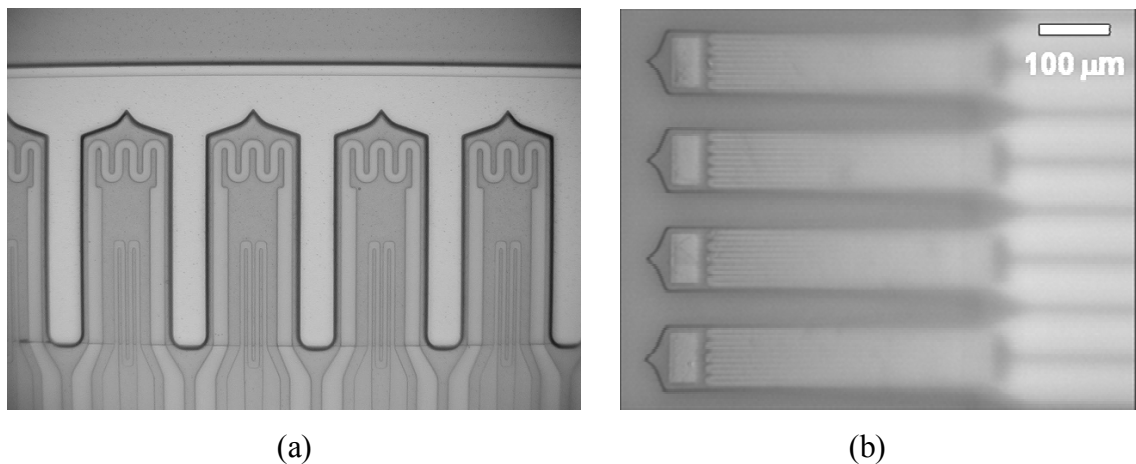


Figure 6-1 (a) Array of Polyimide-Polyimide bimorph cantilevers with outer heaters and inner double meander sensors before etching of the underlying aluminium sacrificial layer. Cantilevers are 225  $\mu\text{m}$  in length and 80  $\mu\text{m}$  in width. (b) Array of released Polyimide-Polyimide bimorph cantilevers with piezoresistive sensors only.

Characterisation of polymer based microcantilever scanning probes provides a foundation for improvement to design and operation of devices. Actuation efficiency of polyimide-polyimide and gold-polyimide scanning probes is presented. This has been measured as set out by the methods described in Chapter 3.3. This provides a direct

comparison to silicon based scanning probes developed within the PRONANO project. Finally, the piezoresistors response during self-oscillation frequency sweep is presented. Metal film gauge factor and thermal sensitivity has been reported previously in Chapter 3.

Measurement of microcantilever tip deflection is a crucial parameter for optimising initial and actuated deflection for exploitation of sensors and actuators. For the scanning probe application it is desirable to achieve a large initial deflection of the multilayer structures otherwise adhesion to the substrate can be an issue in release and performance. The curled deflection is also desirable to achieve surface contact using an in-plane tip. High deflection efficiency is important when considering large arrays as low power dissipation (mW) can become considerable when scaling to thousands of devices. To measure actuation efficiency the tip deflection is first measured at zero input power and then at several increased increments of power. Polyimide-Polyimide scanning probes of 225  $\mu\text{m}$  length, 90  $\mu\text{m}$  width, and 3  $\mu\text{m}$  thickness have an initial deflection of 33.8  $\mu\text{m}$  and an actuation efficiency of 0.53  $\mu\text{m.mW}^{-1}$  away from the substrate. The estimated spring constant measured at the tip from the calculation of combined flexural rigidity is 0.96 N/m. The stiffness is an estimate as the cantilever has a non-uniform cross section along the beam giving a variable flexural rigidity along the beam. Gold-Polyimide scanning probes with equal length and width, and 3.4  $\mu\text{m}$  thickness have an initial deflection of 11.8  $\mu\text{m}$  and an actuation efficiency of 0.03  $\mu\text{m.mW}^{-1}$  towards the substrate. The estimated spring constant measured at the tip is 1.9 N/m. Given the deflection of Gold-Polyimide scanning probes in the measurement is within the error of the measurement technique it is difficult to say with confidence that a measurable deflection is occurring. Silicon scanning probes fabricated in the PRONANO consortium with 250  $\mu\text{m}$  length, 55  $\mu\text{m}$  width, and 3  $\mu\text{m}$  thickness, and having a 1  $\mu\text{m}$  thick Aluminium coating to create a bimorph have achieved an actuation efficiency of 0.2  $\mu\text{m.mW}^{-1}$ .

The results indicate that in comparison to previous gold-polyimide cantilevers characterised in chapter 3.3.2 (8.2  $\mu\text{m.mW}^{-1}$ ) the device operation is very poor when the length of the beam is scaled. The author believes this is the poor design of the concentrated heaters which induces focused heating only at the tip of the beam rather than along the device. In comparison, silicon probes fabricated in the consortium have a



higher efficiency, again showing the poor actuation of polyimide probes using this pattern of heater. Polyimide-Polyimide devices perform well and show the negative deflection that has been seen in the original microvisk cantilevers. This could be exploited in scanning probes to fabricate devices that will curl-up from the substrate but when heated in DC will move towards the substrate rather than back to a flat position.

The amplitude frequency response of polyimide based scanning probes has been investigated to demonstrate self-oscillation and self-sensing. Microcantilevers are fixed and wire bonded to ceramic carriers and placed in the Microsystems Ltd electronics that has been described previously in Chapter 3.4.1. Signal response is measured on the integrated NiCr piezoresistors in a  $\frac{1}{4}$  Wheatstone bridge arrangement with 2.5 Volts bridge excitation. Several frequency sweeps on polyimide-polyimide and gold-polyimide have been conducted using varying actuation level, pulse shape, number of samples at each frequency, and frequency range and step. No vibration isolation was used in the experiments.

Polyimide-Polyimide microcantilevers have shown no clear amplitude peak. In previous work Gaitas et al [149] also found no clear peak in polyimide bimorph AFM probes using thermal actuation and amplitudes below the resolution of the integrated NiCr sensor. A further issue in the current MNTC-STFC probes may arise from thermal crosstalk between the integrated sensor and heater which saturates the signal response. It is noted that improved results may arise from separation of heating and sensor elements either through thermal actuation with optical read-out or external actuation through a piezotube and integrated piezoresistors. Peak amplitude at 27 KHz has been observed for Gold-Polyimide microcantilevers. The expected resonant frequency using the analytical expressions of Sader [71] is 22.4 KHz. The experimental response shown in Figure 6-2 has been acquired using sine excitation with 1.2 Volts peak-to-peak and 0.6 Volts offset on a gold microheater with 75 Ohm resistance. The resistance of the NiCr piezoresistor is 4.5 KOhm. Each data point is the average AC component of the piezoresistor response from 50 cycles at each frequency.

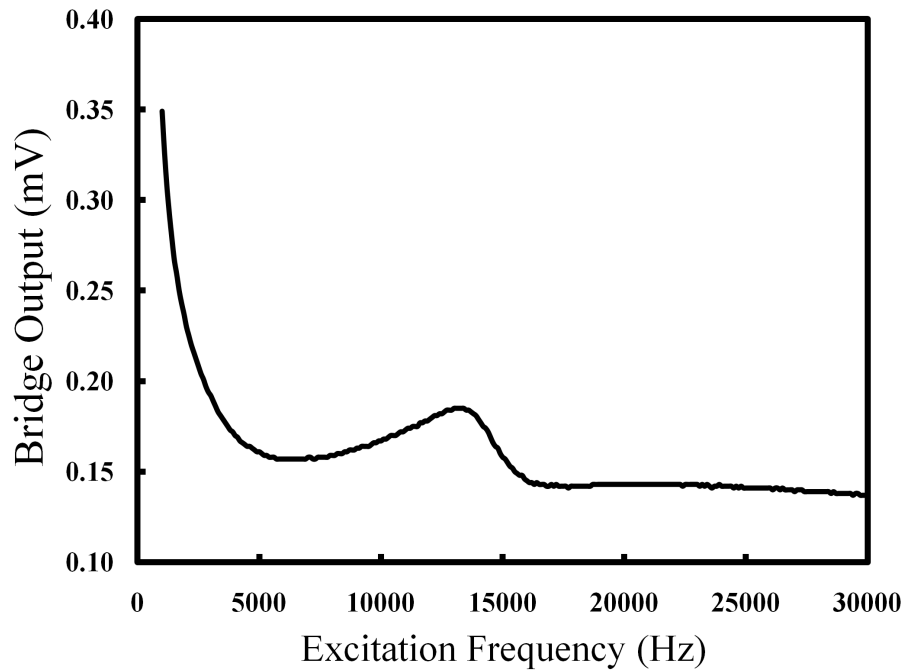


Figure 6-2 Integrated piezoresistor response during periodic thermal excitation of the integrated gold heater

The highest amplitude of the probe is obtained at low frequency with a low Q peak seen at a half frequency of 13.5 KHz. The expected peak frequency of 22.4 KHz is below the measured peak frequency in the beam (27 KHz). The analytical estimate depends on the thickness of the microcantilever layers, which can have variability up to 10%, and on the data sheet Young's Modulus. The most sensitive variable is the Young's Modulus of the Polyimide (PI-2562). The data sheet value is 1.8 GPa but does not account for a biaxial measurement; the figure is also highly dependent on processing conditions. A value between 5 – 6 GPa would increase the expected resonance to 27 KHz.

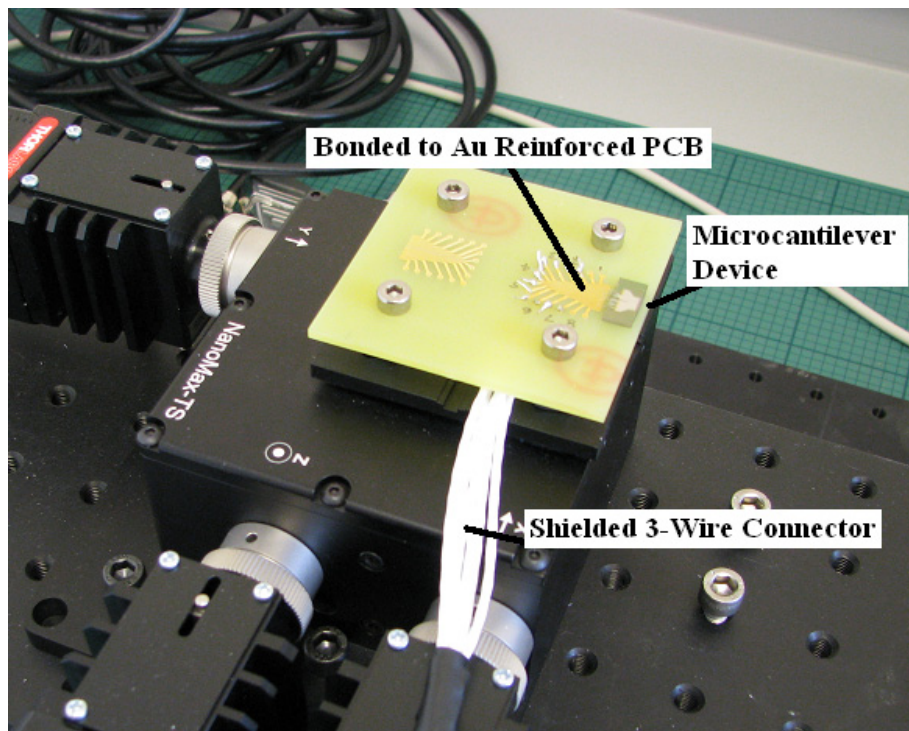
The measurement demonstrates the ability to self-oscillate the microcantilever into a resonance mode which has implications for sensing applications based on the amplitude profile. For example, a shift in the profile has been measured when operated in water. For further demonstration of surface imaging STFC do not have the infrastructure for applying scanning probes in a high frequency mode of operation. A route using contact scanning and piezoresistive sensors only (Figure 6-1b) has therefore been chosen by the author to demonstrate surface metrology.

## 6.2 Demonstration of Surface Imaging

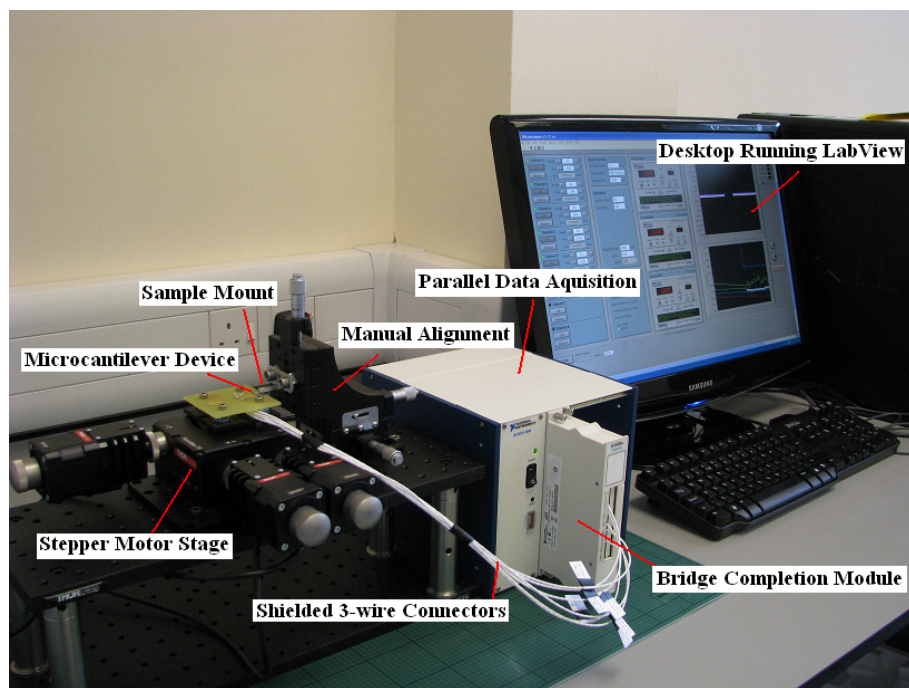
Surface metrology using single and parallel polymer scanning probes with integrated piezoresistors have been realised for contact imaging. Single stylus scanning probes based on stressed polyimide bimorphs (Figure 6-1b) have been used to image a sample with high structural features (c. 8  $\mu\text{m}$ ). The in-line calibration of mechanical sensitivity has been very successful and measured Z-height compares very well to comparison with KLA-Tencor profilometer (P15) results. Parallel lines scans using 4 cantilevers in the polyimide probe array has been achieved but an image has not been obtained due to poor adhesion of electrical contacts which causes the bonding to fail within a few hours.

The scanning platform is based on a 3-axis flexure stage with stepper motors (Thorlabs Nanomax MAX343) and controller (Thorlabs BSC103). The stage provides large travel range (4 mm) that is desirable for mechanical sensitivity and deflection measurements of stressed bimorph microcantilevers. The stage is limited in minimum incremental step (60 nm) and minimum speed (20  $\mu\text{m}\cdot\text{sec}^{-1}$ ). To achieve scanning speed below this limit a step, measurement, repeat algorithm can be used though the controller requires a dwell time of 500 ms before the next command can be received. Surface fabricated polyimide scanning probes microarrays are glued and wire bonded to a gold plated PCB carrier and mounted on the Nanomax scanning stage (Figure 6-3a). In this arrangement the sample to be measured is mounted on a 3-axis manual stage and the final contact is made by computer controlled Z-height of the probes.

The measurement setup is shown in Figure 6-3. Eight piezoresistor scanning probe channels are connected to a National Instrument SCXI Universal Strain Gauge Module (SCXI-1520 and SCXI-1314) using a 3-wire quarter bridge with a passive high precision 22.6 K $\Omega$  completion resistor. The SCXI-1520 module provides parallel measurement of up to 8-channels using track and hold circuitry. This means that all channel voltage output are captured simultaneously and then multiplexed into a single data stream to a PC acquisition card (National Instruments, M-Series PC-6221).



(a)



(b)

Figure 6-3 (a) Microcantilever Array glued to a PCB and mounted on the 3-Axis Nanomax Stage. 8-Channels are connected using a 3-wire bridge arrangement. (b) Scanning setup including the Nanomax stage, manual sample mount and data acquisition.

Each channel is a full Wheatstone bridge with two 5 K $\Omega$  digital potentiometers that can provide automated balancing using 128 step rough potentiometer and 4096 step fine potentiometer analogous to the Microsystem Ltd electronics. The module also offers programmable bridge excitation up to 10 V, selectable gain up to x1000, selectable low pass filter (10 Hz, 100 Hz, 1 KHz, 10 KHz, or bypass), and a shunt calibration circuit. The data capture rate of each channel is limited by the acquisition card sampling, channel settling time, the track time (the minimum time between the last AD conversion of the current scan and engaging the hold signal of the next scan), the hold time, and by the choice of high speed or high accuracy is required. For multiple scanning probes the sampling rate of each channel is limited by the channel settling time. As the accuracy, and not speed, of measurement is important at this stage the settling time is slightly increased reducing our maximum sampling rate to 12.5 KS/s. The SCXI control and data capture and control of the 3-axis Nanomax stage have been developed in LabView 8.6 environment by the author. A post analysis 3-dimensional plotter has also been written in LabView by the author to visualise the results. A development in the software is to balance every channel simultaneously in the array and to incorporate a calibration routine where the probe is displaced by the sample and the resulting linear output is converted to a  $\mu\text{V}.\mu\text{m}^{-1}$  factor.

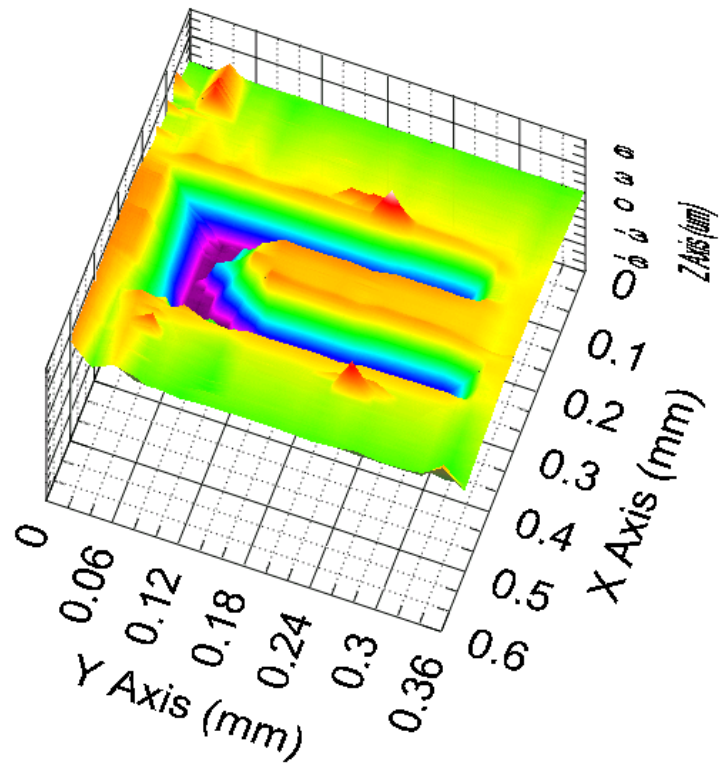
The current setup is subject to large 50 Hz and 60 Hz electrical interference. The measurement that is being conducted is step and repeat, with 2500 samples measured (200 ms) and then a dwell before a command can be sent to the stage controller (500 ms). To reduce the electrical interference a 10 Hz low pass filter has been enabled. Though this reduces the interference it will also have an adverse effect on the microcantilever response when the probe is operated at high speed – effectively smoothing out the data – and therefore a future aim is to control the interference at the source, for example, using a faraday cage.

For demonstration of imaging using stressed polyimide bimorph scanning probes a micro fabricated sample has been chosen with large z- features (c, 8  $\mu\text{m}$ ) and large trench width (c. 50  $\mu\text{m}$ ). The imaging device used is a single device in a 1x32 array of sensor only probes with 400  $\mu\text{m}$  length, 80  $\mu\text{m}$  width, and 3  $\mu\text{m}$  thickness, giving an approximate stiffness measured at the tip of 0.1 – 0.2 N.m $^{-1}$ . The sample is fixed to a mechanical arm from the manual stage and adjusted towards the microcantilever with rough visual inspection. The SCXI electronics is set to a bridge excitation of 2V and

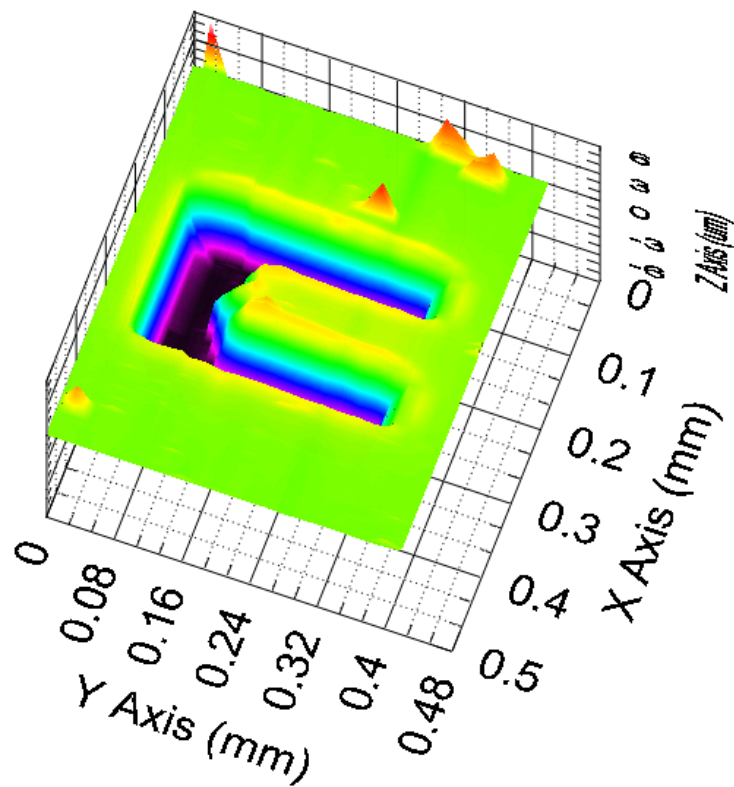
maximum gain ( $\times 1000$ ). The Wheatstone bridge is balanced and z-height of the stage is adjusted in 250 nm steps until the microcantilever has registered contact with the sample. To ensure the cantilever remains in contact during scanning across the sample the cantilever is displaced a further 10 microns ( $1.5 \mu\text{N}$ ) against the sample and the bridge is rebalanced to give zero output.

To calibrate the amplified and filtered Wheatstone bridge output voltage against cantilever position the microcantilever is taken through several incremental steps against a flat surface. Before imaging of the sample using the polyimide bimorph scanning probe the calibration has been repeated 10 times at 2 minute intervals to note reproducibility and therefore the confidence in the voltage to height conversion. The repeated calibration yields an average of  $34.2 \mu\text{V}.\mu\text{m}^{-1}$  with a standard deviation of  $0.2 \mu\text{V}.\mu\text{m}^{-1}$ . This equates to a standard deviation of 5.8 nm which is below the limiting noise of the piezoresistor which has been measured as 30-40 nm. The range of calibration from  $33.9 - 34.5 \mu\text{V}.\mu\text{m}^{-1}$  equates to a range of 17.4 nm in calibration height.

The sample has been scanned using 500 nm lateral steps controlled using the Y-position stage – effectively a  $1 \mu\text{m}.\text{sec}^{-1}$  scan speed given the dwell time of the probe. The probe is scanned 500  $\mu\text{m}$  along the sample, lifted from the surface using the Z-control and returned to zero, shifted 20  $\mu\text{m}$  using the X-position stage to the next scanning line and returned to contact where the Wheatstone bridge output is zero. In total 19 lines have been measured giving a total scan area of  $0.36 \times 0.6 \text{ mm}$ . Due to the current slow scanning of the stage the whole image takes nearly 3 hours to form. To limit drift in the mechanical sensitivity of the probes due to changing ambient temperature a calibration is repeated before each scanning line.



(a)



(b)

Figure 6-4 (a) Reconstructed image using Polyimide bimorph scanning probes.  
(b) Reconstructed image using KLA-Tencor Stylus Profiler P15

Figure 6-4a shows the reconstructed 3-dimensional image from the polyimide bimorph scanning probe. Each scanning line is first compensated for tilt in the image using 50 data points (25 microns) at the start and end of the data file where the response is expected to be flat. The tilt is due to the scanning probe imaging the sample at an angle; as the scanning stage is moved across, the microcantilever remains in contact with the sample but the deflection of the beam changes. If scanning continues eventually the microcantilever would lose contact with the sample therefore limiting current scan area size. The tilt compensated data is then converted to z-height using the calibration that was taken before the line measurement.

For comparison, the imaged sample has been measured with a KLA Tencor P15 stylus profilometer with MicroHead IIsr (std). The Tencor MicroHead IIsr uses a diamond stylus tip with tip radius of 2  $\mu\text{m}$  and 45° cone angle. The tip is contacted to the sample and maintained under a chosen force (1 mg to 50 mg) during scanning. The tip displacement readout is made using a capacitive sensor and 24-bit read-out. The step height repeatability is stated as 0.75 nm or 0.1% (which ever is higher). Data has been recorded using a scanning speed of 5  $\mu\text{m}.\text{sec}^{-1}$ , at a sampling frequency of 100 Hz. Figure 6-4b shows the reconstructed 3-dimensional image from the Tencor data. The Tencor data is automatically filtered to remove electrical interference and each scanning line is again compensated for tilt using 500 data points (25 microns) at the start and end of the data file where the response is expected to be flat.

For direct comparison figure 6-5 shows a cross section of the image attributed to a single line scan using the polyimide bimorph scanning probe and the Tencor profilometer. The polyimide scanning probes shows good reproducibility in height to the Tencor Profilometer but poor side wall reproduction. This is due to the probe having poor initial deflection and therefore imaging in a flat position which cannot fall into the trench. Future improvement would be to engineering near vertical tip deflection and extend the tip.



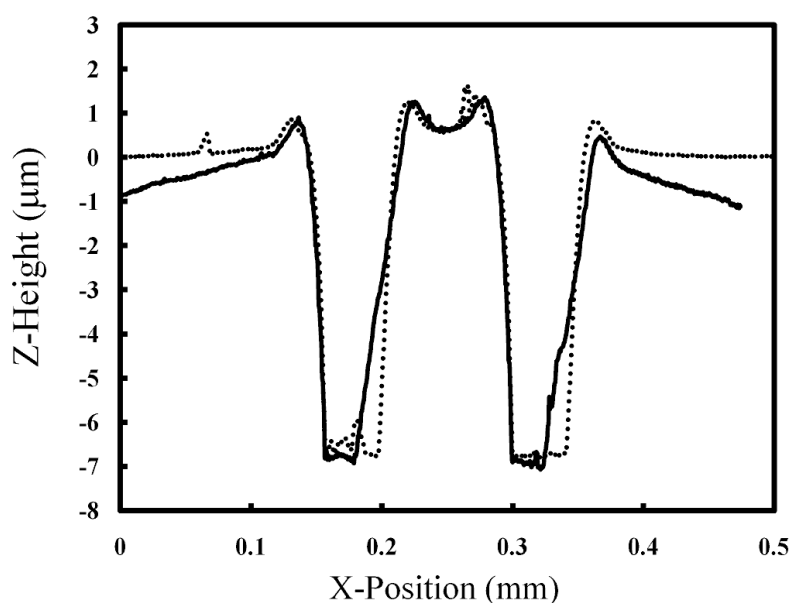


Figure 6-5 Line profile comparison between Polyimide Bimorph Scanning Probes (solid line) and Tencor Stylus Profilometer (dashed line).

An inconsistency in the profile measurements is the polyimide probe signal when the cantilever is in contact with the top photoresist layer. As the probe is scanned the signal increases as it approaches the first trench and decreases away from the second trench, whereas the Tencor produces a flat signal. This can be seen in Figure 6-4b where the KLA tencor scan has a very smooth uniformity. The difference in signal is not due to a thermal conductivity effect whereby the material conducts heat away from the cantilever induced in the sensor self heating otherwise the signal would increase on both sides. The difference is also not due to a self heating effect where the change in the sensor resistance under a fixed voltage reduces the current and therefore power dissipation. Further experimentation with the polymer probe and Tencor is required to understand this difference.

Further imaging using several parallel polyimide bimorphs has not been possible due to poor yield in electrical connection to the devices. To solve further issues with alignment the author and Dr Andreas Schneider (STFC) have designed suspended polymer scanning probes based on SU-8. Figure 6-6 shows a 1x8 SU-8 scanning probe array with integrated sensors and tips fabricated by Dr. Andreas Schneider at the MNTC. This architecture allows the cantilever array to be completely released from the substrate on a 300  $\mu\text{m}$  thick SU-8 holder and for tips to be integrated through moulding of pyramidal pits in the substrate.

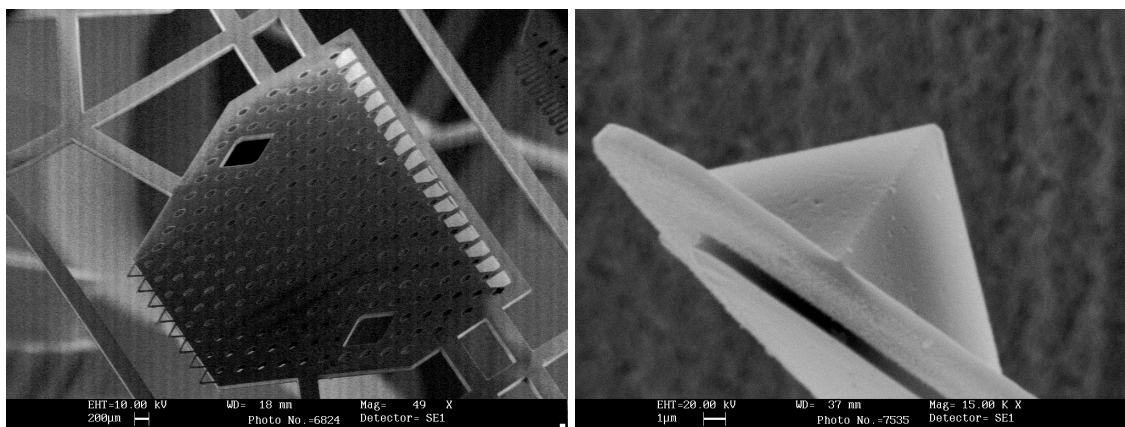


Figure 6-6 SEM images of SU-8 scanning probes arrays with integrated piezoresistor and tips courtesy of Dr Andreas Schneider (STFC).

Overall the resolution of the polyimide scanning probe is limited by the metal piezoresistor to 30-40 nm with additional noise generated in the large lead-in to the device. The expected resistance on the microcantilever is approximately 5 K $\Omega$  but each contact needs to be fanned out to electrical pads and this adds an additional 17.6 K $\Omega$ . In future devices it is desirable to reduce this additional load either through shortening of tracks or through silicon interconnects.

The group are currently investigating Diamond-Like Carbon (DLC) piezoresistors as a potential high gauge factor material and if successful this will be incorporated into future devices.

Current devices also have poor lateral resolution though this was expected as no attempt was made to sharpen or improve the in-plane tip. A simple option is to define a sharper tip in the mask though this is limited by the pattern transfer in photolithography. A possible direction would be to define the tip using direct write methods with sub micron line width though alignment is an obstacle to overcome. It is also possible to directly deposit tips onto the beam but this is not desirable for high-throughput of fabricated devices.

It is concluded that scanning probes with integrated sensors and heaters are interesting devices for niche applications but the majority of interest is in single AFM probes with optical read-out. Future work will therefore be aimed towards single polymer probes with no integration. It is important to note that the development of new piezoresistor materials (e.g. DLC) and operation (e.g. Self-Oscillation) have implication across the

portfolio of microcantilever projects, including the fluid probe, and therefore each element is of interest to move forward.

## References

- [1] G.H. Wu, R.H. Datar, K.M. Hansen, T. Thundat, R.J. Cote, and A. Majumdar, "Bioassay of prostate-specific antigen (PSA) using microcantilever," *Nat. Biotechnol.*, **19**, pp. 856-60, (2001).
- [2] Y. Arntz, J.D. Seelig, H.P. Lang, J. Zhang, P. Hunziker, J.P. Ramseyer, E. Meyer, M. Hegner, and C. Gerber, "Label-free protein assay based on a nanomechanical cantilever array," *Nanotechnology.*, **14**, pp. 86-90 (2003).
- [3] J.H. Lee, K.S. Hwang, J. Park, K.H. Yoon, D.S. Yoon, and T.S. Kim, "Immunoassay of prostate-specific antigen (PSA) using resonant frequency shift of piezoelectric nanomechanical microcantilever," *Biosens. Bioelectron.*, **20**, pp. 2157-62 (2005).
- [4] J. Yinon, "Detection of explosives by electronic noses," *Anal. Chem.*, **75**, pp. 99A-105A (2003).
- [5] L.A. Pinnaduwaage, A. Wig, D.L. Hedden, A. Gehl, D. Yi, T. Thundat, and R.T. Lareau, "Detection of trinitrotoluene via deflagration on a microcantilever," *J. App. Phys.*, **95** (10), pp. 5871-5875 (2004).
- [6] S. Boskovic, J.W.M Chon, P. Mulvaney, and J.E. Sader, "Rheological measurements using microcantilevers," *Journal of Rheology.*, **46** (4), pp. 891-899 (2002).
- [7] T. Thundat, H.F. Ji, and G.M. Brown, "Environmental monitoring using microcantilever sensors," *ACS Symposium Series.*, **904**, pp. 284-305 (2005).
- [8] B. Charlot, F. Parrain, N. Galy, S. Basrour, and B. Courtois, "A sweeping mode integrated fingerprint sensor with 256 tactile microbeams," *J. Micro. Electro. Mech. Sys.*, **13** (4), pp. 636-644 (2004).
- [9] A.C. Stephan, T. Gaulden, A.D. Brown, M. Smith, L.F. Miller, and T. Thundat, "Microcantilever charged-particle flux detector," *Rev. Sci. Instrum.*, **73** (1), pp. 36-41 (2002).
- [10] J. Thayson, A.D. Yalçinkaya, P. Vettiger, and A. Menon, "Polymer-based stress sensor with integrated readout," *J. Phys. D: Appl. Phys.*, **35**, pp. 2698–2703 (2002).
- [11] L. Gammelgaard, P.A. Rasmussen, M. Calleja, P. Vettiger, and A. Boisen, "Microfabricated photoplastic cantilever with integrated photoplastic/carbon based piezoresistive strain sensor," *Appl. Phys. Lett.*, **88**, 113508 (2006).

- [12] V. Djakov, Thesis for Ph. D. at the School of Engineering University of Wales, Cardiff, (2001).
- [13] V. Djakov, and S.E. Huq, "Bimorph Actuators for MOEMS," *Proceedings of the SPIE International Conference on Design, Test, Integration, and Packaging of MEMS/MOEMS, Cannes, France.*, **4755**, pp. 804–814 (2002).
- [14] R.J. Dunn, Thesis for MSc at the School of Engineering and Physical Sciences, Heriot Watt University, Edinburgh (2004).
- [15] J.W. Suh, S.F. Glander, R.B. Darling, C.W. Storment, G.T.A. Kovacs, "Organic thermal and electrostatic ciliary microactuator array for object manipulation," *Sens. & Act. A.*, **58**, pp. 51-60 (1997).
- [16] W. Riethmuller, and W. Benecke, "Thermally excited silicon microactuators," *IEEE Trans. Electron Dev.*, **35** (6), pp. 758–763 (1998).
- [17] B. C. Read, V. M. Bright, and J. H. Comtois, "Mechanical and optical characterization of thermal microactuators fabricated in a CMOS process," *SPIE*. vol. 2642., pp. 22-32, (1995).
- [18] M.Y. Al Aioubi, V. Djakov, S.E. Huq, and P.D. Prewett, "Deflection and load characterisation of bimorph actuators for bioMEMS and other applications," *Microelectronic Engineering.*, **73-74**, pp. 898-903 (2004).
- [19] "Over 7 million people worldwide take oral anticoagulants such as Coumadin® to help reduce the body's chances of forming harmful blood clots"  
<http://www.hemosense.com> accessed: 31-07-2008.
- [20] Britannica.com <http://media-3.web.britannica.com/eb-media/28/98328-004-5514AFAC.jpg> accessed: 31-07-2008
- [21] M. Madou, "Fundamentals of microfabrication - the science of miniaturization", CRC Press, 2<sup>nd</sup> ed, (2002).
- [22] N. Maluf, "An Introduction to Micromechanical Systems Engineering", Artech House, (2000).
- [23] B. Ilic, D. Czaplewski, M. Zalalutdinov, H. G. Craighead, C. Campagnolo and C. Batt. "Single Cell Detection With Micromechanical Oscillators," *J. Vac. Sci. Technol. B.*, **19**, pp. 2825-2828 (2001).
- [24] B. Ilic, H. G. Craighead, S. Krylov, W. Senaratne, C. Ober, and P. Neuzil, "Attogram Detection Using Nanoelectromechanical Oscillators", *J. Appl. Phys.*, **95**, pp. 3694-3703 (2004).

- [25] M. De Volder, J. Peirs, D. Reynaerts, J. Coosemans, R. Puers, O. Smal, and B. Raucant. "Production and characterization of a hydraulic microactuator" *J. Micromech. Microeng.*, **15**, pp. S15-S21 (2005).
- [26] D. Ramos, J. Tamayo, J. Mertens, and M. Calleja, "Photothermal excitation of microcantilevers in liquids," *J. Appl. Phys.*, **99**, 124904 (2006).
- [27] E.W.H. Jager, E. Smela, and O. Inganas. "Microfabricated conjugated polymer actuators," *Science.*, **290**, (5496), pp. 1540-1545 (2000).
- [28] H. Guckel, J. Klein, T. Christen, K. Skrobis, M Landon, and E. G. Lovell, "Thermo-magnetic metal flexure actuators," *Tech. Digest IEEE Solid state Sensor and Actuator Workshop.*, **22-25** , pp. 73-75 (1992).
- [29] S. Alexander, L. Hellemans, O. Marti, J. Schneir, V. Elings, P.K. Hansma, M. Longmire, and J. Gurley, "An atomic resolution atomic-force microscope implemented using an optical lever," *J. Appl. Phys.*, **65**, pp. 164-167 (1989).
- [30] R. Erlandsson, G.M. McClelland, C.M. Mate, and S. Chiang, "AFM using optical interferometry," *J. Vac. Sci. Techno. A.*, **6**, pp. 266-270 (1988).
- [31] D. Rugar, H.J. Mamin, and P. Guethner, "Improved fiber-optic interferometer for atomic force microscopy," *Appl. Phys. Letter.*, **55**, pp. 2588-2590 (1989).
- [32] Y. Martin, C.C. Williams, and H.K. Wickramasinghe, "Atomic force microscope-force mapping and profiling on a sub 100-A scale," *J. Appl. Phys.*, **61**, pp. 4723-4729 (1987).
- [33] C. Schonenberger, and S.F. Alvarado, "A differential Interferometer for force microscopy", *Rev. Sci. Instrum.*, **60**, pp. 3131-3134 (1989).
- [34] D. Anselmetti, Ch. Gerber, B. Michel, H.J. Guntherodt, and H. Rohrer, "Compact, combined scanning tunneling/force microscope," *Rev. Sci. Instrum.*, **63**, pp. 3003-3006 (1992).
- [35] S.R. Manalis, S.C. Minne, A. Atalar, and C.F. Quate, "Interdigital cantilevers for atomic force microscopy," *Appl. Phys. Lett.*, **69**, pp. 3946-3944 (1996).
- [36] G. Binnig, C.F. Quate, and Ch. Gerber, "Atomic Force Microscope," *Phys. Rev. Lett.*, **56**, pp. 930-934 (1986).
- [37] H.J. Hug, Th. Jung, and H.J. Guntherodt, "A high stability and low drift atomic force microscope," *Rev. Sci. Instrum.*, **63**, pp. 3900-3904 (1992).
- [38] T. Göddenhenrich, H. Lemke, U. Hartmann, and C. Heiden, "Force microscope with capacitive displacement detection," *J. Vac. Sci. Tech. A.*, **8**, pp. 383-387 (1990).

- [39] J. Tansock, and C.C. Williams, "Force measurement with a piezoelectric cantilever in a scanning force microscope, *Ultramicroscopy*, **42-44**, pp. 1464-1469 (1992).
- [40] M. Tortonese, R.C. Barrett, and C.F. Quate, "Atomic Resolution with an atomic force microscope using piezoresistive detection," *Appl. Phys. Lett.*, **62**, pp. 834-836 (1992).
- [41] G.G. Yaralioglu, A. Atalar, S.R. Manalis, and C.F. Quate, "Analysis and design of an interdigital cantilever as a displacement sensor," *J. Appl. Phys.*, **83**, 7405-7415 (1998).
- [42] G. Lin, C.J. Kim, S. Konishi, and H. Fujita, "Design, fabrication and testing of a C-shape actuator," *The 8<sup>th</sup> International Conference on Solid State Sensors and Actuators, and Eurosensors IX.*, pp. 416- 419 (1995).
- [43] J.W.L Zhou, H.Y. Chan, T.K.H To, K.W.C. Lai, and W.J. Li, "Polymer MEMS actuators for underwater manipulation," *IEEE/ASME Transactions on Mechatronics.*, **9** (2), pp. 334-341 (2004).
- [44] J.K. Luo, A.J. Flewitt, S.M. Spearing, N.A. Fleck, and W.I. Milne, "Normally closed microgrippers using a highly stressed diamond-like carbon and Ni bimorph structure," *Appl. Phys. Lett.*, **85** (23), pp. 5748-5750 (2004).
- [45] T. Ebefors, E. Kalvesten, and G. Stemme, "New small radius joints based on thermal shrinkage of polyimide in V-grooves for robust self-assembly 3D microstructures," *J. Micromech. Microeng.*, **8**, pp. 188-194 (1998).
- [46] S. Schweizer, P. Cousseau, G. Lammel, S. Calmes, and Ph. Renaud, "Two-dimensional thermally actuated optical microprojector," *Sensors and Actuators A.*, **85**, pp. 424-429 (2000).
- [47] S. Calmes, S. Schweizer, and P. Renaud, "Resonating large angle and low consumption micromachined optical scanner," *Proc of SPIE.*, vol. **3276**, pp. 96-102 (1998).
- [48] T. Ebefors, J.U. Mattsson, E. Kalvesten, and G. Stemme, "A robust micro conveyer realized by arrayed polyimide joint actuators," *J. Micromech. Microeng.*, **10**, pp. 337-349 (2000).
- [49] P.I. Oden, P.G. Datskos, T. Thundat, and R.J. Warmack, "Uncooled thermal imaging using a piezoresistive microcantilever," *App. Phys. Lett.*, **69** (21), pp. 3277-3279 (1996).

- [50] T. Perazzo, M. Mao, O. Kwon, A. Majumdar, J.B. Varesi, and P. Norton, "Infrared vision using uncooled micro-optomechanical camera," *Appl. Phys. Lett.*, **74** (23), pp. 3567-3569 (1999).
- [51] J.L. Corbeil, N.V. Lavrik, S. Rajic, and P.G. Datskos, "Self-leveling uncooled microcantilever thermal detector," *Appl. Phys. Lett.*, **81** (7), pp. 1306-1308 (2002).
- [52] R. Berger, C. Gerber, J.K. Gimzewski, E. Meyer, and H.J. Guntherodt, "Thermal analysis using a micromechanical calorimeter," *Appl. Phys. Lett.*, **69**, pp. 40-42 (1996).
- [53] E.T. Arakawa, N.V. Lavrik, S. Rajiv, and P.G. Datskos, "Detection and differentiation of biological species using microcalorimetric spectroscopy," *Ultramicroscopy*, **97** (1-4), pp. 459-465 (2003).
- [54] N. Abedinov, P. Grabiec, T. Gotszalk, Tz. Ivanov, J. Voigt, and I.W. Rangelow, "Micromachined piezoresistive cantilever array with integrated resistive microheater for calorimetry and mass detection," *J. Vac. Sci. Technol. A*, **19** (6), pp. 2884-2888 (2001).
- [55] W. Benecke and W. Riethmuller, "Applications of silicon microactuators based on bimorph structures," *IEEE Proc. Micro Electro Mechanical Systems*, **20-22**, pp. 116-120 (1989).
- [56] Q. Dong, W. Benecke, and H.J. Schliwinski, "SiON-Au double layer microactuator fabrication," *Microelectronic Engineering*, **15** (1-4), pp. 415-418 (1991).
- [57] W.H. Chu, M. Mehregany, and R.L. Mullen, "Analysis of tip deflection and force of a bimetallic cantilever microactuators," *J. Micromech. Microeng.*, **3**, pp. 3-7 (1993).
- [58] G. Lammel, P. Renaud, and S. Schweizer, "Optical microscanners and microspectrometers using thermal bimorph actuators," Springer Verlag (2002).
- [59] W. Peng, Z. Xiao, and K.R. Farmer, "Bimorph cantilever optimization for maximum deflection," *Technical Proceedings of the Nanotechnology conference and tradeshow*, Vol. 1, pp. 376-379 (2003).
- [60] M. Ataka, A. Omodaka, N. Takeshima, and H. Fujita, "Fabrication and operation of polyimide bimorph actuators for aciliary motion system," *J. Micro. Electro. Mech. Sys.*, **2** (4), pp. 146-150 (1993).



- [61] J.W. Suh, R.B. Darling, K.F. Bohringer, B.R. Donald, H. Baltes, and G.T.A. Kovacs, "CMOS integrated ciliary actuator array as a general purpose micromanipulation tool for small objects" *J. Micro. Electro. Mech. Sys.*, **8** (4), pp. 483-496 (1999).
- [62] J. Reiter, M. Terry, K.F. Bohringer, J.W. Suh, and G.T.A. Kovacs, "Thermo-bimorph microcilia arrays for small spacecraft docking," *MEMS 2000 - ASME International Mechanical Congress and Exposition.*, pp. 57 – 63 (2000).
- [63] M. Terry, J. Reiter, K.F. Bohringer, J.W. Suh, and G.T.A. Kovacs, "A docking system or microsattellites based on MEMS actuator arrays," *Smart Mater. Struct.*, **10**, pp. 1176-1184 (2001).
- [64] H.Y. Chan and W.J. Li, "A thermally actuated polymer micro robotic gripper for manipulation of biological cells," *Proc. 2003 IEEE Int. Robotics and Automation, Taipei, Taiwan.*, pp.288-293 (2003).
- [65] A. Tuantranont, and V. M. Bright, "Micromachined thermal multimorph actuators fabricated by multi-users MEMS process," *Conference on Industrial Technology, IEEE ICIT '02.*, (2), pp. 941-944 (2002).
- [66] S. Inaba, K. Akaishi, T. Mori, and K. Hane, "Analysis of the resonance characteristics of a cantilever vibrated photothermally in a liquid," *J. App. Phys.*, **73** (6), pp. 2654-2658 (1993).
- [67] P.I. Oden, G.Y. Chen, R.A. Steele, R.J. Warmack and T.Thundat, "Viscous drag measurements utilizing microfabricated cantilevers," *Appl. Phys. Lett.*, **68**, pp. 3814-3816 (1996).
- [68] H. Ito and M. Nakazawa, *Trans. IEICE J71-A*, 1069 (1988) (in Japanese).
- [69] G.Y. Chen, R.J. Warmack , T. Thundat, D.P. Allison, and A. Huang, "Resonance response of scanning force microscopy cantilevers," *Rev. Sci. Instrum.*, **65**, pp. 2532-2537 (1994).
- [70] N. Ahmed, D.F. Nino, and V.T. Moy, "Measurement of solution viscosity by atomic force microscopy," *Rev. Sci. Instrum.*, **72** (6), pp. 2731-2734 (2001).
- [71] J.E. Sader, "Frequency response of cantilever beams immersed in viscous fluids with applications to the atomic force microscope", *J. App. Phys.*, **84**, pp. 64-76 (1998).
- [72] J.W.M. Chon, P. Mulvaney, and J.E. Sader, "Experimental validation of theoretical models for the frequency response of atomic force cantilever beams immersed in fluids," *J. App. Phys.*, **87**, pp. 3978-3988 (2000).

- [73] C.P. Green, and J. E. Sader, "Torsional frequency response of cantilever beams immersed in viscous fluids with applications to the atomic force microscope," *J. App. Phys.*, **92**, pp. 6262-6274 (2002).
- [74] C.P. Green. and J. E. Sader, "Frequency response of cantilever beams immersed in viscous fluids near a solid surface with applications to the atomic force microscope," *J. App. Phys.*, **98**, 114913 (2005).
- [75] C.P. Green, and J. E. Sader, "Small amplitude oscillations of a thin beam immersed in a viscous fluid near a solid wall," *Physics of Fluids.*, **17**, 073102 (2005).
- [76] T. Naik, E.K. Longmire, and S.C. Mantell, "Dynamic response of a cantilever in liquid near a solid wall," *Sens. & Act. A.*, **102**, pp. 240-254 (2003).
- [77] C. Bergaud, and L. Nicu, "Viscosity measurements based on experimental investigations of composite cantilever beam eigenfrequencies in viscous media," *Rev. Sci. Instrum.*, **71**, pp. 2487-2491 (2000).
- [78] W.Y. Shih, X. Li, H. Gu, W.H. Shih, and I.A. Aksay, "Simultaneous liquid viscosity and density determination with piezoelectric unimorph cantilevers," *J. App. Phys.*, **89** (2), pp. 1497-1505 (2001).
- [79] T.L. Wilson, G.A. Campbell, and R. Mutharasan, "Viscosity and density values from excitation level response of piezoelectric-excited cantilever sensors," *Sens. & Act. A.*, **138**, pp. 44-51 (2007).
- [80] R.B. Bhiladvala and Z.J. Wang, "Effect of fluids on the Q-factor and resonance frequency of oscillating micrometer and nanometer scale beams", *Phys. Rev. E.*, **69** 036307 (2004).
- [81] M. Papi, G. Arcovito, M.D. Spirito, M. Vassalli, and B. Tiribilli, "Fluid viscosity determination by means of uncalibrated atomic force microscopy cantilevers," *Appl. Phys. Lett.*, **88**, 194102 (2006).
- [82] N. McLoughlin, S.L. Lee, and G. Hahner, "Simultaneous determination of density and viscosity of liquids based on resonance curves of uncalibrated microcantilevers," *Appl. Phys. Lett.*, **89**, 184106 (2006).
- [83] C. Vančura, I. Dufour, S.M. Heinrich, F. Josse, and A. Heirlemann, "Analysis of resonating microcantilevers operating in a viscous liquid environment," *Sens. & Act. A.*, **141**, pp. 43-51 (2008).
- [84] G. Stemme, "Resonant Silicon Sensors", *J. Micromech. Microeng.*, **1** pp. 113-125 (1991).

- [85] L.H. Han and T.J. Lu, "Modeling and optimal design of multilayer cantilever microactuators," *Mater. Res. Soc. Symp. Proc.*, **795**, pp. 1–6 (2004).
- [86] X. Yin, "Design and analysis of a compliant grasper for handling live objects" Thesis for Ph. D. at the Georgia Institute of Technology, (2003).
- [87] K.E. Bishop, and D.C. Drucker, "Large deflection of cantilever beams," *Quarterly of applied Math.*, 3 (3), pp 272-275, (1945).
- [88] T. Beléndez, C. Neipp, and A. Beléndez, "Large and small deflections of a cantilever beam," *Eur. J. Phys.*, **23**, pp. 371-379, (2002).
- [89] J. Thayson, "Cantilever for biochemical sensing integrated in a microliquid handling system," Thesis for Ph. D at the Technical University of Denmark, (2001).
- [90] I. Aștefănoaei, D. Radu, and H. Chiriac, "On dc joule-heating effects in amorphous glass-covered  $\text{Fe}_{77.5}\text{Si}_{7.5}\text{B}_{15}$  microwires," *J. Phys. D: Appl. Phys.*, **38**, pp. 235–243 (2005).
- [91] I. Aștefănoaei, D. Radu, and H. Chiriac, "Internal stress distribution in DC joule-heated amorphous glass-covered microwires," *J. Phys. Condens. Matter.*, **18**, pp. 2689–2716 (2006).
- [92] F.P. Incropera, and D.P. De Witt, "Introduction to Heat Transfer", Second Edition, John Wiley & Sons, New York, NY, (1990).
- [93] G.W.C Kaye, and T.H. Laby, "Tables of physical and chemical constants", 16<sup>th</sup> Edition, Longman, (1995).
- [94] A.M. James, and M.P. Lord, "Macmillian's chemical and physical data", London, Macmillian, (1992).
- [95] HDMicrosystems. *Product Information and Process Guideline. PI2560 Product bulletin series*. Available:  
[http://hdmicrosystems.com/HDMicroSystems/en\\_US/tech\\_info/tech\\_info.html](http://hdmicrosystems.com/HDMicroSystems/en_US/tech_info/tech_info.html)  
Last accessed: 26<sup>th</sup> May 2009.
- [96] HDMicrosystems. *Product Information and Process Guideline. PI2610 Product bulletin series*. Available:  
[http://hdmicrosystems.com/HDMicroSystems/en\\_US/tech\\_info/tech\\_info.html](http://hdmicrosystems.com/HDMicroSystems/en_US/tech_info/tech_info.html)  
Last accessed: 26<sup>th</sup> May 2009.
- [97] Silex Microsystems, "status-report 2008-02-22.pdf", received 22/02/2008
- [98] D.C. Giancoli, "Physics", Fourth Edition, Prentice Hall, (1995).
- [99] Goodfellow. *Material Information Sheet*. Available:  
<http://www.goodfellow.com/E/Constantan-ResistanceAlloy.html>. Last accessed

29 Jan 2009.

- [100] B.S. Verma, and S.K. Sharma, "Effect of thermal strains on the temperature coefficient of resistance," *Thin Solid Films.*, **5**, R44, (1970).
- [101] P.M. Hall. "The effect of expansion mismatch on temperature coefficient of resistance of thin films," 1968 *Appl. Phys. Lett.*, **12**, pp. 212 (1968).
- [102] F. Warkusz, "The size effect and the temperature coefficient of resistance in thin films," *J. Phys. D. Appl. Phys.*, **11**, pp. 689-694, (1978).
- [103] K. Fuchs, "The conductivity of thin metallic films according to the electron theory of metals," *Proc. Camb. Phil. Soc.* **34**, pp. 100-108, (1938).
- [104] E.H. Sondheimer, "The mean free path of electrons in metals," *Adv. Phys.* **1**, pp. 1-42 (1952).
- [105] F. Warkusz, "The size effect and the temperature coefficient of total resistance in thin metal film," *J. Phys. D. Appl. Phys.*, **11**, pp. 2035-2041, (1978).
- [106] L. Miao, Z.L. Dong, and H. Chan, "Modeling the micro robotic gripper using microscopic images sequence for manipulation of biological cells," *Proc. of Intelligent Mechatronics and Automation.* pp. 239-243, (2004).
- [107] F.C.A. Groen, I.T. Young, and G. Ligthart, "A Comparison of Different Focus Functions for Use in Autofocus Algorithms," *Cytometry.*, **6** pp. 81-91 (1985).
- [108] L. Firestone, K. Cook, K. Culp, N. Talsania, and K. Preston Jr, "Comparison of Autofocus Methods for Automated Microscopy," *Cytometry* **12**, pp. 195-206, (1991).
- [109] J.H. Price and D.A. Gough, "Comparison of Phase-Contrast and Fluorescence Digital Autofocus for Scanning Microscopy," *Cytometry.*, **16**, pp. 283-297, (1994).
- [110] J.M. Geusebroek, F. Cornelissen, A.W.M. Smeulders, and H. Geerts, "Robust Autofocusing in Microscopy," *Cytometry.*, **39**, pp. 1-9, (2000).
- [111] J.F. Brenner, B.S. Dew, J.B. Horton, T. King, P.W. Nuerath, and W.D. Selles, "An automated microscope for cytologic research," *J. Histochem. Cytochem.*, **21** (1), pp. 100-111, (1976).
- [112] A. Erteza, "Sharpness index and its application to focus control," *Appl. Opt.*, **15**, pp. 877-881, (1976).
- [113] A. Erteza, "A Depth of convergence of a sharpness index autofocus system," *Appl. Opt.*, **16** pp. 2273-2278, (1977).
- [114] R.A. Muller, A. Buffington, "Real-time correction of atmospherically degraded telescope images through image sharpening," *J. Opt. Soc. Am.*, **64**, pp.1200-

- 1210, (1974).
- [115] R.J. Dunn, “*Microcantilever Testing Presentation*” Microvisk South 22-02-07.ppt. (2007).
  - [116] DOW Chemical Company, *Viscosity of Aqueous Glycerine Solutions*. Available: <http://www.dow.com/glycerine/resources/table18.htm>. Last Accessed 22-03-09
  - [117] DOW Chemical Company, *True Coefficient of Thermal Conductivity of Glycerine Solutions*. Available: <http://www.dow.com/glycerine/resources/table13.htm>. Last Accessed 22-03-09
  - [118] P.A. Tipler, “Physics for Scientists and Engineers”, Fourth Edition., W.H. Freeman, (1999).
  - [119] M.C. Righetti, G Salvetti, and E. Tombari, “Heat capacity of glycerol from 298 to 383 K,” *Thermochimica Acta.*, **316** (2), pp. 193-195, (1998).
  - [120] J. Booth, “S-chip optimisation, Microvisk South 18th-19th October 2007”, File: 071022\_S chip optimisation\_JB.pdf, (2007).
  - [121] D.Hansen, C.C. Ho, and R.C. Kantayya, “Thermal conductivity of high polymers - The influence of molecular weight,” *Polymer Engineering and Science*, **6** (3), pp. 260-262, (1966).
  - [122] K. Venkateshan, and G.P. Johari, “Thermal conductivity of a polymerizing liquid,” *J. Chem. Phys.*, **125**, 054907 (2006).
  - [123] Vilastic Scientific Inc, *Blood Viscoelasticity: Frequently Asked Questions*. Available: [http://www.vilastic.com/FAQ\\_Blood.htm](http://www.vilastic.com/FAQ_Blood.htm). Last Accessed 27-05-09.
  - [124] W.L. Chandler, and G. Schmer. “Evaluation of a new dynamic viscometer for measuring the viscosity and whole blood and plasma,” *Clinical Chemistry.*, **32**, pp. 505-507 (1986).
  - [125] R. Dunn, “*Whole Blood Platform ver1.12*”, File:Whole Blood Platform ver1.12.doc, (2007).
  - [126] Sysmex Corporation, *Automated Blood Coagulation Analyzer*. Available: <http://www.sysmex.com/scj/products/ca-7000/index.html>. Last Accessed 27-05-09.
  - [127] J. Booth, “*Microvisk clinical trial at Queen Mary's School of Medicine and Dentistry, The Royal London Hospital. 2<sup>nd</sup> to 5<sup>th</sup> July 2007*”, File: 070824\_Full report\_Royal London Hospital Trial\_July 07.doc, (2007).
  - [128] World Health Organisation, “Guidelines for thromboplastins and plasma used to control oral anticoagulant therapy”, *WHO Technical Report Series*, **889**,

- Annex 3, pp. 64-91 (1999).
- [129] D.A. Taberner, L. Poller, J.M. Thomson, K.V. Darby, "Effect of international sensitivity index (ISI) of thromboplastins on precision of international normalized ratios (INR)," *J Clin Pathol.*, **42**, pp. 92-96 (1989).
  - [130] US Food and Drug Administration, *Roche Coaguchek XS FDA 510(K) Summary K06292*. Available: <http://www.fda.gov/cdrh/pdf6/K062925.pdf>. Last Accessed 27-05-09.
  - [131] Hemosense. *INRatio Technical Bulliten 106*. Available: [http://www.hemosense.com/docs/5500287\\_TechBulletin106\\_AccuracyPrecisionRevB.pdf](http://www.hemosense.com/docs/5500287_TechBulletin106_AccuracyPrecisionRevB.pdf). Last Accessed 27-05-09.
  - [132] ITC, *A comparative evaluation of three point-of-care prothrombin time tests, Protime, Protime 3, and INRatio, to a laboratory reference standard*. Available: [http://www.protimesystem.com/support/A\\_Comparative\\_Evaluation.pdf](http://www.protimesystem.com/support/A_Comparative_Evaluation.pdf). Last Accessed 27-05-09.
  - [133] NHS Purchasing and Supply Agency Centre for Evidence Based Purchasing, *Report 06034 CoaguChek XS System May 2006*. Available: [www.pasa.nhs.uk/pasa/Doc.aspx?Path=%5BMN%5D%5BSP%5D/NHSprocurement/CEP/POC/Report%2006034.pdf](http://www.pasa.nhs.uk/pasa/Doc.aspx?Path=%5BMN%5D%5BSP%5D/NHSprocurement/CEP/POC/Report%2006034.pdf). Last Accessed 27-05-09.
  - [134] NHS Purchasing and Supply Agency Centre for Evidence Based Purchasing, *Report 06007 Hemosense INratio March 2006*. Available: [www.pasa.nhs.uk/pasa/Doc.aspx?Path=%5BMN%5D%5BSP%5D/NHSprocurement/CEP/POC/Report\\_06007.pdf](http://www.pasa.nhs.uk/pasa/Doc.aspx?Path=%5BMN%5D%5BSP%5D/NHSprocurement/CEP/POC/Report_06007.pdf). Last Accessed 27-05-09.
  - [135] NHS Purchasing and Supply Agency Medicines and Healthcare Products Regulatory Agency. *MHRA 04082 ProTime3 Microcoagulation System*. Available: [www.pasa.nhs.uk/pasa/Doc.aspx?Path=%5BMN%5D%5BSP%5D/NHSprocurement/CEP/POC/MHRA%2004082.pdf](http://www.pasa.nhs.uk/pasa/Doc.aspx?Path=%5BMN%5D%5BSP%5D/NHSprocurement/CEP/POC/MHRA%2004082.pdf). Last Accessed 27-05-09.
  - [136] R.H. Ibbotson, R.J. Dunn, V. Djakov, P.Ko. Ferrigno, and S.E. Huq, "Polyimide microcantilever surface stress sensor using low-cost, rapidly-interchangeable, spring-loaded microprobe connections," *Microelectronic Engineering.*, **85** (5-6), pp. 1314-1317 (2008).
  - [137] R. Linnemann, T. Gotszalk, I.W. Rangelow, P. Dumania, and E. Oesterschulze, "Atomic force microscopy and lateral force microscopy using piezoresistive cantilevers," *J. Vac. Sci. Technol.*, **14** (2), pp. 856-860 (1996).
  - [138] R.J. Dunn, "*Microcantilever Testing Presentation*" Microvisk South 15-11-07.ppt. (2007).

- [139] H. P. Lang, R. Berger, C. Andreoli, J. Brugger, M. Despont, P. Vettiger, Ch. Gerber, J. K. Gimzewski, J. P. Ramseyer, E. Meyer, and H.-J. Güntherodt, "Sequential position readout from arrays of micromechanical cantilever Sensors," *Appl. Phys. Lett.*, **72** (3), pp. 383-385 (1998).
- [140] S. C. Minne, G. Yaralioglu, S. R. Manalis, J. D. Adams, J. Zesch, A. Atalar, and C. F. Quate, "Automated parallel high-speed atomic force microscopy," *Appl. Phys. Lett.*, **72** (18), pp. 2340-2342 (1998).
- [141] P. Vettiger, T. Albrecht, M. Despont, U. Drechsler, U. Durig, B. Gotsmann, D. Jubin, W. Haberle, M.A. Lantz, H. Rothuizen, R. Stutz, D. Wiesmann, G.K. Binnig, P. Bachtold, G. Cherubini, C. Hagleitner, T. Loeliger, A. Pantazi, H. Pozidis, and E. Eleftheriou, "Thousands of microcantilevers for highly parallel and ultra-dense data storage," *Proc. IEEE International Electron Devices Meeting 2003* 32.1.1-4, (2003).
- [142] H.-J. Nama, Y.-S. Kima, C. S. Lee, W.-H. Jin, S.-S. Jang, I.-J. Choa, J.-U. Bua, W.B. Choi, S.W. Choi, "Silicon nitride cantilever array integrated with silicon heaters and piezoelectric detectors for probe-based data storage," *Sensors and Actuators A*, **134**, pp. 329-333 (2007).
- [143] E.M. Chow, H.T. Soh, H.C. Lee, J.D. Adams, S.C. Minne, G. Yaralioglu, A. Atalar, C.F. Quate, and T.W. Kenny, "Integration of through-wafer interconnects with a two-dimensional cantilever array," *Sensors and Actuators*, **83**, pp.118–123 (2000).
- [144] R. Pedrak, Tzv. Ivanov, T. Gotszalk P. Hudek, and I.W. Rangelow, "Micromachined Atomic force microscopy sensor with integrated piezoresistive sensor and thermal bimorph actuator for high-speed tapping-mode AFM and phase-imaging in higher eigenmodes," *J. Vac. Sci. Technology. B*, **21** (6), pp.3102-3107 (2003).
- [145] R. Pechmann, J. M. Köhler, W. Fritzsche, A. Schaper, and T. M. Jovin, "The Novolever: A new cantilever for scanning force microscopy microfabricated from polymeric materials," *Rev. Sci. Instrum.* **65**, pp. 3702-3707 (1994).
- [146] G. Genolet, J. Brugger, M. Despont, U. Drechsler, P. Vettiger, N. F. de Rooij, and D. Anselmetti, "Soft, entirely photoplastic probes for scanning force microscopy," *Rev. Sci. Instrum.*, **70** ( 5), pp. 2398-2401 (1999).
- [147] G. Genolet, M. Despont, P. Vettiger, D. Anselmetti, and N. F. de Rooij, "All-photoplastic, soft cantilever cassette probe for scanning force microscopy," *J. Vac. Sci. Technol. B*, **18** (2), pp.617-620 (2000).

- [148] B. Mitra and A. Gaitas, "Thermally actuated tapping mode atomic force microscopy with polymer microcantilevers," *Rev. Sci. Instrum.* **80**, 023703 (2009).
- [149] A. Gaitas and Y.B. Gianchandani, "An experimental study of the contact mode AFM scanning capability of polyimide cantilever probes", *Ultramicroscopy* **106**, pp.874-880 (2006).
- [150] T. Hantschel, E.M. Chow, D. Rudolph, C. Shih, L. Wong, and D.K. Fork, "Bent metal beams as probes for high-topography substrates in atomic force microscopy (AFM)" . *Micro- and Nanoengineering Conference 2002*; September 16-19; Lugano; Switzerland. (2002).
- [151] T. Hantschel, E.M. Chow, D. Rudolph, C. Shih, L. Wong, and D.K. Fork, "Stressed-metal NiZr probes for atomic force microscopy" *Microelectronic Engineering.*, **67-68** (16): pp. 803-809 (2003).



## Appendix A – Neutral Axis

The neutral axis is defined as the plane in which the resultant axial force acting on the cross section is zero. For a microcantilever with  $n$  layers

$$\int_1 \sigma_1 dA + \int_2 \sigma_2 dA + \dots \int_n \sigma_n dA = 0 \quad (\text{A.1})$$

where  $\sigma_n$  is the normal stress in the  $n^{\text{th}}$  layer and  $A$  is the layer cross sectional area. If the beam is assumed to obey Hookes law the normal stress is equal to

$$\sigma_i = -E_i \varepsilon_i = -E_i \frac{\hat{y}_i}{r} \quad (\text{A.2})$$

where  $\varepsilon_i$  is the longitudinal strain,  $1/r$  is the beam curvature,  $E_i$  is the Young's modulus, and  $\hat{y}_i$  is the distance from the neutral axis to the centre of the layer. Substituting A.2 into equation A.1

$$-\int_1 E_1 \frac{\hat{y}_1}{r} dA - \int_2 E_2 \frac{\hat{y}_2}{r} dA - \dots \int_n E_n \frac{\hat{y}_n}{r} dA = 0 \quad (\text{A.3})$$

The curvature along the beam is constant and therefore A3 can simplify to

$$\int_1 E_1 \hat{y}_1 dA + \int_2 E_2 \hat{y}_2 dA + \dots \int_n E_n \hat{y}_n dA = 0 \quad (\text{A.4})$$

The distance from the neutral axis to the centre of each layer can be written as

$$\hat{y}_n = (h - \sum_{i=1}^{n-1} t_i - \frac{t_n}{2}) \quad (\text{A.5})$$

where  $h$  is the distance from the top surface of the microcantilever to the plane of the neutral axis. Substituting the form of equation A.5 into A.4 and integrating over the area of the layer to give the width multiplied by thickness, equation A.4 becomes

$$E_1(h - \frac{t_1}{2})w_1t_1 + E_2(h - t_1 - \frac{t_2}{2})w_2t_2 + \dots E_n(h - \sum_{i=1}^{n-1}t_i - \frac{t_n}{2})w_nt_n = 0 \quad (\text{A.6})$$

Identifying repeating terms for each added layer in equation A.6 and collecting

$$\sum_{i=1}^n E_i h w_i t_i - \sum_{i=1}^n E_i w_i \frac{t_i^2}{2} - \sum_{i=2}^n \left( E_i w_i t_i \sum_{m=1}^{i-1} t_m \right) = 0 \quad (\text{A.7})$$

Rearranging for the neutral axis  $h$  gives

$$h = \frac{\sum_{i=1}^n E_i w_i \frac{t_i^2}{2} + \sum_{i=2}^n \left( E_i w_i t_i \sum_{m=1}^{i-1} t_m \right)}{\sum_{i=1}^n E_i w_i t_i} \quad (\text{A.8})$$

## Appendix B – Static Bimorph Equation

It can be shown that for small deflections the shape of a released multilayer beam along the neutral axis is given by the Euler-Bernoulli equation

$$\frac{d^2 y}{dx^2} = \frac{1}{r} = \frac{M(E_1, w_1, t_1 \dots E_i, w_i, t_i)}{EI(E_1, w_1, t_1 \dots E_i, w_i, t_i)} \quad [\text{B.1}]$$

where  $d^2 y / dx^2$  is the curvature at a point on the beam,  $M(E_1, t_1 \dots E_i, t_i)$  is the net bending moment acting on the beam due to residual material stress, and  $EI(E_1, t_1 \dots E_i, t_i)$  is the composite flexural rigidity of the beam based on the Young's modulus and second moment of area of each layer.  $E_1$ ,  $w_1$  and  $t_1$  are the Young's modulus, width and thickness of the top layer,  $E_2$ ,  $w_2$  and  $t_2$  are the Young's modulus, width and thickness of the bottom layer.

The composite flexural rigidity of the beam is equal to

$$EI(E_1, w_1, t_1 \dots E_i, w_i, t_i) = \sum_{i=1}^n E_i I_i \quad \text{where} \quad I_i = \frac{1}{12} w_i t_i^3 + w_i t_i \hat{y}_i^2 \quad [\text{B.2}]$$

where the parallel axis theory is used to find the second moment of area  $I_i$  around an arbitrary axis, taken in this case as the neutral axis of the beam.  $\hat{y}_i$  is the distance of the area centroid to the neutral axis. For a bimorph structure the flexural rigidity can be re-written as

$$EI = E_1 \frac{1}{12} w_1 t_1^3 + E_1 w_1 t_1 \hat{y}_1^2 + E_2 \frac{1}{12} w_2 t_2^3 + E_2 w_2 t_2 \hat{y}_2^2 \quad [\text{B.3}]$$

Where the distance to the neutral axis position  $h$  is given by

$$\hat{y}_1 = h - t_1 / 2 \quad \text{and} \quad \hat{y}_2 = h - t_1 - t_2 / 2 \quad [\text{B.4}]$$

From Appendix A the neutral axis of a bimorph is found using

$$h = \frac{1}{2} \frac{E_1 w_1 t_1^2 + E_2 w_2 t_2^2 + 2E_2 w_2 t_2 t_1}{E_1 w_1 t_1 + E_2 w_2 t_2} \quad [\text{B.5}]$$

Substituting equation B.4 into B.3

$$EI = E_1 \frac{1}{12} w_1 t_1^3 + E_1 w_1 t_1 (h - t_1 / 2)^2 + E_2 \frac{1}{12} w_2 t_2^3 + E_2 w_2 t_2 (h - t_1 - t_2 / 2)^2 \quad [\text{B.6}]$$

Substituting equation B.5 into B.6

$$\begin{aligned} EI = & E_1 \frac{1}{12} w_1 t_1^3 + E_1 w_1 t_1 \left( \frac{1}{2} \frac{E_1 w_1 t_1^2 + E_2 w_2 t_2^2 + 2E_2 w_2 t_2 t_1}{E_1 w_1 t_1 + E_2 w_2 t_2} - t_1 / 2 \right)^2 \\ & + E_2 \frac{1}{12} w_2 t_2^3 + E_2 w_2 t_2 \left( \frac{1}{2} \frac{E_1 w_1 t_1^2 + E_2 w_2 t_2^2 + 2E_2 w_2 t_2 t_1}{E_1 w_1 t_1 + E_2 w_2 t_2} - t_1 - t_2 / 2 \right)^2 \end{aligned} \quad [\text{B.7}]$$

Working through the squared factors and simplifying, the flexural rigidity can be written as

$$\frac{1}{12} \left[ \frac{E_1 E_2 w_1 w_2 t_1 t_2}{E_1 w_1 t_1 + E_2 w_2 t_2} \right] \left( \frac{E_2 w_2 t_2^3}{E_1 w_1 t_1} + \frac{E_1 w_1 t_1^3}{E_2 w_2 t_2} + 6t_1 t_2 + 4t_2^2 + 4t_1^2 \right) \quad [\text{B.8}]$$

The initial moment acting on the bimorph can be written as

$$M = \sigma_1 \hat{y}_1 w_1 t_1 + \sigma_2 \hat{y}_2 w_2 t_2 \quad \text{where} \quad \sigma_i = -E_i (\varepsilon_i + \Delta\varepsilon - \frac{\hat{y}_i}{r}) \quad [\text{B.9}]$$

where  $\varepsilon_i$  is the mean strain due to process conditions,  $\Delta\varepsilon$  is the strain variation when the beam is released, and  $-\hat{y}_i/r$  is the strain due to the curvature  $r$  of the cantilever [58]. Substituting B.4 into B.9 and noting that the unreleased microcantilever has effectively infinite curvature

$$M = -E_1 (\varepsilon_1 + \Delta\varepsilon) (h - t_1 / 2) w_1 t_1 - E_2 (\varepsilon_2 + \Delta\varepsilon) (h - t_1 - t_2 / 2) w_2 t_2 \quad [\text{B.10}]$$

Substituting equation B.5 into B.10

$$\begin{aligned}
M = & -E_1(\varepsilon_1 + \Delta\varepsilon)\left(\frac{1}{2}\frac{E_1w_1t_1^2 + E_2w_2t_2^2 + 2E_2w_2t_2t_1}{E_1w_1t_1 + E_2w_2t_2} - t_1/2\right)w_1t_1 \\
& - E_2(\varepsilon_2 + \Delta\varepsilon)\left(\frac{1}{2}\frac{E_1w_1t_1^2 + E_2w_2t_2^2 + 2E_2w_2t_2t_1}{E_1w_1t_1 + E_2w_2t_2} - t_1 - t_2/2\right)w_2t_2
\end{aligned} \tag{B.11}$$

Simplifying the initial bending moment, equation B.11 can be re-written as

$$M = \frac{1}{2}\left[\frac{E_1E_2w_1w_2t_1t_2}{E_1w_1t_1 + E_2w_2t_2}\right](t_1 + t_2)(\varepsilon_1 - \varepsilon_2) \tag{B.12}$$

Substituting the Moment [B.12] and flexural rigidity [B.8] into equation [B.1]

$$\frac{1}{r_{initial}} = \frac{M}{EI} = \frac{\frac{1}{2}\left[\frac{E_1E_2w_1w_2t_1t_2}{E_1w_1t_1 + E_2w_2t_2}\right](t_1 + t_2)(\varepsilon_1 - \varepsilon_2)}{\frac{1}{12}\left[\frac{E_1E_2w_1w_2t_1t_2}{E_1w_1t_1 + E_2w_2t_2}\right]\left(\frac{E_2w_2t_2^3}{E_1w_1t_1} + \frac{E_1w_1t_1^3}{E_2w_2t_2} + 6t_1t_2 + 4t_2^2 + 4t_1^2\right)} \tag{B.13}$$

This simplifies to the familiar bimorph equation

$$\frac{1}{r_{initial}} = \frac{M}{EI} = \frac{6(t_1 + t_2)(\varepsilon_1 - \varepsilon_2)}{\left(\frac{E_2w_2t_2^3}{E_1w_1t_1} + \frac{E_1w_1t_1^3}{E_2w_2t_2} + 6t_1t_2 + 4t_2^2 + 4t_1^2\right)} \tag{B.14}$$

## Appendix C – Support Letter

$\alpha\beta\chi\delta$

JP/sh

18 December 2007

Mr. J. Curtis  
Microvisk Ltd.  
Building 173  
Curie Avenue  
Harwell International Business Centre  
Didcot  
Oxfordshire  
OX11 0DG

**HAEMOPHILIA CENTRE**  
Professor K J Pasi  
Professor of Haemostasis and Thrombosis

Whitechapel  
London  
E1 1BB

Tel: 020 7377 7000 Ext 3496  
Fax: 020 7377 7182

e-mail: k.j.pasi@qmul.ac.uk

Dear John

### Microcantilever-Based Clotting Detection System (Microvisk Technology)

Thank you for giving Katie Langley, Sean Bevan and myself the opportunity to come down and visit you and review all the data on the recent work that we did together. The technology is clearly very exciting and provides the opportunity for a very promising potential product for assessment of coagulation and, in the short-term, INR values.

The technology has proven to be very promising, robust and equally provides us with the opportunity to look forward for other significant applications within coagulation, to produce novel systems and more rapid ways of assessing coagulation based on this unique technology.

We look forward to taking this forward with you in the coming year.

Kind regards

Yours sincerely,



John Pasi

$\rho\eta$

The Royal Hospital of St. Bartholomew, The Royal London Hospital,  
The London Chest Hospital, The Queen Elizabeth Children's Service.